Indian Journal of
Engineering, Science, and
Technology

A Refereed Research Journal

Indian Journal of Engineering, Science, and Technology

CONTENTS

Excerpt from the Proceeding of National Conference

Aeroacoustic Studies of an Axisymmetric Rectangular Cavity in a Ducted Flow

M.Raju[1], M.Thirumoorthy[2] and Dr.K.M.Parammasivam[3]

[1&3]Associate Professor, Department of Aerospace Engineering, Madras Institute of Technology,
Chennai - 600 044, Tamil Nadu
[2]Scientist, ASL, DRDO, Hyderabad - 500 005, India.

Abstract

Aeroacoustic studies were carried out for a flow through a duct with axisymmetric rectangular cavity. The effect of velocities on the acoustic frequency and amplitude was studied by using the standard numerical simulation FLUENT 14.5 software packages. Time step size is calculated based on the cavity width and velocity of the flow. The vortex shedding frequency was measured at different location on the numerical simulation model by using the acoustic model and FFT plot. The shedding of vortices in the cavity zone and the impingement of the vortices in the cavity wall are the main acoustic source which causes the acoustic oscillation. The acoustic pressure and dominant frequency in the flow were obtained from the simulation due to the presence of the rectangular cavity. The experimental values were agreeing with the predicted computational values within 5% error.

Keywords: Aero acoustics, Axisymmetric rectangular cavity, Computational fluid dynamics, Vortex shedding.

1. INTRODUCTION

The operation of the solid rocket motor is governed by the initial internal shape of the propellant grain since the propellant grain is the main source of energy for the solid rocket motor to produce required amount of thrust. The vortex shedding induced acoustic oscillation is a cause of concern for the solid rocket motors where the oscillations in thrust may produce detrimental effect to the payload. The strength of the vortex shedding will be more if the surface of the propellant has the shape which will lead to flow separation. There is little attention to the above said phenomena of vortex shedding that is caused due to change in the shape of the propellant like rectangular shaped axisymmetric cavities. These rectangular axisymmetric cavities are used in solid rocket motors to maximize the burn surface area with minimum propellant volume. Numerical simulations of these axisymmetric cavities were carried out for cold flow conditions, where it can be compared with experimental data. The present studies of shear layer oscillations helps in predicting the acoustic oscillations of these cavities.

2. SOLUTION METHODOLOGY

The two dimensional axisymmetric [9] viscous flow analyses were carried out using FLUENT 14.5. The simulation involves a duct with axisymmetric rectangular cavity.

2.1 PROBLEM DESCRIPTION

The diameter of the duct for the numerical simulation D=3.44W, the rectangular cavity is located 1.29W from the inlet. The sensors are located to capture the acoustic parameters of the flow field due to the influence of the vortex shedding in the cavity on the acoustic property. The ratio of width to height of the rectangular cavity is 1.16. The length of the duct downstream of the cavity is 2.3W.

2.2 GRID STARTEGY

The grid generation for the numerical simulation was carried out by using standard meshing software Gambit 2.2.30. The boundary layer velocity has to be predicted accurately in order to capture accurately the vortex shedding phenomenon. The final boundary layer mesh has been arrived based on the procedure as given below. The boundary layer domain was initially meshed coarsely and the steady simulations were carried out. The wall y^+ values were determined and the cells near the walls were refined and the simulations were repeated. The procedure was repeated until the values of wall y^+ were ~1 which was mentioned in reference. The boundary layer mesh was carried for the first layer thickness, growth rate and number of layers 0.01, 1.2 and 20 respectively. The mesh with 41000 cells and boundary layer is shown in figure1.

M.Raju[1], M.Thirumoorthy[2] and Dr.K.M.Parammasivam[3]
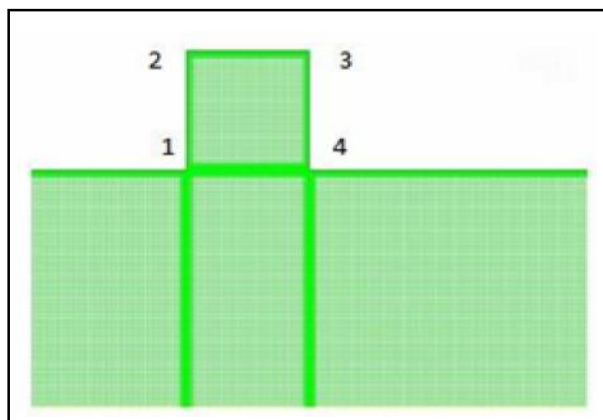
Fig.1 Grid for the numerical simulation

The grids near the wall have to be refined where the vortex shedding impinges on the wall at the trailing edge of the cavity. The grid near the leading edge of the cavity should be fine to capture the flow separation where the vortices were generated. The grids should not be very fine since the vortices will be not captured due to numerical dissipation. Grid independent studies were carried out with mesh size of 41000, 82000, 130000 and the results were within 1% error.

2.3 BOUNDARY CONDITIONS

The velocity was given as inlet boundary condition. The numerical model was considered as 2D axisymmetric model and the axisymmetric boundary condition was given at the midline of the duct. The basic assumption here is the ring vortices due to axisymmetric condition do not interact with each other. The 3D model work is currently in progress which will give the effect of ring vortices in azimuthal direction. The no slip boundary condition was given at the wall. The exit of the duct was given as pressure outlet.

2.4 SOLVER CONDITIONS

Implicit time scheme was used to march the solution in time. The resulting implicit equations were solved iteratively at each time step level before moving to the next time step. The advantage of the implicit scheme is that it is unconditionally stable with respect to time step size. The time step size is the main parameter for the unsteady Aeroacoustic simulation which was calculated as mentioned in the literature for the rectangular cavity. Time step size, $t = (0.01W)/U$, Where W = width of the rectangular cavity& U = flow velocity. The unsteady simulation was carried out based on the above mentioned time step size formula. As the velocity increases, the time

step size will decrease. Hence the simulation time will be very high to calculate the flow time of milliseconds. The simulation was carried out for different velocities ranges from 30m/s to 120m/s in increasing order of 30m/s. The time step size calculated for simulation of unsteady analysis was of the order of 10^-5 to 10^-6. The unsteady simulations were carried out for the time of 0.03s. The Simulations were carried out with ANSYS (Fluent) with 8 node, 128 core (each node is 2*8core), High Performance Computing.

2.5 TURBULENCE MODELING

The standard K-Epsilon turbulence model was used to model turbulence. The two additional transport equations for the turbulent kinetic energy K and the turbulence dissipation rate were also solved along with the transport equations. Initially, the time marching of the governing equations was carried out until a steady state solution is reached. The steady simulations were carried out first to conserve the continuity, energy and momentum equations.

2.6 ACOUSTIC MODEL AND RECEIVER FIXING

Acoustics-Ffowcs-Williams & Hawking model was used to capture the acoustic parameters at required location with the help of receiver fixing. Totally six receivers were fixed to find the variations of the amplitudes along the wall due to vortex shedding. Four receivers (Rec_1-4) were fixed at corners of the rectangular cavity and another fixed 7mm (Rec_5) and 14mm (Rec_6) after the cavity location. The acoustic parameters at the above corresponding locations were obtained after the unsteady solution.

3. RESULTS AND DISCUSSIONS
3.1 FLOW RESULTS

The frequency of acoustic oscillations was obtained by using the Fast Fourier Transform 9FFT) which is normally used for acoustic analysis in experiments. The typical acoustic pressure vs time was shown in figure 2. The frequencies for different velocities at receiver location, 7mm (rec_5) after cavity were shown in figure 3. The first dominant frequency and amplitude increases for the increase in velocity.
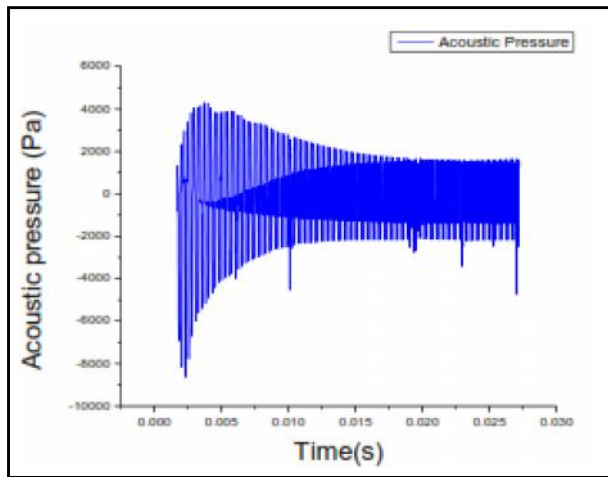
Fig.2 Acoustic pressure Vs Time

As the velocity increases, the jump in frequency from one mode to another mode occurred and the corresponding increase in amplitude also noticed.

The frequencies for the six receiver location are shown in figure 4. The maximum amplitude was found in the receiver location 2 and receiver location 3 because the maximum vortex takes place near the location of those receivers.
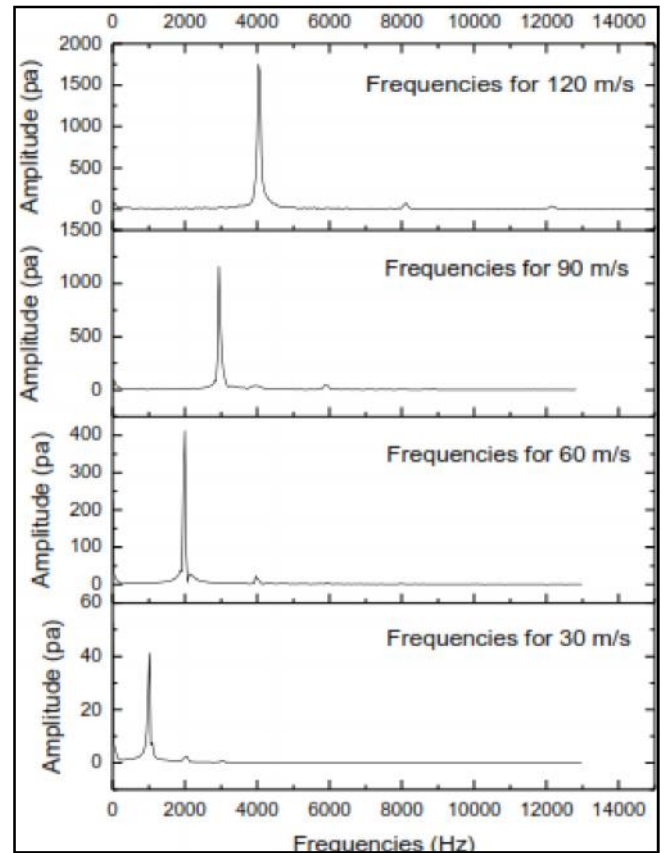
Fig.3 Frequencies for different velocities
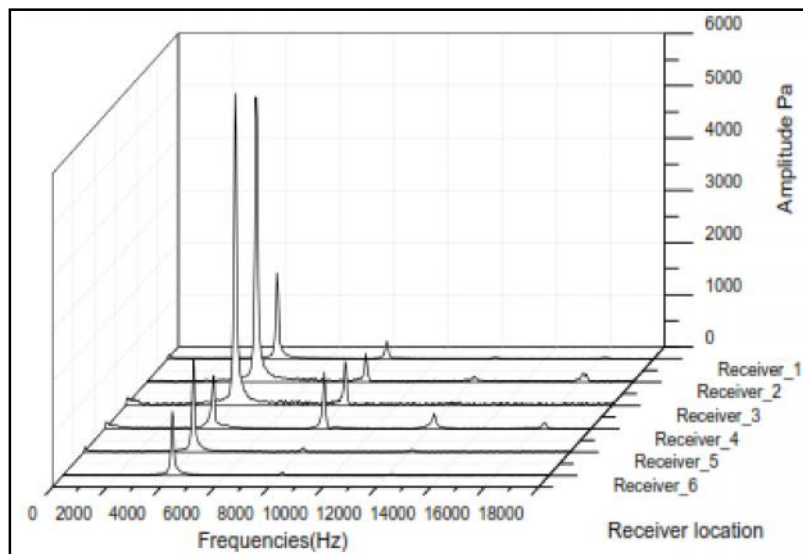
Fig.4 Frequencies for different Receiver location

The amplitude from the receiver 4 to receive 5 gets decay because the intensity of the vortex was reduced along the length after the cavity. After certain length the amplitude decays exponentially due to the absence of the vortex. The velocity vector plot shows the vortex region in the rectangular cavity. The vortex level in the each corner of the cavity varies which causes the amplitude variation in the edge of the cavity.

3.2 FLOW PATTERNS

The velocity vector for flow velocity of 120m/s was shown in figure 5. The vortex region of the flow pattern near the corner was shown in figure 6.

M.Raju[1], M.Thirumoorthy[2] and Dr.K.M.Parammasivam[3]
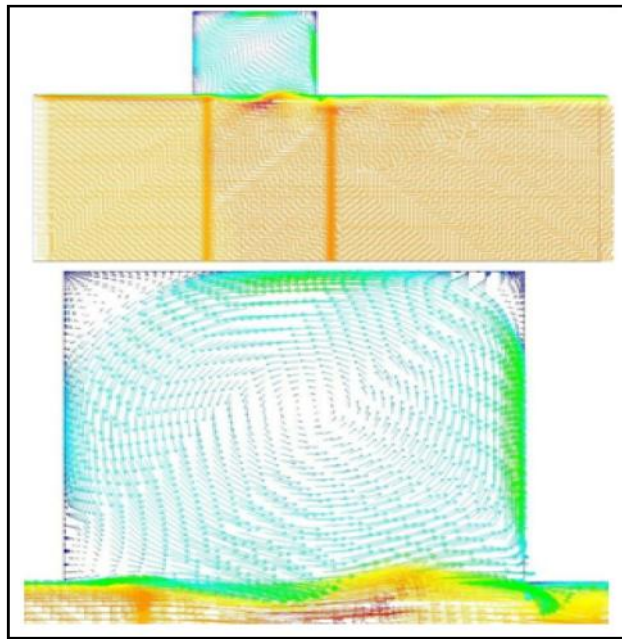
Fig.5 velocity vector for the velocity 120 m/s
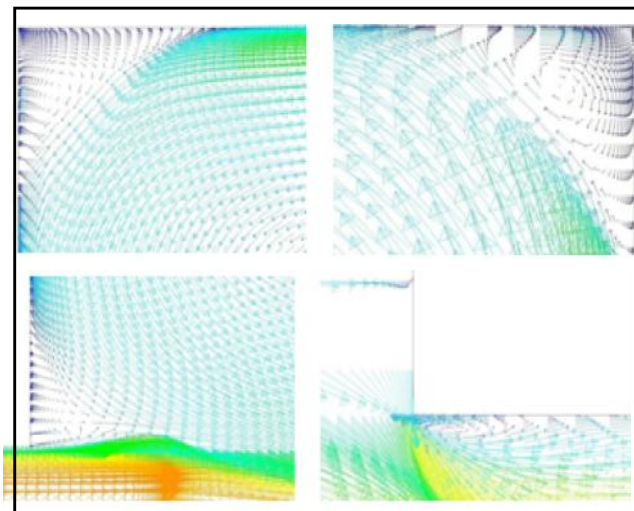
Fig. 6 Vortex pattern at the four corner of the rectangular cavity

4. VALIDATION

The experiments were carried out with PCB Piezoelectric sensors along the length and circumference of the duct .The sensor was measured before and after the cavity. Along the circumference of the cavity around 16 places the acoustic pressure were measured. Due to confidential reason, the experimental values could not be included. The experimental values were agreeing with the predicted computational values within 5% error.

5. CONCLUSION

The numerical simulations were used to predict the acoustic frequency due to the vortex shedding in the axisymmetric rectangular cavity. The results show that the circumferential mode exists since the frequency was high. The amplitude gets decay exponentially along the length of the model after the cavity. The amplitude level is varying based on the vortices present along the length of the cavity.

REFERENCES

[1] Dangguo Yang, Jianqiang Li, Jun Liu, Yi Zhang, Yaohua Li, "Analysis on Physical Mechanism of Sound Generation inside Cavities Based on Acoustic Analogy Method", Open Journal of Fluid Dynamics, Vol.3, 2013, pp.23-31.

[2] D. Caridi , A. Wade and D. Cokljat, "Numerical Simulation Of Subsonic Flow-Induced Cavity Noise Turbulence", Heat and Mass Transfer 6, 2009.

[3] D. H. Lee, H. J. Sung, " Experimental Study of Turbulent Axisymmetric Cavity Flow", Experiments in fluids, Vol.17, 1994, pp. 272-281.

[4] D. Rockwell and E. Naudascher, "Review - Self-Sustaining Oscillations of Flow Past Cavities", Transactions of the ASME (1978), Vol.100, 1978, pp.152-65.

[5] G. Nakiboglu, H. B. M. Manders and A. Hirschberg, "Aero acoustic Power Generated By A Compact Axisymmetric Cavity: Prediction of Self-Sustained Oscillation And Influence of The Depth", Journal of Fluid Mechanics, Vol.703, 2012, pp.163-191.

[6] K. Aly and S.Ziada, "Azimuthal Behavior of Flow-Excited Diametral Modes of Internal Shallow Cavities", Journal of Sound and Vibration, 2012.

[7] Konstantin A.Kurbatskii , Florian Menter , Jochen Schuetze and Akira Fujii, "Numerical Simulation of Transonic Cavity Noise using Scale- Adaptive Simulation(SAS) Turbulence Model", Inter-noise 2011.

[8] Masaaki Kawahashi, Eric Brocher and Paul Collini, "Coupling of Vortex Shedding with a Cavity", Fluid Dynamic Research, Vol.3, 1988, pp.369-375.

[9] S. Abdul Raheem and V. Babu, "Numerical Simulations of Unsteady Flows in Solid Rocket Motors", AIAA paper 2004-2878, 2004.

[10] Xavier Amandolese, Pascal Hemon and Clotilde Regardin, "An Experimental Study of the Acoustic Oscillations by Flows Over Cavities", Transactions of the ASME, Journal of Vibration and Acoustics, Vol.126, 2004, pp.190-195.

Performance Evaluation and Prediction of Particulates by Thermodynamic Combustion Modeling on CRDI Diesel Engine

Hemalatha Tahapa[1] and G.Devaradjane[2]

[1&2] Automobile Engineering Department, Madras Institute of Technology, Anna University, Chennai - 600 044, Tamil Nadu.

Abstract

The objective of this work is to minimize the particulate emissions and focus on the combustion strategies, understand the concept to reduce the emission pollutants and find a way to relate the performance operating parameters characteristics to the total pollutants liberated. In the first phase of the work, the proper study of pollution formation and its control was done. The performance curves, base emission readings plus p( ) curve generation were evaluated experimentally and plotted. The thorough study of thermodynamic combustion modelling and necessary mathematical sub models were developed using the computational tool MATLAB. The ideal cycle simulation (ICS) of CI Engines has been dealt with employing thermodynamic relations and using air as a working medium. Fuel air cycle simulation carried using appropriate equations which included the influence of various operating parameters on engine performance. Progressive combustion simulation (PCS) using rate equations and zero-dimensional model have been incorporated by means of some empirical relations. The overall objective of this research is to utilize current understanding presented from modern methods of experimentation to develop a new phenomenological model of particulate emissions that is flexible, computationally inexpensive while maintaining a reasonable fidelity. A phenomenological model is introduced by applying established conceptual models of soot formation for direct injection combustion to develop a mathematical description of events.

Keywords: Combustion strategies, Diesel engines, Modeling, Particulate emissions, Soot formation.

1. INTRODUCTION

The diesel engine is an attractive power unit used widely in many fields, for its great advantages over petrol engines such as lower fuel consumption, lower carbon monoxide emissions, better torque characteristics and higher reliability (Heywood 1988; Stone 1999). However, they are among the main contributors to air pollutions for the large amount of emissions, especially particulates and nitrogen oxides (NOx) (Heywood 1988). How to control these emissions is one of the most important aspects of modern air quality management. The concentration of carbonaceous particulate matter in the exhaust of diesel engines depends on the rates of formation and oxidation of soot in the combustion chamber. Soot forms early in the combustion process when local fuel-rich areas exist, whereas soot oxidation occurs later when more air is entrained into the fuel spray. Based on this understanding, a phenomenological combustion model is established. In the model, the cylinder volume is divided into four zones: a rich fuel spray core, a premixed-burning/burned gas zone, a mixing controlled burning zone and a lean air zone. Soot formation takes place in the mixing controlled burning zone where the local

C/O ratio is above the criticalvalue. Soot oxidation occurs in the premixed-burning/burned gas zone as air is entrained. The phenomenological model strikes a balance between the complexity and the computational cost. In this type of model, some of the physical and chemical processes involved in the combustion are simplified using empirical formulas based on experimental data. The model thus will be limited in use to the specific engine system, or to the type of engine system upon which the model is built.

2. CONCEPTUAL MODEL

The fuel is injected into the combustion chamber slightly before the desired time of combustion, as the piston reaches the end of the compression stroke. The liquid fuel atomizes into small droplets, evaporates and mixes with the hot and compressed air of the combustion chamber. Because the air temperature and pressure are above the fuel's ignition point, spontaneous ignition occurs after a short delay. The time interval between the start of injection and the first heat release is called the ignition delay. After the ignition delay period, the subsequent Diesel combustion process is commonly divided into two stages. During the initial phase the fuel

Hemalatha Tahapa[1] and G.Devaradjane[2]

which has mixed with air to within the flammability limits combusts rapidly. This phase of the combustion process is commonly referred to as premixed phase and is associated with high rates of heat release over a few crank angle degrees. The combustion heat-release history during this interval depends strongly on the fuel-air mixture prepared during the ignition delay period. DEC (1997), describes the formation and features of a quasi-steady diesel fuel jet, as shown in figure 1. It should be noted that this conceptual model applies to large bore, quiescent chamber combustion or a free fuel jet without wall interactions. At the start of injection, fuel begins to penetrate into the combustion chamber and high temperature air is entrained into the spray.
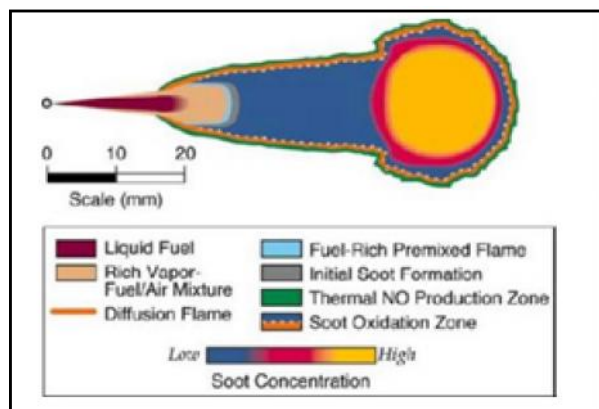
Fig.1 Quasi-steady Diesel combustion plume as presented by DEC (1997) Courtesy Dr. John E. Dec (Sandia NationalLaboratories)

The hot air evaporates the fuel and beyond a fixed length, knows as the liquid length, no liquid fuel exists. The liquid length shortens slightly after the start of combustion but remains relatively constant until the end of injection. Beyond the liquid length, the rich premixed fuel and air continue to be heated until they react in the rich premixed reaction zone. The products of rich combustion continue downstream and diffuse and mix radially outward until reaching the surrounding cylinder gases. At a location where the rich products and cylinder gases mix to produce a Stoichiometric mixture, a diffusion flame is produced. The diffusion flame surrounds the jet in a thin turbulent sheet, which extends upstream toward the nozzle. The axial distance from the nozzle exit ato the diffusion flame is the Lift-Off length. According to SIEBERS & HIGGINS (2001) the Lift-Off length. controls the amount of oxygen entrained into the fuel jet and therefore the stoichiometry of the fuelrich zone. Soot is burned out and NOX is produced on the outside of the diffusion flame, where temperatures are high and oxygen and nitrogen are

abundant. Initial pyrolysis of fuel usually identifies a very rich combustion region. The products of this initial pyrolysis have abundant amounts of soot precursors, like C2H2, C2H4, and the radical C3H3, for seed particles, as well as unburned Hydrocarbons, for growth species. Initial soot particles form and grow in size through agglomeration, direct deposit, and surface growth. The soot particles, soot precursors and growth species, are all oxidized as they mix with surrounding air at high temperatures. The initial pyrolysis of the fuel occurs at the rich initial reaction that exists just downstream of the liquid length. Furthermore, just downstream of this reaction, observations from DEC (1997) have shown the existence of a zone where small soot particles begin to form. The particles take root and grow as they move down the turbulent fuel jet toward the head vortex. Oxidation of the soot particles occurs when they pass close to, or through the diffusion flame formed around the periphery of the spray plume, where the particles are exposed to oxygen. SIEBERS & HIGGINS (2001) found the equivalence ratio of the rich initial reaction was dependent On the Lift-Off length. The only oxygen for the initial reaction comes from the air entrained in the fuel spray; the diffusion flame sheath prevents further entrainment. A larger Lift-Off length allows more air entrainment and a lower equivalence ratio for the initial reaction. Lower equivalence ratios for the reaction, would result in fewer unburned hydrocarbons in the products. A vast majority of the soot particles formed during the Diesel combustion are oxidized before the combustion event is quenched (HEYWOOD, 1988). In the final stage of the combustion event a "race" occurs between the dropping temperature due the expansion cooling and the rate of the soot oxidation. The particulate matter left when the final stage of combustion is quenched, becomes the soot expunged from the cylinder and into the exhaust of the engine.

3. PARTICULATES

Particulates are tiny solid and liquid particles and are sometimes referred to as particulate matter (PM) or fine particles, and their sizes, which are strongly linked to human health issues, vary from several nanometers to several hundred microns (World Resources Institute *et al.* 1998; C. Arden Pope III 2002; Eastwood 2008). Generally, particulates from engines can be categorized into three distinct types according to their sizes: nucleation mode (<50 nm), accumulation mode (50-1000 nm) and coarse mode (>1000 nm) (Kittelson 1997) (Figure 2). There are

also definitions, which are different in the size range, as nucleation mode (<100 nm), accumulation mode (100-900 nm) and coarse mode (>900 nm) (Eastwood 2008). Coarse mode particles are mainly composed of particles forming from the other two modes or a typical rust and scale from the exhaust system. They can easily be stored and released in the exhaust system and this inconsistency makes its manner unpredictable and thus less studied (Eastwood 2008). For the past few years, attention has been mainly drawn on the accumulation mode particles, which have more to do with the particle mass. They consist of some basic blocks called primary particles or spherules (Heywood 1988). The spherules' diameters are around 20-50 nm and their numbers determine the size of the particles. The spherules are composed of solid core parts and some liquid or semi liquid materials attached to the

surface of their aggregations, making them "wet" (Eastwood 2008).

Nucleation mode particles are more related to the particle number and they are relatively less studied for their obscure and irreproducible nature. Some of them are volatiles and some are solids. Based on the conceptual model recommended by Peter (Eastwood 2008), particulates can be divided into non- volatile/non-soluble, which are mainly generated in the engine, and volatile/soluble, which form later in the exhaust. The former includes the soot and ash fractions while the sulphate, organic and nitrate fractions are categorized in the latter. For the particle growth mechanism, this empirical equation is suggested (Sunderland et al. 1996).

$$\omega_g = k_g(T)[C_2H_2]^n$$
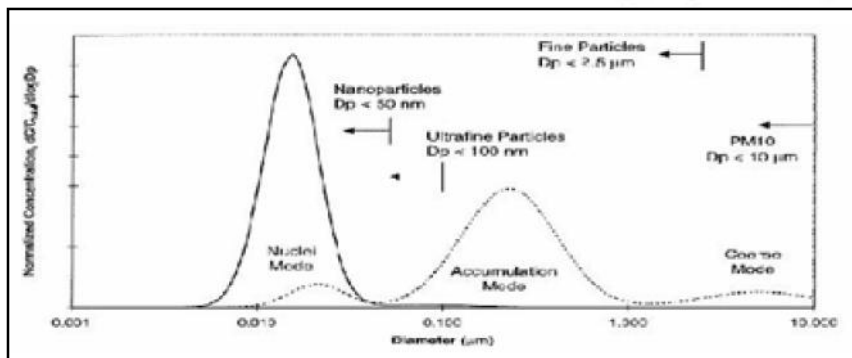
Fig.2 Different modes of particles formed.

Where ωg is the rate of surface growth (kg/m2s), kg (T) is an Arrhenius expression and n is an index. This equation can be used for simple hydrocarbon flames, based on its association with acetylene.

The reactions include:

$$(C_{soot} - H) + H \Leftrightarrow C_{soot}^* + H_2$$
$$(C_{soot} - H) + OH \Leftrightarrow C_{soot}^* + H_2O$$
$$C_{soot}^* + H \rightarrow C_{soot}^* - H_2$$
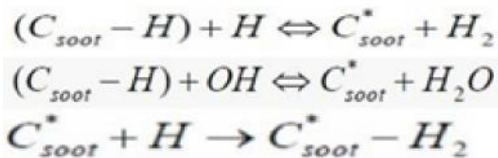
For the particles' agglomeration and oxidation, the Smoluchowski equation and oxidation model (Tao *et al.* 2004) are used respectively as:

$$\frac{dN}{dt} = -kN^2$$

Where N is the number concentration and k is the agglomeration coefficient.

4. WORK APPROACH

PHASE-1

Base engine reading, calculation, recordings and generation of P- ( ) curves.

Developing basic thermodynamic models for the corresponding to different stages of operation over a four stroke compression ignition engine for simulating the data.

PHASE-2

Develop an emission prediction model for Steady state conditions.

To conform the operating parameters which would help reduce the particulate matter formation.

Hemalatha Tahapa[1] and G.Devaradjane[2]

5. EXPERIMENTAL SET UP

Fig.3 Experimental set up

With automation system, it is possible to conduct the power, smoke (steady & transient) and emission measurement tests (steady state) in AUTO mode with the final result calculation and report generation.

6. CONVENTIONAL TEST PROCEDURE

The engine is started and allowed to attain a steady speed condition at a zero load condition.

For this engine it took thirteen stages to attain that max speed for no load condition hence at that condition brake power, specific fuel consumed everything was calculated.

Both the lubricating oil level and the conditions of the lubricant were checked Coolant was supplied to the engine and was monitored properly for appropriate supply and run the engine.

Table 2 Engine Specifications

SNO	ENGINE PARAMETER	SPECIFICATIONS
1	Engine model	PT014
2	No of cylinders	3
3	Cylinder bore stroke	85/110
4	Compression ratio	17.5
5	Inlet ports	Tangential and swirl type
6	Maximum power	42kw
7	Rated speed	3300
8	Fuel injection pressure	300-1400bar
9	Fuel injection system	Direct injection
10	High pressure system	Common rail CP-4.1BOSCH
11	Engine management system	AVL-RPEMS+ETK-7 BOSCH
12	Valve per cylinder	2 INLET 1 EXHAUST
13	Valve train type	DOHC Cam follower
14	Air intake system	Turbocharged

Engine was started pick up the rated speed Load was applied gradually from the dynamometer at 0%, 20%, 40% 60% 80% 100%. For each load, fuel rate was set and specific fuel consumption and the engine torque was noted.
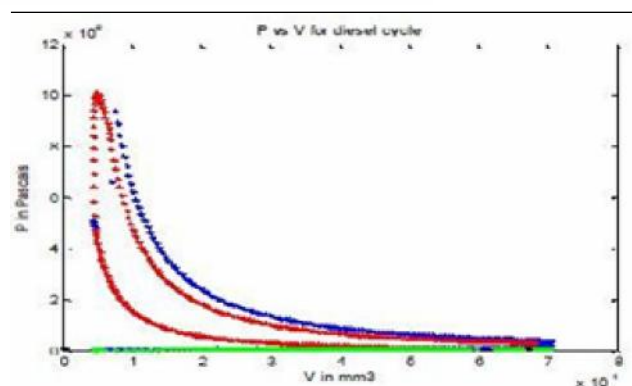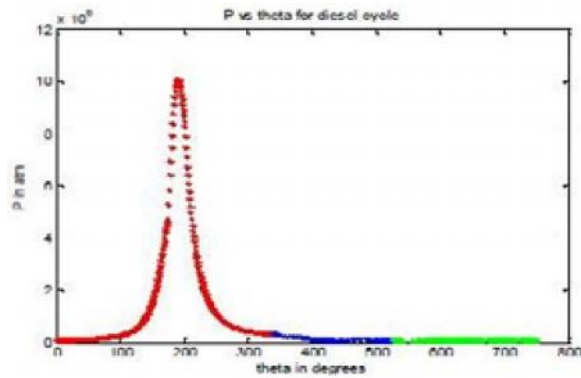
a) Progressive combustion model

The above figure shows comparison
Comparison of two models:

Red: Progressive combustion model

Blue: Zero dimensional model

Peak pressure obtained in both the models is almost the same There is slight variation in the expansion processes in both the combustion models due to slight difference in peak pressure obtained.

Combustion starts slightly late (2o-3o) in zero dimensional model(since ignition delay[2][3] is considered) which can be observed in the graph.

7. EXPERIMENTAL RESULTS AND DISCUSSIONS
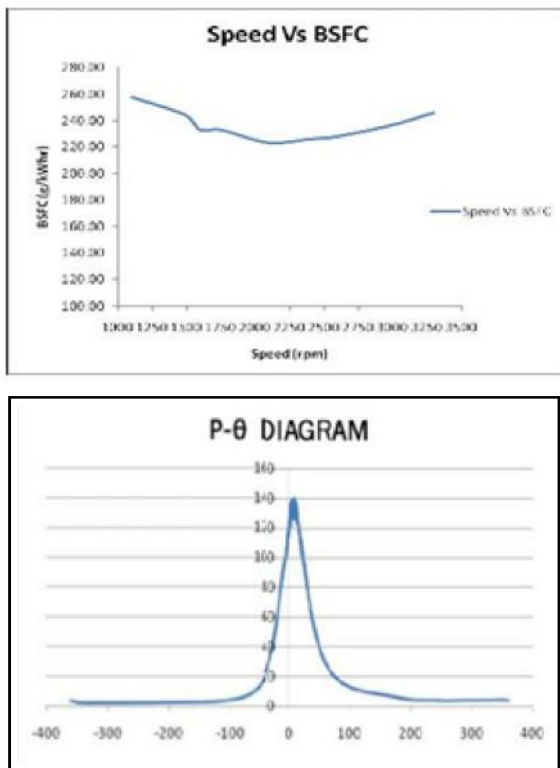
Fig.4 Graphical representation of the speed v/s torque

The above p( ) curve is generated at 3300rpm 120Nm. The pressure responsive transducer and its support components form an instantaneous pressure indicator. The advantage of this system is that each individual pressure cycle of the engine can be represented and therefore, variations in pressure from cycle to cycle can be studied and as well rapid fluctuations of pressure that occur with explosive knock.

8. CONCLUSION

The results and discussion inferred are collected for further development of the correlation soot modeling, predicting the emissions and the factors affecting the performance of the engine, emission concentrations will be observed. The maximum effort is put to keen improvise the basic concepts, study the behavior of engine and learn to simulate the model of the real system, physical system representing actual processes and analyze the same. The model is mathematical one representing the actual processes through a set of algebraic, differential or integral equations and the analysis is made using MATLAB.

FUTURE SCOPE OF THE WORK

This analysis can be extended into higher combustion models to predict the characteristics of engine even better. The mathematical correlations can also be derived with respect to the soot modelling. Each parameter variation how affects the performance of the engine and its emission characteristics can be studied with ease. This will serve as a good platform to develop better models in MATLAB.

REFERENCES

[1] "Review of Diesel Engine", Vol.125, Journal of Engineering for Gas Turbine and Power.

[2] Dennis Assanis, "Simulation, Validation and Integration of Diesel Engine Process Models", Presentation at University of Michigan", May 1999.

[3] V. Ganesan, "Computer simulation of Compression Ignition Engine Processes", University Press Edition, 2000.

[4] V. Ganesan, "Internal Combustion Engines", Third Edition, Tata McGraw Hill Edition, 2007.

[5] http://openwam.webs.upv.es/manual/index.php?title=Four_Wiebes_simu lation

Hemalatha Tahapa[1] and G.Devaradjane[2]

[6] Model for Prediction of Incylinder and Exhaust Soot Emissions from Diesel Engines, SAE 881251,P S MEHTA *et al.* University of Roorkee.

[7] John B. Heywood, "Internal Combustion Engine Fundamentals", McGraw Hill Edition, 2003.

[8] Oliver Philipp, Robert Hoepler, Cornelius Chucholowski, Tesis Dynaware, "Zero-Dimensional Combustion Simulation in Real Time", Springer Verlag, 2007.

[9] T. Ganapathy, K Murugesan, R P Gakkhar, "Performance Optimization of Jatropha Biodiesel Engine Model using Taguchi Approach", Publisher: Elsevier Ltd, Vol.86, No.11, Applied Energy, 2009, pp.2476-2486.

[10] Diesel emissions in review- corning inc.

[11] Strategies Towards Meeting Future Particulate Matter Emissions Requirements In Homogenous Gasoline Direct Injection Engines- Delphi Powertrain Systems.

[12] Potential Challenges of a 3000bar Common Rail Injection System Considering Engine Behavior and Emission Level.- Tecnische Univ munchen.

[13] An Evaluation of Particle Size Distributions and Particle Number-based Reductions from Various PM Emission Control Technologies.- Johnson matthey ect.

Multi-Temporal Remote Sensing Image Fusion Using Improved Nonlinear IHS Transform

M. Meera Banu, R. Muganya, R. M. Jai Kanimoli and S.P. Velmurugan

Department of Electronics and Communication Engineering, Kalasalingam University, Krishnankoil - 626 126, Tamil Nadu

Abstract

Remote sensing image fusion is the process of obtaining a highly informative color image from a set of remotely sensed gray scale panchromatic image (PAN) and multispectral color image. Fusion methods such as Intensity-Hue-Saturation (IHS), wavelet based fusion, contourlet, curvelet, linear IHS, Nonlinear IHS and other existing method causes gamut problem, resulting color distortion and loss of information in the fused image. It is not possible to derive specific information from the resultant image, because of high spectral distortion than the original image. To avoid the high spectral distortion and to overcome the gamut problem in image fusion, Improved Nonlinear IHS transform using high pass filter (HPF) fusion rule is proposed in this paper. Improved Nonlinear IHS transform using High Pass Filter fusion rule produce an image with less spectral distortion, no gamut problem and the fused image will have high spatial information and high spectral information than the existing methods.

Keywords: High pass filter (HPF), Image fusion, Intensity-Hue-Saturation, Improved Nonlinear IHS Transform (iNIHS).

1. INTRODUCTION

Remote sensors collect data by detecting the energy that is reflected from earth. These sensors can be on satellites or mounted on aircraft. The images produced from these sensors are such as panchromatic image and multispectral image. Where, panchromatic image is said to be a high resolution black and white image and multispectral image is said to be a low resolution color image. Both the panchromatic and multispectral images are fused to get a high resolution color image. This high resolution color image is used in several applications like surveillance, feature detection, change detection, etc…

Intensity-Hue-Saturation, defines colors mathematically, using cylindrical or spherical coordinates. Hue component refers to the dominant wavelength 0 and 360º. Intensity refers to the total brightness or dullness of a color. Saturation refers to the purity of the color. Both the intensity and saturation component ranges between 0 and 1. Image fusion using linear IHS transform and nonlinear IHS transform produces gamut problem. Linear IHS color space is said to be in a cube model. After the image fusion, the resulting color point will not be the same as which is present inside RGB cube. It is said to be a gamut problem. Usually gamut problem is resolved by using either one of three types of clipping techniques as discussed in [3].

The nonlinear IHS color space is said to be in cylindrical model with collapsed top, if the color point of the image after backward nonlinear transformation falls into the collapsed portion causes gamut problem. It can be solved by clipping method. But when the collapsed top of the nonlinear cylinder is reshaped to a complete cylinder, it is possible to avoid the gamut problem without going for clipping method [4]. Image fusion using nonlinear IHS transform resolve the gamut problem and uses à trous wavelet filter based additive image fusion rule to overcome the spectral distortion, still exists high spectral distortion and contrast reduction [12] in the fused image [4]. If there any spectral distortion in the fused image, it is impossible to derive a sufficient information from the fused image. To completely overcome the high spectral distortion in the resultant fused image, Improved Nonlinear Intensity-Hue-Saturation transform (iNIHS) is proposed with the fusion rule of High Pass Filter. High pass filter amplifies the noise and reduces the quality of the image to obtain high frequency spatial information which is not present in the multispectral (MS) image and this obtained high frequency component is inserted into the multispectral (MS) image to remove high spectral distortion in the resultant image and to increase the spatial and spectral resolutions of the fused image.

In the remainder of this paper, the proposed method of Improved Nonlinear IHS color space using High Pass Filter fusion rule is presented in Section 2.0. Experimental results in Section 3.0, followed by the conclusion in Section 4.0.

2. PROPOSED METHOD

A gamut is said to be a subset of color. Certain colors which cannot be expressed within a given color space is said to be a gamut problem. In this paper, to avoid gamut problem, a truncated portion in the nonlinear cylinder is reshaped to form a complete cylinder and called as Improved Nonlinear IHS color space. According to the proposed method, transform each and every pixel in MS image into iNIHS color space and after image fusion, each pixel in iNIHS color space should transform back into their corresponding color space, either RGB (Red, Green, Blue which is a additive color) and CMY (Cyan, Magenta, Yellow which is substitutive color).

To transform MS image in iNIHS color space, decide each pixel in MS image falls into RGB color space or CMY color space. If the color point of a pixel falls within a RGB cube, and that particular pixel is said to be in RGB color space or else it is said to be in CMY color space pixel's color point can be determined with the help of Intensity and Hue value. For reverse transformation, the entire Hue range present in the iNIHS color space is separated into three sections to transform back the pixel's into corresponding color space. In proposed method, iNIHS can be processed along with High Pass Filter fusion rule.

In this paper, Low Pass Filter is applied only to the Panchromatic image (PAN). The low resolution panchromatic image is smoothened by LPF to suppress noise. Low pass filtered image is subtracted from the original panchromatic image to attain high spatial information. This technique is called High Pass Filtering [8] [9] and this high spatial information is inserted into the intensity component of MS image.
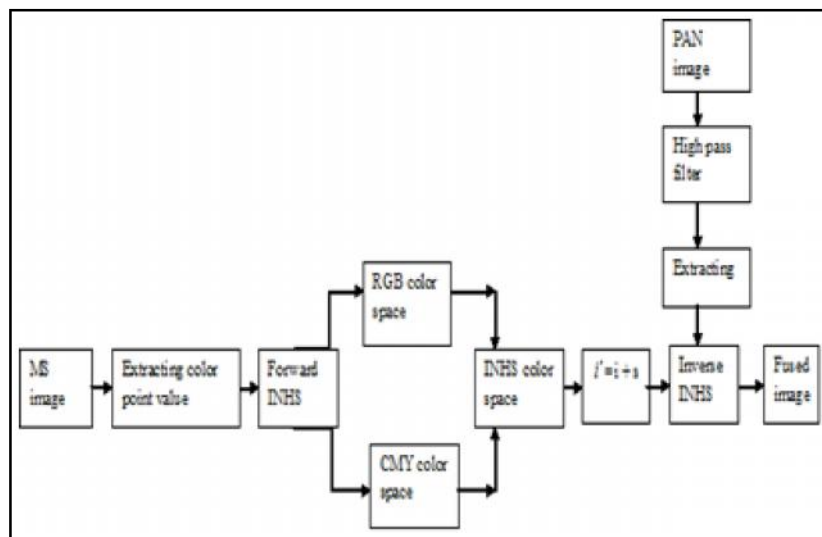
Fig.2 Image fusion using iNIHS transform

The proposed method involves the following steps:

2.1 Transforming MS into iNIHS

Nonlinear IHS color space has collapsed portion at the top of the cylinder as shown in figure 2.1(a). If the color point of a pixel falls into the collapsed portion, a gamut problem will arise.

To overcome gamut problem, the collapsed portion in Nonlinear IHS is reshaped to form a complete cylinder as shown in figure 2.1(b) and it is said to be an iNIHS color space. Improved Nonlinear IHS color space has two symmetric portions as H_{upper} and H_{lower} as indicated in figure 2.1(c).

If the color point of pixel falls into the upper portion, then the pixel is said to be in CMY portion or else it falls into the lower portion and the pixel is said to be in RGB.

Two separate the iNIHS color space into two symmetric parts, a saturation line is drawn in between gray axis line edges as shown in figure2.1(d).
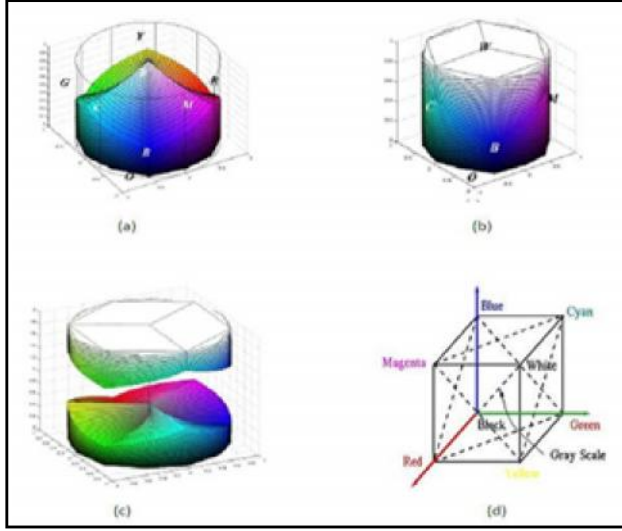
Fig.2.1 (a) Nonlinear HIS color space, (b) iNIHS color space, (c) iNIHS is separated into two parts as H_{upper} and H_{lower}, (d) separated portions of RGB and CMY

Consider a MS image which has a low resolution and has to be converted into iNIHS color space on taking FIHS. When forward transformation is taken, Intensity and Hue values are obtained first. With the help of intensity and hue values, each pixel can be determined, whether it is in RGB or CMY color space.

If $i_c \leq 2/3 - \left| h_{c \bmod 120^\circ} - 60^\circ \right| / 180^\circ$, then c is in H_{lower};

Else, in H_{upper} (1)

The saturation point (s) of each pixel can be found using the color space they have been placed (RGB or CMY). Finally the MS have been converted into IHS color space. MS into Nonlinear IHS can be calculated as follows, as suggested in [4].

$$a = \frac{(2b - g - r)/2}{\sqrt{(b-g)^2 + (b-r)(g-r)}}; i = \frac{r+g+b}{3};$$

$$if\ b \leq g,\ then\ h = \cos^{-1}(a);\ else\ h = 2\Pi - \cos^{-1}(a);$$

$$if\ i \leq \frac{2}{3} - \frac{\left| h_{\bmod 120^\circ} - 60^\circ \right|}{180^\circ},$$

$$then\ s = 1 - \frac{3 \times \min(r,g,b)}{r+g+b}\ (conventional);$$

$$else\ s = 1 - \frac{3(1 - \max(r,g,b))}{3 - (r+g+b)}\ (improved);$$

2.2 Fusion Rule

Consider a panchromatic image which has a high resolution. Smoothen the panchromatic image from the low pass filter can reduce noise. Then the low pass filter image ($PAN^{\smile}$) will have low frequency information. High spatial information obtained from the panchromatic image is added with the intensity component of the MS image and it is denoted as $I^{\smile}$.

2.3 iNIHS into Coressponding Color Space

Inverse IHS transformation is taken to transform back the resulting image from fusion operation into corresponding color space to display images. The iNIHS color space which has two symmetric portions, RGB and CMY in the lower and upper portion respectively is divided into three sections each 120° depending upon its Hue range as represented in [4].

The upper half CMY is divided into CM [180, 300], MY [300, 60] and YC [60, 180]. Similarly, RGB is divided into RG [360, 120], GB [120, 240] and BR [240, 360].

Nonlinear IHS to RGB transformation for color points the lower half of the iNIHS space as suggested in [4].

1. Section RG ($0^\circ \leq h < 120^\circ$ and $i \leq 2/3 - h - 60^\circ/180^\circ$); $b = i(1 - s)$;
   r=i[1+s cos h/cos($60^\circ - h$)]; (3)
   g = 3i $- (b + r)$

2. Section GB ($120^\circ \leq h < 240^\circ$ and $i \leq 2/3 - h - 180^\circ/180^\circ$) h=h$-120^\circ$; r=i(1$-s$); (4)
   g = i[1 + s cos h / cos(60 $- h$)]; $b = 3i - (r + b)$.

3. Section BR ($240^o \leq h < 360^\circ$ and $i \leq 2/3 - h - 300^\circ/180^\circ$); h = h - 240^0; g = i (i - s); (5)
   b = i[1 + s cos h / cos($60^\circ - h$)]; r = 3i - (g + b).

Nonlinear IHS to CMY transformation for color points in the upper half of the iNIHS space.

1. Section YC ($60^O < h$ 180° and $i > 1/3 + h - 120^O/180^O$); h = h - 240° ;
   m = (1 - i)(1 - s); (6)
   y = (1 - i)[1 + s cos h / cos(60° - h)];
   c = 3(1 - i) - (m + y).

2. Section CM ($180^O < h$ 300° and $i > 1/3 + h$ -$240^o/180^o$ y = (1 - i)(1 - s);
   c = (1 - i)[1 + s cos h / cos(60° - h)];
   m = 3(1 - i) - (c + y). (7)

3. Section MY (($-60^O < h < 0^O$ and $i > 1 / 3 + (360^O - h)$) or ($0^O < h < 60^O$ and $i > 1 / 3 + h / 180^O$));
$h = h - 120^O$; $c = (1 - i)(1 - s)$;
$m = (1 - i)[1 + s \cos h / \cos(60^o - h)]$;
$y = 3(1-i)-(c+m)$. (8)

High pass filter is usually used to sharpen the image and to extract the finer details of the image by using negative values. The high pass filter sharpens the highest signal to noise ratio parts.

High Pass Filter also called sharpening filter. HPF sharpens the image by subtracting, the low pass filtered image and the original image.

HIGHPASS = ORIGINAL - LOWPASS

Major advantage of the high pass filter is to neglect the high spectral distortion by gaining high frequency spatial information [10]. In this paper only the panchromatic image is dealt with high pass filter.

The resultant image is a sharpened image of high spatial information. This high frequency information is added into the intensity component of multispectral image.

3. EXPERIMENTAL RESULTS

Experiments were conducted to evaluate the performance of the proposed method by fusing the data set of pairs. For the data sets, image size of low resolution multispectral image was 512 512 pixels.

The proposed method of HPF image fusion in the iNIHS color space was applied to the PAN and MS image, the resulting image will have all the colors present within the gamut is shown in figure 3.0

Image fusion using iNIHS with HPF fusion rule is evaluated and the obtained results is better than the existing method.
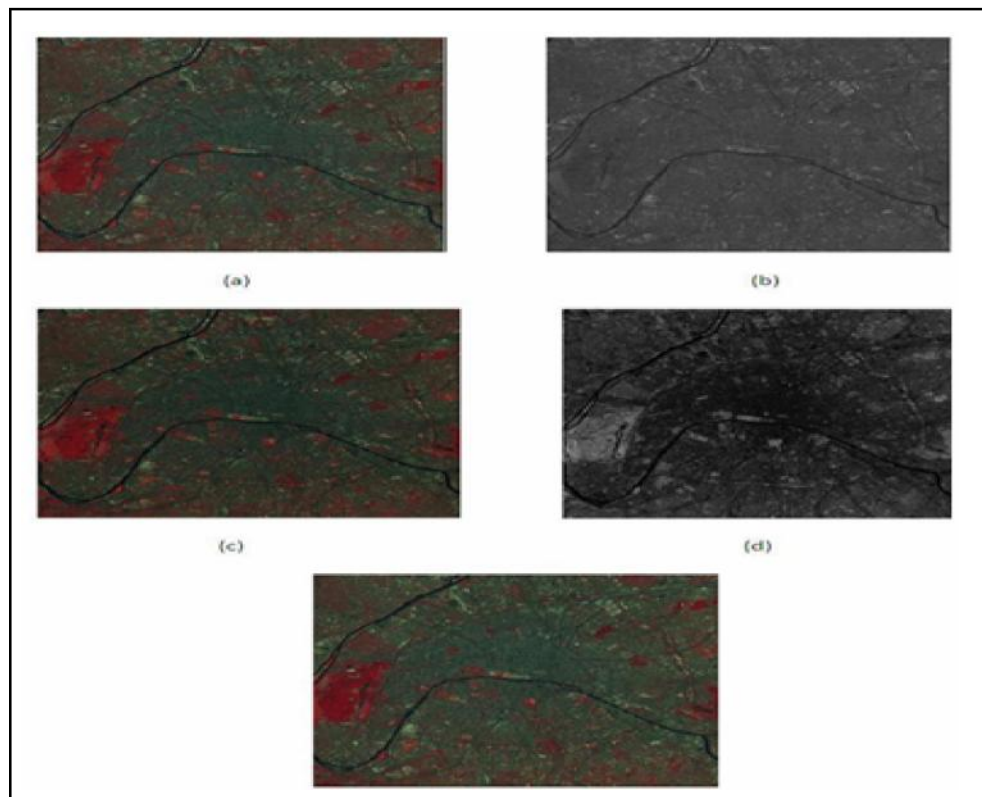
Fig.3.0 (a) conversion of MS into iNIHS, (b) intensity component from the PAN image, (c) high spatial resolution from PAN image, (d) fused image after intensity substitution, (d) final fused image after reverse transformation.

4. CONCLUSION

RGB into linear & Nonlinear IHS transformation causes gamut problem. iNIHS method with à trous wavelet filter is used to solve the gamut problem. But the resultant image still has a high spectral distortion and contrast reduction. To overcome the gamut problem with less spectral distortion and contrast reduction, iNIHS is used along with high pass filter fusion rule and the obtained image has less spectral distortions with no out of gamut colors.

REFERENCES

[1] C. C. Yang and S. H. Kwok, "Efficient Gamut Clipping for Color Image Processing Using LHS and YIQ", Opt. Eng., Vol. 42, No.3, Mar. 2003, pp.701–711.

[2] C. K. Munechika, J. S. Warnick, C. Salvaggio and J. R. Schott, "Reso-lution Enhancement Of Multispectral Image Data To Improve Classification Accuracy", Photogramm. Eng. Remote Sens., Vol.59, No.1, Jan. 1993, pp.67-72.

[3] Chun-Liang Chien and Wen-Hsiang Tsai, Senior Member, IEEE, "Image Fusion With No Gamut Problem by Improved Nonlinear IHS Transforms for Remote Sensing", IEEE Trans. Geosci. Remote Sens., Vol.52, No.1, Jan. 2014, pp. 651–663.

[4] G. Xiao, Z. Jing, J. Li, and H. Leung, "Analysis of Color Distortion and Improvement for IHS Image Fusion", in Proc. IEEE Intell. Transp. Syst., 2003, Vol.1, pp. 80–85.

[5] M. González-Audícana, X. Otazu, O. Fors, and A. Seco, "Comparison between Mallat's and the 'a trous' Discrete Wavelet Transform based Algorithms for the Fusion of Multispectral and Panchromatic Images", Int. J. Remote Sens., Vol.26, No.3, Feb. 2005, pp.595–614.

[6] M. Gonzalez-Audicana, J. L. Saleta, R. G. Catalan, and R. Garcia, "Fusion of Multispectral And Panchromatic Images Using Improved IHS and PCA Mergers based on Wavelet Decomposition", IEEE Trans. Geosci. Remote Sens., Vol.42, No.6, Jun. 2004, pp.1291–1299.

[7] P. S. Chavez and J. Bowell, "Comparison of the Spectral Information Content of Landsat Thematic Mapper and SPOT for Three Different sites in Phoenix, Arizona Region", Photogramm. Eng. Remote Sens., Vol. 54, Dec. 1988, pp. 1699–1708.

[8] P. S. Chavez, "Digital merging of Landsat TM and digitized NHAP data for 1:24.000 Scale Image Mapping", Photogramm. Eng. Remote Sens., Vol.52, Oct.1986, pp. 1637–1646.

[9] R. A. Schowengerdt, "Reconstruction of Multispatial, Multispectral Image Using Spatial Frequency Contents", Photogramm. Eng. Remote Sens., Vol.46, Oct. 1980, pp. 1325–1334.

[10] T. M. Tu, S. C. Su, H. C. Shyu, and P. S. Huang, "A New look at IHS-like Image Fusion Methods", Inf. Fusion, Vol. 2, No.3, Sep. 2001. pp. 177–186.

[11] R. C. Gonzalez and R. E. Woods, "Digital Image Processing", Upper Saddle River, NJ, USA: Prentice-Hall, 2007.

Enhancement of Amylolitic Enzyme Production in Chemically Mutagenic Bacterial Consortium for Bioremediation

Harashit Kumar Mandal

Ph.D. Research Scholar in Environment and Microbial Biotechnology, Jodhpur National University, Narnadi,
Jhanwar Road, Bornada, Jodhpur (Rajasthan) India
E-mail: harashit@gmail.com

Abstract

The impact of industrial toxics and hazardous wastes on aquatic life including microorganisms cannot be over-stressed. Consequently, upon the industrial revolution, many production and manufacturing companies have due to improper waste management techniques, added toxic and hazardous wastes including synthetic compounds into the aquatic environment. These wastes are also discharged into water without any treatment as a result of improper or deliberate channeling of the wastes into aquatic environment. The presence of these wastes in the environment causes extensive damage to the water quality characteristics and the ecology of the environment, especially when microbial degradation activities fail to remove these pollutants fast enough to prevent environmental degradation. Micro-organisms can be considered chemical factories. They have the capacity to convert a raw material into end products. If the end products have value for human use then it becomes attractive to exploit the microbiological process. Also these micro-organisms can be isolated for various hydrolysis and fermentation activities e.g. carbohydrates, lipids and protein etc. and they use for bioremediation. It is a technology for removing pollutants from the environment, restoring contaminated sites and preventing future pollution. This capacity could be improved by applying the Genetically Modified Microorganisms (GMMs). Genetically modification can be done with the help of different kinds of mutagens such as physical, chemical, or both. It has been found that hydrogen peroxide (H_2O_2) plays a vital role in water purification and act as a chemical mutagen to modify genetically of microbes. In the present study researcher tried to develop some genetically modified amylolytic bacterial consortium for better enzyme production through hydrogen peroxide for bioremediation.

Keywords: *Amylolytic, Bacterial consortium, Bioremediation, Chemical mutagen, Hydrogen peroxide, Industrial Effluents of phagwara, Genetic modification, etc.*

1. INTRODUCTION

Living cells produce **enzymes** to conduct biological reaction in an orderly and well define manner. These enzymes with a high degree of specificity and efficiency speed up the reaction rate. The most characteristic feature of enzymes is that they never used up by the substrate and product as well. Even a small quantity of enzyme is adequate to carry out chemical reactions, liberating numerous metabolic and products. Based on their role in metabolic pathways, they are located in different components of cells, tissues and body fluids. Specifically, **starch** is a biodegradable polysaccharide. It is composed of several molecules of glucose linked together by glycosidic bonds. It is a mixture of amylose (linear form) and amylopectin (highly branched form). Being complex in nature, starch needs the amylase enzymatic activity for hydrolysis. Amylase acts on 1-4 glycosidic linkage of starch and hydrolyses them into fragments of dextrines and then to maltose molecules.

Further hydrolysis to soluble glucose requires the presence of another enzyme maltase. To hydrolyze starch, organisms must produce amylase.

Amylolyticmicroorganisms commonly found in soil, **freshwater reservoirs**, and seawater hydrolyzes starch into mono- and disaccharide units.

Microorganisms are modified with the help of certain **mutagens**like **hydrogen peroxide**. Mutagens are a physical and chemical agent that changes the genetic material, usually DNA for an organism. Hydrogen peroxide is a chemical compound. Its molecular formula is H_2O_2. It is used as strong mutagen. It is a colorless, odorless liquid. It is usually in water soluble. It is used as a cleaner. It causes DNA damage because of the FENTON-TYPE reaction. It releases nascent oxygen which is highly reactive. It combines and oxidizes necrotic matter and bacteria. It cause G:C to T:A transverse in bacteria which ultimately cause a changes in integrity of

the cell wall and the organisms is killed by action of lysozyme. The changes in nucleic acid sequences by mutation include substitution of nucleotide base pairs and insertions and deletions of one or more nucleotide in DNA sequences. Although some of these mutations are lethal, or cause serious disease, many have minor effects, as the changes they cause in the sequence of encoded proteins are not significant. Many mutations cause no visible effects at all, either because they occur in introns or because they do not change the amino-acid sequence, due to redundancy of codons. On rare occasions they can create beneficial mutations and can spur evolutionary change in a population. These beneficial mutants may be used for **bioremediation**, to return the environment altered by contaminants to its original condition.

2. LITERATURE SURVEY

The above theoretical background may be supported by previous researcher in some extent in following literatures. **Hebrard *et al.* (2009)** worked on Redundant Hydrogen Peroxide Scavengers Contribute to *Salmonella* Virulence and Oxidative Stress Resistance in at Institut de Microbiologie de la Me´diterrane´e, Chemin Joseph Aiguier, France and found that *Salmonella enterica* serovar Typhimurium is an intracellular pathogen that can survive and replicate within macrophages. One of the host defense mechanisms that *Salmonella* encounters during infection is the production of reactive oxygen species by the phagocyte NADPH oxidase. Among them, hydrogen peroxide can diffuse across bacterial membranes and damage biomolecules. Data indicated that *Salmonella* catalases and alkyl hydroperoxide reductases are required to degrade H_2O_2 and contribute to the virulence.[3]

Mai-Prochnow *et al*. (2008) worked on Hydrogen Peroxide Linked to Lysine Oxidase Activity Facilitates Biofilm Differentiation and Dispersal in Several Gram-Negative Bacteria at School of Biotechnology and Biomolecular Sciences and Centre for Marine Bio-Innovation, University of New South Wales, Sydney. They observed that the marine bacterium *Pseudoalteromonas tunicata* produces an antibacterial and autolytic protein, AlpP. AlpP homologues also occur in several other gram-negative bacteria from diverse environments. Their results show that subpopulations of cells in microcolonies also die during biofilm formation in two of these organisms, *Chromobacterium violaceum* and *Caulobacter crescentus*. In all organisms, hydrogen peroxide was implicated in biofilm cell death, because it

could be detected at the same time as the killing occurred, and the addition of catalase significantly reduced biofilm killing. They propose that biofilm killing through hydrogen peroxide can be linked to AlpP homologue activity and plays an important role in dispersal and colonization across a range of gram-negative bacteria.[4]

Julia & Pueyo1 (1999) they studied the mutagenicity of hydrogen peroxide (H_2O_2) was compared with that of coffee, a complex mixture which generates H_2O_2. An *Escherichia coli* strain defective in catalaseactivity (katG katE double mutant) and carrying a singlecopymucAB (pRW144) plasmid was constructed to enhance the mutagenic response to oxidants. The ability of themucAB genes to in uence the type, frequency and distribution of H_2O_2-induced mutations was also investigated in isogenic bacteria lacking pRW144. Induced mutational spectra were characterized and compared with that of spontaneous mutagenesis. A total of 444 independent for-ward mutations affecting the first 210 bp of the lacI genewere identi ed by DNA sequence analysis. The spontaneousmutation spectrum showed no bias (PJ 0.52) for substitutions at G:C base pairs. In contrast, in the H_2O_2-inducedspectrum substitutions occurred preferentially at G:C base pairs (P < 0.0001) with a preponderance of G:C$\rightarrow$ T:Atransversions (43.4% of H_2O_2-induced mutants versus 17.3% of spontaneous mutants). These data su$\rightarrow$rt the view that 7,8-dihydro-8-oxoguanine is the main premutagenic lesion induced by H_2O_2 and that catalase-defective bacteria have elevated levels of 8-oxoguanine in chromosome DNA after H_2O_2 exposure. Coffee produced a similar distribution of mutational events as H_2O_2 (P > 0.05), suggesting that this compound may be the main cause of the coffee-induced mutagenesis. The presence of plasmid pRW144 did not affect the frequency of H_2O_2-induced G:C $\rightarrow$ T:A transversions, but caused an increase in A:T $\rightarrow$ T:A transversions and a decrease in –1 base frameshifts. Although the frequencies of G:C $\rightarrow$ T:A transversions were similar in all three induced spectra (H_2O_2 and coffee KpRW144), differences were observed in location of mutations throughout the target gene.[5]

Pollution of water was being caused particularly by various industries in **Phagwara Tehsilof Punjab (Refer Figure 1)**. Harmful chemicals were releasing from these factories into **peripheral water bodies** every day (Refer Figure 2). Several people in villages die due to jaundice

caused because of highly polluted drinking water. Among these pollutants **starch residues** which also generated from various **food processing industries** of Phagwara enhance pollution in the water bodies in a drastic way (Refer Figure 3).

Table 1 Different Concentration of H_2O_2 in 25 ml

% Age of the Concentration	Volume of H_2O_2 (ml)	Volume of Distilled Water (ml)
0.25	1.04	24.96
0.50	2.04	22.92
0.75	3.125	21.875
1.00	4.16	20.94
1.25	6.20	19.80
1.50	6.25	19.75
1.75	7.29	17.71
2.00	8.33	16.67
2.25	10.40	15.60
2.50	12.50	13.50

Fig.1 Map of Punjab (place of research)

Fig.2 Sugarcane factory, Sangatpur, Phagwara

Fig.3 Wahid sandhar sugar mill, phagwara, punjab

To eliminate those starch pollutants researcher is trying to develop an amylolytic mutant bacterial consortium with the treatment of different concentration of hydrogen peroxide mutagenic solution, with following objectives.

Ob1. To prepare the Selective Starch Agar Media.
Ob2. To inoculate Amylolytic Bacterial Consortium in Petri Plates.
Ob3. To prepare different Concentrations of Hydrogen Peroxide solution.
Ob4. To give H_2O_2 Treatment for Various Concentrations of that Inoculated Bacterial Consortium in Petri Plates.
Ob5. To identify the Genetically Modified Amylolytic Bacterial Consortium for better Enzymatic Activity.
Ob6. To separate those Modified GMOs for further study.

3. EXPERIMENTAL MATERIALS AND METHODS
3.1 To Demonstrate Starch Hydrolysis:
Preparation of Selective Starch Agar Media

3.1.1 Material required: Laboratory Glass Wares
Petri plates
Pipette

3.1.2 Laboratory equipments
Autoclave
Insulator

3.1.3 Medium
a. **Starch agar medium**

Peptone	5 g
Beef extract	3 g
Soluble starch	2 g
Agar	15 g
pH	7.0

b. **Iodine solution**

Iodine	1 g
Potassium sodium	2 g
Distilled water	300 ml

Crush the iodine and potassium iodide in a mortar and pestle. Dissolve the mixed powder in 300 ml water and stir vigorously. Store it in amber bottles for further use.

3.1.4 Procedure

i.   Heat the starch agar till the medium content melts.
ii. Autoclave it at 121°C for 15 minutes.
iii. After 10 minutes pour the medium into the sterilized Petri plates (15-20 ml).
iv. Allow it to solidify.
v.   Then under aseptic condition, transfer a loopful of growth from sample tube and perform single-line streaking across the centre of the Petri plate.
vi. Incubate the plates at 37°C for 24 hours.
vii. Following the incubation period, flood the plates with iodine solution.
viii. Appearance of clear zone, around the microbial growth indicates positive results.[1](**Refer Fig. 4 & 5**)
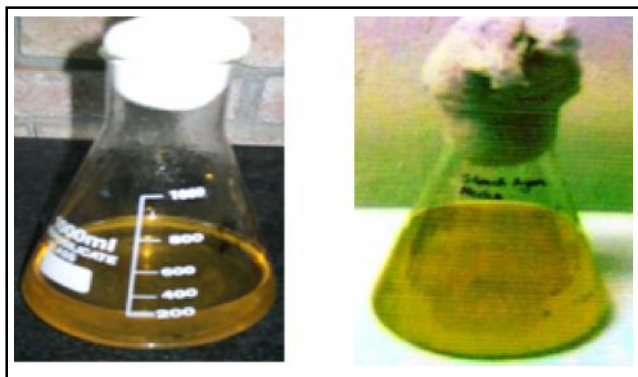
Fig. 4 and 5 Preparation of selective starch agar media

4. FLOW CHART FOR ISOLATION OF AMYLOLYTIC BACTERIA THROUGH SELECTIVE MEDIA

Preparation of selective broth and divide into 20 ml in 10 conical flasks   Inoculate it with different amylolytic consortium   Incubate for 24 hours at 37°C   Prepare selective media plates   Inoculate them with broth of conical flask to corresponding plates (Refer Figures 6 & 7).

Fig.6 Inoculated starch broth conical flask were kept inside shaker for overnight
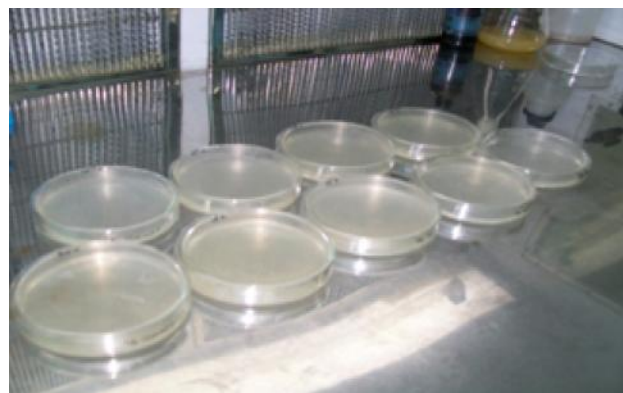
Fig.7 Starch agar plates

4.1 To Prepare Different Concentrations of Hydrogen Peroxide Solution.

4.1.1 Material required
Laboratory Glass Wares
Pipette
Caped Glass Test Tubes

4.1.2 Chemical Required
H_2O_2
Distilled H_2O

4.1.3 Procedure

The different concentration of H_2O_2 was prepared as per Table No.1 and kept in capped Glass Tubes for further use (Refer Fig. 8).
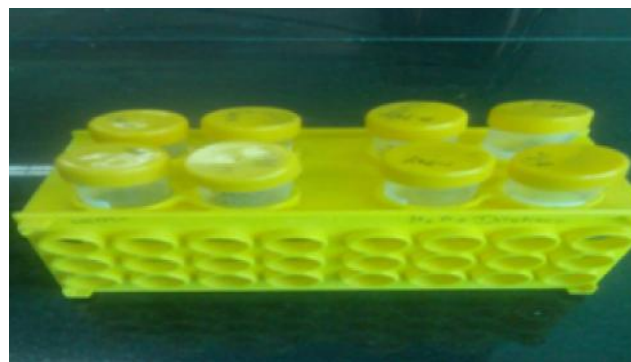
Fig.8 Hydrogen peroxide solutions

To give H_2O_2 Treatment for Various Concentrations of that Inoculated Bacterial Consortium in Petri Plates

Fresh starch agar media plates were inoculated with 1 ml of 24 hour old incubated broth and 1 ml of corresponding percentage concentration of H_2O_2. These plates were incubated at least for 24 hours as before. Then on the basis of hydrolysis of media by the bacterial consortium the results were observed (Refer Figures 9 to 20).
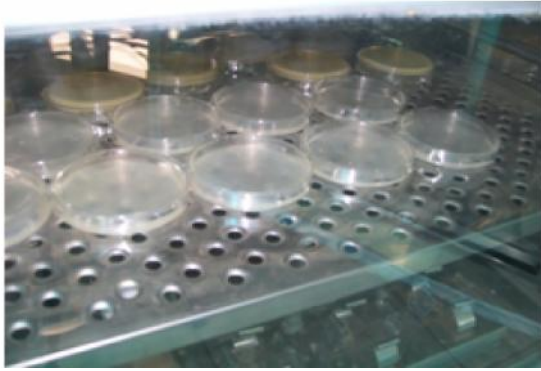
Fig.9 Inoculated Starch Agar Plates with H_2O_2 solutions in Incubator

Fig.10 Control Plate without H_2O_2 treatment
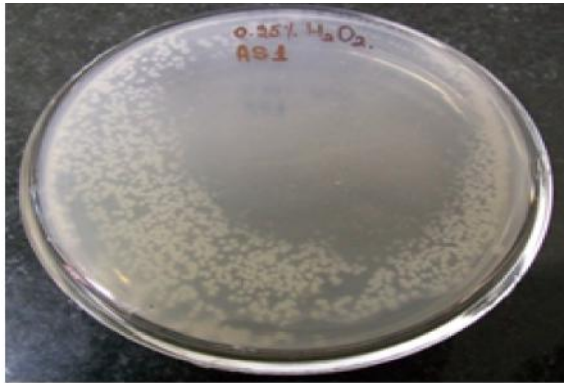
Fig.11 Plate with 0.25% H_2O_2 treatment
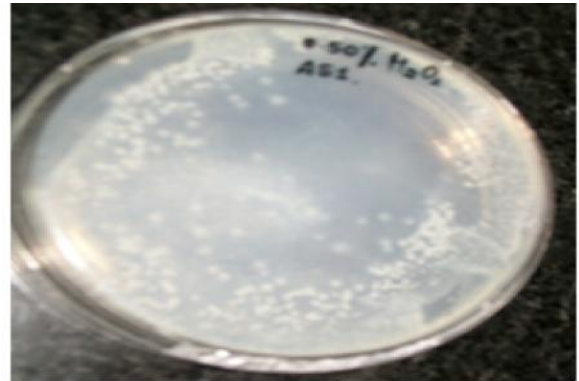
Fig.12 Plate with 0.50% H_2O_2 treatment
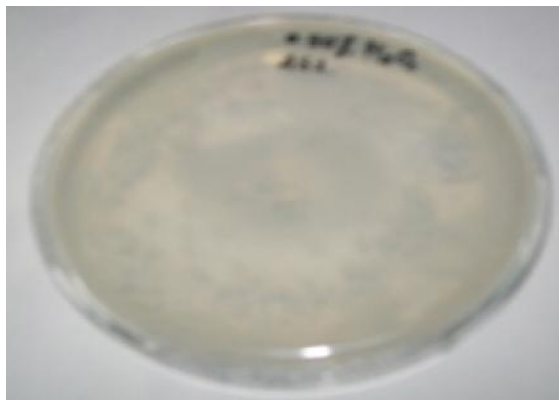
Fig.13 Plate with 0.75% H_2O_2 treatment

Fig.14 Plate with 1% H_2O_2 treatment
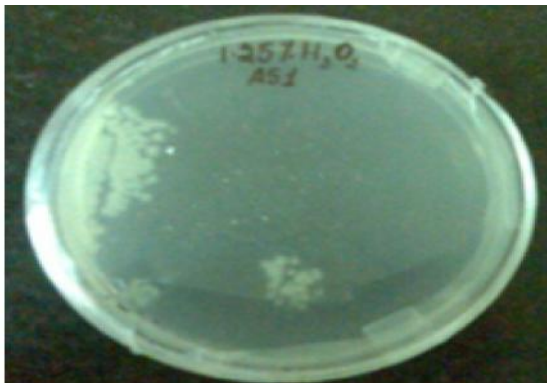
Fig.15 Plate with 1.25% H_2O_2 treatment
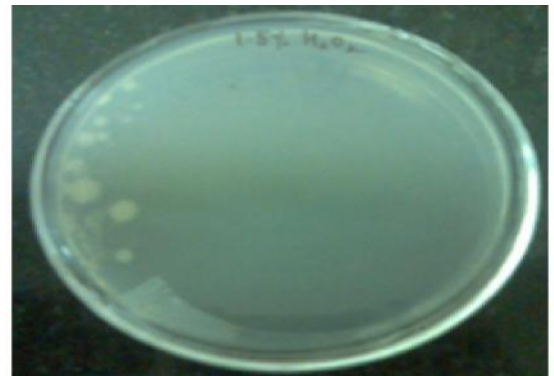
Fig.16 Plate with 1.5% H_2O_2 treatment

Fig.17 Plate with 1.75% H_2O_2 treatment

Fig.18 Plate with 2% H_2O_2 treatment

Fig.19 Plate with 2.25% H_2O_2 treatment

Fig.20 Plate with 2.5% H_2O_2 treatment

5. RESULTS AND DISCUSSION

After the several no. of trials with the cell suspension of amylolytic bacterial consortium with hydrogen peroxide (H_2O_2) solutions it was found that the numerous colonies were spread over the control plate having no hydrogen peroxide (H_2O_2) treatment (Refer Figure 10). But there were remarkably differentiations observed in different percentage of hydrogen peroxide (H_2O_2) concentration containing cell suspension plates (Refer Figures 11 to 20). Though hydrogen peroxide (H_2O_2) acts as a chemical mutagen to bacteria then also the previously isolated from waste water amylolytic bacterial consortium showed their tolerance level up to 2% of hydrogen peroxide (H_2O_2). Beyond the 2% of hydrogen peroxide (H_2O_2) the amylolytic bacterial consortium were observed sensitive. The genetically modified amylolytic bacterial consortium which was showed its maximum optical density in 1.5%, 1.75% and 2% hydrogen peroxide (H_2O_2) treated plates (Refer Figures 16, 17 & 18). They produced larger size colonies with distinct and prominent features. At 2.25% & 2.5% of hydrogen peroxide (H_2O_2) containing plates were showed sensitive and lethal to that concentration to amylolytic bacterial consortium (Refer Figures 19 & 20).

So, in this study it was reviled that the amylolytic bacterial consortium can be modified genetically through hydrogen peroxide (H_2O_2) treatment. It was also observed that at 1.5%, 1.75% and 2% hydrogen peroxide (H_2O_2) treatments modify genetically of amylolytic bacterial consortium for better enzyme production for starch hydrolysis.

6. CONCLUSION

From the figures & results, it was found that amylolytic bacterial consortium can be modified genetically with hydrogen peroxide (H_2O_2) treatments. It was also observed that the hydrogen peroxide (H_2O_2) treatment for 1.5%, 1.75% and 2% were able to generate the most Genetically Modified Organisms (GMOs) i.e. in this case amylolytic bacterial consortium for better enzymatic activity which can be used to reduce industrial starch pollutants to enhance the process of bioremediation.

REFERENCES

[1] A. G. Murugesan and C. Rajakumari, "Environmental Science and Biotechnology, Theory and Techniques", MJP Pub. Chennai, 2005, pp. 349-350, 370-372.

[2] S. H. Imam and R. E. Harry-O'Kuru, "Adhesion of Lactobacillus amylovorus to Insoluble and Derivatized Cornstarch Granules", Applied And Evironme Tal Microbiology, Vol. 57, No.4, 1991, pp.1128-1133.

[3] M. Hébrard, J. P. M. Viala, S. Méresse, F. Barras and L. J.Aussel, "Redundant Hydrogen Peroxide Scavengers Contribute to *Salmonella* Virulence and Oxidative Stress Resistance.J Bacteriol, July 2009, Vol.191, No.14, pp.4605-4614.

[4] A. Mai-Prochnow, P. Lucas-Elio, S.Egan, T. Thomas, J.S. Webb, A.Sanchez-Amat and S. Kjelleberg, "Hydrogen Peroxide Linked to Lysine Oxidase Activity Facilitates Biofilm Differentiation and Dispersal in Several Gram-Negative Bacteria", Journal of Bacteriology, Vol.190, 2008, pp.5493–5501.

[5] L. Julia Ruiz and C. Pueyol, "Hydrogen Peroxide and Coffee Induce G:C'!T:A Transversions in the lacI Gene of catalase-defective", Escherichia coli. Mutagenesis, Vol.14, No.1, 1999, pp.95–102.

Spontaneous Health Monitoring of Workers in Factory Using Zigbee Technology to Prevent Mishap

D. Maria Monica, J.J.Nandhini and C.V.Dharani

Department of Power Electronics and Drives, Kongu Engineering College, Erode - 638 052, Tamil Nadu
E-mail: monicanancy1927@gmail.com, jjnandhini29@gmail.com and dharanikongu21@gmail.com

Abstract

Health monitoring is the major development area in the field of medicine. Continuous health monitoring of patients are gaining more importance because a doctor cannot be able to monitor all the patients every time. In industries, there are many areas, where continuous health monitoring of workers is essential. The workers are working at hazardous regions like mines, power plants etc., The emission of various radiations, rise of temperature, lack of oxygen, etc., leads to many problems. At that time workers need the medical assistance. In present days, all factories are using protective measures for workers. But there is no method for continuous health monitoring of workers. In this paper we adopt the method through which all the important health parameters are monitored and information can be transmitted using Zigbee to the health inspector.

Keywords: *Continuous health monitoring, Factories, Hazardous regions, Health parameters, Medicine, Zigbee.*

1. INTRODUCTION

There are various health problems which are faced by the factory workers. Some of them are listed below.

1.1 Respiratory Problems Faced By Workers:

Coal combustion contributes to smog through the release of oxides of nitrogen, which react with volatile organic compounds in the presence of sunlight to produce ground-level ozone, the primary ingredient in smog. Air pollution triggers attacks of asthma, which now affects more than 9% of all U.S. children, who are particularly susceptible to the development of pollution-related asthma attacks. There are now tens of thousands of hospital visits and asthma attacks each year. Coal pollutants also play a role in the development of chronic obstructive pulmonary disease (COPD), a lung disease characterized by permanent narrowing of airways.

Fig.1 Coalmine workers mainly affected
by respiratory problem

1.2 Cardiovascular Effects

Air pollution is known to negatively impact cardiovascular health. The mechanisms have not been definitively identified, but studies in both animals and humans suggest they are the same as those for respiratory disease: pulmonary inflammation and oxidative stress. Pollutants produced by coal combustion can lead to cardiovascular disease, such as artery blockages leading to heart attacks, and tissue death and heart damage due to oxygen deprivation.

2. MEASURABLE AND NON-MEASURABLE HEALTH PARAMETERS

There are various parameters in our body which can cause illness to the human beings. We are not able to monitor all the parameters. Some of the parameters that can be measured and non measured are given in the following Figure 2.
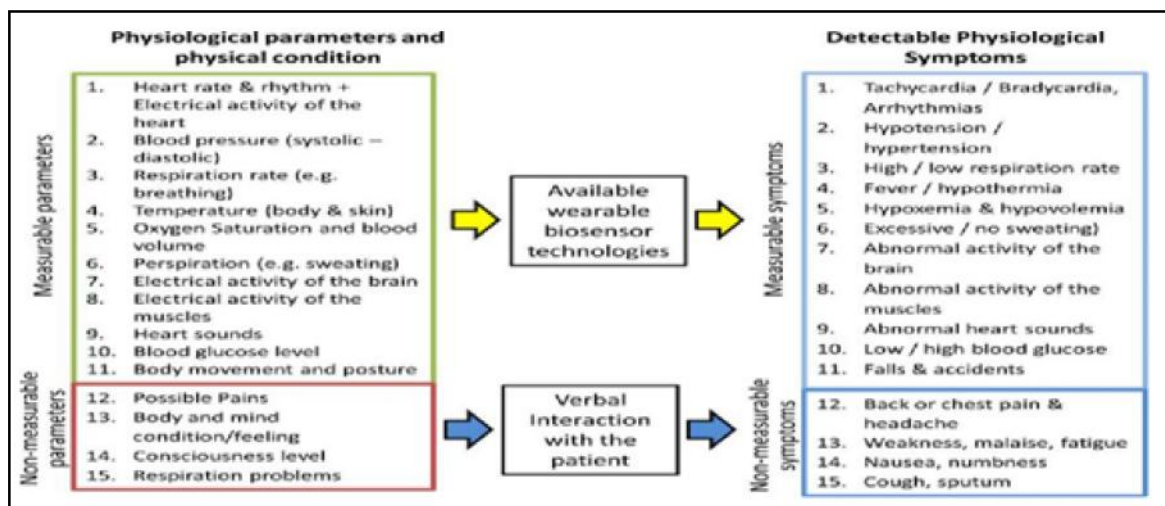
Fig.2 Measurable and Non Measurable Parameters and their Symptoms

3. DESCRIPTION OF THE PAPER

The field of safety precaution for factory workers involves continuous health monitoring of the workers. Our project mainly focuses on the protection of the workers at emergency situation. This is mainly needed for the thermal, nuclear power plants where the health of factory workers is very essential in order to prevent any mishap, here the parameters like heart rate, body temperature and stress level of workers are measured. Another important application is in the mines where the oxygen level may vary often so the O2 sensor is used to measure the O2 level. These types of sensors are available in the market, from this the information are collected and can be displayed in the LCD. By using this method the health of the workers can be monitored continuously from the distant location and required steps can be taken at emergency.

4. BLOCK DIAGRAM

In our project, we have three different blocks. The blocks are power supply, transmitting block and receiving block.

4.1 Transmitter Section:
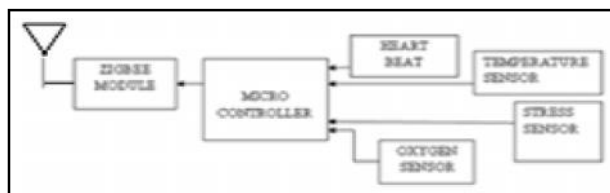
Fig.3 Block diagram of transmitter section
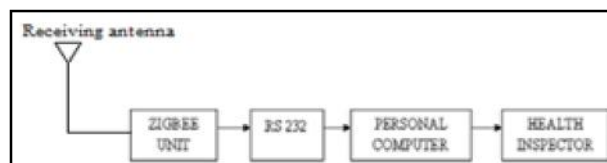
Fig.4 Block diagram of receiver section

5. HARDWARE DESCRIPTION

In the hardware implementation of our project, we have five modules as represented in the block diagram.

i. Power supply module
ii. Sensor module
iii. Microcontroller module
iv. Interface module
v. Output module

5.1 Sensor Module

In sensor module, sensors are used to sense the various health parameters. In our project we use sensors to monitor heart rate, temperature, and stress and oxygen level. Various sensors used are listed below.

i. Heart rate sensor
ii. Stress sensor
iii. Temperature sensor
iv. Oxygen level sensor

5.1.1 Heart Beat Sensor (Ir Base Heart Rate Sensor)

The heart beat sensor provides a simple way to study

the heart's function. The Heart rate varies between individuals. This sensor monitors the flow of blood through finger. As the heart forces blood through the blood vessels in the finger, the amount of blood in the finger changes with time. The sensor shines a light lobe (small High Bright LED) through the ear and measures the light that id transmitted to LDR. The signal is amplified, inverted and filtered, in the circuit. By graphing the signal, the heart rate can be determined, and some details of the pumping action of heart can be seen on the graph Figure 6. Figure 6 shows that the blood flowing through the finger raises at the heartbeat. This is caused by the contraction of the ventricles forcing blood into the arteries. Soon after the first peak of a second, smaller peak is observed. This is caused by the shutting of the heart valve, at the end of the active phase, which raises the pressure in the arteries and earlobe.

Fig.5 Heart beat sensor taken & allied circuit
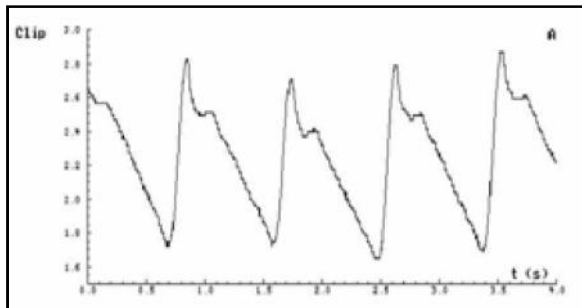
Fig.6 A Sample Measurement with the heartbeat sensor

5.1.2 Temperature Sensor (Thermistor)

Circuits with thermistors can have reasonable output voltages not the mill volt outputs thermocouples have. Because of these qualities, thermistors are widely used for simple temperature measurements. They're not used for high temperatures, but in the temperature ranges where they work they are widely used.

5.1.3 Oxygen Sensor (Mq-5)

An oxygen sensor (or lambda sensor) is an electronic device that measures the n proportion of oxygen (O_2) in the gas or liquid being analyzed. Divers also use a similar device to measure the partial pressure of oxygen in their breathing gas. Scientists use oxygen sensors to measure respiration or production of oxygen and use a different approach. Oxygen sensors are used in oxygen analyzers which find a lot of use in medical applications such as anesthesia monitors, respirators and oxygen concentrators.

5.1.4 Stress Sensor

The problem of job stress is generally recognized as one of the major factors leading to a spectrum of health problems. People with certain professions, like intensive care specialists or call-center operators, and people in certain phases of their lives, like working parents with young children, area increased risk of getting overstressed. Stress management should start far before the stress start causing illness.

The current state of sensor technology allows developing systems measuring physical symptoms reûecting the stress level. Using this sensor we can detect the problem of stress identiûcation.
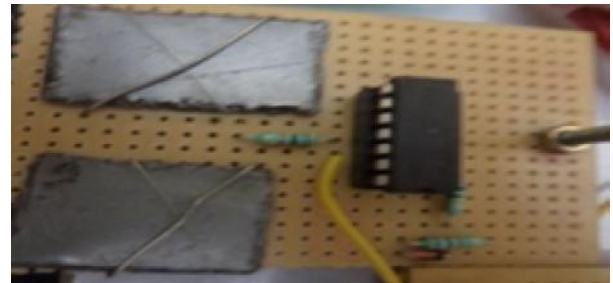
Fig.8 Stress sensor

6. CIRCUIT DIAGRAM

In our paper we have three sections. The various sections are described and corresponding circuit diagrams are also shown.

6.1 Transmitter Circuit

In the transmission circuit, the four health parameters such as heart rate,oxygen level,stress microcontroller is programmed then the outputs are taken out from the digital outputs of microcontroller. The output pins are connected to the LCD display where the digital values of heart rate, oxygen level,stress level and temperature are displayed in it respectively then these output signals are transmitted through zigbee.
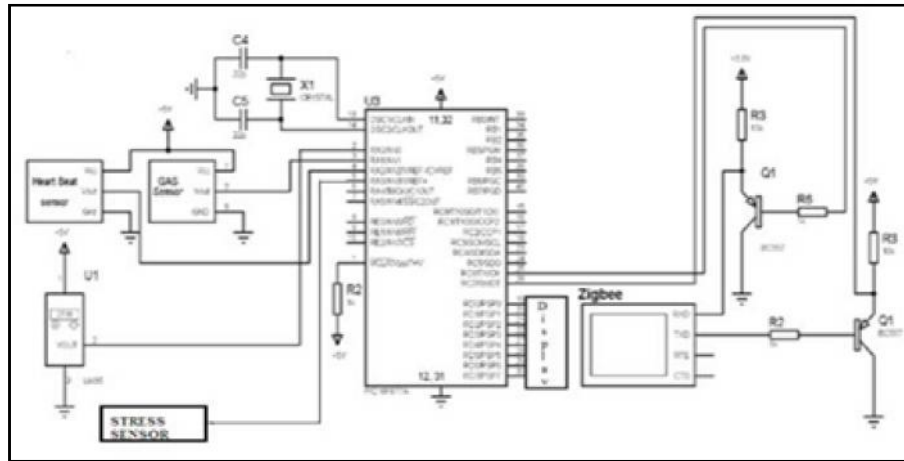
Fig.9 Transmitter circuit

6.2 Receiver Circuit

In the receiver circuit, the information is collected from the zigbee and they are given to the personal computer through serial communication interface RS-232.
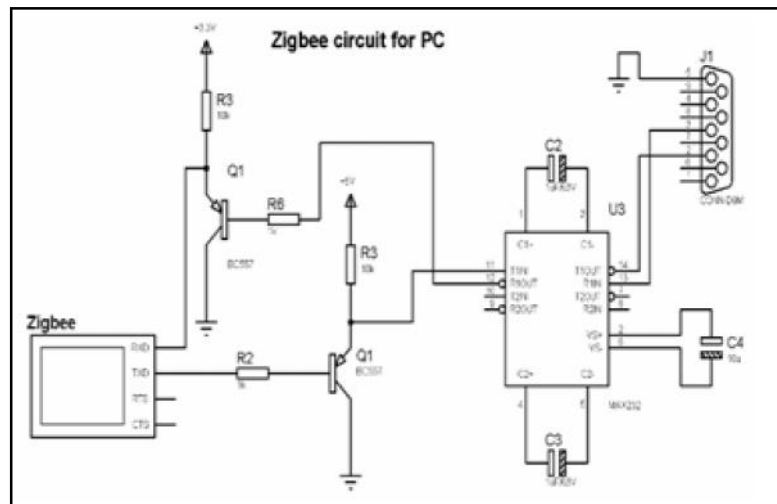
Fig.10 Receiver circuit

7. HARDWARE IMPLEMENTATION AND RESULT

The following figure shows the hardware that is implemented.

Fig.11 Overall arrangement kit

Fig. 12 PC monitor display

8. CONCLUSION

Thus by our paper we have continuously monitored the health parameters of factory workers and the information is transmitted to the health inspector through the zigbee by which we can prevent mal operation in factory and we also provide necessary safety measures to the workers. This method uses zigbee technology so information can be transmitted to long distance and simultaneously information will be updated spontaneously. It will be very useful for mine workers and other risk ful jobs. Hence, by implementing this work it must be highly useful for the society.

REFERENCE

[1] Nabil Hamza, Farid Touati and Lazhar Khriji, "Wireless Biomedical System Design Based on Zigbee Technology for Autonomous Healthcare", International Conference On Communication, Computer And Power, 2009.

[2] Rifat Shahriyar, Md. Faizul Bari, Gourab Kundu, Sheikh Iqbal Ahamed, and Md. Mostofa, "Intelligent Mobile Health Monitoring System (IMHMS)", Automation Vol.2, No.3, September 2009.

[3] P.Murali Krishna Dr.K.Padma Priya, "Remote Wireless Health Care Monitoring System Using Zigbee", Proceedings of International Journal of Engineering Research & Technology (IJERT) in Vol. 1, No.6, August – 2012,

[4] S.Josephine Selvarani, "Online Health Monitoring System Using Zigbee", International Journal on Computer Science and Engineering (IJCSE) Vol. 3, No. 4, Apr 2011, .

[5] Chris A. Otto, Emil Jovanov, and Aleksandar Milenkovic, "A WBAN-based System for Health Monitoring at Home", Journal of Mobile Multimedia, Vol.1, 2006.

[6] A. van Halteren, R. Bults, K. Wac, N. Dokovsky, G. Koprinkov, I. Widya, D. Konstantas, V. Jones, and R. Herzog, " Wireless Body Area Networks for Healthcare: the Mobihealth Project. Stud Health Technol", Inform, 108:181-193, 2004.

[7] D. Konstantas, A. Van Halteren, R. Bults, K. Wac, I. Widya, N. Dokovsky, G. Koprinkov, V. Jones,and R. Herzog, "Mobile Patient Monitoring: the Mobihealth System. Stud Health Technol Inform", 103:307-314, 2004.

[8] Milenkovic, C. Otto, and E. Jovanov, "Wireless Sensor Networks for Personal Health Monitoring: Issues and an Implementation", Computer Communications, 2006.

[9] Jovanov, P. Gelabert, R. Adhami, P. Smith, "Real-time Portable Heart Monitoring using Low Power DSP", International Conference on Signal Processing Applications and Technology, Dallas, Texas, October 2000.

Modelling of Photovolatic Cell and MPPT Algorithm

P. Komalavalli and T. Abinayasaraswathy

Department of Electrical and Electronics Engineering, Sri Manakula Vinayakar Engineering College,
Puducherry - 605 107
E-mail: komu.atp@gmail.com, nclrpwr296@gmail.com

Abstract

The potential for solar energy as a sustainable source of energy is well understood. With the ever increasing use of solar power the necessity of a model is accentuated. The aim of this work is to present the modeling and simulation of photovoltaic model and maximum power point tracking algorithm (MPPT)updating these control algorithms, which would lead to an immediate increase in PV power using MATLAB/Simulink.

Keywords: *Modeling, Photovoltaic module, Simulink model*

1. INTRODUTION

Photovoltaic energy is a source of interesting energy. It is renewable, inexhaustible and non polluting, and that it is more and more intensively used as energy sources in various applications. Photovoltaic systems have been the worldwide fast growing energy source because of the increase in energy demand and the fact that fossil energy sources are finite, and that they are expensive Furthermore, the impacts that the energy technology has on the environment which make the photovoltaic become a mature technology used in [1]. The increase in a number of Photovoltaic system installed all over the world brought the need for proper supervision and control algorithms as well as modeling and simulation tool for researcher and practitioners involved in its application is very necessary.

The modeling and simulation of photovoltaic (PV) have made a great transition and form an important part of power generation in this present age. The modeling of PV module generally involves the approximation of the non-linear I-V curve. Many researchers used circuit based approach to characterize the PV module of which the simplest model is the current source in parallel to a diode[2]. In a PV system, peak power point changes continuously due to environmental variations, sometime substantial drop in power especially during partial shading conditions. Several computational methods are proposed by several researchers [3] Simple circuit-based photovoltaic model has proposed in [4]. Although some of these methods are impractical, complicated and require high computational effort, and some of these modeling was limited to simulation of photovoltaic module characteristics. Thus, because of the numerous challenges, an accurate and comprehensive design of PV system using the detailed circuit model in MATLAB Simulink model was proposed.

The circuit model of the PV module system is shown.,the mathematical equations of the PV module (cells) and the Simulink model for these equations of the PV module is presented. The numerical results for different temperature and irradiance conditions is presented. Detailed of the circuit model of the PV cell is discussed in the next section.

2. CIRCUIT MODELS OF THE PV

Photovoltaic cell models have long been a source for the description of photovoltaic cell behaviors for researchers and professionals. The most common model used to predict energy production in photovoltaic cell modeling is the single diode circuit model [5] is shown in fig 1. The ideal photovoltaic module consists of a single diode connected in parallel with a light generated current source I_{SC} shown in Figure-1. The equation for the output current is given by:

$$I = I_{SC} - I_d \qquad (1)$$
$$I_d = I_{Scref} < \exp(qVoc|kAT) - 1 \qquad (2)$$
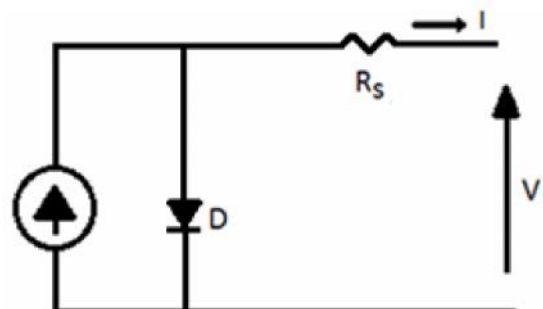
Fig.1 Solar cell model using single diode

The light current depends on both irradiance and temperature. It is measured at some reference conditions. Thus,

$$I_{SC} = [()_{SC\ REF} + k_i\ (T_{k-}\ T_{ref})]*/1000 \tag{3}$$

Where I_{SC} is the photocurrent in (A) which is the light-generated current at the nominal condition (25^oC and $1000W/m2$), Ki is the short-circuit current/ temperature coefficient I_{scref} at ($0.0017A/K$), T_K and T_{ref} are the actual and reference temperature in K, is the irradiance on the device surface, and $1000W/m2$ is the nominal irradiation. Equation (2) does not adequately represent the behavior of the cell when subjected to environmental variations, especially at low voltage [6] A more practical model is shown in Figure-2 where R_s and R_P represents series and parallel resistance, respectively.
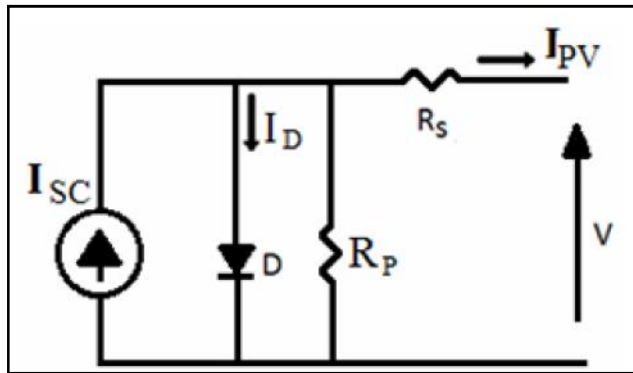
Fig.2 Solar cell model using single diode with R_s and R_P

In this propose model, a current source which depends on solar radiation and cell temperature; a diode in which the inverse saturation current depends mainly on the operating temperature; a series resistance and a shunt resistance which takes into account the resistive losses.

$$I_{sc} - I_D - V_{D/}\ R_p - I_{pv} = 0 \tag{4}$$

Thus,

$$I_{pv} = I_{sc} - I_D - V_{D/}\ R_F \tag{5}$$

And the reverse saturation I_{PS} current is given as:

$$_{rs=scref}\ [\ exp(\ qV_{oc}\ /NskAT) - 1] \tag{6}$$

The module saturation current varies with the cell temperature which is given by

$$I_0 = I_{rs}\ [(T/T_{ref})^3\ e^{\wedge}qcg/Ak*(1/Tref-\ 1/T)] \tag{7}$$

Where I_0 is the diode saturation current (A). The basic equation that describes the current output of the photovoltaic (PV) module I_{PV} of the single-diode model is as given in equation (8).

$$Ipv = NpI_{sc} - NsI_0$$

$$\{exp(qVpv + Ipv\ Rs)\ |\ NsAkT) - 1\} - Vpv + \left(\frac{IpvRs}{Rp}\right) \tag{8}$$

The equation that describes the I-V characteristic Where k is the Boltzmann constant ($1.38 \times 10-23$ JK-1), q is the electronic charge ($1.602 \times 10-19$ C), T is the cell temperature (K); A is the diode ideality factor, the series R_S resistance (Ω) and R_p is the shunt resistance (Ω). Is the number of cells connected in series = 36. Np is the number of cells connected in parallel = 1, The nonlinear and implicit equation given by Equation (4) depend on the incident solar irradiance, the cell temperature, and on their reference values [6]. These reference values are generally provided by manufacturers of PV modules for specified operating condition. for which the irradiance is 1000 W/m2 and the equation that describes the I-V characteristic of the circuit cell temperature is 25^oC. Real operating conditions are always different from the standard conditions, and mismatch effects can also affect the real values of these parameters.

The use of the simplified circuit model for this work makes it suitable for power electronics designers to have an easy and effective model for the simulation of photovoltaic devices with power converters. The value of the Rp parallel resistance is generally high and hence neglected to simplify the model A procedure based on Simulink model to determine the values to these parameters is proposed. The evaluation of these model parameters at real condition of irradiance and temperature of the target PV modules are then determined according to their initial values.

3. SIMULINK MODELING FOR PV MODULE

PV Module is taken as the reference module for simulation and the data are given. A block diagram of the stage by stage model based upon the equations of PV model is represented in Simulink environment as given in Figures 3 to 9. These models are developed in moderate complexity to include the temperature dependence of the photo current source, the saturation current through the diode, and a series resistance is considered based upon the shackle diode equation as in (1)-(8). where the maximum power is 60w and maximum voltage 17v.

Stage A
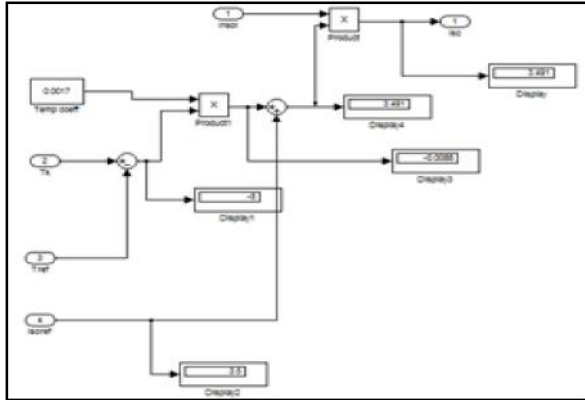
Fig.3 This model calculates the short circuit current at given operating temperature

Stage B

Fig.4 Calculates the reverse saturation current through the diode using equation 6.

Stage C

Fig.5 Reverse saturation current, module reference

Stage E

Fig.6 Operating temperature in Kelvin and calculates the product NsAkT.

Stage E

Fig.7 This model executes the function given by equation 8
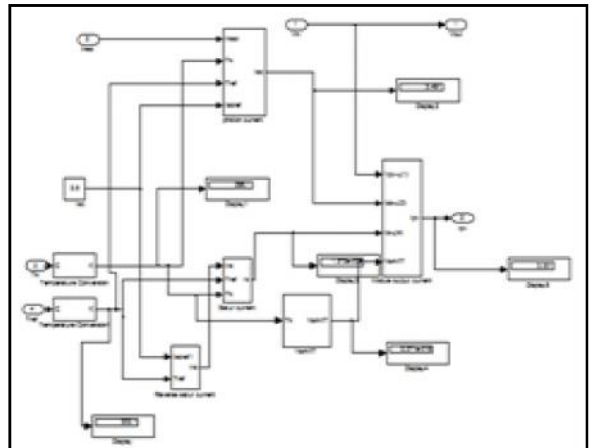
Stage F

Fig.8 All the six model interconnected together.

Stage G
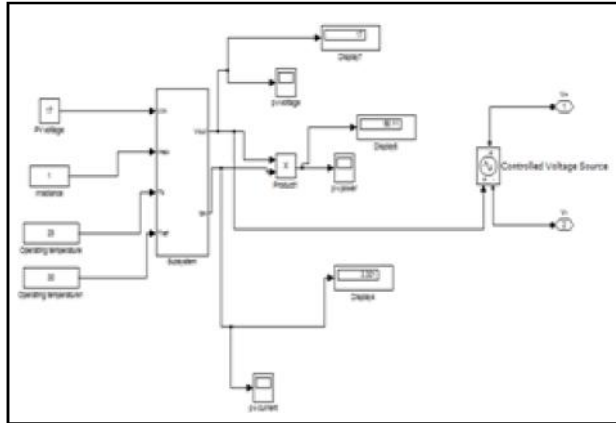
Fig.9 Final model which takes irradiation, operating temperature

4. MAXIMUM POWER POINT TRACKING

The efficiency of a solar cell is very low. In order to increase the efficiency, methods are to be undertaken to match the source and load properly. One such method is the Maximum Power Point Tracking (MPPT). This is a technique used to obtain the maximum possible power from a varying source. In photovoltaic systems the I-V curve is non-linear, thereby making it difficult to be used to power a certain load. This is done by utilizing a boost converter whose duty cycle is varied by using a mppt algorithm. A boost converter is used on the load side and a solar panel is used to power this converter.

4.1 Perturb and Observe Method

This method is the most common. In this method very less number of sensors are utilized. The operating voltage is sampled and the algorithm changes the operating voltage in the required direction and samples dP/dV. If dP/dV is positive, then the algorithm increases the voltage value towards the MPP until dp/dV is negative. This iteration is continued until the algorithm finally reaches the MPP. This algorithm is not suitable when the variation in the solar irradiation is high. The voltage never actually reaches an exact value but perturbs around the maximum power point (MPP).

5. BOOST CONVERTER

Boost converter steps up the input voltage magnitude to a required output voltage magnitude without the use of a transformer. The main components of a boost converter are an inductor, a diode and a high frequency switch. These in a co-ordinated manner supply power to the load at a voltage greater than the input voltage

magnitude. The control strategy lies in the manipulation of the duty cycle of the switch which causes the voltage change.
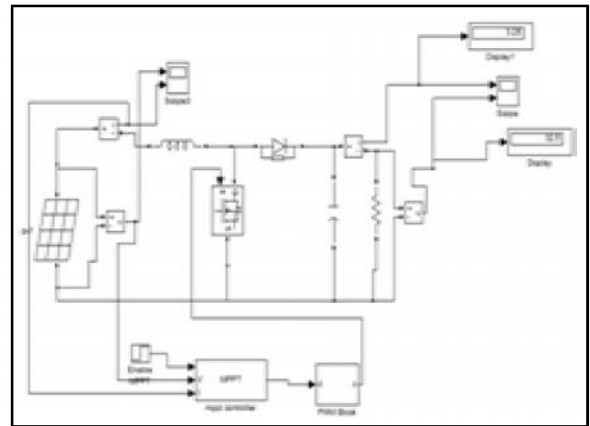
Fig.10 PV with boost converter and MPPT

6. SIMULATION RESULTS

The model of the PV module was implemented using a Matlab Simulink model. The model parameters are evaluated during execution using the equations listed as in the previous section. The PV module chosen for this simulation is which provides 60W nominal maximum power and has 36 series connected cells. The parameter specification of the module is as stages as indicated above starting from stage A to the final model. The subsystem contains all the mathematical equations of every stage model block Figure-11 shows the output characteristics of PV module with varying irradiance at the constant temperatures. It is depicted that the PV output current varies drastically with insulation conditions and there is an optimum operating point such that the PV system delivers its maximum possible power to the load. The optimum operating points changes with the solar insulation, temperature and load conditions.

Fig.11 Output voltage of PV

P. Komalavalli and T. Abinaya saraswathy
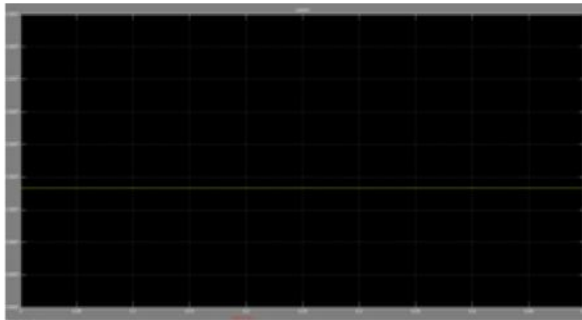
Fig.12 Output current of PV
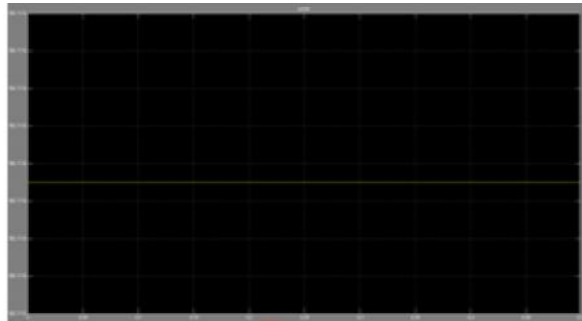
Fig.13 Output power of PV

Fig.14 Output voltage and current from boost converter

7. CONCLUSION

An accurate PV module electrical model is presented and demonstrated in Matlab Simulink. It can be seen that the PV current Isc is a function of the solar irradiation and is the only energy conversion process in which light energy is converted to electrical energy. The physical equations governing the PV module is elaborately presented with numerical values of module saturation current at various temperatures.The frequency of operation was 10 KHz which was set by using a repeating sequence generator. This generator was utilized for generating the pulse signal that was compared with the signal generated from the MPPT unit to give out the gating signal to the switch. When MPPT is used there is no need to input the duty cycle, the algorithm iterates and decides the duty cycle by itself. But if MPPT had not been used, then the user would have had to input the duty cycle to the system. When there is change in the solar irradiation the maximum power point changes and thus the required duty cycle for the operation of the model also changes. But if constant duty cycle is used then maximum power point cannot be tracked and thus the system is less efficient.

REFERENCES

[1] I. H. Altas and A.M.Sharaf, "A Photovoltaic Array Simulation Model for Matlab-Simulink GUI Environment", IEEE, Clean Electrical Power, International Conference on Clean Electrical Power (ICCEP '07), June 14-16, Ischia,Italy, 2007.

[2] S. Chowdhury, S.P. Chowdhury, G. A.Taylor and Y.H. Song, "Mathematical Modeling and Performance Evaluation of a Stand-Alone Polycrystalline PV Plant with MPPT Facility", IEEE Power and Energy Society General Meeting Conversion and Delivery of Electrical Energy in the 1st Century, July 20-24, Pittsburg, USA, 2008.

[3] R. M. Da Silva and J. L. M. Fernandes, "Hybrid Photovoltaic/thermal (PV/T) Solar Systems Simulation with Simulink/Matlab", Solar Energy. Vol.84, 1985-1996.

[4] R. V. Dell Aquila, "A New Approach: Modeling, Simulation, Development And Implementation of a Commercial Grid-Connected Transformer Less PV Inverter", pp.1422-1429.

[5] J. H. Jung and S. Ahmed, "Model Construction of Single Crystalline Photovoltaic Panels for Real-Time Simulation", 2010, pp. 342-349.

[6] M. G. Villalva, J. R. Gazoli, E. Ruppert F, "Comprehensive Approach to Modeling and Simulation of Photovoltaic Arrays", IEEE Transactions on Power Electronics, ISSN 0885-8993, Vol.25, No.5, 2009, pp. 1198—1208,

[7] R. Sridhar, Dr. Jeevananathan, N. Thamizh Selvan, "Modeling of PV Array and Performance Enhancement by MPPT Algorithm", International Journal of Computer Applications (0975 – 8887) Vol.7, No.5, September 2010.

[8] Huan-Liang Tsai, Ci-Siang Tu, and Yi-Jie Su, "Development of Generalized Photovoltaic Model Using MATLAB/SIMULINK", Proceedings of the World Congress on Engineering and Computer Science 2008 WCECS 2008, October 22 - 24, 2008, San Francisco, USA.

Design of Single-Input Dual-Output Dc-Dc Boost Converter

P. Sujitha[1] and K. Sankar[2]

[1]PG Scholar, [2]Assistant Professor, Department of Electrical and Electronics Engineering,
Roever Engineering College, Perambalur - 621 212, Tamil Nadu
E-mail: suji.engg89@gmail.com, ammsankar@gmail.com

Abstract

This paper deals with a fully integrated boost dc-dc converter that provides two different output's with a 100vinput using only one inductor is presented. This converter works under PI control mode to have better efficiency, uses fewer power switches/external compensation components to reduce cost, and is thus suitable for portable application. it is consider monolithic device with both output voltages generated by the same integrated power converter. Besides the proposal of the suitable power converter, this paper present its control strategy and modulation approach. Selected simulated results are presented as well as.

Keywords: Boost converter, DC-DC Converter, Single inductor.

I. INTRODUCTION

Today's modern battery-operated portable products demands for advanced power management integration in portable application .To minimize power consumption, multiple supply voltages and dynamic voltage scaling schemes are widely adopted [2]. Recently, several single-inductor multiple-output (SIMO) DC-DC converters [3-10] have been proposed as the most promising solution to minimize component (inductor and power switch) counts/footprints and production cost. However, there exists many design challenges for the SIMO converters, such as cross-regulation, efficiency, system stability, and flexibility, for achieving better step-up conversion.

In many applications, there are need for a single-inductor dual- output DC-DC converter with one output voltage set to be higher (boost) than the supply voltage. In traditional SIDO Fig.1 (c) topology which has three power switches, and it uses power-distributive control from [6] and applies them to voltage control. Thus, there needs only one output compensation loop, which reduce the amount of external compensated components used, such as [6]. Moreover, this paper also extends the availability of Fig.1(c) topology to implement Boost converter according to different demands.

In this paper, operation and control of the proposed SIDO converter and the effect of cross regulation are discussed in Section II. Section III presents circuit design and implementation issues. Post-layout simulation and results are shown in Section IV. The conclusions are given in Section IV.
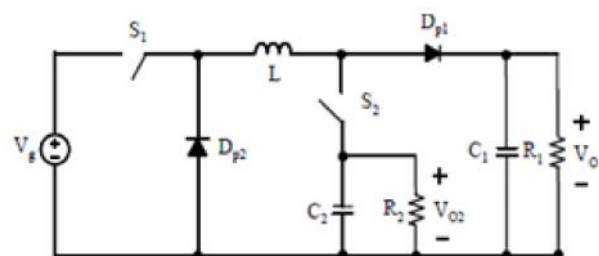
Fig.1Conventional buck type single input dual output dc-dc converter

2. PROPOSED TOPOLOGIES
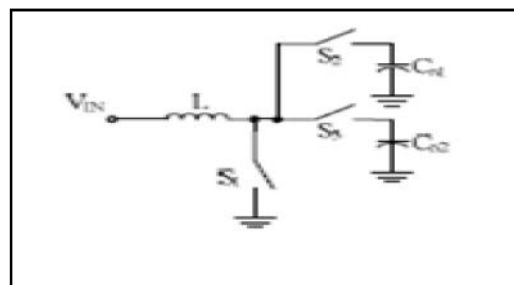
Fig.2 Architecture of boost converter

The single-inductor multi-output DC-DC converters [12-16] were developed to effectively reduce the amount of electronic components for providing multiple output voltages, as shown in Figure 1 [3]. In order to further save the switch Sa or Sb from the single-inductor multi-output DC-DC converter showed in Figure 1, the prior work in [6] presented a novel boost-type single-inductor dual-output DC-DC converter, as shown in Figure 2.

P.Sujitha[1] and K.Sankar[2]
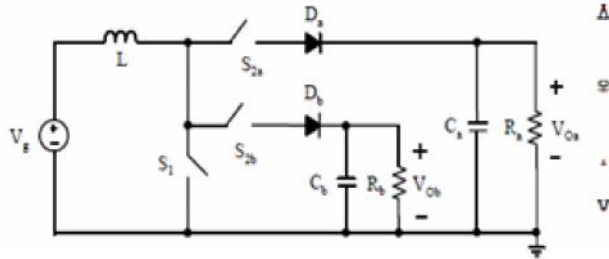
Fig.3 Single-Inductor multi-output switching converter

Fig.4 Boost type Single-Inductor Dual-output dc-dc converter

(b) stage(t_1~t_2)

(c)stage(t_2~t_3)

Fig.5 Operational principle of single-input dual-output dc-dc boost converter

3. BOOST-TYPE SINGLE-INDUCTOR DUAL-OUTPUT DC-DC CONVERTER

3.1 Operational Principles

The operation of the boost-type single-inductor dual output DC-DC converter can be divided into three operating stages at steady state, as shown in Figure 3. At Stage 1, the switches S1 and S2 are turned on simultaneously at time t0. The inductor L is charged by the input DC source and the inductor current increases, as shown in Figure 4(a). At Stage 2, the switch S1 is turned OFF at time t1 but switch S2 is still kept ON until t2. Meanwhile, the inductor discharges to the low-voltage side with output capacitor C2 and load resistor R2 through diode Dp2, such that the inductor current decreases, as shown in Figure 4(b). At Stage 3, the switch S2 is turned OFF at time t2 but switch S1 is still kept OFF until t3. Meantime, the inductor discharges to the high-voltage side with output capacitor C1 and load resistor R1 through diode Dp1, which makes the inductor current decrease more rapidly, as shown in Figure 4(c).

(a)Stage1 (t_0~t_1)

3.2 Derivation of Voltage Ratios

At Stage 1, the incremental inductor current, as shown in Figure 5, can be obtained from Equation (1).

$$\Delta I_1 = \frac{V_g \cdot D_1 \cdot T}{L}, \tag{1}$$

Where D1 is the duty cycle of the switch S1, and T is the switching period.

During Stage 2, to fulfill the requirement of the volt second balance at steady state, the decrease I2 in inductor current can be calculated by Equation(2).

$$\Delta I_2 = \frac{(V_{O2} - V_g) \cdot (D_2 - D_1) \cdot T}{L}, \tag{2}$$

where D2 is the duty cycle of the switch S2.

Similarly, during Stage 3, the decrease 3 ΔI in inductor current can be obtained, as shown in Equation (3).

$$\Delta I_3 = \frac{(V_{O1} - V_g) \cdot (1 - D_2) \cdot T}{L}, \text{ and} \tag{3}$$

At steady state, the increase in the inductor current 1 is equal to the summation of the decreases ($\Delta I_2 + \Delta I_3$), in the inductor current. Therefore, the voltage ratio relationship in between Vg, VO1 and VO2 can be obtained, as shown in Equation (4).
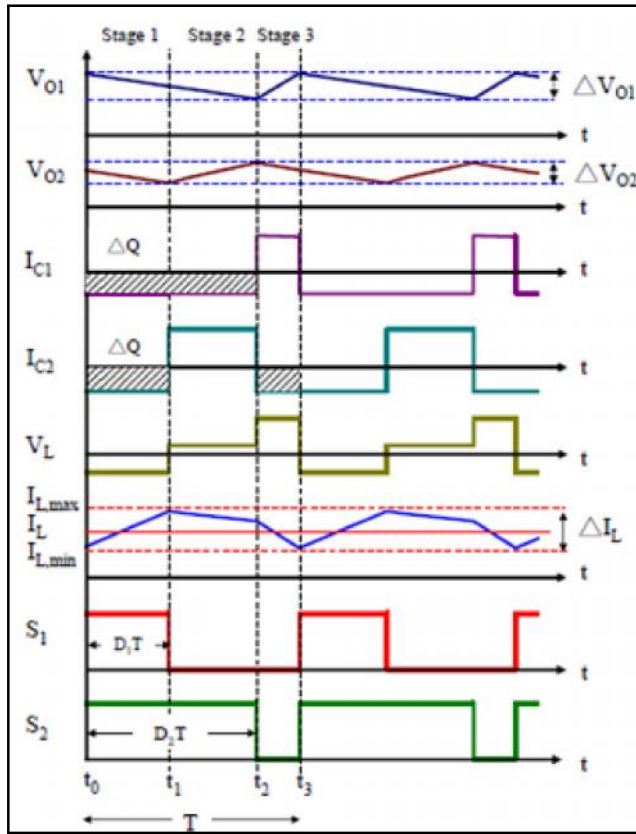
Fig. 6 Key waveforms of single-inductor dual-output dc-dc boost converter

$$\Delta V_{O1} = \frac{T}{C_1} \cdot \frac{(1-D_2)}{R_1} \cdot V_{O1}. \tag{7}$$

$$\Delta V_{O2} = \frac{T}{C_2} \cdot \frac{[1-(D_2-D_1)]}{R_2} \cdot V_{O2}. \tag{8}$$

4. SIMULATION RESULT

The simulation was used to verify the feedback loop design for steady state and large dynamic signal pertubation. Figure 5 shows the simulation results of boost converter with PI controller, converting universal AC input voltage at A100V to a load at 250V DC and 1.6 kW. Figure7 illustrates: No Filtering technique. Middle: The boost inductor current with PI control applied, and Bottom: Series capacitor current in the coupled inductor filter.
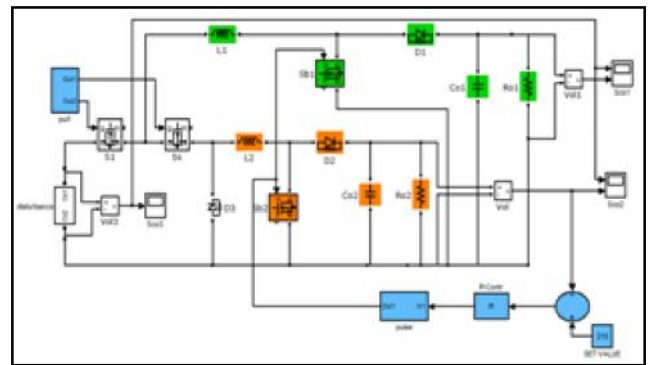
Fig.7 Simulation circuit diagram of single input dual-output dc-dc boost converter

3.3 Derivation of Minimum Inductance in CCM

In order to ensure the operation of CCM condition, the inductance must be greater than a minimum value, as shown in Figure 3, which can be derived by utilizing the principles of energy conservation, as shown in Equation (5).

$$P_{in} = V_g \cdot I_L = P_O = \frac{V_{O1}^2}{R_1} + \frac{V_{O2}^2}{R_2}. \tag{5}$$

where Pin is the input power, and PO is the output power. Based on Equation (4) and the minimum level of inductor current IL,min in Figure 3, the minimal inductance Lmin can be obtained, as shown in Equation (6).

$$L_{min} \geq \frac{[V_{O1} \cdot D_2 \cdot (1-D_2)+V_{O2} \cdot (D_2^2-D_1^2 \cdot D_2+D_1)] \cdot [V_{O1} \cdot (1-D_2)+V_{O2} \cdot (D_2-D_1)] \cdot T \cdot R_1 \cdot R_2}{2 \cdot (R_2 \cdot V_{O1}^2+R_1 \cdot V_{O2}^2)}.$$

3.4 Derivation of Output-Voltage Ripples

Since the capacitors C1 and C2 are connected to the two output terminals of the boost-type single-inductor dual output DC-DC converter, the output voltage ripples ³%VO1 and ³%VO2 of the output capacitors C1 and C2 can be calculated by utilizing the amp-second balance principle, as shown in Equations (7) and (8), respectively.

The proposed output is steady state and dynamic response improved. The steady state response in output constant voltage maintain in system.

(a) DC input voltage

P.Sujitha[1] and K.Sankar[2]
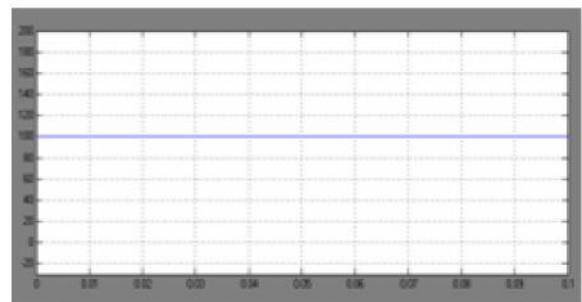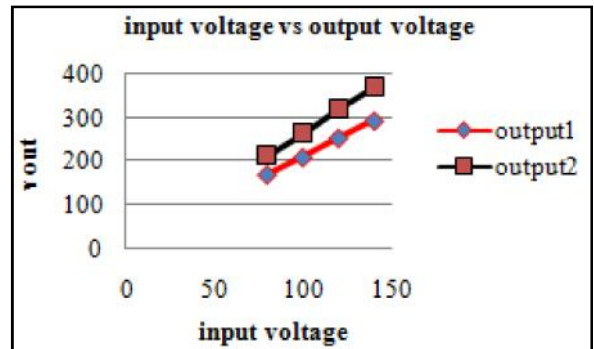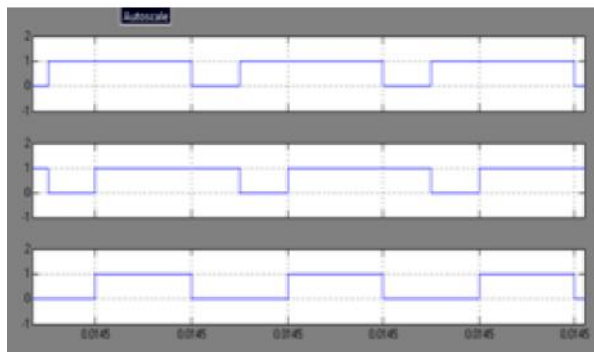
(b) Gate pulses for switches
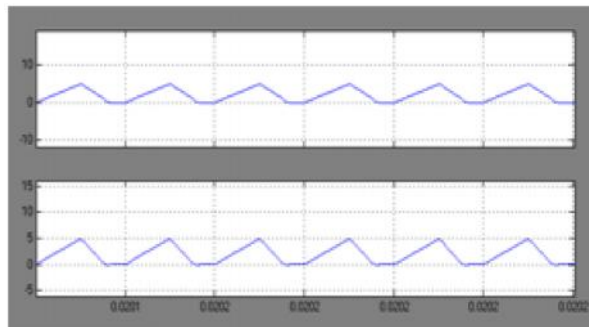
(c) Inductor current through L_1 and L_2

Fig. 8 DC input voltage (a) gate pulses for switches
(b) inductor current L_1 and L_2(c)
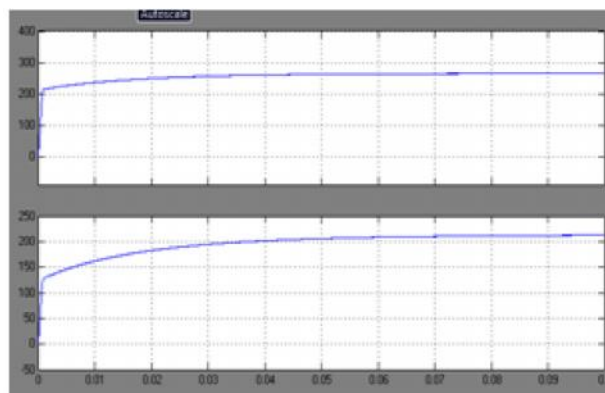
Fig.9 Simulation result of Dc output voltage 1 and voltage2

5. CONCLUSION

This paper has presented the single inductor dual-output DC-DC converters. The boost-type single-inductor dual-output DC-DC converter has been introduced and analyzed, including the output voltage ripples, the voltage ratios and the minimum inductance in CCM by using amp-second balance principle and volt second balance principle . Further more, the boost-type single-inductor multi-output DC-DC converter can be extended from the boost-type single-inductor dual-output DC-DC converter. Additionally, the experimental results show the waveforms of the output voltages, inductor current and duty cycles for the boost-type single-inductor dual-output DC-DC converter. Finally, the experimental results are in good accordance with the operation the boost-type single inductor dual-output DC-DC converter at steady state.

REFERENCES

[1] Q. Chen, M. M. Jovanovic, and F. C. Lee, "Analysis and Design of Weighted Voltage-Mode Control for a Multiple-Output Forward Converters", Proc. IEEE Applied Power Electronics Conf, 7-11 Mar. 1993, pp.449- 455.

[2] F. Kurokawa, and H. Matsuo, "A New Multiple-Output Hybrid Power Supply", IEEE Transactions on Power Electronics, Vol.3, No.4, Oct. 1988, pp. 412-419.

[3] H. Matsuo, and K. Harada, "New energy-storage dc-dc converter with multiple outputs," IEEE Trans. Magn., vol. 14, no. 5, pp. 1005- 1007, Sept. 1978.

[4] A. P. Dancy, R. Amirtharajah, and A. P. Chandrakasan, "High Efficiency Multiple-output DC-DC Conversion for Low-voltage Systems", IEEE Trans. VLSI Systems, Vol. 8, No. 3, Jun. 2000, pp. 252-263.

[5] J. M. Chang and M. Pedram, "Energy Minimization Using Multiple Supply Voltages", IEEE Trans. VLSI System, Vol. 5, No. 4, Dec. 1997, pp. 436-443.

[6] Q. Chen, F. C. Lee, and M. M. Jovanovic, "Small-Signal Analysis and Design of Weighted Voltage-Mode Control for a Multiple- Output Forward Converter", Proceedings of 1993 IEEE Power Electronics Specialists Conference, Seattle, 20-24 Jun.1993, pp. 749-756.

[7] S. -K. Hoon, N. Culp, J. Chen, and F.Maloberti, "A PWM dual-output dc/dc Boost Converter in a 0.13um CMOS Technology for Cellular Phone Backlight Application", Proc. European Solid-State Circuits Conference, 2005, pp.81-84.

[8] S. Koon, Y.-H. Lam, and W.-H. Ki, "Integrated Charge-control Single Inductor Dual-output Step-up/step-down Converter", in *Proc.* IEEE Int. Symp. Circuits Syst., May 2005, pp. 3071–3074.

[9] C.-S. Chae, H.-P. Le, K.-C. Lee, G.-H. Cho, and G.-H. Cho, "A Single Inductor Step-up dc–dc Switching Converter with Bipolar Outputs for Active Matrix OLED Mobile Display Panels", in Proc. *IEEE ISSCC Dig. Tech. Papers*, Feb. 2007, pp. 136–137.

[10] H.-P. Le, C.-S. Chae, K.-C. Lee, S.-W. Wang, G.-H. Cho and G.-H. Cho, "A Single-inductor Switching DC–DC Converter with Five Outputs and Ordered Power-Distributive Control", IEEE J. Solid-State Circuits, Vol. 42, No.12, Dec. 2007, pp. 2706–2714.

[11] Y.-J. Woo, H.-P. Le, G.-H. Cho, G.-H. Cho and S.-I. Kim, "Load Independent Control of Switching DC–DC Converters with Freewheeling Current Feedback", IEEE J. Solid-State Circuits, Vol.43, No.12, Dec. 2008, pp. 2798-2808.

[12] K.-S. Seol, Y.-J. Woo, G.-H. Cho, G.-H. Gho and J.-W. Lee, "A Synchronous Multi Output Step-up/down DC–DC Converter with Return Current Control", IEEE Trans. Circuits Syst. II, Exp. Briefs, Vol.56, No.3, Mar. 2009, pp.210–214.

[13] M. Chen and G. A. Rinc n-Mora, "Single Inductor, Multiple Input, Multiple Output Power Mixer–charger–supply System", in Proc. Int. Symp. Low Power Electron. Des., Aug. 2007, pp. 301–315.

[14] S. Kim and G. A. Rinc n-Mora, "Single-inductor Dual-input Dual-output Buck–boost Fuel-cell–Li-ion Charging DC–DC Supply", in Proc. IEEE ISSCC Dig. Tech. Papers, Feb. 2009, pp. 444–445.

[15] M. Belloni, E. Bonizzoni, E. Kiseliovas, P. Malcovati, F. Maloberti, T. Peltola and T. Teppo, "A 4-output Single Inductor DC–DC Buck Converter with Self-boosted Switch Drivers and 1.2 A Total Output Current", in Proc.IEEE ISSCC Dig. Tech. Papers, Feb. 2008, pp. 444–445.

PFC Sepic Converter Based Control of PMBLDC Motor Drive

M. Maruthu Pandi and D.Deenadayalan

Department of Electrical & Electronics Engineering, Anna University, Regional Centre,
Coimbatore - 641 047, Tamil Nadu
E-mail: maruthu21@gmail.com, ddayalan.eee@gmail.com

Abstract

In this paper, a permanent magnet brushless DC motor (PMBLDCM) is working in air-conditioning systems and functioned at rated torque and variable speed to accomplish energy management. A single-phase single-switch power factor correction (PFC) based single ended primary inductor converter (SEPIC) is used to standardize DC bus voltage of voltage source inverter (VSI) to feed PMBLDCM. The investigation, scheme and performance evaluation of the suggested PFC converter is carried out for a 1.2 kW, 1200 rpm, 164V PMBLDCM used in air-conditioning system. The suggested PFC converter is demonstrated and its performance is simulated in MATLAB/SIMULINK atmosphere. An extensive calculation of its performance is carried out to establish better power factor in wide range of speed of the drive and AC input voltage.

Keywords: PFC converter, SEPIC, PMBLDC motor, air conditioning, power quality (PQ)

1. INTRODUCTION

Air-conditioners (Air-Cons) create a considerable amount of load in ac distribution system [1]. However, most of the present air-conditioners are not energy effective and thereby, provide a scope for energy conservation. Air-Cons in local area are usually driven by a single-phase induction motor running at constant rated torque with on-off control [1]. A permanent magnet brushless DC motor (PMBLDCM) is a good drive for air conditioners due to its great effectiveness, noiseless process, compressed dimension, high consistency, simplicity of control and low maintenance requirements. A PMBLDCM is a kind of three-phase synchronous motor having permanent magnets on the rotor [2-7]. Generally these PMBLDCMs in small Air-Cons are driven from single phase AC mains over a diode bridge rectifier (DBR) using smoothening DC capacitor and a three-phase voltage source inverter (VSI) [3-4, 6-7]. Because of precise charging of DC link capacitor, the AC mains current waveform is a pulsated waveform containing a peak value higher than the amplitude of the fundamental input current as shown in Fig. 1. The power factor (PF) is 0.741 and crest factor (CF) of AC mains current is 2.2 with 67% efficiency of the drive. Therefore, many power quality (PQ) problems arise at input AC mains comprising poor power factor, improved total harmonic distortion (THD) and high crest factor (CF) of AC mains current etc. These power quality problems as lectured in IEC 61000-3-2 [8] especially in low power applications become severe for the utility when many such drives

are working instantaneously at adjacent areas. Therefore, PMBLDCM drives having in-built power factor correction (PFC) become the favored choice for the Air-Cons. The PFC converter draws sinusoidal current from AC mains in phase with its voltage. In this PFC converter a DC-DC converter topology is commonly used among some existing topologies [9-16] e.g. boost, buck-boost, Cuk, SEPIC, zeta converters with variations of capacitive/inductive energy transfer. It results in an better performance, such as reduction of AC mains current harmonics, acoustic noise, electromagnetic interference (EMI) and number of components; improved efficiency, wide input voltage range utilization etc. Some attempts [11,13,16] have been made to introduce PFC feature in PMBLDCM drives using uni-polar excitation [13] and bipolar excitation [11,16] of PMBLDCMs.
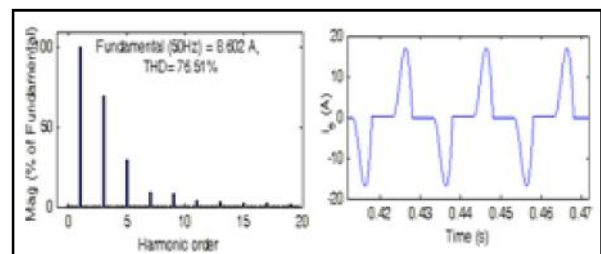
Fig. 1 Supply current and harmonic spectrum (at 220VAC) of a DBR fed PMBLDCM drive at rated load

For automotive air-conditioning a low voltage PMBLDCM drive has been described [15] with compact size of the complete system. However, a PMBLDCM is best well-matched for air conditioning

system due to simple mechanism and its high average torque. When single ended primary inductor converter (SEPIC) used as a power factor correction converter, which give the advantages such as uninterrupted input current, reduced ripple current.

Therefore, a SEPIC converter is proposed for PFC in a PMBLDCM drive used to drive air-conditioners. This paper, deals with complete design and exhaustive performance valuation of the SEPIC converter as a PFC converter, for PMBLDCM driven air conditioner system.

2. OPERATION AND CONTROL OF SEPIC CONVERTER FED PMBLDCM

Figure 2 shows the suggested SEPIC based PFC converter fed PMBLDCM drive for the speed control as well as power factor correction (PFC) in wide range of input AC voltage. A proportional-integral (PI) controller [4] is used for the speed control of the PMBLDCM driving constant torque compressor of air conditioner. The speed signal transformed from the rotor position of PMBLDCM (sensed using Hall Effect sensors) is matched with the reference speed. The resultant speed error is fed to a speed controller to give the torque which is converted to current signal. This signal is reproduced with a quadrilateral unit pattern in phase with top flat portion of motor s back EMF to get reference currents of the motor. These reference motor currents are equated with sensed motor currents to give current error. These current errors are amplified and compared with trilateral carrier wave to generate the PWM pulses for VSI switches.
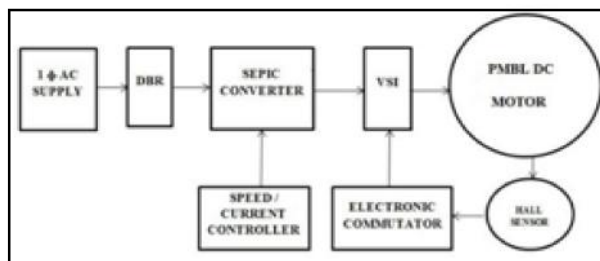
Fig. 2 Block diagram of PFC based SEPIC Converter fed PMBLDCM Drive

The SEPIC based PFC converter has a conventional diode bridge rectifier(DBR) fed from single-phase AC mains followed by the SEPIC DC-DC converter, an output ripple filter and a three-phase voltage source inverter(VSI) to feed the PMBLDC motor. The DC-DC converter offers a precise DC voltage from uncontrolled DC output of DBR, with PFC action

through high frequency switching. The duty ratio (D) of the DC-DC converter is controlled by the DC voltages at its input and output. The switching frequency (fs) is decided by the switching device used, power range and switching losses of the device. In this work, insulated gate bipolar transistors (IGBTs) are used as the switching devices in the PFC switch as well as in VSI bridge, because IGBTs can work in wide switching frequency range to make optimal balance between magnetic, size of filter components and switching losses. The PFC controller has outer voltage control loop and inner current control loop. An average current control arrangement with current multiplier methodology is used in this topology and a continuous conduction mode (CCM) operation of SEPIC is considered for PMBLDCM drive. The voltage control loop starts with sensing of DC link voltage which is compared with the reference DC link voltage. The error DC voltage is passed through a voltage PI controller to give the modulating current signal. This signal is multiplied with a unit pattern of input AC voltage and the resultant signal is related with DC current detected after the DBR to give current error. This current error is enlarged and improved signal is then compared with saw-tooth carrier wave to generate the PWM switching pulses for the DC-DC converter switch.

3. DESIGN OF SEPIC PFC CONVERTER FOR PMBLDCM

Figure 3 shows the simulink diagram of suggested SEPIC converter for PMBLDCM drive. The SEPIC converter attains high power density and fast transient reaction when functioned at high switching frequency [16]. It is intended for constant current in the intermediate inductor (Lo) as it operates on the principle of an inductive energy transfer [17]. The boost inductor (Li), and capacitors (C1, Co) are designed permitting to extreme permissible current and voltage ripple during transient situations of the PMBLDCM drive.
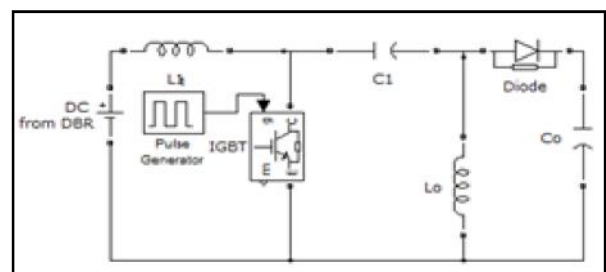
Fig. 3 Simulink diagram of PFC based SEPIC converter

PMBLDCM with boost PFC converter [11] and PMSM with enhanced power quality converter [12] have been described for domestic Air-Cons. The design equations governing the duty ratio and other component values are as follows.

Output voltage V_{dc}=D Vin /(1-D) (1)

Boost inductor Li= D Vin/ {fs (ILi)} (2)

Intermediate capacitor C1=D/{(Rfs) (VC1/ Co)} (3)

Output filter inductor Lo= (1-D)Vdc/{fs(ILo) (4)

Output filter capacitor Co=Iav/(2 Vdc) (5)

The PFC converter is designed for a constant DC link voltage Vdc = 400V at Vin = 198V for Vs = 220V. Other design data are fs = 40kHz, Iav = 5A, R= 80 , ILi= 0.75A, ILo= 0.75 A (15% of Iav), Vdc= 5V (1.25% of Vdc), VC1=15V (3.75% of Vdc). The design parameters calculated are Li=4.5mH, C1=5µF, Lo=4.5mH,Co=1600µF.

4. MODELING OF PROPOSED PFC CONVERTER BASED PMBLDCM DRIVE

The modeling of proposed PFC converter fed PMBLDCM drive involves modeling of a PFC converter and PMBLDCM drive. The PFC converter consists of a DBR and a SEPIC converter with output ripple filter. Various components of PMBLDCM drive are a speed controller, a reference current generator, a PWM current controller, VSI and a PMBLDC motor. All these components of a PMBLDCM drive are demonstrated by mathematical equations and the complete drive is characterized by mixture of these models.

4.1 PFC Converter

The modeling of a PFC converter involves the modeling of a voltage controller, a reference current generator and a PWM controller as given below.

4.1.1. Voltage Controller

The voltage controller is back-bone of PFC converter, it affects the performance of complete drive. A PI controller is used to control the DC link voltage. If at kth instant of time, V*dc(k) is reference DC link voltage, Vdc(k) is sensed DC link voltage then the voltage error Ve(k) is calculated as,

Ve(k) =V*dc(k)-Vdc(k) (6)

The voltage (PI) controller gives desired control signal after processing this voltage error. The output of the controller Ic(k) at kth instant is given as,

Ic (k) = Ic (k-1) + Kpv{Ve(k)−Ve(k-1)}+KivVe(k) (7)

Where Kpv and Kiv are the proportional and integral gains of the voltage controller.

4.1.2 Reference Current Generator

The reference inductor current of the SEPIC converter is denoted by idc* and given as,

Idc* = Ic (k) uvs (8)

Where uvs is the unit template of the voltage at input AC mains, calculated as,

uvs = vd/Vsm; vd = |vs|; vs= Vsm sin ωt (9)

where ω is frequency in rad/sec at input AC mains.

4.1.3. PWM Controller

The reference inductor current of the SEPIC converter (Idc*)is compared with its sensed current (Idc) to generate the current error Δidc=(Idc* - Idc). This current error is amplified by gain kdc and compared with fixed frequency (fs) saw tooth carrier waveform md(t) to get the switching signals for the IGBT of the PFC converter as,

If kdcΔidc> md (t) then S = 1 (10)

If kdcΔidc<= md (t) then S = 0 (11)

where S is the switching function representing 'on' position of IGBT of PFC converter with S=1 and its 'off' position with S=0.

4.2 PMBLDCM Drive

The modeling of a speed controller is quite important as the performance of the drive depends on this controller. If at kth instant of time, ω*r(k) is reference speed, ωr(k) is rotor speed then the speed error ωe(k) can be calculated as

ωe(k)=ω*r(k)-ωr(k) (12)

This speed error is processed through a speed controller to get desired control signal.

4.2.1. Speed Controller

The speed controller used in this work is a PI controller due to its simplicity. Its output at kth instant is given as

T(k) = T(k-1) + Kpω{ωe(k) – ωe(k-1)} + Kiω ωe(k) (13)

where Kpω and Kiω are the proportional and integral gains of the speed PI controller.

4.2.2. Reference Winding Currents

The amplitude of stator winding current is calculated as $I^* = T(k) / (2Kb)$ (14) where, Kb is the back emf constant of the PMBLDCM. The reference three-phase currents of the motor windings are denoted by ia*, ib*, ic* for phases a, b, c respectively and given as

$i_a^* = I^*, i_b^* = - I^*, i_c^* = 0$ for $0^o \leq \theta \leq 60^o$ (15)

$i_a^* = I^*, i_b^* = 0, i_c^* = - I^*$ for $60^o \leq \theta \leq 120^o$ (16)

$i_a^* = 0, i_b^* = I^*, i_c^* = - I^*$ for $120^o \leq \theta \leq 180^o$ (17)

$i_a^* = -I^*, i_b^* = I^*, i_c^* = 0$ for $180^o \leq \theta \leq 240^o$ (18)

$i_a^* = -I^*, i_b^* = 0, i_c^* = I^*$ for $240^o \leq \theta \leq 300^o$ (19)

$i_a^* = 0, i_b^* = -I^*, i_c^* = I^*$ for $120^o \leq \theta \leq 180^o$ (20)

where θ is rotor position angle in electrical radian/sec.

These reference currents are compared with sensed phase currents to generate the current errors $\Delta i_a = (i_a^* - i_a)$, $\Delta i_b = (i_b^* - i_b)$, $\Delta i_c = (i_c^* - i_c)$ for three phases of the motor. These current errors Δi_a, Δi_b, Δi_c are amplified by gain k1 before feeding through the PWM current controller.

4.2.3. PWM Current Controller

The PWM current controller compares these amplified current errors of each phase with carrier waveform m(t) of a fixed frequency and generates the switching sequence for the voltage source inverter based on the logic given for phase "a" as,
If $k1 \Delta i_a > m(t)$ then $S_a = 1$ (21)
If $k1 \Delta i_a <= m(t)$ then $S_a = 0$ (22)
The switching sequences S_b and S_c are generated using similar logic for other two phases of the VSI feeding PMBLDC motor.

4.2.4. Voltage Source Inverter

Figure 4 shows an equivalent circuit of a VSI fed PMBLDCM. The output of VSI to be fed to phase 'a' of the PMBLDC motor is given as,
$v_{ao} = (V_{dc}/2)$ for $S_{a1} = 1, S_{a2} = 0$ (23)
$v_{ao} = (-V_{dc}/2)$ for $S_{a1} = 0, S_{a2} = 1$ (24)
$v_{ao} = 0$ for $I_{a^*} = 0$ (25)
$v_{an} = v_{ao} - v_{no}$ (26)

Using similar logic v_{bo}, v_{co}, v_{bn}, v_{cn} are generated for other two phases of the voltage source inveter feeding PMBLDC motor, where v_{ao}, v_{bo}, v_{co}, and v_{no} are

voltages of three-phases and neutral with respect to virtual(fundamental) mid-point of the capacitor shown as 'o' in Figure 3. The voltages v_{an}, v_{bn}, v_{cn} are voltages of three phases with respect to neutral and V_{dc} is the DC link voltage. The equations (Table 1) represent the dynamic model of the PMBLDC motor. Various symbols used in these equations are the reference currents of the PMBLDCM for phases a, b, c are i_{a^*}, i_{b^*}, i_{c^*}, current error of phase "a" is i_a, error gain k1 and carrier waveform for the PWM current controller m(t).
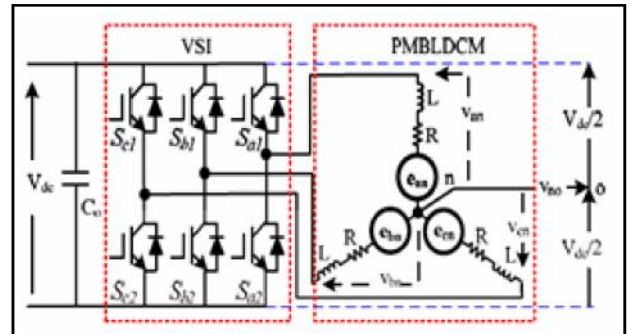
Fig. 4 Equivalent circuit of VSI fed PMBLDC Motor drive

4.2.5. PMBLDC Motor

The PMBLDCM is modeled in the form of a set of differential equations given in Table 1. Voltages of the three-phases and neutral point (n) with respect to virtual mid-point of the DC link voltage 'o', v_{ao}, v_{bo}, v_{co}, and v_{no}, voltages of three phases with respect to neutral point (n) v_{an}, v_{bn}, v_{cn} and the DC link voltage V_{dc} as shown in Figure 2.

Table 1 Modeling Equations of PMBLDC Motor

$v_{xn} = Ri_x + p\lambda_x + e_{xn}$,

$\lambda_a = Li_a - M(i_b + i_c)$;

$\lambda_b = Li_b - M(i_a + i_c)$;

$\lambda_c = Li_c - M(i_b + i_a)$;

$i_a + i_b + i_c = 0$;

$V_{an} = V_{ao} - V_{no}$;

$V_{no} = \{V_{ao} + V_{bo} + V_{co} - (e_{an} + e_{bn} + e_{cn})\}/3$;

$\lambda_a = (L+M) i_a, \lambda_b = (L+M) i_b, \lambda_c = (L+M) i_c$;

$pi_x = (v_{xn} - i_x R - e_{xn})/(L+M)$;

$T_e = (e_{an} i_a + e_{bn} i_b + e_{cn} i_c)/ \omega$ and

$e_{xn} = Kb f_x(\theta) \omega$

$f_a(\theta) = 1$ for $0 < \theta < 2\pi/3$

$f_a(\theta) = \{(6/\pi)(\pi - \theta)\} - 1$ for $2\pi/3 < \theta < \pi$

$f_a(\theta) = -1$ for $\pi < \theta < 5\pi/3$

$f_a(\theta) = \{(6/\pi)(\theta - 2\pi)\} + 1$ for $5\pi/3 < \theta < 2\pi$

$T_e = Kb\{f_a(\theta) i_a + f_b(\theta) i_b + f_c(\theta) i_c\}$

$p\omega = (P/2) (T_e - T_L - B\omega)/(J)$

R is resistance of motor/phase, L is self-inductance/ phase, M is mutual inductance of motor winding/phase and x represents any of the phases a, b or c, p is a differential operator (d/dt), i_a, i_b, i_c are line currents, e_{an}, e_{bn}, e_{cn} are phase to neutral back emfs, θ is rotor position and ω=pθ is speed of PMBLDCM in rad/sec, P is number of poles, TL is load torque in Nm, J is moment of inertia in kg-m2 and B is friction coefficient in Nms/Rad.

5. PERFORMANCE EVALUATION

The proposed PMBLDCM drive is modeled in Matlab- Simulink environment and its performance is evaluated for a compressor load of an Air-Con. A constant torque load equal to rated torque mimics the compressor load of air conditioner, while running at variable speed as per requirement of air-conditioning system.
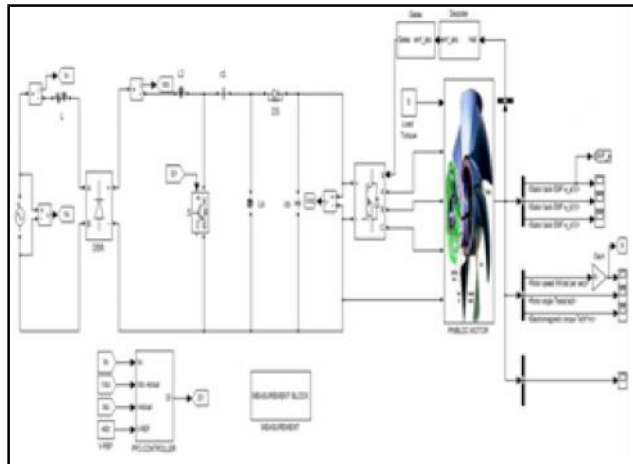
Fig. 5 Simulink diagram of the sepic converter based

5.1 PMBLDCM Drive

The PMBLDCM of 1.2 kW, 164V, 5 A rating, with 1200 rpm rated speed and 9.61 Nm rated torque is used to drive such load. The performance of the drive is simulated for constant rated torque (9.61 Nm) at rated speed. The DC link voltage is kept constant at 400 V with an input AC rms voltage of 220V. The controller gains are tuned to get the desired PQ parameters and the values of controller gains are given in Appendix. The performance evaluation is made on the basis of various PQ parameters i.e. total harmonic distortion of current (THDi) at input AC mains, displacement power factor (DPF), power factor (PF), crest factor (CF), rms value of input AC current (Is) and efficiency (çdrive) of the drive.

5.1.1. Performance During Starting

The starting of the drive is smooth with rated torque (9.61 Nm) and power factor correction is achieved during the starting of the drive. The motor is started from 220 Vrms AC input at rated torque with reference speed set at rated speed i.e. 125.7 rad/s (1200 rpm). The motor speed reaches the reference speed within 0.1 second and resumes the rated value of stator current and motor torque within a cycle of AC mains frequency.

For 300V supply voltage, 8A input ac main current, 1400 rpm is achieved with rated torque (5 Nm) which is shown in figure 6. The current THD at input AC mains in steady state conditions always remains within the standards of IEC 61000-3-2 [8] and the power factor remains near unity. Moreover, an improved performance of the drive is observed in rms of reduced ripples in torque, current and speed during steady state conditions.
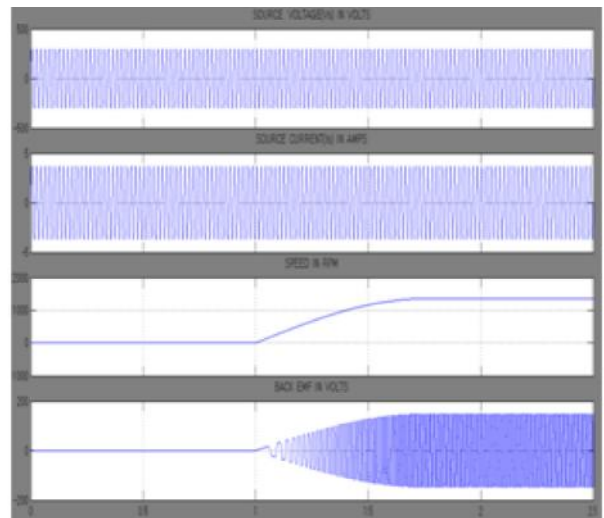
Fig.6 Simulated waveforms of PMBLDC Motor for the supply voltage 300V /5 Nm torque
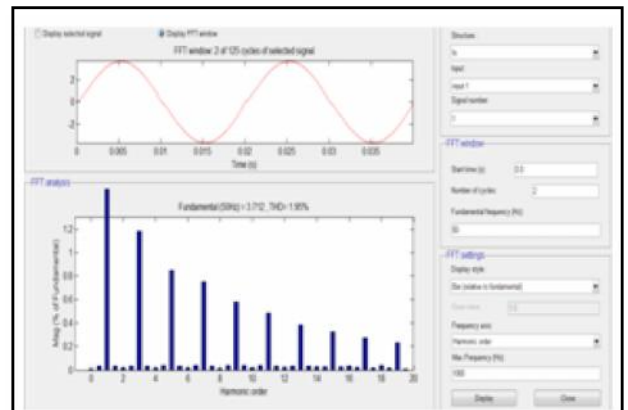
Fig.7 Supply current and harmonic spectra (300V) of a SEPIC converter fed PMBLDCM drive at rated torque (5 Nm)

The maximum allowable torque and the stator current during transient condition are limited to double the rated value.The variation of PQ parameters and drive efficiency with load (variable speed at rated torque) is shown in Table 2.

Table 2 PQ Parameters at Variable Speed and Rated Torque at 220V Input at 400 V DC Link Voltage

Load (%)	THD (%)	DPF	PF	CF	I, (A)	ηdrive
10	1.9	0.989	0.989	1.41	1.02	53.5
20	1.25	0.989	0.989	1.41	1.59	69.1
30	0.95	0.999	0.999	1.41	2.15	76.5
40	0.85	0.999	0.999	1.41	2.72	80.7
50	0.78	0.999	0.999	1.41	3.28	83.2
60	0.74	0.999	0.999	1.41	3.83	86.1
70	0.77	0.999	0.999	1.41	4.37	88.0
80	0.88	0.999	0.999	1.41	4.91	89.4
90	0.97	0.999	0.999	1.41	5.47	90.1
100	1.54	0.999	0.999	1.41	6.02	91.1

The current THD at AC mains remains less than 5% with near unity power factor in the wide range of speed control of PMBLDCM drive.
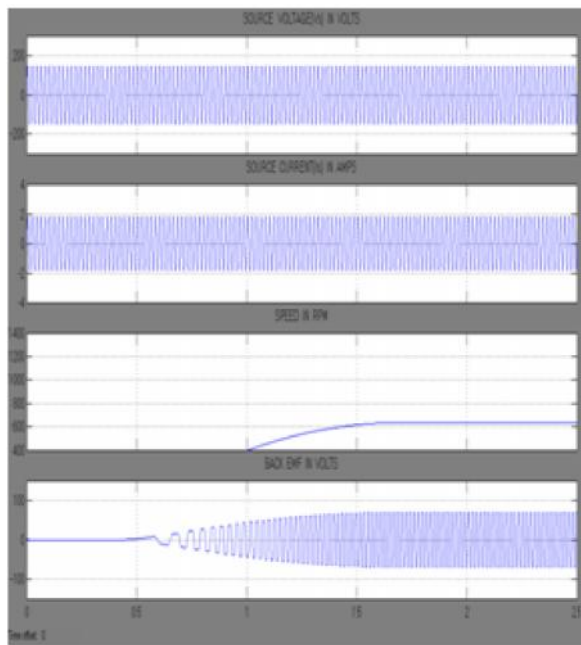
Fig. 8 Simulated waveforms of PMBLDC Motor for the supply voltage 150V /1 Nm torque

These results show reduced THD of AC mains current (less than 5%) and near unity PF in wide range of input AC voltage. The efficiency of the drive remains more than 91% in the complete voltage range. The transient and steady state performances, current waveforms and its harmonic spectra and PQ parameter(power factor, Total harmonic distortion, crest factor) variation with speed and input voltage are shown to provide an exhaustive evaluation of the proposed drive system.
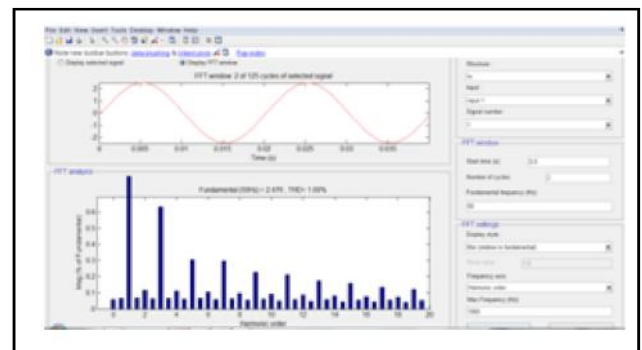
Fig. 9 Supply current and harmonic spectra (150V) of a SEPIC converter fed PMBLDCM drive at rated torque (1 Nm)

6.CONCLUSION

A PFC based SEPIC converter for a PMBLDCM drive has been planned for a compressor load of an air conditioner. The PFC converter has ensured sensible high power factor secure to unity in wide range of the speed as well as input AC voltage. Moreover, performance parameters show an improved power quality with less torque ripple, smooth speed control of the PMBLDCM drive. The THD of AC mains current is observed well below 5% in most of the cases and satisfies the international standards[8].The performance of the drive is very good in the wide range of input AC voltage with desired power quality parameters. This converter has been found suitable for the speed control at constant torque load of air-conditioning systems.

APPENDIX

Rated Power: 1.2 kW, Rated Voltage: 164 V, Rated Speed: 1200 rpm, Rated Current: 5.0 A, Rated torque: 9.61 Nm, No of poles: 6, Resistance R: 1.91 Ω/ph., Inductance (L+M): 9.55 mH/ph., Torque constant KT : 0.332 Nm/A, Inertia J= 0.00776 Kg-m2. The Circuit Parameters used for simulations: Source impedance: 0.03 pu, Switching frequency of PFC switch = 40 kHz. The gains of voltage and speed PI controllers: Kpv=0.485, Kiv=6.85, Kpω=0.11, Kiω=1.2.

REFERENCES

[1] A. M. Jungreis and A.W. Kelley, "Adjustable Speed Drive for Residential Applications", IEEE Trans. Ind. Appl., Vol.31, No.6, Nov.-Dec. 1995, pp.1315 – 1322.

[2] T. Kenjo and S. Nagamori, "Permanent Magnet Brushless DC Motors", Clarendon Press, Oxford, 1985.

[3] T. J. Sokira and W. Jaffe, "Brushless DC Motors: Electronic Commutation and Control", Tab Books USA,1989.

[4] J. R. Hendershort Jr and T. J. E. Miller, "Design of Brushless Permanent-Magnet Motors", Clarendon Press, Oxford, 1994.

[5] J. F. Gieras and M. Wing, "Permanent Magnet Motor Technology – Design and Application", Marcel Dekker Inc., New York, 2002.

[6] N. Matsui, "Sensorless PM Brushless DC Motor Drives", IEEE Trans. Ind. Electron., Vol.43, No.2, April 1996, pp. 300-308.

[7] P. Pillay and R. Krishnan, "Modeling, Simulation and Analysis of a Permanent Magnet Brushless DC Motor Drives, part II: the Brushless DC Motor Drive", IEEE Trans. Ind. Appl., Vol. 25, No.2, Mar. Apr 1989, pp.274-279.

[8] Limits for Harmonic Current Emissions (Equipment input current d"16 A per phase), International Standard IEC 61000-3-2, 2000.

[9] J. Sebastian, J. A. Cobos, J.M. Lopera and U. Uceda, "The Determination of the Boundaries between Continuous and Discontinuous Conduction Modes in PWM DC-to-DC Converters used as Power Factor Preregulators", IEEE Trans. Power Electron., Vol.10, No.5, Sept. 1995, pp. 574 – 582.

[10] D. S. L. Simonetti, J. Sebastian and J. Uceda, "The Discontinuous Conduction Mode Sepic and Cuk Power Factor Preregulators: Analysis and Design", IEEE Trans. Ind. Electron., Vol.44, No.5, Oct. 1997, pp. 630 – 637.

[11] Bhim Singh, B.P. Singh and M Kumar, "PFC converter fed PMBLDC Motor Drive for Air Conditioning", IE(I) Journal-EL, Vol. 84, June 2003, pp. 22-27.

[12] B. Singh, SS Murthy, BP Singh and M. Kumar, "Improved Power Quality Converter Fed Permanent Magnet AC Motor for Air Conditioning", Electric Power System Research, Vol. 65, No.3, 2003, pp 239-245.

[13] T. Gopalarathnam, and H. A. Toliyat, "A New Topology for Unipolar Brushless DC Motor Drive with High Power Factor", IEEE Trans. Power Electron., Vol.18, No. 6, Nov. 2003, pp. 1397-1404.

[14] O. García, J.A. Cobos, R. Prieto, P. Alou and J. Uceda, "Single Phase Power Factor Correction: A Survey", IEEE Trans. Power Electron., Vol. 18, May 2003, pp. 749-755.

[15] M. Naidu, T.W. Nehl, S. Gopalakrishnan and L. Wurth, "Keeping Cool While Saving Space and Money: A Semi Integrated, Sensor Less PM Brushless Drive for a 42-V Automotive HVAC Compressor", IEEE Ind. Appl. Mag., Vol. 11, No. 4, July-Aug, 2005 pp.20-28.

[16] J.M. Kwon, W.Y. Choi, J.J. Lee, E.H. Kim and B.H. Kwon, "Continuous-conduction-mode SEPIC Converter with Low Reverse-recovery Loss for Power Factor Correction", Proc. IEE –EPA, Vol.153, No.5, Sep. 2006, pp.673-681.

Effect of Independent Variables on the Maximization of Gasoline Yield and Closed Loop Studies in Catalytic Cracking Unit

R.Raja Nandhini, M. Mythily and Dr. D.Manamalli

Department of Instrumentation Engineering, Madras Institute of Technology, Chennai - 600 044, Tamil Nadu

E-mail: nandhinisarmi@gmail.com, mythily_eie@yahoo.co.in, manamalli_m@yahoo.com

Abstract

Fluid catalytic cracking unit (FCCU) is an important processing unit in an oil refinery. Fluid catalytic cracking is a process used to convert heavy petroleum products to light products such as gasoline, light fuel oil, and petroleum gas. In the fluid catalytic cracking reactor heavy gas oil is cracked into more valuable lighter hydrocarbon products. The reactor input (the gas oil feed to the reactor) is a mixture of hydrocarbons that makes the reaction kinetics very complicated due to the involved reactions. The process is highly nonlinear and multi variable with severe interactions. For the simulated dynamic model of FCCU plugged with yield model, sensitivity studies has been carried out to study the effects of independent variables such as feed preheat temperature, feed flow rate and air flow rate in maximizing gasoline yield. With the optimized model, the closed loop studies have been carried out for reactor and regenerator temperature control of FCCU with minimum overshoot as the performance criteria.

Keywords: FCCU, Sensitivity analysis, Gasoline yield, Reactor and Regenerator temperature control, Minimum overshoot - performance criteria.

1.INTRODUCTION

Fluidized Catalytic Cracking Unit (FCCU) of gasoil is one of the most important processes in the petroleum refineries. FCCU receives multiple feeds consisting of high boiling point components from several other refinery process units and cracks these streams into lighter and more valuable components. After further processing, the FCCU product streams are blended from other refinery units to produce a number of products, e.g. distillate and various grades of gasoline. Economic operation of FCCUs (a large refinery may have more than one) plays an important role in the overall economic performance of the refinery. Gasoline yield is an important product from FCCU process since it has a very high market value. Gasoline yield in FCCU depends on various parameters like reactor temperature, regenerator temperature, air flow into regenerator, catalyst circulation rates, etc. Therefore, sensitivity analysis is needed to determine the variable which has strong influence on gasoline yield.

2. MODELING OF FCC UNIT
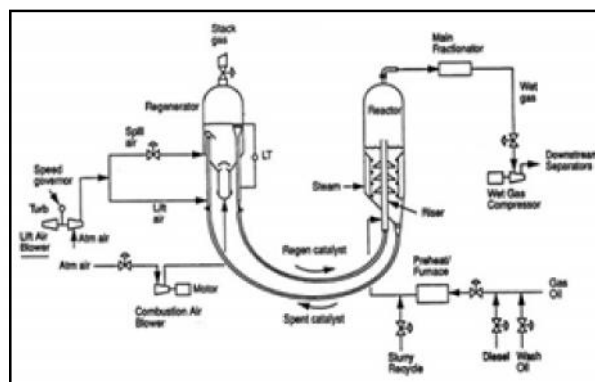
The model captures the major dynamic effects that occur in a real FCCU plant. It is multivariable, strongly interacting and highly non-linear. The non-linear model was developed for the following sub models and integrated.

i   Feed, Preheat system
ii Reactor
iii Wet gas compressor
iv Regenerator
v   Air blowers
vi Catalyst circulation line

The simulated model captures the major dynamic effects that occur in a real FCCU plant. The complete FCCU model was simulated in MATLAB Simulink and validated [1].

Many complex reactions occur during the FCC process and the product consists of a mixture of many compounds. The description of complex mixtures by lumping large number of chemical compounds into smaller groups of pseudo-components has been widely used by researchers to provide number of kinetic equations. The simulated 4-lump model plugged with FCCU model is similar to the 3-lump model of Weekman, the main difference being that coke is independently considered as a lump. Other lumps are feed, gasoline and gas.
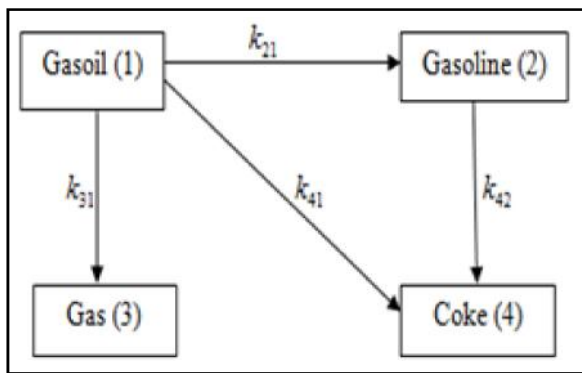
Fig. 2 Reaction scheme of 4 lump yield model

It is assumed that the gas oil is cracked into the most desired gasoline, and the by-products of gas and coke. Since the FCC reactor is operating at high temperature, the secondary cracking reaction occurs for gasoline to form coke and gas. There is no inter-reaction between coke and gas [2].

3. SENSITIVITY ANALYSIS IN FCCU

For the simulated model, the sensitivity studies have been carried out i.e., the effects of the following independent variables on gasoline yield have been analyzed [3].

i Temperature of the fresh feed entering the furnace
ii Flow of the fresh feed into reactor riser
iii Stack gas valve position which has influence on the air flow into regenerator

To carry out this sensitivity studies, these independent variables were operated between -30% and +30% of their nominal values. The nominal values of temperature of fresh entering the furnace is 461°F, flow of fresh feed entering the reactor riser is 126 lb/s and the stack gas valve position is 0.64.

The values of those variables at which the maximum yield has been obtained were fixed as the optimum values. For the optimized model, the closed loop studies have been carried out with PI controller at the regulatory level. Feed preheat temperature plays an important role in controlling the temperature in the riser reactor and hence the cracking reactions. Keeping feed flow into reactor riser (126 lb/s) constant, when the temperature of the fresh feed entering the furnace increases, then the gasoline yield gets decreased.

Keeping the temperature of fresh feed entering the furnace (461°F) constant, when the flow of fresh feed to reactor riser increases, then gasoline yield gets increased because increase in flow rate will lead to more amount of feed taking part in the reaction inside the reactor riser unit.

Keeping the feed flow rate (126 lb/s) and feed temperature (461°F) constant, increase in stack gas valve position will lead to a decrease in pressure inside the regenerator which demands more amount of air flow into regenerator. Increase in air flow rate into regenerator will cause an increase in the regenerated catalyst flow rate due to which the reactor temperature gets increased. When the reactor temperature crosses its optimum temperature it will lead to decrease in the gasoline yield.

It has been observed from the sensitivity analysis that optimum yield is obtained at the temperature of fresh feed entering the furnace = 401.2°F, the flow of fresh feed to reactor riser = 100.3 lb/s and the valve position at 0.448 (air flow into regenerator = 2.1236 moles/s).

Table 1 shows the operating ranges of the independent variables used for the study of the sensitivity effect on the gasoline yield and their impact on it.

The figures 4 and 5 show the responses of the yield and their variations before sensitivity analysis and after sensitivity analysis.
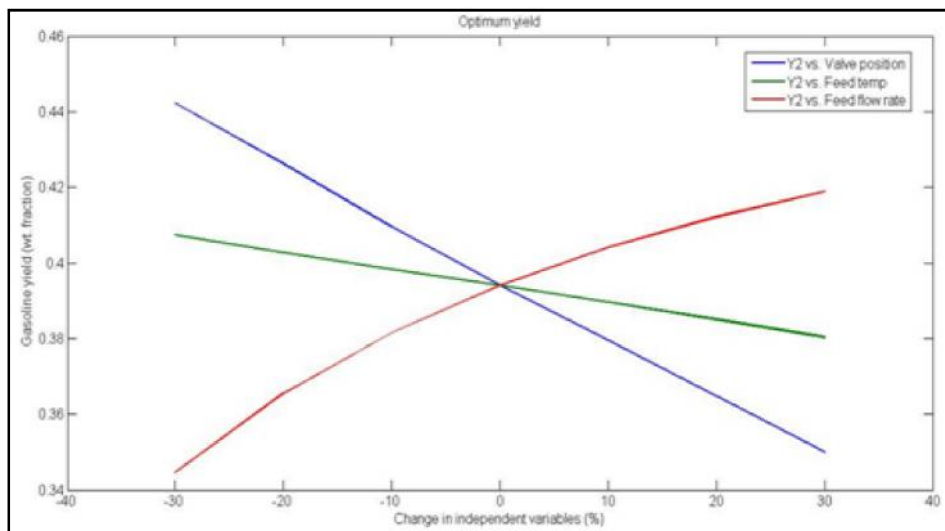
Fig. 3 Optimum yield based on the sensitivity analysis

Table 1 Effect of Independent Variables on the Gasoline Yield

Independent Variables	Range	Impact on Gasoline	Remarks
Temperature of Fresh Feed Entering Furnace (F)	320 to 560	Decreases	Flow of Fresh Feed to Reactor Riser is Having More Influence on the Gasoline Yield
Flow of Fresh Feed To Reactor Riser (lb/s)	88 to 164	Increases	
Valve Position	0 to 1	Decreases	
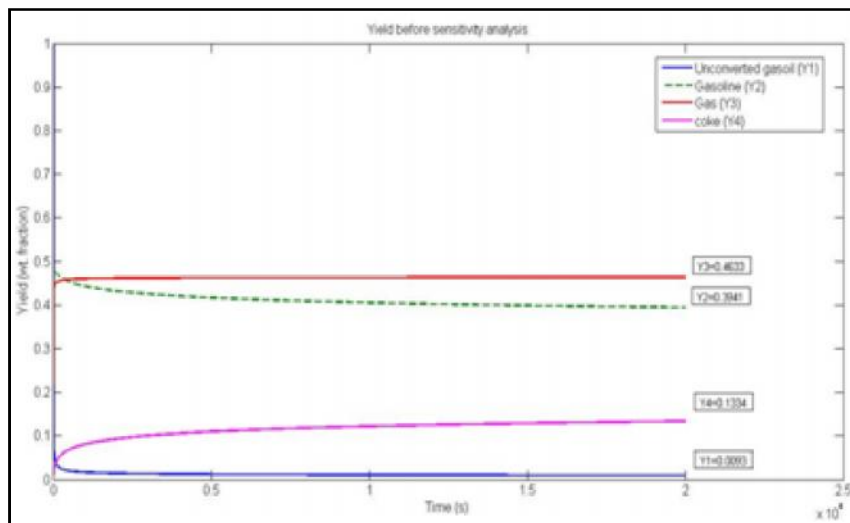
Fig. 4 Yield response before sensitivity analysis
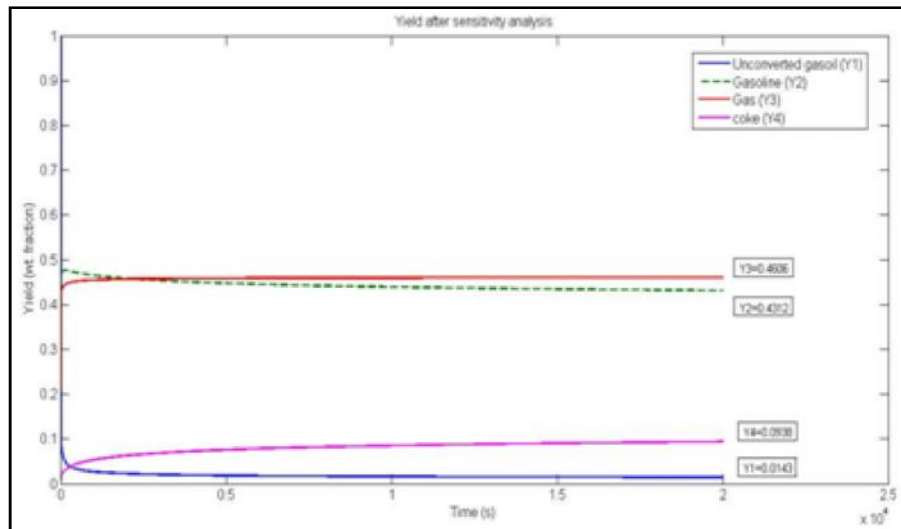
Fig. 5 Yield response after sensitivity analysis

The table 2 lists the response of the gasoline and coke yield before and after sensitivity studies.

Table 2 Yield of Gasoline and Coke after Sensitivity Analysis

Yield (wt.fraction)	Before Sensitivity Analysis	After Sensitivity Analysis	% Increase / % Decrease
Gasoline (Y2)	0.3941	0.4312	+9.4
Coke (Y4)	0.1334	0.0938	-29.7

It has been observed from the table 2 that there is considerable increase in gasoline yield and decrease in the coke formation after fixing the values of independent variables for maximizing gasoline in the simulated model.

4. CONTROL OF REACTOR AND REGENERATOR TEMPERATURE

4.1 Multiloop Control

Each manipulated variable depends on only a single controlled variable i.e., a set of conventional feedback controllers. In most of the chemical industries, the processes are basically MIMO systems. The controlled variables have been selected to provide, through control, a safe and economic operation. The reactor temperature and regenerator temperature are selected as a controlled variable. The manipulated variables are flow of regenerated catalyst and flow rate of air.

The control structure selection was done based on Relative Gain Array (RGA) analysis.
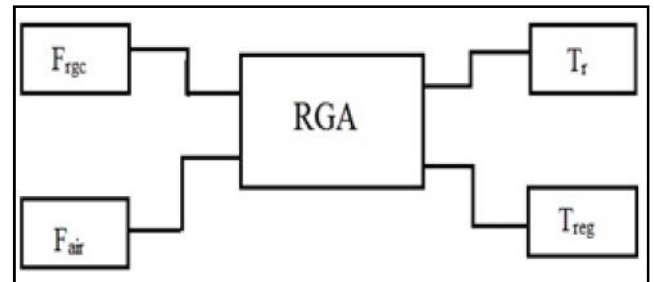
Fig. 6 Control structure based on RGA analysis

The input and output relationship are given as

$$T_r = \frac{0.142}{1606\,s+1}F_{rgc} + \frac{3.2112}{4037\,s+1}F_{air}$$

$$T_{reg} = \frac{0.2984}{1602\,s+1}F_{rgc} + \frac{26.89}{1575\,s+1}F_{air}$$

The above transfer functions were found out by using the process reaction curve method.

The steady (gain) model is expressed as

$$k = \begin{bmatrix} k_{11} & k_{12} \\ k_{21} & k_{22} \end{bmatrix} = \begin{bmatrix} 0.142 & 3.2112 \\ 0.2984 & 26.89 \end{bmatrix}$$

Thus, the relative gain array for a 2×2 system can be expressed as given below

$$= \begin{bmatrix} 1.335 & -0.335 \\ -0.335 & 1.335 \end{bmatrix}$$

Pair the controlled and manipulated variables so that corresponding relative gains are positive and as close to one as possible. From this RGA matrix, we can conclude that pairing of manipulated variables with control variables (i.e., flow rate of regenerated catalyst is used to control reactor temperature and flow rate of air is used to control regenerator temperature) is best.

The figure 7 shows the schematic of the closed loop system with the PI controller.
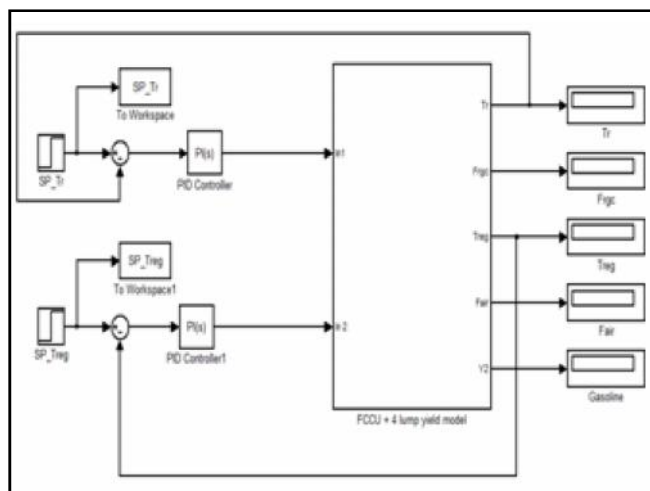
Fig. 7 Schematic diagram of closed loop system with PI controller

The reactor temperature must be maintained at a certain level to provide a desired maximum conversion of feed oil. The regenerator temperature must be maintained at a certain level in order to allow a stable coke from the catalyst. Permanent catalyst deactivation is produced by exceeding the high temperature limit. The proportional-integral (PI) controller is used at regulatory level. The specified reactor temperature is maintained by using a PI controller to adjust the flow of regenerated catalyst. Also the specified regenerator temperature is maintained by using a PI controller to adjust the air flow into regenerator.

4.2 PI Tuning Rules

Before performing closed loop studies on any dynamic model, the best performance criteria for the specific control variable need to be studied. As per the conversation with experts working in CPCL, minimum overshoot was chosen as the performance criteria for the reactor and regenerator temperature control of FCC unit.

With minimum overshoot as the performance criteria, the following tuning rules have been used to tune the PI controller. (Ref: A.O'Dwyer - PI and PID controller tuning rules for time delay processes).

Table 3 PI Tuning Rules and The Parameters

Sl. No	RULE	K_C	τ_I
1	Direct synthesis	$\dfrac{\tau}{k_p\lambda}$	τ
2	Atkinson and Davey	$0.25K_u$	$0.75T_u$

Where K_c = Proportional gain

τ_I = Integral time constant

λ = Adjustable parameter

K_u = Ultimate gain of the sustained oscillations

T_u = Ultimate time period of the sustained oscillations.

The control signal from the tuned PI controller has been applied to the whole simulated FCCU model and not to the transfer function that has been obtained through process reaction curve method. The transfer function was used only to establish the input-output relationship between the controlled variable and the manipulated variable.

4.3 Control of Reactor Temperature (T_r)

The reactor temperature must be maintained at a certain level to provide a desired maximum conversion of feed oil. The PI tuning parameters for the reactor temperature control process for different PI tuning rules is listed in the following table.

Table 4 PI Tuning Parameters for Reactor Temperature Control

PI Tuning Rule	Proportional Gain (K_P)	Integral Gain (K_I)
Direct synthesis	7.0422	0.004385
Atkinson and Davey	16.001	0.0267

The reactor temperature was operated for three different set points (990^0F, 993^0F and 995^0F) and their responses for the different PI tuning rules have been shown below.
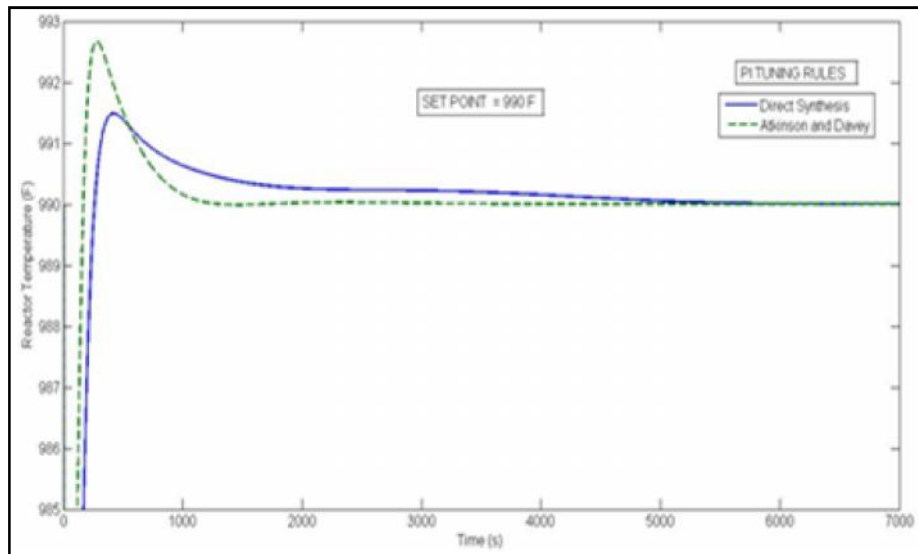
Fig. 8 Control of reactor temperature for different PI tuning rules (990^{0}F set point)
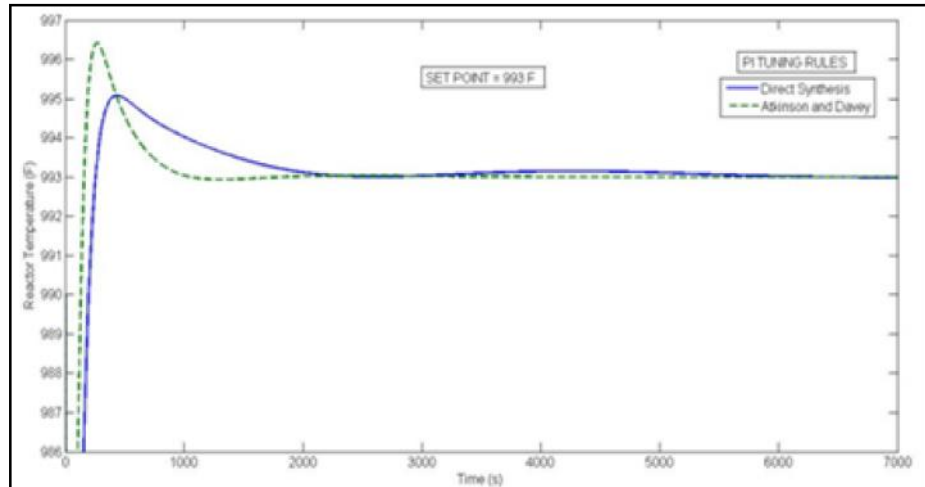
Fig. 9 Control of reactor temperature for different PI tuning rules (993^{0}F set point)
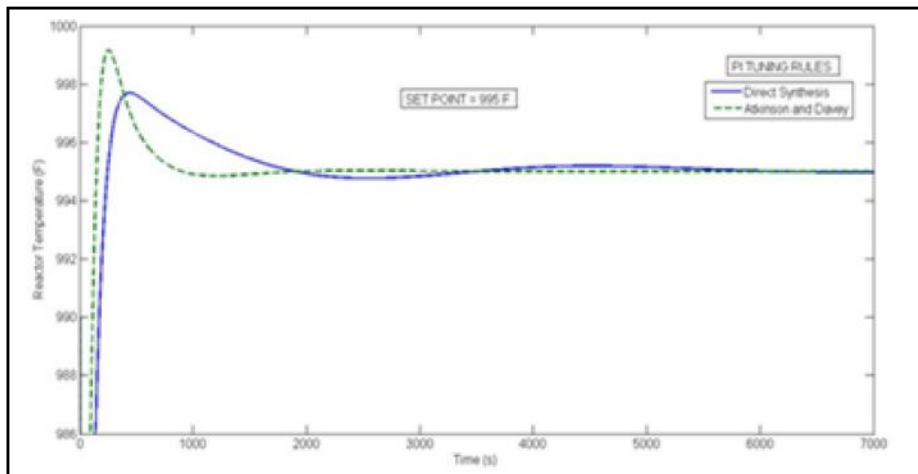
Fig. 10 Control of reactor temperature for different PI tuning rules (995^{0}F set point)

From figure 8, 9 and 10, it can be inferred that the same tuning parameters as given in table 4 can be applied to any operating point. Also it shows that the direct synthesis method is having minimum overshoot but having a sluggish response. So it is better to choose the Atkinson and Davey PI tuning rule for the controller as it gives the next best response with minimum overshoot and quicker settling time.
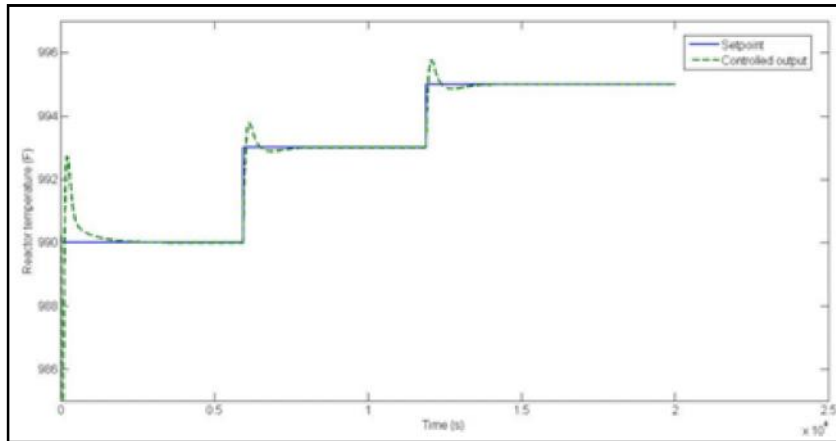
Fig. 11 Reactor temperature control for different operating points using Atkinson and Davey PI tuning rule

After the steady state was reached, disturbance has been given to the effective coke factor (p_f) from 1 to 1.5 at 7000s and from 1 to 0.5 at 12000s and the controller performance was studied.
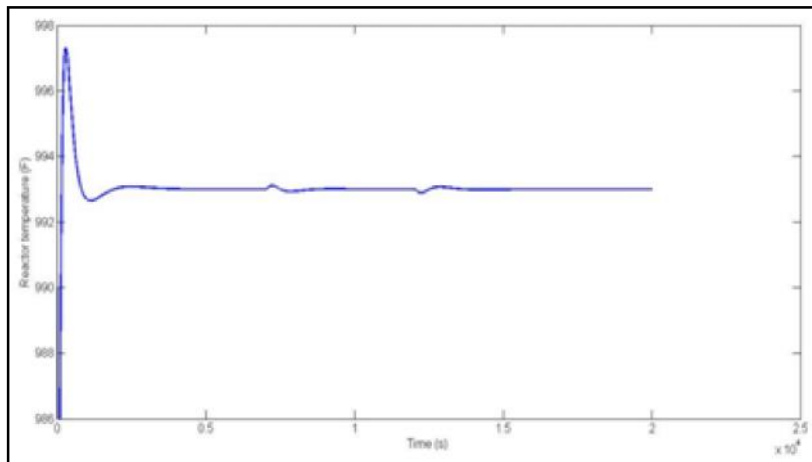
Fig. 12 Control of reactor temperature with disturbance in effective coke factor

4.4 Control of Regenerator Temperature (T_r)

The PI tuning parameters for the regenerator temperature control process for different PI tuning rules is listed in the following table 5.

The regenerator temperature was operated for three different set points (1265°F, 1275°F and 1285°F) and their responses for the different PI tuning rules have been shown below.

Table 5 PI Tuning Parameters for Regenerator Temperature Control

PI Tuning Rule	Proportional Gain (K_P)	Integral Gain (K_I)
Direct Synthesis	0.017597	0.000037887
Atkinson and Davey	0.082675	0.0001378
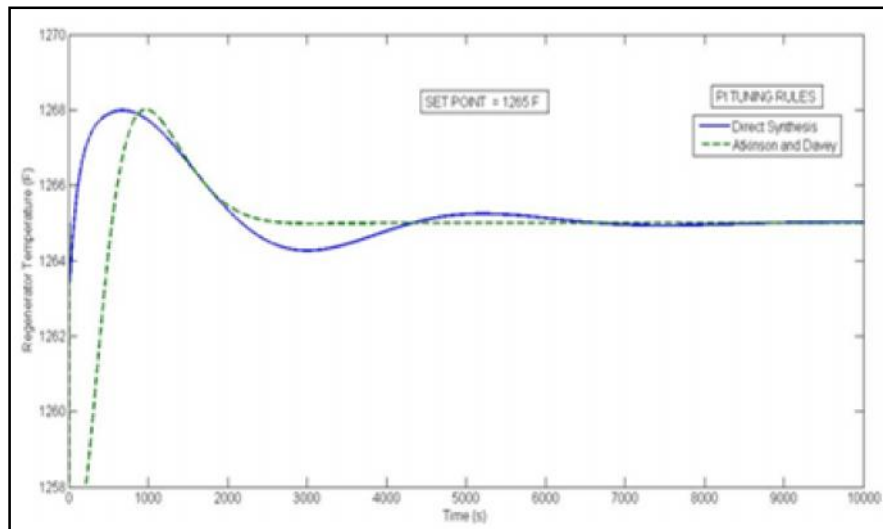
Fig. 13 Control of regenerator temperature for different PI tuning rules (1265^{0}F set point)
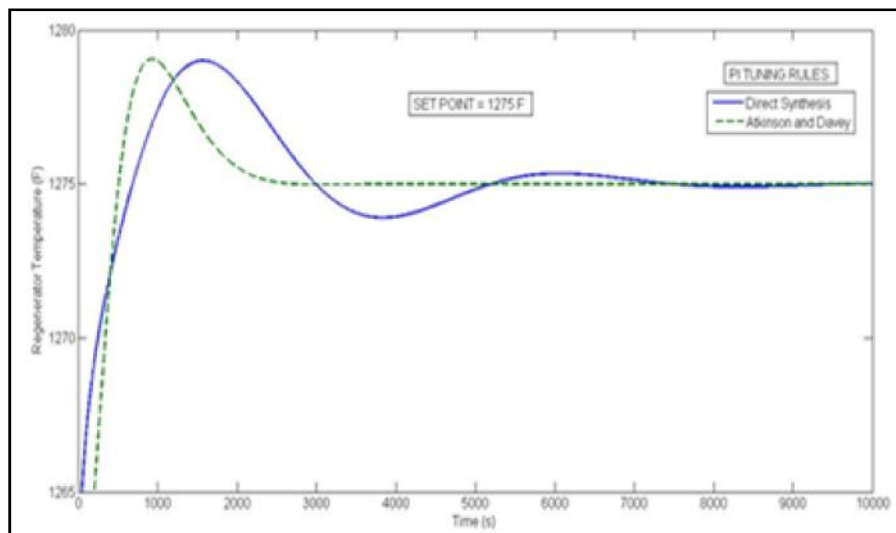
Fig. 14 Control of regenerator temperature for different PI tuning rules (1275^{0}F set point)
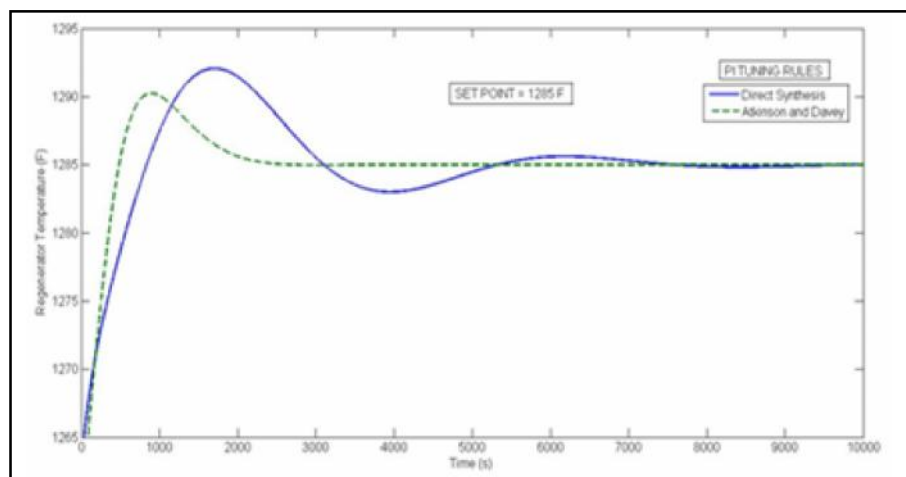
Fig. 15 Control of regenerator temperature for different PI tuning rules (1285^{0}F set point)

From figure 13, 14 and 15, it can be inferred that the same tuning parameters as given in table 5 can be applied to any operating point. Also it shows that the direct synthesis method is having minimum overshoot but having a sluggish response. So it is better to choose the Atkinson and Davey PI tuning rule for the controller as it gives the next best response with minimum overshoot and quicker settling time.
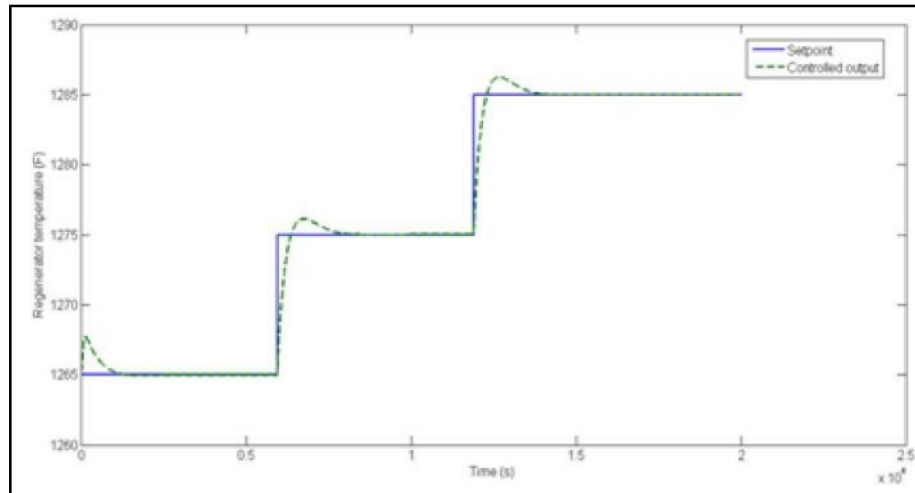
Fig. 16 Regenerator temperature control for different operating points using Atkinson and Davey PI tuning rule

After the steady state was reached, disturbance has been given to the effective coke factor (p_f) from 1 to 1.5 at 7000s and from 1 to 0.5 at 12000s and the controller performance was studied.
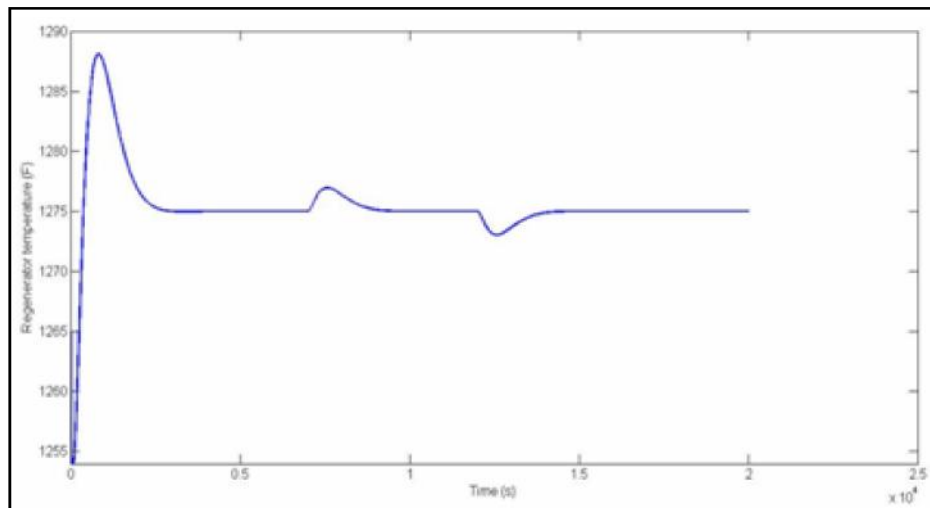
Fig. 17 Control of regenerator temperature with disturbance in effective coke factor

4.5 Yield Response Under Closed Loop Condition

The table 4 describes the variation of gasoline yield and coke yield for different PI control tuning methods when the reactor temperature is controlled at 993^0F and regenerator temperature is controlled at 1275^0F.

Table 5 Variation of Gasoline Yield with Different PI Tuning Rules

Yield (wt. Fraction)	Before Sensitivity Analysis	After Sensitivity Analysis	
		PI Tuning Rules	
		Direct Synthesis	Atkins and Davey
Unconverted Gasoil (Y1)	0.0122	0.0137	0.0147
Gasoline (Y2)	0.4215	0.4268	0.4316
Gas (Y3)	0.4619	0.4557	0.4497
Coke (Y4)	0.1044	0.1038	0.1040

5. CONCLUSION

The "process" is represented by a simulated dynamic model of a model IV FCC unit which is combined with a steady-state yield model for the FCC reactor. The dynamic model will calculate the time-varying states of the FCC unit at any point in time while the yield model uses the reactor conditions to calculate the conversion and the distribution of products.

The sensitivity analysis of certain independent variables was performed results show that the gasoline yield can be increased by decreasing the temperature of the fresh feed entering the furnace and air flow into regenerator (by minimizing the valve opening) when the flow of fresh feed to reactor riser is increased.

From the closed loop performance study it is concluded that Atkinson and Davey PI tuning rule proves to be the best PI tuning rule when performance criteria of minimum overshoot was considered.

REFERENCES

[1] M.Mythily, D.Manamalli and P.Manikandan, "Dynamic Modeling, Simulation and Multivariable Control Strategy Applied to Catalytic Cracking Unit", IEEE International Cconference on Process Automation, Control and Computing (IEEE - PACC), 2011.

[2] S.Prabha, M.Mythily and D.Manamalli, "Investigation on the Closed Loop Response of Dynamic Catalytic Cracking Unit for Improvisation of Petroleum Gasoline", Journal of Emerging Technology in Mechanical Science and Engineering, ISSN No : 0976 – 2558, 2012, pp.125-133.

[3] Prabha K.Dasila, Indranil Choudhury, Deoki Saraf, Sawaran Chopra and Ajay Dalai, "Parametric Sensitivity Studies in a Commercial FCC Unit", Advances in Chemical Engineering and Science, 2011, pp.136-149.

[4] H. Kurihara, "Optimal Control of Fluid Catalytic Cracking Processes", PhD Thesis, (MIT, Cambridge, USA), 1967.

[5] L.S. Lee, Y.W. Chen, T.N. Haung and W.Y. Pan, "Four Lump Kinetic Model for Fluid Catalytic Cracking Process", Can J Chem Eng, 67, 1989, pp. 615-619.

[6] R.C. McFarlane, R.C. Reinemen, J.F. Bartee and C. Georgaki, "Dynamic Simulator for a model IV Fluid Catalytic Cracking Unit", Computers and Chemical Engineering, Vol.17, No.3, 1993, pp. 275-300.

[7] Ramasubramanian Sundaralingam, "Optimization of a model IV Fluidized Catalytic Cracking Unit", Chemical Engineering, 2001.

[8] Rama S. Iyer, Rein Luus and Stephen S. Woo, "Optimization of a model IV Fluidized Catalytic Cracking Unit", The Canadian Journal of Chemical Engineering, Vol 79, 2001, pp. 542-547.

[9] V.M. Weekman and D.M. Nace, "Kinetic and Dynamics of Catalytic Cracking Selectivity in Fixed Bed Reactor", American Institute of Chemical Journal, Vol.16, 1970, pp. 397-404.

[10] A.O'Dwyer, "PI and PID Controller Tuning Rules for Time Delay Processes", School of Control Systems and Electrical Engineering, Dublin Institute of Technology, Ireland, 2000.

Optimum Design of Mechanically Stabilized Earth Walls Using Genetic Algorithm

Narayana Sabhahit[1], Asha U Rao[2], Sathvika T Shetty[3] and Radhika Bhandary[4]
[1]Professor, [2]Associate Professor, [3]Post Graduate Student and [4]Assistant Professor
Department of Civil Engineering, Manipal Institute of Technology, Manipal, India
E-mail: sabha4@rediffmail.com, asha.prabhu@manipal.edu,
sathvika.shetty18@gmail.com,radhika.st@manipal.edu

Abstract

This paper couples a complete mechanically stabilized earth wall design routine with a highly efficient optimization model for optimum design of mechanically stabilized earth walls. An optimal total length of the reinforced earth wall has been found using Genetic Algorithm (GA) choosing the vertical spacing and horizontal spacing of reinforcements as a feasible design vector. The design algorithm benefits from limit equilibrium technique to calculate the external and internal stability of the wall considering common safety factors. The safety factors are treated as constraint to the problem and a computer program is developed in FORTRAN 95 for the design of reinforced earth. GA is used as a search technique to optimize the total length of the reinforcement. Parametric study is made on GA parameters and their effects on results are obtained.

Keywords: Genetic algorithm, Optimum design, Reinforced earth wall

1. INTRODUCTION

Reinforced earth is a construction material composed of soil fill strengthened by the inclusion of rods, bars, fibers or nets which interact with the soil by means of frictional resistance. The concept of strengthening soil with rods or fibers is not new. Throughout the ages attempts have been made to improve the quality of adobe brick by adding straw. The present practice is to use thin metal strips, geotextiles and geogrids as reinforcing materials for the construction of reinforced earth retaining walls. The metal strips extend from the panel back into the soil to serve the dual role of anchoring the facing units and being restrained through the frictional stresses mobilized between the strips and the backfill soil. The backfill soil creates the lateral pressure and interacts with the strips to resist it. The walls are relatively flexible compared to massive gravity structures. These flexible walls offer many advantages including significant lower cost per square meter of exposed surface. There are many types of facing units of the reinforced earth walls. The soil behind the wall facing is said to be mechanically stabilized earth (MSE) and the wall system is generally called MSE wall. The three components of MSE wall are the facing unit, the backfill and the reinforcing material. The backfill, is limited to cohesion less, free draining material (such as sand), and thus the key properties are the density and the angle of internal friction. The reinforcements may be strips or rods of metal or sheets of geotextile, wire grids or geogrids. The one considered for current study is facing panels with metal strip reinforcement.

The design of reinforced soil retaining walls is based on coherent gravity method. The walls are designed for both external and internal stability criteria. There are several possible failure modes considered in the design of reinforced soil retaining walls to satisfy both external and internal stability. The reinforcement length is governed by the external stability conditions and the vertical spacing of reinforcements is governed by the internal stability conditions. Further the wall is designed to satisfy minimum safety factors for all failure modes under static as well as dynamic loading. The major design considerations for a reinforced soil structure are the stability assessment of the potential external failure modes of the wall.

Basudhar *et al.* (2007) have studied optimum cost design of geosynthetic reinforced earth retaining walls subjected to static and dynamic loading. They have used Sequential Unconstrained Minimization Technique (SUMT) for multidimensional and unidirectional minimization to arrive at the minimum cost of the reinforced earth wall and found that saving of the order of 7–8% can be made over the conventional design of mechanically stabilized earth (MSE) walls designed with the aid of design charts [1]. Basha and Babu (2009) have presented a method to evaluate the internal stability of reinforced soil structures against tension and pullout

Narayana Sabhahit[1], Asha U Rao[2], Sathvika T Shetty[3] and Radhika Bhandary[4]

modes of failure using pseudo-static method for earthquake conditions. The developed method provided a closed form solution for the active earth pressure acting on the reinforced soil structures using rotational log-spiral failure mechanism under earthquake loading ensuring safety against tension and pullout modes of failure [2]. Anderson *et al.* (2012) have discussed the correct ways to design MSE walls, to apply traffic surcharge, to select design parameters and backfill, to assess service life, to address special design conditions such as bridge abutments, traffic barriers and earthquakes, and to select the wall design method itself. They summarize on the reliable methods of MSE design that have been proven in the field for more than forty years [3]. McCombie and Wilkinson (2002) applied a simple genetic algorithm (SGA) to find the minimum factor of safety in slope stability analysis. The simple genetic algorithm can be applied successfully to the search for the critical circle in slope stability analysis [4]. Elsayed et al. (2014) have shown that efficiency of GA could be improved by adopting a new crossover operator with a diversity operator. The proposed algorithm was analyzed by solving constrained optimization problems and several real world test problems. The algorithm showed a superior performance in comparison with other algorithms [5]. Ghiassian and Aladini(2009) have coupled a complete MSE wall design with a highly efficient optimization model for optimum design of mechanically stabilized earth walls. The coupled MSE wall simulation module and the GA optimization algorithm locate the reinforcements at appropriate locations with optimum spacing in vertical and horizontal directions. It is assumed that the critical slip surface is bilinear and passes through the toe of the wall [6].The focus of the present study is to find the best vertical and horizontal spacing of reinforcements to obtain the minimum reinforcement length for failure mode considered in the design. The search technique that has been used for the above purpose in this study is Genetic Algorithm and then the effect of GA parameters on result has been studied.

2. FORMULATION OF THE PROBLEM

The problem of determining the minimum reinforcement length using the vertical spacing and horizontal spacing of reinforcements as variable parameter has been formulated as a constrained minimization problem. It is formulated as a mathematical programming problem and a computer program is developed in FORTRAN 95. Genetic Algorithm, a non-traditional optimization technique is used to obtain the optimum solutions.

2.1 Analysis of Reinforced Earth
2.1.1. External Stability Analysis

Two potential external failure mechanisms are considered in analysis of MSE walls. The present study:
a) Sliding on the base
b) Overturning which limits the location of the resultant of all forces

The Factor of Safety for sliding is usually calculated as the ratio of the shear resistance along the base of the MSE wall to the active thrust due to lateral earth pressure. The Factor of Safety for overturning is calculated as the ratio of the resisting moment to driving moment. MSE wall profile with surcharge load is shown in Figure 1.

The coefficient of active earth pressure, K_a, is computed using the Rankine theory

$$K_a = \tan^2\left(\frac{\pi}{4} - \frac{\varphi}{2}\right) \tag{1}$$

Total active earth pressure is computed as

$$P_a = \frac{1}{2}K_a\gamma H^2. \tag{2}$$

Having determined all parameters, the Factor of Safety against sliding and overturning are calculated as

$$FS_{SL} = \frac{W\tan\varphi_F}{P_a}. \tag{3}$$

$$FS_{OT} = \frac{3WL}{2F_T H}. \tag{4}$$
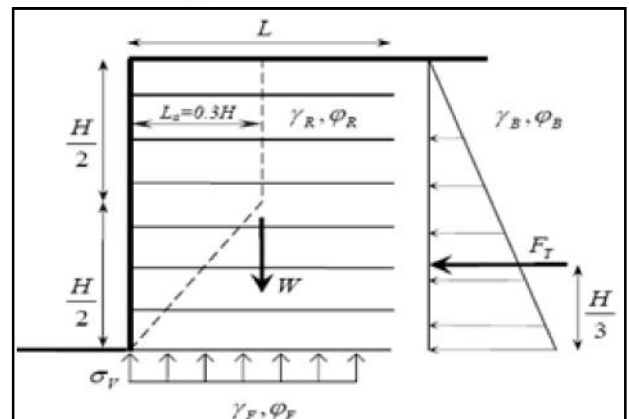
Fig. 1 Reinforced Earth-Wall profile with surcharge load

2.1.2. Internal Stability Analysis

For a vertical wall the earth pressure reduces to the Rankine equation,

$$K_a = \tan^2\left(\frac{\pi}{4} - \frac{\varphi}{2}\right)$$

Length of the reinforcement

$$L = L_R + L_e .$$ (5)

Where, $L_R = 0.6(H - z)$. (6a)

for walls with inextensible reinforcement from the base up to H/2

And $L_R = 0.3H$. (6b)

for the upper half of a wall with inextensible reinforcements

L_e = Effective length of reinforcement outside the failure zone

$$L_e = \frac{F_s T}{2\gamma zbtan\delta} .$$ (7)

Where, b=width of the strip

t=thickness of the reinforcement

And δ= soil-reinforcement interface friction angle

Maximum tension T_{max} in each reinforcement layer is now determined based on the vertical spacing S_v and horizontal spacing S_H as

$$T_{max} = (\gamma zK_a + q_h)S_v S_H .$$ (8)

Factor of safety against pullout failure is given as [2] the available resisting force (Pri) on the embedded reinforcement length (L_e) of layer should be more than the maximum load in the soil reinforcement,

$$FS_{PO} = \frac{P_{ri}}{T_{max}} .$$ (9)

Where, $P_{ri} = 2\sigma_{vi} L_e btan\delta$, and

$\sigma_{vi} = z\gamma + q$ is the effective vertical stress acting on the embedded reinforcement length.

3. OBJECTIVE FUNCTION AND DECISION VARIABLE

The objective of the study is to find the best vertical and horizontal spacing of the reinforcements that corresponds to minimum total reinforcement length. Hence, the total length of the reinforcements will be the objective function and the vertical and horizontal spacing of the reinforcements represents the design variables. i.e. $f(x) = f(S_v, S_h)$

3.1 Constraints

In order to ascertain the vertical spacing of the reinforcements, some constraints need to be placed. In the present study, checks for external stability, internal

stability and allowable tension are applied which can be expressed in the following form.

Check for sliding - $FS_{SL} > 1.5$
Check for overturning - $FS_{OT} > 2.0$
Check for pullout - $FS_{PO} > 1.5$
Allowable tension- $T_a = fy*t*b$

$$\frac{\text{---------}}{F_s} > T_{max}$$

Where f_y is the yield stress of steel and F_s is the factor of safety for steel.

3.2 Variable Bounds

As the design variables are continuous, the decoding scheme to be used for such variables is to fix the variable bounds, i.e., value between given lower and upper bounds are assigned for continuous variables. The vertical spacing may range from 20 to 150 cm (8 to 60 in.) and horizontal spacing may be on the order of 80 to 150 cm (30 to 60 in.). In the present study, the bound considered for vertical spacing varies from 30 to 150 cm and the bound for horizontal spacing varies from 80 to 150 cm. GA randomly selects different vertical and horizontal spacing and gives the best spacing to be taken for minimum reinforcement length to be obtained.

3.3 Penalized Objective Function

Originally, GA was developed for solving unconstrained optimization problems. However, most of the practical problems are constrained one. Hence, one must transform the constrained problem into an unconstrained one by using a suitable penalty function. In this study, penalty function suggested by Rajeev and Krishnamoorthy (1992) is used. i.e.

f(x)=F(1+KC)

Where parameter 'K' has to be judiciously selected depending on the required influence of a violated individual; for the problems considered in this study, the value of K = 100 is found to be most suitable. 'C' is the constraint violation function and is computed in the following manner,

$$C = \sum_{j=1}^{m} C_j$$

Where, m = number of constraint equations.
In the above equation C_j is calculated in the following manner.

Narayana Sabhahit[1], Asha U Rao[2], Sathvika T Shetty[3] and Radhika Bhandary[4]

If the constraint is violated, then $C_j = 100$
If the constraint is not violated, then $C_j = 0$

4. RESULTS AND DISCUSSION

In the previous section, the problem of retaining wall analysis has been formulated as an optimization problem. The results obtained from the above formulation are studied. The problem studied by Ghiassian and Aladini(2009) is considered for the present study.

4.1. Literature Problem Details

The total design height of the wall = 7.8 meter
Width of the strip = 0.05 meter
Thickness of the strip = 0.004 meter

Traffic surcharge = $9.4 kN/m^2$
Effective angle of internal friction of the reinforced soil = 34 degree.
Effective angle of internal friction of the backfill= 30 degree.
Unit weight of the backfill = $18.8 kN/m^3$
Effective angle of internal friction of the foundation soil = 30 degree
Yield stress of the steel= 250MPa

In this study, the total cost accounts for the reinforcement and fill costs and is referred as Design Specific Cost (DSC). Therefore this method attempts to minimize the DSC and is compared with the result from a literature [6].

Table 1 Design Specific Cost (DSC) Obtained from Simulation-Optimization Approach and Genetic Algorithm

	H (m)	S_h(m)	S_v (m)	b (m)	t (m)	DSC ($)
Simulation-Optimization[6]	7.8	0.45	1.12	0.074	0.003	331
Genetic Algorithm	7.8	0.8	1.35	0.05	0.004	274

4.2 Parametric Study

In order to study the sensitivity of GA parameters on the results, a parametric study has been carried out. These parameters include population size, generation number, crossover probability and mutation probability. While studying the effect of these parameters on the results, the random seed is kept constant as 0.123 (Deb, 1996).

Figure2 shows the variation of total length of reinforcement with the generation number for different population size such as 8, 10 and 12. The crossover and mutation probabilities are kept constant as 0.8 and 0.01 respectively. As generation number increases the length decreases for all population size. At generation number 150, the total length obtained for population size 8, 10 and 12 are respectively 64.1, 63.1 and 62.9 meter indicating a marginal influence of population size on the convergence rate. The length obtained for population size 12 is minimum. However, further increase in population size does not affect the value of minimum total length significantly. Hence, a population size of 12 is used in this study.

In GA, crossover is a very important parameter which transfers the character of the parents to the offspring partly. Though 100% crossover is not necessary, it is essential to use high crossover probability in order to carry out the global search. Figure 2 shows the variation of total length with the crossover probabilities varying from 0.1 to 1.0.

It can be observed from Figure 3 that the variation between total length and crossover probability for different population size has no definite trend. However, it can be concluded that the crossover probability 0.7 for population size 12 provides the minimum length. Hence, crossover probability of value 0.7 is kept constant for further studies.

If GA is used with only selection and crossover operators, then there will be a possibility of some design space unsearched within the variable bounds. In order to avoid this situation, a low probability of mutation is used. Figure 4 shows the variation of total length of the reinforcement for the values of mutation probability varying from 0.01 to 0.1. It can be observed from graph that there is no specific trend in the variation. However, mutation probability of 0.0125 gives the lowest length for population size 12.
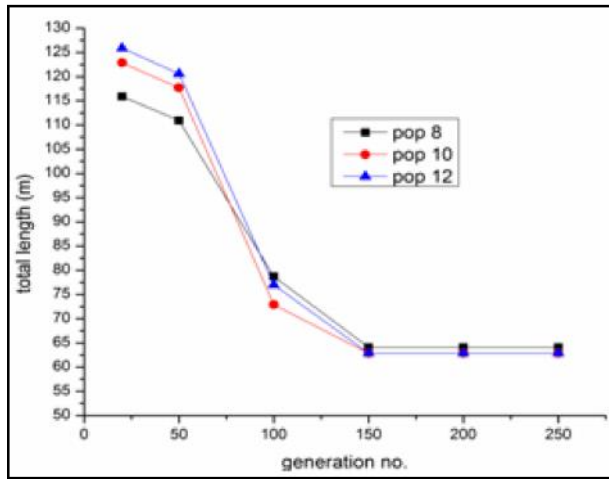
Fig. 2 Effect of generation number on length
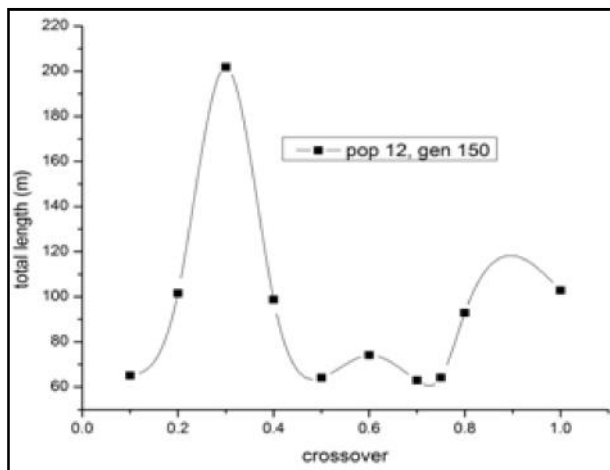
Fig.3 Effect of crossover probability on total length
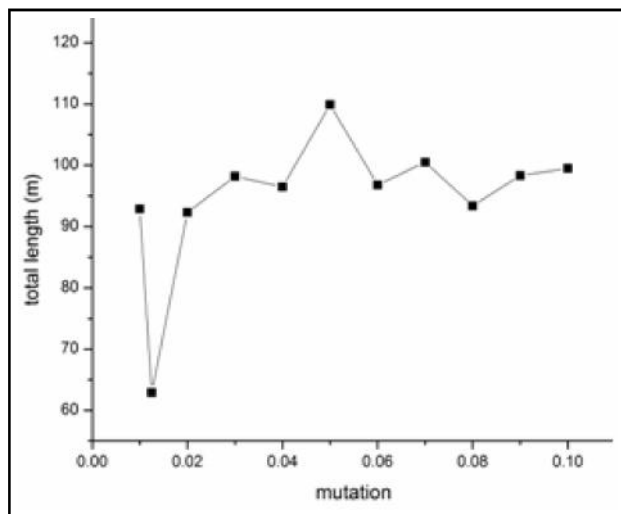
Fig. 4 Effect of mutation probability on total length

5. CONCLUSION

Based on the limited study carried out, the following preliminary conclusions are made.

- Best vertical spacing of 1.35m and horizontal spacing of 0.8m is obtained to get minimum total length of 62.9m.
- Simulation-optimization approach gives DSC of $331[6] and the same obtained from Genetic Algorithm technique is $274. Thus, the present method predicts 17% minimum cost value as compared to the example problem from literature [6] which is shown in table 1.
- In literature [6] the length of the reinforcement is assumed to be constant throughout the height of the wall. Whereas in the above study length of each reinforcement is calculated using equations (5 to 7) which is more economical.
- The accuracy of GA depends on its parameters, such as, population size, generation number, crossover probability and mutation probability. For the problem considered in this paper, the GA parameters can be selected as: population size 12, generation number 150, and crossover probability 0.7 and mutation probability 0.0125.

REFERENCES

[1] P. K. Basudhar, AmolVashistha, Kousik Deb and ArindamDey, Sourav De, "Optimal Cost Analysis Of Reinforced Earth Walls",M.Tech Thesis in Geotechnical Engg, Department of Civil Engineering, Indian Institute of Technology Kanpur, Kanpur, 2007.

[2] B. MunwarBasha and G.L. SivakumarBabu, "Earthquake Resistant Design of Reinforced Soil Structures Using Pseudo Static Method", American J. of Engineering and Applied Sciences, Vol. 2, No.3, 2009, pp 565-572.

[3] Peter L. Anderson, Robert A. Gladstone, John E. Sankey, "State of the Practice of MSE Wall Design for Highway Structures", the Reinforced Earth Company and Association for Metallically Stabilized Earth, 2012.

[4] P. W. Paul McCombiea, "The Use of The Simple Genetic Algorithm in Finding the Critical Factor of Safety in Slope Stability Analysis", Computers and Geotechnics, Vol.29, 2002, pp 699-714.

[5] Saber M. Elsayed, Ruhul A. Sarker, Daryl L. Essam, "A New Genetic Algorithm for Solving Optimization Problems", Engineering Applications of Artificial Intelligence, Vol.27, 2014, pp 57-69.

[6] H.Ghiassian and K.Aladini, "Optimum Design of Reinforced Earth Walls With Metal Strips; Simulation-Optimization Approach", Asian Journal

Narayana Sabhahit[1], Asha U Rao[2], Sathvika T Shetty[3] and Radhika Bhandary[4]

of Civil Engineering (building and housing), Vol. 10, No.6, 2009, pp.641-655.

[7] D.E.Goldberg, "Genetic Algorithms in Search, Optimization And Machine Learning", Addison-Wesley, Reading Mass, 1989.

[8] S. Rajeev and C.S. Krishnamoorthy, "Discrete Optimization of Structures Using Genetic Algorithms", Journal of Structural Engineering, ASCE, Vol.118, No.5, 1992, pp.1233-1250.

[9] V.N.S. Murthy, "Advanced Foundation Engineering", Geotechnical Engineering Series, 2007.

Job Scheduling Algorithm for Computational Grid in Grid Computing Environment

G.Priyanka[1], P. Pravina[2] and T. Tharani[3]

Department of Computer Science and Engineering, JCT College of Engineering and Technology,
Coimbatore -641 105, Tamil Nadu.
E-mail: crtharani@gmail.com, priyankaebnazer@gmail.com

Abstract

Grid Computing allow sharing of resources from heterogeneous and distributed locations. Grid Computing has wide variety of application areas including science, medical and research areas. But there are also some challenges which arise in the environment of grid computing. One of the main challenges is Resource or Job scheduling in the grid. This paper presents such an algorithm which helps in scheduling computational resource to the jobs in efficient way.

Keywords: Computational grid, Deadline, Grid computing, Job Scheduling, Scheduling Algorithm.

1. INTRODUCTION

Grid computing has emerged as a distributed methodology that coordinates the resources that are spread in the heterogeneous distributed environment [1]. Grid is a type of parallel and distributed system that enables the sharing, selection and aggregation of resources distributed across multiple administrative domains based on their availability, capability, Performance, cost and user's quality-of-service requirements [2]. A Grid is loosely coupled, geographically distributed and heterogeneous computers in the grid donate printers, application software, disk storage, CPU power etc. Grid uses a middleware layer to communicate with heterogeneous hardware and datasets. Grid can be of many types like data grid, computational grid utility grid, network grid. **Computational** grid has processing power as main computing resource that is shared among the nodes. Grid computing helps in reducing computing cost, turnaround time of each job and it also helps in increasing computing resources and productivity. But there are also some problems related to it like security, complexity and resource scheduling. To realize the full potential of grid computing, grid middleware needs to support various services such as security, uniform access, resource management, job scheduling, application composition, economic computation, and accounting [3]. **Job Scheduling** is choosing the most suitable resource for a job to complete its execution either in terms of waiting time, turnaround time or cost. Scheduler is used to manage the jobs and resources. Scheduler performs two main functions; First scheduler selects the appropriate computational resource for the job and then assigns the resource to the jobs.Job Scheduling is done in order to

make the efficient use of resources and for seamless execution of jobs. The main objective of scheduling is to reduce the completion time of an application by properly allocating the jobs to the processors.

2. RELATED WORK

K.Somasundaram, S.Radhakrishnan and M.Gowathyanayagan stated highest response next scheduling algorithm in order to correct some of the weakness in both shortest job first and FCFS. HRN is a non-preemptive algorithm where priority of job is function of job's service time and also amount of time job has been waiting for service. Somasundaram, S. Radhakrishnan [6] proposed a Swift Scheduler and compared it with First Come First Serve (FCFS),Shortest Job First (SJF) and with Simple Fair Task Order (SFTO) based on processing time analysis, cost analysis and resource utilization. Daphne Lopez, S. V. Kasmir raja [7] has described and compared Fair Scheduling algorithm with First Come First Serve (FCFS) and Round Robin (RR) schemes. Sunita Bansal, Bhavik Kothari and Chittaranjan Hota [8] describe an approach to schedule tasks efficiently in a grid environment, without having prior information on workload of incoming tasks. An enhancement to the existing round-robin heuristic by prioritizing tasks eligible for replication is proposed. Mayank Kumar Maheshwari and Abhay Bansal [9] presented the design of new scheduling algorithm Priority Scheduler. The proposed Priority Scheduler which completes a task by using highly utilized low cost resources with minimum computational time. Gaurav Sharma and Preeti Bansal [10] enhanced the Min-Min algorithm by classifying it according to the QOS parameters. QOS guided Min-Min scheduling algorithm

G.Priyanka[1], P. Pravina[2] and T. Tharani[3]

outperform the traditional Min-Min heuristic on the same set of task.

3. SCHEDULING MODEL

i. **Users:** The user enters the jobs to be executed on processor in computational grid.
ii. **Resource Broker:** Users typically do not interact with Grid services directly. Resource Broker is used to discover computing resources with the help of Information System and provide the jobs suitable resource for their computation. Resource broker is used to find the appropriate resource for the jobs, to do so it contacts the grid information server that keeps the status of all the currently available resources in the grid system.
iii. **Grid Information Service:** GIS maintains the information of all resources that is needed by the broker for scheduling the jobs in efficient way. Then resource broker selects the best resource for the job to be executed. After allocation of resource, updating is performed. After successful completion of a job, the information about the status of resource is again updated. This procedure is repeated until all the jobs are assigned to the resources.
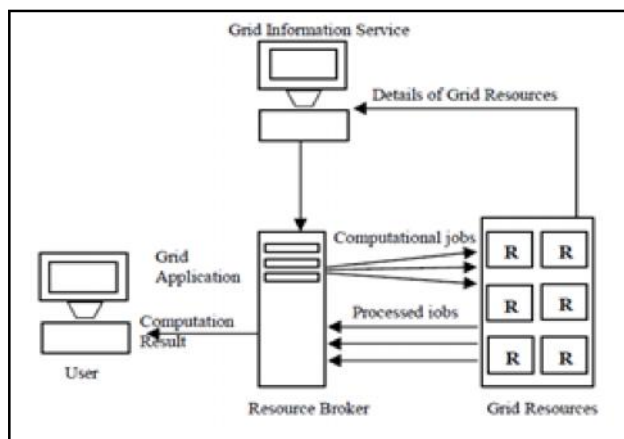
Fig.1 Basic grid model [4]

4. PROPOSED WORK

We have implemented a job scheduling algorithm; EDSRTF in C++. In implementation we assume there are six processors and maximum of 10 jobs can be entered at a time. We have considered three nodes Node 1, Node 2, Node 3 and each node consists of 2 processors P1, P2, P3, P4, P5 and P6 respectively.

4.1 Earliest Deadline First With Shortest Remaining Time

Earliest deadline first With Shortest Remaining Time (EDSRTF) is a scheduling algorithm in which scheduling is done according to the deadline of jobs and remaining time. The job with the earliest deadline will get resource first while the job with large value of deadline will have to wait irrespective of their execution time.

In EDSRTF scheduling algorithm first execution time along with the deadline of the job is entered. Then according to this scheduling algorithm, first six jobs are directly assigned to the processor P1, P2, P3, P4, P5 and P6 respectively. For the next jobs; processors are assigned according to the deadline of the jobs. If the current job on the processor has large value of deadline than the arriving job, then processor will stop executing the job and will execute the new coming job as its value of deadline is small. But if the current job has small deadline value then processor will keep executing the current job. Then in this case the next processor will be checked for the job and this process will continue until the job gets the processor for its execution. This process is repeated for each job. In the case if no processor satisfied this deadline condition then job will get the processor with shortest remaining time.
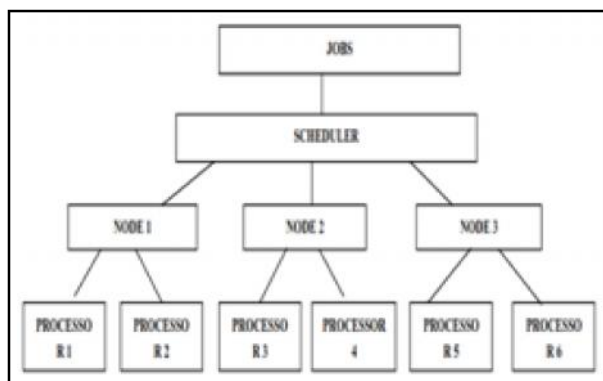
Fig.2 Diagram for EDSRTF

ALGORITHM

STEP 1: Enter number of Jobs, their Execution Time and their Deadline.
STEP 2: Assign first six jobs directly to processor P1, P2, P3, P4, P5, P6 and set status of processors; SP1=0, SP2=0, SP3=0, SP4=0, SP5=0, SP6=0.
STEP 3: Repeat following for each job from i=7; to i<=11. (Here we have taken 10 jobs)
i. If((P1==0)&&(d[1]>d[i]))

i. Assign it to P1 and P1 will first execute this job then after its execution it will execute the previous job and calculate waiting and turnaround time of job and set SP1==1, status of job i =1.

ii. Else If((P2==0) &&(d[2]>d[i])).Assign it to P2 and P2 will first execute this job then after its execution it will execute the previous job and calculate waiting and turnaround time of job and set SP2==1, status of job i =1.

iii. Else If((P3==0) &&(d[3]>d[i])) Assign it to P3 and P3 will first execute. This job then after its execution it will Execute the previous job and calculate Waiting turnaround time of job and set SP3==1, status of job i =1.

iv. Else If((P4==0) &&(d[4]>d[i])) Assign it to P4 and P4 will first execute this job then after its execution it will execute the previous job and calculate waiting and turnaround time of job and set SP4==1, status of job i =1.

v. Else If((P5==0) &&(d[5]>d[i])) Assign it to P5 and P5 will first execute this job then after its execution it will execute the previous job and calculate waiting and turnaround time of job and set SP5==1, status of job i =1.

vi. Else If((P6==0) &&(d[1]>d[i])) Assign it to P6 and P6 will first execute this job then after its execution it will execute the previous job and calculate waiting and turnaround time of job and set SP6==1, status of job i =1.

STEP 4: Now check status of every job and if job's status is still = 0, then compare remaining time of each processor and assign the job to the processor with small remaining time. Calculate waiting and turnaround time of job.
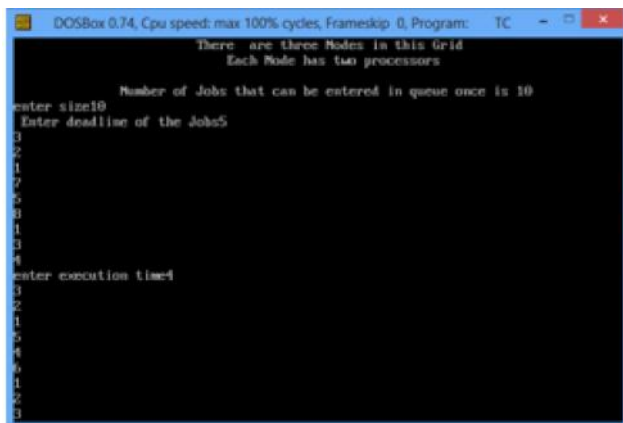
Fig.3 Execution time and deadline of jobs according to EDSRTF
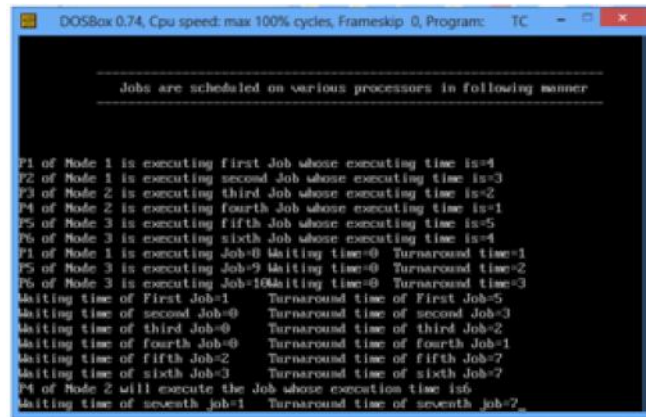
Fig.4 Scheduling according to EDSRTF

5. COMPARISON with OTHER SCHEDULING ALGORITHMS

Comparison of the proposed algorithm EDSRTF with two other algorithms FCFS and LJF is also done in this paper.

5.1 Longest Job First: In longest job first scheduling, the job with large execution time is executed first in comparison to job with shortest execution time. It means a job whose execution time is small will have to wait because of a job which has large execution time than that job.
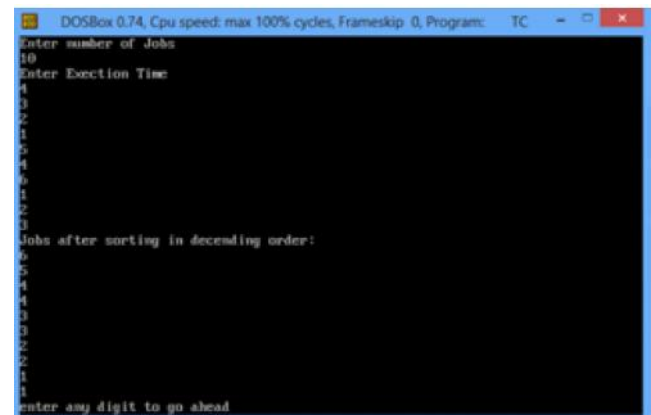
Fig.5 Execution time of jobs
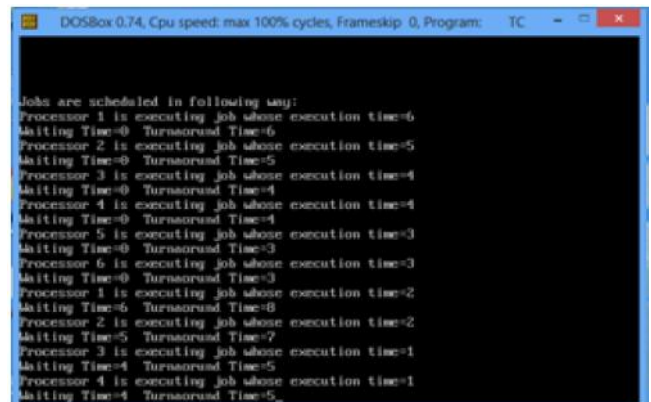
Fig.6 Scheduling according to LJF

G.Priyanka[1], P. Pravina[2] and T. Tharani[3]

5.2. First Come-First Serve: First-Come-First-Serve is one of the simplest scheduling algorithms. Jobs get the processors according their arrival. Job which will enter first will get the processor first. It is a non preemptive scheduling algorithm, once a process gets processor, it runs to completion.
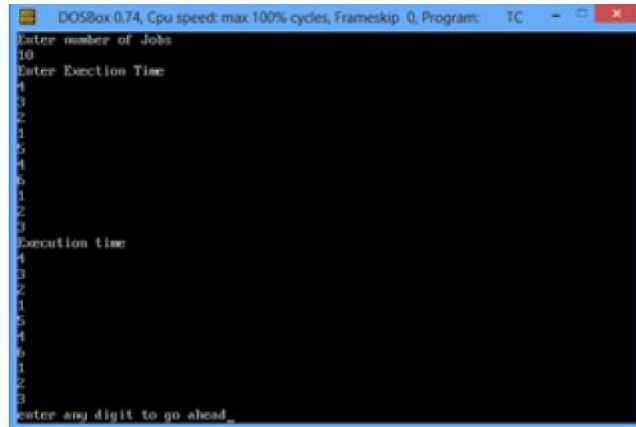
Fig.7 Execution time of jobs
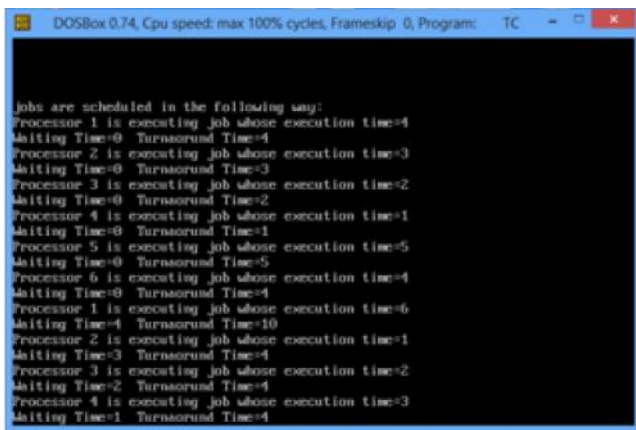
Fig.8 Scheduling according to FCFS
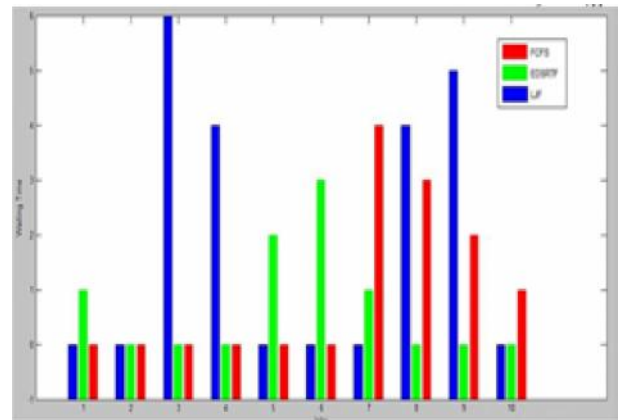
Fig.9 Waiting time ccomparison of 10 Jobs using EDSRTF, LJF and FCFS

Fig.10 Turnaround time comparison of 10 Jobs using EDSRTF, LJF and FCFS

Table 1 Waiting and Turnaround Time of Jobs using LJF, EDSRTF and FCFS

Jobs	LJF		EDSRTF		FCFS	
	Waiting Time	Turnaround Time	Waiting Time	Turnaround Time	Waiting Time	Turnaround Time
1	0	4	1	5	0	4
2	0	3	0	3	0	3
3	6	8	0	2	0	2
4	4	5	0	1	0	1
5	0	5	2	7	0	5
6	0	4	3	7	0	4
7	0	6	1	7	4	10
8	4	5	0	1	3	4
9	5	7	0	2	2	4
10	0	3	0	3	1	4

Average Waiting Time = i=1 Σ Wi/n
Average Turnaround Time = i=1n Σ Ti/n

Table 2 Average Waiting and Average Turnaround Time of Jobs using LJF, FCFS and EDSRTF

	LJF	FCFS	EDSRTF
Average Waiting Time	1.9	1.0	0.7
Average Turnaround Time	5.0	4.1	3.8
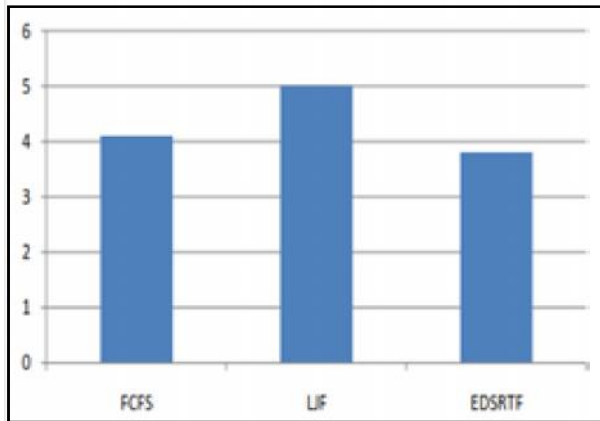
Fig.11 Average waiting time comparison of different scheduling algorithms
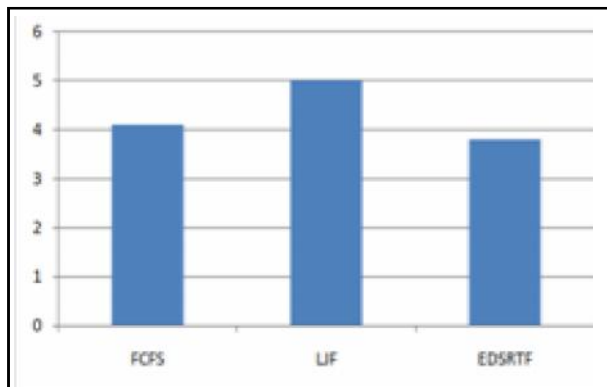
Fig.12 Average turnaround time comparison of different scheduling algorithms

6. CONCLUSION AND FUTURE WORK

Grid computing can solve more complex tasks in less time and utilizes the resources efficiently. To make grid work properly, best job scheduling strategies have to be employed. Scheduling helps the jobs to get resources properly. In this paper we have proposed a scheduling algorithm EDSRTF and also done its comparison in terms of waiting and turnaround time of jobs with two other algorithms FCFS, LJF. Average waiting time and average turnaround time of jobs is also calculated. Average waiting time and average turnaround time of proposed algorithm

is less in comparison to other scheduling algorithms so EDSRTF is best among them. We have considered here number of jobs as fixed 10; in future this number can be made dynamic.

REFERENCES

[1] Mrs. Radha and Dr. V. Sumathy "A Detailed Study of Resource Scheduling and Fault Tolerance in Grid", 2011.

[2] N.A. Azeez, A.P. idoye, A.O. Adesina, K.K. Agbele, Iyamu Tiko and I.M. Venter, "Peer to Peer Computing and Grid Computing: Towards a Better Understanding", 2011.

[3] Manoj Kumar, Mishra Prithviraj Mohanty and G. B. Mund, "A Time-minimization Dynamic Job Grouping-based Scheduling in Grid Computing", 2012.

[4] Raksha Sharma, Vishnu Kant Soni, Manoj Kumar Mishra and Prachet Bhuyan, "A Survey of Job Scheduling and Resource Management in Grid Computing", 2010.

[5] K. Somasundaram, S. Radhakrishnan and M. Gowathyanayagan, "In Efficient Utilization of Computing Resources Using Highest Response Next Scheduling in Grid", 2007.

[6] K. Somasundaram and S. Radhakrishnan, "Task Resource Allocation in Grid using Swift Scheduler", 2009.

[7] Daphne Lopez, S. V. Kasmir raja, "A Dynamic Error Based Fair Scheduling Algorithm For A Computational Grid", 2009.

[8] Sunita Bansal, Bhavik Kothari and Chittaranjan Hota, "Dynamic Task-Scheduling in Grid Computing using Prioritized Round Robin Algorithm", 2011.

[9] Mayank Kumar Maheshwari and Abhay Bansal "Process Resource Allocation in Grid Computing using Priority Scheduler", 2012.

[10] Gaurav Sharma, Preeti Bansal, "Min-Min Approach for Scheduling in Grid Environment", 2012.

Poly-β-hydroxybutyrate and Poly(3-hydroxybutyrate-*co*-3-hydroxyvalerate) Accumulation in Aulosira Fertilissima: Effects of Nitrogen and Phosphorus Deficiencies

Shilalipi Samantaray and Nirupama Mallick

Department of Agricultural and Food Engineering, Indian Institute of Technology, Kharagpur -721 302, India
E-mail: shilalipisamantaray@gmail.com

Abstract

Polyhydroxyalkanoates are a class of naturally occurring biodegradable polyesters, accumulated intracellularly as carbon and energy reserve materials by a wide variety of prokaryotes including cyanobacteria under unbalanced growth conditions. These polymers have attracted the commercial as well as academic interest as raw materials for biodegradable plastics owing to their properties like high molecular weight, biodegradability, biocompatibility, optical purity, hydrophobicityand piezoelectricity.Exploring polyhydroxyalkanoates (PHAs) production with a filamentous diazotrophic cyanobacterium, Aulosira fertilissima CCC 444 resulted into poly-β-hydroxybutyrate (PHB)accumulation up to 6.4% of dry cell weight (dcw) under photoautotrophic growth condition on 14th day of incubation. A significant enhancement in PHB pool was observed under phosphate deficiency on day 4 (10.6% dcw), whereas under nitrogen deficiency the value reached upto 9.9% (dcw). The co-polymers of Poly(3-hydroxybutyrate-co-3-hydroxyvalerate)P(3HB-co-3HV) could only be produced in presence of propionate/ valerate in the culture medium. Maximum P(3HB-co-3HV) co-polymer accumulation reached up to 38.6% (dcw) with 89.4 mol% 3HB and 10.6 mol% 3HV units under 0.4% propionate supplementation, followed by 36.4% (dcw) under 0.4% valerate supplementation with 74.4 mol% 3HB and 25.6 mol% 3HV units on day 14 of incubation. In N-deficient medium, the maximum P(3HB-co-3HV) content was achieved to 72.3% (dcw) under 0.4% valerate-supplemented condition, a value ~2-fold higher than the control within 5 days of incubation. Maximum P(3HB-co-3HV) co-polymer accumulation up to 45.3% (dcw) was observed in P-deficient medium supplemented with 0.4% valerate. Chemoheterotrophy with 0.4% (w/v) valerate umder P/N-deficiency enhanced the polymer accumulation up to 38-40% (w/w) dry cells, the value almost 6-fold higher with respect to photoautotrophic condition. However, productivity of A. fertilissimabiomass was found to be affected under N- and P-limitations. This necessitates a two-stage cultivation practice, where at the first stage A. fertilissimacell must be grown under carbon-supplemented condition to reach a high cell density; followed by a second stage, deficient condition as in this study, for efficient polymer accumulation. Thus, Aulosira biomass could be explored further as a potent source of raw material for bioplastic production.

Keywords: Aulosira fertilissima, Chemoheterotrophy, N- deficiency, P- deficiency, Poly-β-hydroxybutyrate, Poly(3-hydroxybutyrate-co-3-hydroxyvalerate).

1. INTRODUCTION

Problems associated with the conventional plastics on global environment have generated interest in the development of biodegradable plastic polymers. The search for such biodegradable plastics has led to a number of partially or completely biodegradable products such as polylactides, polyglycolic acids, aliphatic polyesters, polyhydroxyalkanoates, polysaccharides and their blends. Amongst them, the microbially-originated polyhydroxyalkanoates (PHAs) offer much potential for significant contributions as 'bioplastics'.

Polyhydroxyalkanoates are synthesized and stored in the cell cytoplasm as water insoluble inclusions. Poly-*b*-hydroxybutyrate (PHB) is the best-characterized member of PHA family, and is prevalent in prokaryotic organisms [1]. PHB has various properties such as natural origin, biodegradability, biocompatibility, streospecificity, piezoelectricity, optical activity and thermoplasticity, which makes it suitable for a variety of applications in health industry. It has ideal biocompatibility because the polymer as such and its derivatives are the only products of cell metabolism and are present in blood and tissues [2]. Its ability to degrade and resorb in the

human body environment makes it a suitable candidate as the matrix for bioactive and biodegradable composite implants that will guide tissue growth and be replaced eventually by newly formed tissue. Nowadays, PHB and Poly(3-hydroxybutyrate-*co*-3-hydroxyvalerate)P(3HB-*co*-3HV) has attracted much attention for a variety of medical applications, which include controlled drug release system, surgical sutures, fracture repair, bone and cartilage remolding and as a pericardial substitute [3].

To date, accumulation of polymer has been reported mainly in bacterial species. Commercial production of polymer is being carried under fermentative condition. However, the cost of fermentative polymer production, due to high carbon requirement and oxygen demand, is a major obstacle for presenting polymer as a commodity material. Therefore,to reduce this limitation, cyanobacteria can be considered as an alternative host system due to their minimal nutrient requirements and photoautotrophic nature.These organisms with a short generation time need some simple inorganic nutrients for their growth and multiplication. To date, about 50 cynobacterial species, belonging to more than 50 different genera have been analysed for the presence of PHAs, but the contents, in general, are found to be low and amounted less than 10% of dry cell weight (dcw) under phototrophic growth condition [4]. A major break-through in cyanobacterial polyhydroxyalkanoates research was however, obtained by Miyake and his group with a thermophilic cyanobacterium, *Synechococcus* MA19, isolated from the surface of a wet volcanic rock in Japan reported to accumulate PHB upto 55% (dcw) under phosphate-limited condition [5].Furthermore, Mallick and her group demonstrated PHB accumulation upto 43% and 35% (dcw), in *Nostoc muscorum* and *Synechocystis* sp. PCC 6803, respectively under various specific conditions [6, 7]. Mallick and her co-workers [8] also observed the accumulation of P(3HB-*co*---3HV) co-polymer up to 31% (dcw) in a N_2-fixing cyanobacterium, *Nostoc muscorum* under propionate-supplemented condition. Further study was conducted by Bhati and Mallick [9], where in *Nostoc muscorum,* accumulation of P(3HB-*co*---3HV) co-polymer up to 60% (dcw) under valerate-supplemented condition was recorded. In this report, PHB and P(3HB-*co*---3HV) co-polymer biosynthesis in the culture of *Aulosira fertilissima* have been studied with an aim to establish the actual potential of the organisms, and also how its biosynthesis is regulated under limitation of phosphate and nitrogen.

2. MATERIAL AND METHODS
2.1 Test Organism and Experimental Conditions

Axenic cultures of *Aulosira fertilissima* were grown in 150 ml Erlenmeyer flasks containing 50 ml of nitrate-free BG-11 medium at pH 8.5 [10]. The medium was buffered with Tris buffer (4 mM) to maintain the pH. Cultures were incubated in an air-conditioned culture room at 28 ± 2 ^{0}C and illuminated with 40 W fluorescent tubes for a photoperiod of 14:10 h (light-dark) at light intensity of 75 µmol photon m^{-2} s^{-1} PAR. The co-polymers of P(3HB-*co*-3HV) could only be produced in presence of precursor substrates sodium valerate and sodium propionate in the culture medium, as reported in Samantaray and Mallick [11].

2.2 Impact of Phosphorus and Nitrogen Deficiencies

Deficiency of various nutrients was achieved by replacing the medium constituent(s) with equimolar concentration(s) of other nutrient(s). To study the impact of phosphorus deficiency on PHB accumulation, *A. fertilissima*was grown in phosphate-deficient medium, where K_2HPO_4 of the medium was substituted by equimolar concentrations of KCl. For nitrogen deficiency, the medium was substituted by equimolar concentrations of ferric citrate and $CoCl_2.6H_2O$, respectively in place of ferrous ammonium citrate and $Co(NO_3)_2.6H_2O$. Cultures pre-grown in BG-11 medium were obtained by centrifugation, washed with BG-11 medium without the specific nutrient for 2-3 times and transferred to the deficient medium.

2.3 Impact of Chemoheterotrophy

For chemoheterotrophic condition, the stationary phase photoautotrophic cultures supplemented with various carbon doses were incubated under complete darkness. Polymer content and biomass concentration was analyzed at fixed time intervals.

2.4 Analytical Procedures

Extraction of the polymer was done following the protocol of Yellore and Desia [12]. Polymer content were determined following the propanolysis method of Riis and Mai [13] using a gas chromatograph (Clarus 500; Perkin-Elmer, Shelton, CT, USA). Growth was measured in terms of cell dry weight; it was determined gravimetrically following Rai et al. [14]. Total co-polymer content was obtained by adding both the components obtained from

gas chromatographic analysis. All experiments were performed in triplicate to check the reproducibility. Results were statistically analysed by Duncan's new multiple range test.

3. RESULT AND DISCUSSION
3.1 Impact of N-/P- deficiency on PHB biosynthesis

The stationary phase *Aulosira* cultures when transferred to P- and N-deficient medium, a significant rise in PHB pool up to 10.6% (dcw) was observed under phosphate deficiency on day 4, whereas under nitrogen deficiency the value reached up to 9.8% (dcw) (Fig. 1B). Enhanced PHB accumulation under P-deficiency in the test cyanobacterium affirms the earlier findings of Sharma and Mallick [6] and Panda et al. [15], as PHB biosynthesis is expected to increase under phosphate starvation, when reducing power would be in excess, because ATP production is known to decrease markedly with the onset of phosphate limitation, while the reduction of NADP through non-cyclic photosynthetic electron flow is not inhibited [16]. Under nitrogen deficiency also NADPH consumption was decreased due to limitation of nitrogen source, which blocks the amino acid synthesis pathways, especially the reaction from a-ketoglutarate to glutamate, thus resulting into accumulation of excess NADPH in the cells. This residual NADPH might be responsible for the enhanced PHB accumulation in nitrogen/phosphate-deficient cells [17]. In general, nitrogen and phosphorous deficiency in the medium lead to a decrease in biomass concentration. In control vessel, the final concentration reached up to 496.7 mg l^{-1} on day 14, whereas under N- and P- deficient conditions the final values were 122.8 mg l^{-1} and 187.4 mg l^{-1} respectively on 14th day (Fig. 1A).
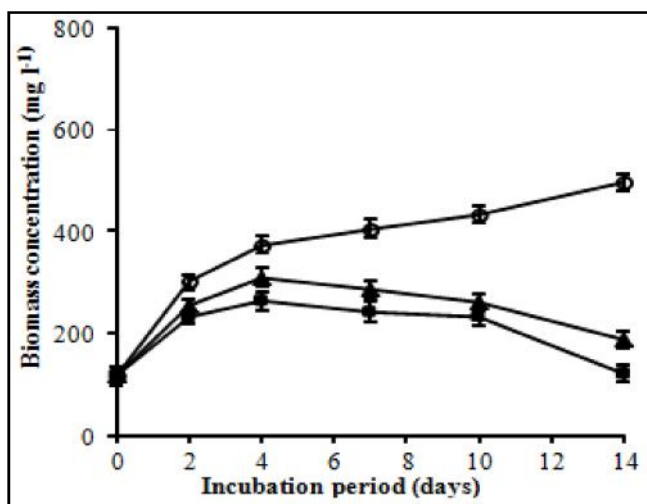
Fig.1 Impact of nitrogen and phosphorous deficiencies on (A) Biomass concentration

3.2 Impact of N-/P- Deficiency onP(3HB-co-3HV) co-polymer Accumulation

The co-polymers of Poly(3-hydroxybutyrate-*co*-3-hydroxyvalerate)P(3HB-*co*-3HV) could only be produced in presence of propionate/ valerate in the culture medium. Maximum P(3HB-*co*-3HV) co-polymer accumulation reached up to 205.7 mg l^{-1}(36.4%, dcw)with 74.4 mol% 3HB and 25.6 mol% 3HV units under 0.4% valerate supplementation, followed by 183.6 mg l^{-1}(38.6%, dcw)under 0.4% propionate supplementation with 89.4 mol% 3HB and 10.6 mol% 3HV units on day 14 of incubation.The P(3HB-*co*-3HV) co-polymer and 3HV content from valerate were higher than those from propionate. This indicated that *A. fertilissima* utilized valerate better than propionate to synthesize 3HV monomers (data not shown). During the biosynthesis of this copolymer, 3-hydroxyvaleryl-CoA (3HV-CoA) is an intermediate to be converted into 3HV monomer. This important intermediate is synthesized from the condensation of propionyl-CoA to 3-ketovaleryl-CoA, subsequently followed by reduction to 3HV-CoA [18]. It has been observed that a wider range of 3HV monomer composition could be achieved when sodium valerate was used instead of sodium propionate [19]. This is mainly because sodium propionate does not generate 3HV units exclusively; it is also condensed to acetyl-CoA, which is the intermediate substrate for 3HB units [20]. Therefore, both 3HB and 3HV units are generated when sodium propionate is used as a 3HV precursor. Conversely, sodium valerate is metabolized via -oxidation pathway so that it could be directly incorporated into the polymer chain without breakdown of its carbon chain length [21].

To investigate the effect of N-/P- deficiency on P(3HB-*co*-3HV) accumulation, the cells were cultured in media supplemented with varied concentration of propionate and valerate in which phosphate and nitrogen were eliminated (Table 1 and 2). In N-deficient medium, the maximum P(3HB-*co*-3HV) content was achieved to 72.3% (dcw), a value <"2-fold higher than the control within 5 days of incubation under 0.4% valerate, followed by 67.8% (dcw) under 0.4% propionate-supplemented condition (Table 1), which agrees well with earlier reports of Koyama and Doi [22] and Son et al. [23]. Maximum P(3HB-*co*-3HV) co-polymer accumulation up to 45.3 and 39.4% (dcw) was observed in P-deficient medium supplemented with 0.4% valerate and 0.2% propionate, respectively (Table 2).

Table 1 Impact of Nitrogen Deficiency at Varied Concentration of Propionate and Valerate

Carbon Concentration (% w/v)		Biomass concentration (mg l⁻¹)	P(3HB-*co*-3HV) content		Polymer composition (mol %)	
			(mg l⁻¹)	(% dcw)	3HB	3HV
Control (photoautotrophic)		263.5±2.01ᵉ	25.8±0.23ᵃ	9.8±0.07ᵃ	100	0
Propionate	0.1	232.7±3.09ᵇ	90.1±0.77ᵇ	38.7±0.09ᶜᵈ	94.2	5.8
	0.2	250.4±2.26ᵈ	104.9±1.09ᵈ	41.9±0.19ᵈ	92.4	7.6
	0.4	242.9±3.01ᶜ	164.6±1.00ᶠ	67.8±0.66ᶠ	90.4	9.6
	0.6	197.7±1.79ᵃ	104.1±0.98ᵈ	52.7±0.43ᵉ	88.2	11.8
Valerate	0.1	410.4±3.07ʰ	96.8±0.78ᶜ	23.6±0.11ᵇ	94.7	5.3
	0.2	445.7±3.19ⁱ	162.7±1.17ᵉ	36.5±0.23ᶜ	87.6	12.4
	0.4	331.7±2.86ᵍ	239.8±1.68ʰ	72.3±0.61ᵍ	74.4	25.6
	0.6	319.8±2.77ᶠ	171.1±0.88ᵍ	53.5±0.34ᵉ	62.5	37.5

Incubation period: 4 days

Values are mean ± SE, n=3.

Values in the column superscripted by different letters are significantly ($P< 0.05$) different from each other (Duncan's new multiple range test).

Separate analysis was done for each column.

Table 2 Impact of Phosphate Deficiency at Varied Concentration of Propionate and Valerate

Carbon Concentration (% w/v)		Biomass concentration (mg l⁻¹)	P(3HB-*co*-3HV) content		Polymer composition	
			(mg l⁻¹)	(% dcw)	3HB	3HV
Control (photoautotrophic)		310.6±3.01ᵉ	32.5±0.33ᵃ	10.6±0.07ᵃ	100	0
Propionate	0.1	226.9±3.35ᵇ	40.2±0.63ᵇ	17.7±0.08ᵇ	92.5	7.5
	0.2	276.2±3.26ᵈ	108.8±1.27ᵉ	39.4±0.17ᵍ	91.4	8.6
	0.4	247.9±3.11ᶜ	73.9±1.03ᵈ	29.8±0.21ᵉ	90.4	9.6
	0.6	223.7±2.71ᵃ	56.1±0.85ᶜ	25.1±0.13ᵈ	86.9	13.1
Valerate	0.1	316.7±3.97ᶠ	72.2±0.98ᵈ	22.8±0.09ᶜ	93.7	6.3
	0.2	367.6±3.82ⁱ	154.8±1.09ᵍ	42.1±0.16ʰ	85.6	14.4
	0.4	346.7±3.76ʰ	157.1±1.13ʰ	45.3±0.19ⁱ	72.4	27.6
	0.6	340.7±2.88ᵍ	114.8±1.08ᶠ	33.7±0.18ᶠ	64.5	35.5

Incubation period: 4 days

Values are mean ± SE, n=3.

Values in the column superscripted by different letters are significantly ($P< 0.05$) different from each other (Duncan's new multiple range test).

Separate analysis was done for each column.

The biomass concentration was found to be affected negatively in presence of propionate rather than valerate-supplementation under P- and N- deficiencies.The inhibitory effects of propionate on growth of *A. fertilissima* could be due to the toxic effects of organic acid, which agree well with the earlier reports of Kim et al. [24] and Lama et al. [25], respectively for *W. eutropha* and *A. cylindrica* 10 C. As compared to valerate, propionate exhibited more detrimental effect to the cells because it has shorter n-alkyl chains [26].

3.3 Impact of Chemoheterotrophy

The cultures (14 day old) grown under usual 'light-dark' cycles when incubated under dark for 5 days depicted a PHB accumulation up to 13.5% (dcw) (Table 3).This could possibly be due to the degradation of glycogen to supply acetyl-CoA, the substrate for PHB biosynthesis, or the sudden decrease in ATP pool by transferring the cultures to dark aerobic condition [27]. Interestingly, addition of 0.4% valerate at the initiation of dark incubation under P-deficiency was found to boost P(3HB-*co*-3HV) accumulation up to 222.1 mg l^{-1}, about 6-fold higher against control (light-dark cycle). This could be explained as polymer biosynthesis is expected to increase under dark incubation with carbon supplementation, through increased NADPH production, as reported for *Aphanocapsa* 6714 [28]. Further increase in co-polymer accumulation up to 40.1% (dcw) was observed, when supplemented in N-deficient medium with 0.4% valerate and subjected to dark incubation of 5 days (Table 3). Thus, combined effects of valerate and N-deficiency under dark incubation were found stimulatory for P(3HB-*co*-3HV) accumulation.

Table 3 Chemoheterotrophic Accumulation of P(3HB-*co*-3HV) co-polymer in *A. fertilissima* after 5 Days of Incubation

Carbon Concentration (% w/v)	Biomass concentration (mg l^{-1})	P(3HB-*co*-3HV) content		Polymer composition (mol %)	
		(mg l^{-1})	(% dcw)	3HB	3HV
Control (L:D cycle)	627.3±3.18[h]	38.3±0.18[a]	6.1±0.04[a]	100	0
Dark	576.3±2.72[e]	77.8±0.63[b]	13.5±0.11[b]	100	0
Dark + P (0.4)	586.2±2.35[f]	109.0±0.99[c]	18.6±0.15[c]	87.3	12.7
Dark + V (0.4)	601.7±3.19[g]	149.2±1.15[d]	24.8±0.17[d]	45.9	54.1
Dark + P (0.4) + P⁻	543.6±2.97[b]	176.6±1.36[e]	32.5±0.22[e]	82.2	17.8
Dark + V (0.4) + P⁻	573.9±3.07[d]	222.1±1.55[g]	38.7±0.26[g]	76.3	23.7
Dark + P (0.2) + N⁻	515.9±2.99[a]	185.2±1.39[f]	35.9±0.23[f]	89.2	10.8
Dark + V (0.4) + N⁻	552.7±3.12[c]	221.6±1.51[g]	40.1±0.31[h]	78.7	21.3

P: propionate, V: valerate, P⁻: phosphorus deficiency, N⁻: nitrogen deficiency and L:D cycle: light:dark cycle
Values are mean ± SE, n=3.
Values in the column superscripted by different letters are significantly ($P < 0.05$) different from each other (Duncan's new multiple range test).
Separate analysis was done for each column.
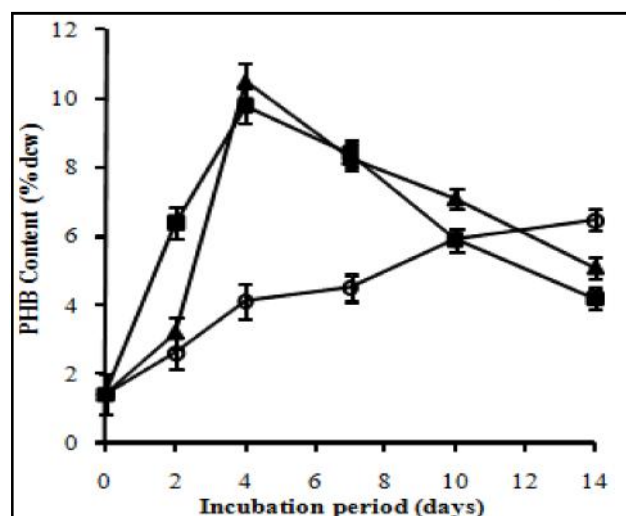
(B) PHB content of *A. fertilissima*. (Ë%): control, (%): N-deficiency, and (²%): P- deficiency

4. CONCLUSION

When we compared the cyanobacterial PHB production with heterotrophic bacteria, a significantly lower accumulation was observed for the former. Though the latter depicted a much higher expression level, the requirement of large amount of exogenous carbon supplementation and continuous oxygen supply made the fermentative production of bacterial PHB much more expensive than that of the normal synthetic plastics. Algae, including the blue–greens, constitute a major group of primary producers in the aquatic environment and account for over half of the total annual carbon fixation. The cyanobacteria or blue–green algae are of the most ancient group of organisms, which exist in almost all conceivable habitats. Due to their minimal nutrient requirement and ability to grow even in wastewaters in presence of CO_2 and sunlight these photoautotrophs could be explored as an alternative source for polymer production, as the biomass could be inexpensively converted into biodegradable plastics by solar energy. This study has led to the finding of a diazotrophic cyanobacterial species, *Aulosira fertilissima* capable of producing Poly- -hydroxybutyrate up to 10% (dcw) and Poly(3-hydroxybutyrate-*co*-3-hydroxyvalerate) up to 72% (dcw) underP-deficiency and N-deficiency, respectively. Chemoheterotrophy with 0.4% (w/v) valerate umder P/N-deficiency enhanced the polymer accumulation up to 38–40% (w/w) dry cells, the value almost 6-fold higher with respect to photoautotrophic condition. However, biomass productivity of *A. fertilissima* was affected under N/P-deficiency. This necessitates a two-stage cultivation practice, where at the first stage *A. fertilissima* cell must be grown under carbon-supplemented condition to reach a high cell density; followed by a second stage, deficient condition as in this study, for efficient polymer accumulation.. Thus, cyanobacterial PHB production though seems challenging but an economically feasible approach. This may lead to the introduction of PHB and P(3HB-*co*-3HV) ('Cyano-Plastic' as we may call it) from photosynthetic organism in to the field of pharmaceuticals and biomedical science.

REFERENCES

[1] M. Liebergesell, K. Sonomoto, M. Madkour, F. Mayer and A. Steinbüchel, "Purification and Characterization of the Poly(hydroxyalkanoic acid) Synthase from Chromatium Vinosum and Localization of the Enzyme at the Surface of Poly(hydroxyalkanoic acid) Granules", Eur J Biochem, Vol. 226, 1994, pp. 71-80.

[2] R.N. Reusch, A.W. Sparrow and J. Gardiner, "Transport of poly-betahydroxybutyrate in Human Plasma", Biochim Biophys Acta 112333–40. 1992.

[3] O. Duvernoy, T. Malm, J. Rasmtrom and S. Bowald, "A Biodegradable Patch used as a Pericardial Substitute after Cardiac Surgery: 6- and 24-Month Evaluation with CT", Throac Cardiovasc Surg. Vol.43, 1995, pp.271.

[4] M. Vincenzini and R. De Philippis, "Polyhydroxyalkanoates", InChemicals from Microalgae.Cohen, Z. pp. 292-312. USA: Taylor and Francis Inc. 1999.

[5] M. Nishioka, K. Nakai, M. Miyake, Y. Asada, and M. Taya, "Production of poly-β-hydroyxybutyrate by Thermophilic Cyanobacterium, Synechococcus sp. MA19, Under Phosphate Limitation. Biotechnol Lett.Vol.23, 2001, pp.1095-1099.

[6] L. Sharma and N. Mallick, "Accumulation of Poly-β-hydroyxybutyrate in Nostoc Muscorum: Regulation by pH, light-dark Cycles, N and P status and Carbon Sources", Bioresource Technol, Vol.96, 2005, pp.1304-1310.

[7] B. Panda and N. Mallick, "Enhanced poly-β-Hydroxybutyrate Accumulation in a Unicellular Cyanobactrium, Synechocystis sp. PCC 6803. Lett Appl Microbio, Vol.l44, 2007, pp.194-198.

[8] N. Mallick, S. Gupta, B. Panda and R. Sen, "Process Optimization for Poly(3-hydroxybutyrate-co-3-hydroxyvalerate) Co-polymer Production by Nostoc Muscorum", Biochem Eng J37, 2007, pp.125-130.

[9] R. Bhati and N. Mallick, "Production and Characterization of poly(3-hydroxybutyrate-co-3-hydroxyvalerate) Co-polymer by a N_2-Fixing Cyanobacterium, Nostoc Muscorum Agardh. J Chem Tech Biotech, Vol.87, 2012, pp.505-512.

[10] R. Rippka, J. Deruelles, J. B.Waterbury, M. Herdman and R.Y. Stanier, "Generic Assignments, Strain Histories and Properties of Pure Cultures of Cyanobacteria", J Gen Microbiol, Vol.111, 1979, pp.1-61.

[11] S. Samantaray and N. Mallick, "Production and Characterization of Poly-β-hydroxybutyrate (PHB) Polymer from Aulosira Fertilissima", J Appl Phycol, 24, 2012, pp.803-814.

[12] V. Yellore and A. Desia, "Production of Poly-β-Hydroxybutyrate from Lactose and Whey by Methylobacterium sp. ZP24", Lett Appl Microbiol, Vol.26, 1998, pp.391-394.

[13] V. Riis and W. Mai, "Gas Chromatographic Determination of Poly-β-hydroxybutyric Acid in Microbial Biomass after Hydrochloric Acid Propanolysis", J Chromatogr, Vol.445, 1988, pp. 285-289.

[14] L.C. Rai, N. Mallick, J.B. Singh and H.D. Kumar, "Physiological and Biochemical Characteristics of A Copper Tolerant and A Wild Type Strain of Anabaena Doliolum Under Copper Stress", J Plant Physiol, Vol.138, 1991, pp.68-74.

[15] B. Panda, P.Jain, L. Sharma and N. Mallick, "Optimization of Cultural and Nutritional Conditions for Accumulation of Poly-β-hydroxybutyrate in Synechocystis sp. PCC 6803", Bioresource Technol, Vol.97, 2006, pp.1296-1301.

[16] A. Konopka and M. Schnur, "Biochemical Composition and Photosynthetic Carbon Metabolism of Nutrient Limited Cultures of Merismopedia Tenuissima (Cyanophyceae)", J Phycol, Vol.17, 1981, pp.118-122.

[17] S.Y. Lee, S.H. Hong, S. J. Park, R. Van Wegen and A.P.J. Middelberg, "Metabolic Flux Analysis on the Production of Poly(3-hydroxybutyrate). InPolyesters I: Biological Systems and Biotechnological Production", Y. Doi and A. Steinbüchel, Weinheim, Germany: Wiley-VCH Publishers, 2001, pp. 249-261.

[18] A. Steinbüchel and T. Lütke-Eversloh, "Metabolic Engineering and Pathway Construction for Biotechnological Production of Relevant Polyhydroxyalkanoates in Microorganisms", J. Biochem Eng, Vol.16, 2003, 81-96.

[19] Y. Doi, "Microbial Polyesters", New York, USA: VCH Publishers, 1990,pp.166.

[20] Y. Doi, M. Kunioka, Y. Nakamura and K. Soga, "Biosynthesis of Copolyesters in Alcaligenes Eutrophus H16 from ^{13}C-lebeled acetate and Propionate. Macromolecules, Vol.20, 1987, pp. 2988-2991.

[21] Y. Doi, A.Tamaki, M. Kunioka and K. Soga, "Production of Copolyesters of 3-hydroxybutyrate and 3-hydroxyvalerate by Alcaligenes Eutrophus from Butyric and Pentanoic Acids", Appl Microbiol Biot, Vol.28, 1988, pp.330-334.

[22] N. Koyama and Y. Doi, "Production of poly(3-hydroxybutyrate-co-3-hydroxyvalerate) from Various Carbon Sources by Batch-fed Cultures of Alcaligenes Eutrophus", J Environ Polym Degr, Vol.1, 1993, pp.235-240.

[23] H.Son, G. Park and S. Lee, "Growth Associated Production of Poly-β-hydroxybutyrate from Glucose or Alcoholic Distillery Wastewater by Actinobacillus sp", EL-9. Biotechnol Lett18, 1996, pp.1229-1234.

[24] B. S. Kim, S. C. Lee, S. Y. Lee, H. N. Chang, Y. K. Chang and S.I. Woo, "Production of Poly(3-Hydroxybutyric-co-3-hydroxyvaleric acid) by Fed-Batch Culture of Alcaligenes Eutrophus with Substrate Control Using On-line Glucose Analyzer. Enzyme Microb Tech., Vol.16, 1994, pp.556-561.

[25] L. Lama, B. Nicolaus, V. Calandrelli, M.C. Maria, I. Romano and A. Gambacorta, "Effect of Growth Conditions on Endo- and Exopolymer Biosynthesis in Anabaena Cylindrica 10 C", Phytochem., Vol. 42, 1996, pp.655-659.

[26] C.Y. Loo and K. Sudesh, "Polyhydroxyalkanoates: Bio-based Microbial Plastics and their Properties.", Malaysian Polymer J 2, 2007, pp.31-57.

[27] A.J. Smith, "Modes of Cyanobacterial Carbon Metabolism", In The Biology of Cyanobacteria.Carr, N.G. and Whitton, B.A. pp. 47-85. Oxford, UK: Blackwell Scientific Publishers., 1982.

[28] R.A. Pelroy, G.A. Levine and J.A. Basham, "Kinetics of Light-dark CO_2 Fixation and Glucose Assimilation by Aphanocapsa 6714", J Bacteriol Vol. 128, 1976, pp.633-643.

Bactericidal Activity of Medicinal Plants Used in Treating UTI (Urinary Tract Infection)

J.Dhanalakshmi[1] and S. Selvi[2]

[1]Research and Development Centre, Bharathiar University, Coimbatore - 641 046, Tamil Nadu

[2]Assistant Professor, Department of Biochemistry, Bharathidasan College of Arts and Science, Erode - 638 116, Tamil Nadu

Email : dhanajd26@gmail.com

Abstract

Urinary tract infections (UTIs) are caused by bacteria and are 10 times more common among women than men. More than 50% of women will have at least one UTI during their lifetime; for most of these infections, patients need to see a doctor and be treated with antibiotics. The present study was to investigate the Antibacterial Activity of Some Medicinal Plants which are used against UTI Causing Pathogens. Bacteria were isolated from the UTI infected patients and characterized by using microscopic, staining, morphological and biochemical methods. The Ethanolic Extracts from plants were prepared and then used to check their antibacterial activity against the bacteria isolated from UTI infected patients and the zone of inhibitions were compared with the zone of inhibition of standard antibiotics. Results from the present study revealedthat Tribulus terrestris exhibited high antibacterial activity against the bacteria isolated from UTI. Enthuciased with the above result further work is planned to extract the compound(s) responsible for antibacterial activity from Tribulus terrestris and analysis its anticancer property against Urinary Bladder Carcinoma.

Keywords: *Antibacterial Activity, Bladder carcinoma, Antibiotics, Tribulus terrestris, Urinary Tract Infection,.*

1. INTRODUCTION

A urinary tract infection (UTI) (also known as acute cystitis or bladder infection) is an infection that affects part of the urinary tract. When it affects the lower urinary tract it is known as a simple cystitis (a bladder infection) and when it affects the upper urinary tract it is known as pyelonephritis (a kidney infection). Symptoms from a lower urinary tract include painful urination and either frequent urination or urge to urinate (or both), while those of pyelonephritis include fever and flank pain in addition to the symptoms of a lower UTI. The main causal agent of both types is Escherichia coli, however other bacteria, viruses or fungi may rarely be the cause.

Urinary tract infections are the second most common type of infection in the body, accounting for about 8.1 million visits to health care providers each year. Women are especially prone to UTIs for anatomical reasons. One factor is that a woman's urethra is shorter, allowing bacteria quicker access to the bladder. Also, a woman's urethral opening is near sources of bacteria from the anus and vagina [14]. For women, the lifetime risk of having a UTI is greater than 50%[2]. UTIs in men are not as common as in women but can be serious when they occur. More than 95% of UTI are caused by single bacterial species E. coli which is the most frequently infecting organisms [10]. However, many other bacteria can also because an infection for example Klebsiella, Pseudomonas, Enterobacter, Proteus, Staphylococcus, Mycoplasma, Chlamydia, Serratia and Neisseria spp. It is reported that about 35% of healthy women suffer symptoms of Urinary tract infection and about 5% of women each year suffer with the problem of painful urination (dysuria) and frequency [7]. The incidence of UTI is greater in women as compared to men. Several potent antibiotics are available for the treatment of UTI, but increasing drug resistance among bacteria has made therapy of UTI difficult. Bacteria have the genetic ability to transmit and acquire resistance to drugs [15]. Essential extracts of certain plants have been shown to have antimicrobial effects, as well as imparting flavor to foods [6]. The synergistic effect of the mixture of phytochemicals plays an important role to use plant extracts as an antimicrobial agents [12]. It has been suggested that volatile oils, either inhaled or applied to the skin, act by means of their lipophilic fraction reacting with the lipid parts of the cell membranes, and as a result, modify the activity of the calcium ion channels [5]. The antimicrobial and other biological activities of the plant extracts varied depending upon the origins and cultivars [8].

J.Dhanalakshmi[1] and S. Selvi[2]

In this study antimicrobial activity of the medicinal plants Tribulusterrestris, Cinnamom verum and Punica granatum were checked against the bacterial isolates from patients (Pregnant Women) with UTI. Bladder cancer is any of several types of malignancy arising from the epithelial lining (i.e., the urothelium) of the urinary bladder. Rarely the bladder is involved by non-epithelial cancers, such as lymphoma or sarcoma, but these are not ordinarily included in the colloquial term "bladder cancer." It is a disease in which abnormal cells multiply without control in the bladder. It is estimated that there are 383,000 cases of bladder cancer worldwide.

2. MATERIALS AND METHODS

Isolation and identification of bacteria from UTI infected patients: First the microorganism present in urine samples of UTI infected patients were cultured in the nutrient broth and the morphology of organisms were studied with the help of light microscope and shape, size, odour, margin and surface characteristics of bacteria. Gram staining procedure was adopted to differentiate between gram positive and gram negative organisms. Selective agar medium was used for further identification.

Different media for different organism were used as given below:
i.   Mac Conkey : E. coli and Staphylococcus
ii. EMB   :   E. coli
iii. MSA   : Staphylococcus
iv. PABM   : Pseudomonas
v.   XLDA   : Shigella
vi. Blood agar   : Proteus

After this step final identification of bacteria was done on the bases of biochemical testing.

3. BIOCHEMICAL TESTS

Seven biochemical tests were performed for each organism as given below:
i.   Catalase test
ii. Indole production test
iii. Citrate utilization test
iv. TSI (Triple sugar iron) agar test
v.   Urease activity test
vi. MR and VP test

4. ETHANOLIC EXTRACTION OF MEDICINAL PLANTS

The three Medicinal plants namely Tribulusterrestris - Nerungi, Punicagranatum-Madhulai and Cinnamom verum - Ilavangam were selcected and their antimicrobial activities were tested againstbacteria affecting Urinary Tract. Dried plant material (10g) was finely ground and extracted with Distilled Water and 99.9% Ethanol using Soxhlet's apparatus. The extract was kept in oven at 50^0C for 1hrs to evaporate excess ethanol and water. The residues (both ethanolic and aqueous extract) were suspended in DMSO to give 100 mg residue/ml by following procedure described [15].

5. TESTING OF ANTIMICROBIAL ACTIVITY
5.1 Testing the Antimicrobial Activity by Disc Diffusion Method

The paper disc diffusion method [4] was used to screen the antibacterial activity of plant extracts and performed by using Mueller Hinton agar (HA). Sterilized filter paper discs (Whatman, 6 mm in diameter) were placed on the surface of the solidified media soaked with 20 µl of a solution of each plant extracts. The standard antibiotic strips were also used for comparison. DMSO was used as negative control. The inoculated plates were stored at 4°C for 2hrs and then incubated at 37°C for 24hrs in the inverted position. The diameters (mm) of the inhibition zones were measured (diameter of paper disc, 6 mm is included). Studies were performed in triplicate and the results are expressed as means along with the Standard Deviaton (SD) of three parallel measurements.

6. RESULTS & DISCUSSION

25 urine samples were obtained from urinary tract infected pregnant women respectively who were admitted at Namakkal Government Hospital, Namakkal. Table 1 shows percentage contribution of bacterial isolates isolated from urinary tract infected patients.

After studying the colony morphology on nutrient agar medium, colony morphology was also studied on the selective media. After the secondary identification on selective media, all samples were examined microscopically here the shape, size arrangement (pair, cluster and chain) and motility was checked and the gram staining techniques were followed Table 2. The final identification were done on the basis of biochemical analysis Table 3 and Plate-1.

Table 1 Etiology in 25 cases of Urinary Tract Infection were Studied During the Study Period

Sl. No	Pathogens	No. of Positive Cases	%
1	Escherichia Coli	9	36%
2	Klebsiella Pnemoniae	6	24%
3	Pseudomonas Aeruginosa	5	16%
4	Proteus Vulgaris	3	14%
5	Staphylococcus Aureus	2	10%

Table 2 Morphology and Staining of Test Isolates

Sl.No.	Name of the Bacterial Species	Gram Staining	Morphology	Motility
1	Escherichia coli	-	GNR	Motile
2	Klebsiella Pnenumoniae	-	GNR	Non Motile
3	Pseudomonas Aeruginosa	-	GNR	Motile
4	Proteus Vulgaris	-	GNR	Motile
5	Staphylococcus Aureus	+	GPC	Non Motile

(-) – Negative;　　(+) – Positive; GNR – Gram negative rod;　GPC – Gram positive cocci.

Table 3 Biochemical Tests of Recovered Isolates of Urine Samples

Sl.No	Name of the Bacterial Species Confirmed	Indole	MR	VP	Citrate	TSI	H 2 S	Urease
1	Escherichia Coli	+	+	-	-	A/A	-	-
2	Klesiella Pneumoniae	-	-	+	+	A/A G+ve	+	+
3	Pseudomonas Aeruginosa	-	-	-	+	A/A G+ve	-	-
4	Proteus Vulgaris	+	+	-	-	AK/H2S	+	+
5	Staphylococcus Aureus	-	+	+	-	A/A G-ve	-	-

PLATE – 1: IMViC test reactions of the Test isolates.

TribulusTerristris extract against E.coli

Cinnamomum verum extract against E.coli

Punica grannatum *extract against E.coli*
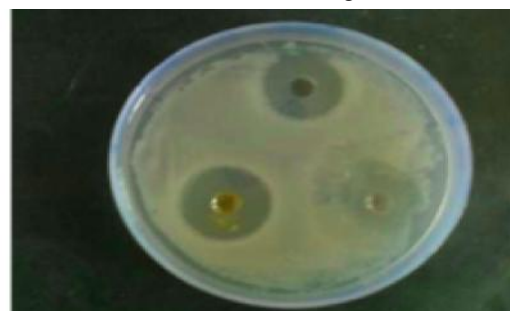
Cinnamomum verum against K. pneumo

J.Dhanalakshmi[1] and S. Selvi[2]

6.1 Antimicrobial Activity

Three plant extracts of the Tribulusterrestris, Cinnamom verum presl and Punica granatum were extracted to test the antimicrobial activity on the five different bacteria isolated from urine samples of UTI infected patients with respect to standard antibiotic by the "Disc diffusion diffusion method" and the diameter zone of inhibition was measured in mm. Antimicrobial activity of different plant extracts on the different organisms is given as in Table 4 and Plate 2.

Results showed that the ethnolic extracts ofPunica grannatum has greater anti bacterial activity among all the other extracts its maximum value of the zone of the inhibition is noted against E.coli 29mm than Norfloxacin 22mm. Then Punica grannatum andCinnamomum verum presl extracts has showed almost equal activity, Punica grannatum has maximum activity against Staphylococcus with diameter 30mm in comparison to

Gentamycin 19mm. Cinnamon extract had showed maximum results of antimicrobial activity against the organisms Proteus vulgarisand Pseudomonas 26mm in comparison to Norfloxacin 22mm and 20mm. After that Cinnamomum verum presl has showed almost equal results to the antibiotics with maximum activity 26mm against the bacteria E. coli in comparison to Norfloxacin 22mm and the TribulusTerristris has show least activity of all the plant extracts and also less than the standard antibiotic maximum zone of inhibition 15mm in comparison to standard antibiotic ciprofloxacin 25mm. Cinnamomumverumpresl bark possess potent antimicrobial properties against Staphylococcus aureus and dermatophytic fungi. It is useful in the tropical treatment of superficial skin infections [9]. Punica granatum used to treat urinary astrigent, abdominal ulcers, glycosuria and skin diseases [11]. Prior study also reported that presence of inhibitory effect in Punica granatum against Salmonella, E. coli, and Staphyllococcus aureus[13].

Table 4 Diameter of Zone of Inhibition Shown By Various Isolates against Standard Antibiotic And Various Plants Extracts

Sl.No.	Organism	TribulusTerristris (Inhibitionzone in mm)	Cinnamomum Verum Presl (Inhibition zone in mm)	Punica Grannatum (Inhibition zone in mm)	Antibiotics
1	Escherichia coli	11	26	29	Norfloxacin-22
2	Klesiella pneumoniae	15	22	25	Norfloxacin-22
3	Pseudomonas aeruginosa	10	24	18	Norfloxacin-23
4	Proteus vulgaris	12	25	26	Ciprofloxacin -25
5	Staphylococcus aureus	10	25	30	Gentamycin-19

Plate 2 : Zone of Inhibition of Various Isolates Against Standard Antibiotic and Various Plants Extracts

Punica grannatum extract against K. pneumonia

Punica grannatum extract against S.aureus

TribulusTerristris K. pneumonia

Cinnamomum verum presl S.aureus

7. CONCLUSION

From the above results we can conclude that extracts of plants origin has remarkable antimicrobial activity as compare to standard antibiotics. We know that organisms are gaining resistance day by day towards the antibiotics, so that some natural products should be tried to overcome these antibiotic resistant organisms. The plants extracts or oils have no side effect; medicinal products may be one of our choices because it contains hydrophobic liquid which can be easily extracted by the process of distillation. Plant products or oils contain volatile aroma and phytochemicals which show the antimicrobial activity. More over plants can be grown easily and the production of their products is sophisticated than antibiotics. Expense on these material is bearable than antibiotic. The present study has been undertaken to identify effective herbal medicines to control UTI caused by bacterial organisms because, for all human beings herbal medicines are available in our environment and safe also. It does not cause any side effects. From these properties of plants we can say that natural medicine can take place of antibiotics in future. The further extensive study is planned to isolate the compound responsible for the antibacterial and anticancer properties of Tribulus terristris compared with those of an anticancer drugs as the positive control is currently under way. Efficacy and Mechanism of the action in various normal and cancer cell models in vitro, coupled with bioassay guided purification inorder to elucidate active anticancer compound(s)from the crude extract will be reported in due course.

REFERENCES

[1] O A. Aiyegoro, O O.Igbinosa, I N.Ogunmwonyi, E E.Odjadjare, O E.Igbinosa and A I.Okoh, "Incidence of Urinary Tract Infections (UTI) Among Children and Adolescents in Ile-Ife", Nigeria. Afr. J. Microbiol. Res, 2007, pp. 013-019.

[2] Amit kumar, Neeraj Jhadwal, Madan lal and Manjeet Singh, "Antibacterial Activity of Some Medicinal Plants Used Against UTI Causing Pathogens ", Int. Jr. of Drug Development & Research, Vol.4, No.2, April-June 2012.

[3] Anju Puri, Tanvir Khaliq, Rajendran, Geetika Bhatia and Ramesh Chandra, "Antidyslipidemic Activity of I.tinctoria", Journal of Herbal Pharmacotheraphy, Vol.7, No.1, 2007, pp.50-153.

[4] A. W. Bauer, D. M. Perry and W. M. M. Kirby, "Single Disc Antibiotic Sensitivity Testing of Staphylococci", A.M.A. Arch. Intern. Med. Vol.104, 1959, pp.208-216.

[5] G. Buchbauer, L. Jirovetz, "Aromatherapy Use of Fragrances and Essential Oils as Medicaments", Flav. Fragr. J. Vol.9, 1994, pp.217-222.

[6] S. Burt, "Essential Oils: Their Antimicrobial Properties and Potential Aapplication in Foods-A Review", International Journal of Food Microbiology., Vol.94, 2004,pp.223-253.

[7] T M.Hootan, "Urinary Tract Infection in Adults", In: R.J.Johnson, J.Feehally,(Eds). Comprehensive Clinical Nephrology, 2nd ed, London: Mosby, 2003, 731-744.

[8] A I.Hussain, F. Anwar, S.T.H.Sherazi and R.Przybylski, "Chemical Composition. Antioxidant and Antimicrobial Activities of Basil (Ocimum basilicum) Essential Oils Depends on Seasonal Variations", Food Chemistry, Vol.108, 2008, pp.986-995.

[9] P. Kannan, B.Shanmugavadivu, C.Petchiammal and W.Hopper, "Invitro Antimircobial Activity of W.tinctoria leaf Extracts Against Skin Microorganisms", Journal of Acta Botanica Hungarica, Vol.48, 2006, pp.323-329.

[10] A N.Kebira, P. Ochola and S.A.Khamadi, "Isolation and Antimicrobial Susceptibility Testing of Escherichia coli Causing Urinary Tract Infections", J. Appl. Biosci. 2009, pp.1320-1325.

[11] Narayan Das, Prajapati, Purohit, Arunk Sharma and Tarun Kumar, " A Hand Book of Medicinal plants", 2003, pp.217.

[12] A. Pauli Amicbase", Essential Oils Supplementary Information. Review Science", 90513 Zirndorf, Further Str.

[13] R.Ravi, R.Venkatanarayanan, S M.Sivakumar, R. Binokingsly, R.Hemalatha, S.M.Satheshkumar, Suriyaprakash, "Anti Hepto Toxic Activity of I.tinctoria. Nigerian Journal of Natural Products and Medicine, Vol.8, 2004, pp.43-44.

[14] SM.Schappert, EA.Rechtsteiner, "Ambulatory Medical Care Utilization Estimates for 2006", National Health Statistics Reports; No 8. Hyattsville, MD: National Center for Health Statistics; 2008.

[15] D. Srinivasan, Sangeethan Nathan, T. Suresh, P.Lakshmana and Permalsamy, "Antibacterial Activity of Neem (AzadirachTA INDICA) and Tamarind (Tamarindus Indica) leaves, Asian Jr. of Microbiol Biotech & Env. SC. Vol.3, No.1-2, 2001, pp.67-73.

[16] J. Soulsby, "Resistance to Antimicrobials in Humans and Animals", Braz. J. Med. Vol.331, 2005, pp.1219-1220.

Nitrification-denitrification Biofilter for Toxic Nitrogen Removal from Aquaria

V. Gopi, N.Dineshkumar, C. Saravanakumar and S.V. Alavandi

Aquatic Animal Health and Environment Division, Central Institute of Brackishwater Aquaculture,
Chennai - 600 028, Tamil Nadu
E-mail:svalavandi@yahoo.com

Abstract

In modern intensive and semi-intensive aquaculture, water quality becomes a limiting factor due to accumulation of NH_3 (ammonia) and NO_2 (nitrite). Ammonia is a major end product of protein catabolism, excreted by fish, crustaceans, and molluscs into the culture system. Unionized ammonia is most toxic to aquatic organisms as it can readily diffuse through cell membranes and is highly lipid-soluble. Nitrite an intermediate product of nitrification is also one of the toxic forms of nitrogen that can be found in aquaculture ecosystems. These substances despite being toxic to the cultured animals per se increase their susceptibility to diseases, particularly shrimp which are bottom dwelling organisms. Hence, it is extremely important that these inorganic pollutants generated during aquaculture be mitigated to achieve optimal aquaculture productivity.

This study was designed to evaluate nitrifying and denitrifying bacteria for toxic nitrogen removal using the nitrification-denitrification concept. Commercially available materials such as bio-rings bio-balls, Aqua-clay balls and filter floss were colonized with well characterized nitrifying and denitrifying bacteria packed in an external biofilter and tested for ammonia, nitrite and nitrate removal from aquaria. Results showed that use of external biofilter is an ideal alternative for optimizing nitrification-denitrification for complete removal of ammonia, nitrite and nitrate from aquaculture systems. The biofilter system needs to be scaled-up and optimized for management of ammonia and nitrite in large volumes of water, which could be exploited for better management of water quality in shrimp hatcheries and for bioremediation of aquaculture discharge.

1. INTRODUCTION

Intensive aquaculture relies on high protein-content feeds that are rich in nitrogen (5-6.5%N). Feed application in these systems often reaches 60gm⁻³ day⁻¹(3). Most of the nitrogen in the feed (approximately 70%) remains in the pond water and deteriorates water quality (2,5). Biological removal of ammonia in these ponds takes place by several biological processes including ammonification, nitrification and denitrification (9, 4, 6).Bacteria transform nitrogen in the feed remnants to ammonia. Unionized ammonia is most toxic to aquatic organisms as it can readily diffuse through cell membranes and is highly lipid-soluble and consequently traverses biological membranes and causes extensive damage to tissues, especially gills and kidney; physiological imbalances; impaired growth and death. In aquaculture ponds, ammonia is oxidized by bacteria to nitrite and then to nitrate. Nitrite is highly toxic to animals even at very low concentrations. While nitrate is considered non-toxic, at high nitrate concentrations it can affect the growth of commercially cultured aquatic organisms, such as eel (7) and shrimp (8).

The biological conversion of ammonia to nitrite is carried out by ammonia oxidizing bacteria (AOB) and the subsequent oxidation of nitrite to nitrate by nitrite-oxidizing bacteria (NOB), the process called nitrification. AOB such as *Nitrosomonas* spp. and *Nitrosococcus* spp and NOB such as *Nitrobacter* spp. and *Nitrococcus* spp. are involved in these processes.

$$NH_3 + O_2 \longrightarrow NO_2^- + 3H^+ + 2e^-$$
$$NO_2^- + H_2O \longrightarrow NO_3^- + 2H^+ + 2e^-$$

Denitrification is a respiratory process, carried out by heterotrophic bacteria in which nitrate and nitrite are reduced to gaseous nitrogen intermediates viz. nitric oxide (NO), Nitrous oxide (N_2O) and nitrogen (N_2). The organisms involved in this process are called denitrifying bacteria (DNB). Bacteria such as *Bacillus, Paracoccus denitrificans, Pseudomonas* are can carry out these processes.

$$NO_3^- \longrightarrow NO_2^- \longrightarrow NO \longrightarrow N_2O \longrightarrow N_2$$

Nitrification and denitrification play a key role in aquaculture ponds that receive large amount of organic and inorganic nitrogenous compounds. To evaluate the

effectiveness of nitrification-denitrification process, this study was conducted using an external biofilter. A biological filter is nothing more than a chemically inert porous sponge, which provides greatly enlarged surface area on which these bacteria can develop. External biofilter are used in aquaculture system to recirculate water through a series of different filter media colonized with environmentally relevant bacteria.

2. MATERIALS AND METHODS
2.1 Enrichment of Nitrifying and Denitrifying Isolates

Well characterized and identified nitrifying enrichments and denitrifying bacteria were used in this study. Further, the efficiency of nitrifying enrichments and denitrifying isolates were tested for their activity *in vitro* (unpublished results, data not shown). Nitrifying enrichments and DNB were colonized in commercially available carrier materials like aquaclay balls, aquamats, bio-balls, bio-rings, filter floss and 5 µm mesh by incubating them at 30 ± 2 °C for a week in the respective culture broths. The colonized materials were periodically monitored for ammonia and nitrite oxidation and denitrification.
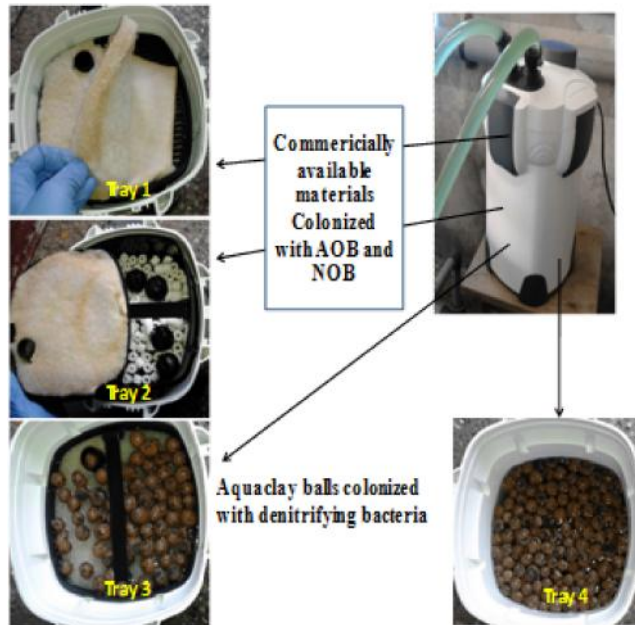
Fig.1 External biofilter assembly withaquaclay balls, aquamats, bio-balls, bio-rings, filter floss and 5 µm mesh

Fig.2 Evaluation of external biofilter for ammonia removal

3. EXPERIMENTAL SETUP

A commercially available external biofilter was used in this study. The biofilter contained four trays, the first tray was packed with aquamats, filter floss, and 5 µm mesh, the second tray was packed with bio-balls and bio-rings, the third and fourth trays were packed with aquaclay balls (Figure1). The colonized materials were packed inside the biofilter in an order depending on the buildup of end products. The external biofilter was connected to a FRP tank with 100L of filtered seawater (salinity 15ppt) spiked with 500ppm of ammonium chloride ($NH_4Cl_2.2H_2O$). Flow rate of the external biofilter was maintained at 1000L/hr and the seawater was monitored for nitrite levels using sulphanilamide and N-(1-Naphthyl) ethylenediamine dihydrochloride (NED) reagents and OD was measured spectrophotometerically at 540nm (1).

4. RESULTS AND DISCUSSION

Since the addition of AOB colonized materials (aquamats, filter floss and 5 µm mesh) to the biofilter, nitrite levels were found to increase from 0 to 0.4 µg/ml at 90 hours due to ammonia oxidation. Hence to initiate nitrite oxidation, NOB colonized materials (bio-balls and bio-rings) were packed at 90 hours into the filter and activity was monitored. Despite addition of NOB, nitrite levels in the seawater was not found to drop and continued to increase from 0.4 to 0.56 µg/ml (Figure 3). This indicated that NOB used in this study could not

able to oxidize nitrite completely, hence DNB colonized materials (Aquaclay balls) were packed at 143 hours and nitrite levels were found to drop from 0.56 to 0.51 µg/ml at 160 hours. However at 169 hours, nitrite level reached a peak of 0.74 µg/ml indicating that denitrification did not occur. This could be attributed to the inadequacy of Carbon source for DNB.

Hence carbon source (Sodium citrate) was added twice to the seawater to facilitate denitrification at 170 and 187 hours. After addition of Sodium citrate, nitrite levels dropped from 0.74 µg/ml to 0.36 µg/ml, however seawater became turbid due to excessive proliferation of DNB. The experiment was terminated after 11 days
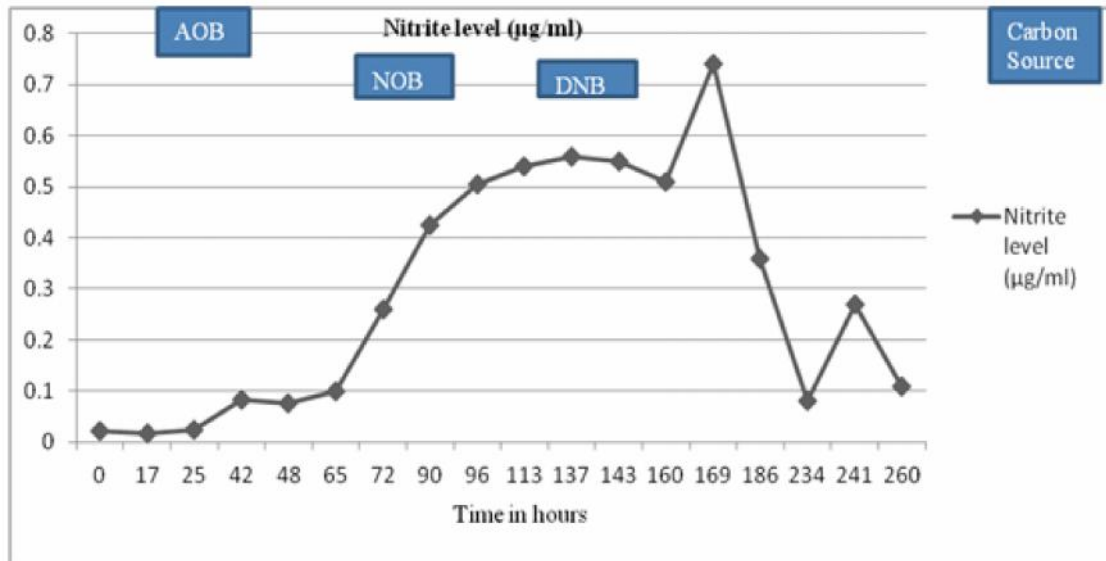
Fig.3 Nitrite level in aquarium tank fitted with nitrification-denitrification biofilter

5. CONCLUSION

Efficient isolates have been used to construct nitrifying-denitrifying biofilter that are capable of simultaneous nitrification and denitrification for complete removal of ammonia, nitrite and nitrate and maintains a pH between 7.5-8.0 without the need for alkalinity supplements (10). Biofilter system developed here is novel in that it is completely aerobic process using aerobic denitrifying bacteria for the first time. However the biofilter had some limitations. DNB required periodic addition of carbon source periodically for maintaining the biomass and activity. The system needs to be scaled-up and optimized for mitigation of ammonia and nitrite in large volumes of water, which could be exploited for better management of water quality in shrimp hatcheries and for bioremediation of aquaculture discharge.

REFERENCES

[1]   American Public Health Association (APHA), American Works Association, Water Environment Federation. 1998.In: Clesceri, L.S. Greenberg, A.E. Eaton, A.D (Eds), "Standard methods for the Examination of Water and Wastewater", 20th ed. United book press, Inc., Baltimore, Maryland.

[2]   C.E. Boyd, "Chemical Budgets for Channel Catfish Ponds", Transactions of the American Fisheries Society, Vol.114, 1985, pp.291-298.

[3]   R.L.Creswell, "Aquaculture Desk Reference", Chapman & Hall, New York, NY, USA. 1993, pp.206.

[4]   S. Diab, M. Shilo, "Transformation of Nitrogen in Sediments of Fish Ponds in Israel", Bamidgeh, Vol.38, 1986pp.67-88.

[5]   A. Gross, C.E. Boyd, C.W.Wood, "Nitrogen Budget and Transformations in Channel Catfish Ponds", Aquaculture Engineering, Vol. 24, 2000, pp.113-132.

[6]   J.A. Hargreaves, "Nitrogen Biogeochemistry of Aquaculture Ponds", Aquaculture, Vol.166, 1998, pp.181-212.

[7]   A. Kamstra, J.W.Van der Heul, "The Effect of Denitrification on Feed Intake and Feed Conversion of European eel Anguilla anguilla L. In: Grizel, H., Kestermont, P. (Eds.), Aquaculture and Water: Fish Culture, Shellfish Culture and Water Usage. European Aquaculture Society Special Publication No.26, Oostende, Belgium, 1998, pp.128-129.

[8]   P.R. Muir, D.C.Sutton, L. Owens, "Nitrate Toxicity to Penaeus Monodon Protozoea", Mar. Biol., Vol.108, 1991, pp.67-71.

[9] M. Shilo and A.Rimon, "Factors which Affect the Intensification of Fish Breeding in Israel. 2. Ammonia Transformation in Intensive Fishponds", Bamidgeh, Vol.34, 1982, pp.101-114.

[10] J. Van Rijn, "The Potential for Integrated Biological Treatment Systems in Recirculating Fish Culture-A Review", Aquaculture, Vol.139, 1996, pp.181–201.

Isolation of Cellulose Producing Bacteria from Glucose Rich Sources

K.P. Vanitha[1] and B.E. Rangaswamy[2]

Department of Biotechnology and Research Centre, Bapuji Institute of Engineering and Technology,
Davangere - 577 005, Karnataka.
E-mail: vanidwani@gmail.com

Abstract

The present study is to isolate cellulose producing bacteria from samples like rotten fruits, rotten vegetables and sugar cane molasses were collected and inoculated into Hestrin-schramm media incubated at 30^0c for 4 days and observed for pellicle formation followed by confirmatory test for cellulose production. Screening and Identification were carried out based on morphological and biochemical tests. Organisms were confirmed to produce cellulose are Acetobacter sp.,Pseudomonas sp. These organisms were further confirmed with reference cultures. The isolates obtained were used for fermentative production and is expected to facilitate the development of fermentation process which able industrialist to commercialize the product.

1. INTRODUCTION

Cellulose is a Natures abundant biopolymer it can be synthesized by microbes. Traditionally, cellulose is harvested from plants, but microbial cellulose has superior characteristics such as high purity, high degree of polymerization, high tensile strength and water holding capacity (Brown, 2004). However MC as wide application in the field of pharmaceutical for artificial vein, skin born transfer and wound healing, food industry used it as raw material for desserts and ice-cream preparation, paper industry for high quality paper products making, audio speaker diaphragm preparation and cosmetic industry for facial cream preparation it acts as a very good moisturizing agent. Due to era of declining forest, global climate changes to balance the nature eco-friendly cellulose production from microbial origin shows great impact on environment and biotech industry.

Microbial cellulose is produced by microorganism such as *Gluconacetobacter*, *Agrobacterium, Aerobacter,Achromobacter, Azotobacter, Rhizobium, Pseudomonas, sarcina*and *salmonella* (Brown, 1989; Chwala et al., 2009). These are organism which reported to produce cellulose.

Research on microbial cellulose was done by static, submerged and agitated methods. The Cost effective production of cellulose with good yield as to achieve further to commercialize the product. The aim of the present work is to isolate and screening cellulose producing bacteria from glucose rich sources such as rotten fruits, rotten vegetables and sugar cane molasses. Further work as to carry out to obtain high yield producer followed by optimization of media, temperature and PH.

2. EXPERIMENTAL MATERIALS AND METHODS
2.1 Samples Collected

Rotten fruits (apple, orange, sweet lime, grapes and pomegranate)**,** rotten vegetables (Carrot, potato, tomato, brinjal)and Sugar cane molasses (collected from Shammnur sugars limited, Duggavathi, Harihara, Davangere.

2.2 Chemicals and Reagents

Hestrin- scharamm media (Himedia), Fluorescent brightener 28 (sigma Aldrich) and Biochemical test kit KB001and Carbohydrate fermentation kit KB009 Himedia (Hungund, 2010)

2.3 Isolation and Screening of Cellulose Producing Bacteria

The samples like rotten fruits, rotten vegetables and sugar cane molasses were collected and inoculated into saline and incubated at 30^0c for one hour in shaker incubator. Then these samples were inoculated into Hestrin-Schramm broth (glucose -20g/L, yeast extract 5g/L, peptone 5g/L, disodium hydrogen phosphate-2.7g/L and citric acid-1.15g/L) pH-6.0 were incubated at 30^0C for 4 days. Pellicle were formed at air-liquid interface observed in the medium those flasks were selected and purified the culture by repeated streaking on nutrient agar/ Hestrin-Schramm agar plates to obtain isolated colonies. Each distinct isolate were inoculated on screening media i.e. Hestrin schramm agar (HSA) with fluorescent brightener dye (0.2%) and antifungal

agent cycloheximide incubated at 30^{0}C for 3 days. The fluorescent dye was bind to the cellulose content in the media which is produced by organism. So the fluorescence colonies were selected as cellulose producers. Further Gram-staining, colony morphology, hanging drop motility test, biochemical test were carried out to identify the organism.

Table 1 Screening of Isolates Obtained From Different Sources

Sample Number	Source	Isolates	Organism	Cellulose Production
1	Rotten apple	VA01	*Acetobacter sp.*	+
2	Rotten sweet lime	VA02	*Acetobacter sp.*	+
3	Rotten potato	VA14	*Pseudomonas sp.*	+
4	Sugar cane molasses	VA04	*Actinomycetes sp.*	-
5	Rotten carrot	VA16	To be identified	+
6	Rotten grapes	VA08	To be identified	+

2.4 Identification of Cellulose Producer

Colony morphology, Gram-staining, motility test, biochemical test and carbohydrate fermentation test were carried out to identify the organism.

2.5 Detection of Cellulose Production

The pellicle formed broth was treated with 0.5N NaOH at 80^{0}c for 1 hourthen pellicle were washed three times with distilled water and dried at room temperature.

3. RESULTS AND DISCUSSION
3.1 Isolation and Screening of cellulose producing Bacteria

In the present study, six bacterial strains were isolated from total of 25 glucose rich sources screened. Among those, two isolates showed cellulose production. Among these 25 glucose rich sources screened more production was obtained from rotten fruits, followed by rotten vegetables and cellulose production not found in sugar cane molasses. The isolates which obtained VA01,(rotten apple) VA02 (rotten sweet lime) and VA14 (rotten potato) are good producer compare to other isolates (Table1).

Researchers reported cellulose productions are from fruits and vegetables (Chawala, et al., 2009; Firdaus Jahan et al., 2012). In the similar study, many reported most potent producer from rotten fruits and nowhere studied for sugar cane molasses. Glucose is key ingredients which responsible for cellulose production further isolation and screening will be carry out with other glucose sources.

3.2 Identification of Cellulose Producer

The isolates were found to be a Gram negative rod shaped showed similar characteristics to genera *Acetobacter sp.* and *Pseudomonas sp*. These strains showed similar pattern of Biochemical test characteristics to *Acetobacter sp.* and *Pseudomonas sp*. Bergey's Manual of Determinative Bacteriology (Buchanan, 1974). Further carbohydrate fermentation test were compared with reference strains. Therefore, by analyzing the colony morphology (figure1), gram reaction biochemical and carbohydrate fermentation characteristics, the isolates VA01, VA02 and VA14 were identified be a strains of *Acetobacter sp.* and *Pseudomonas sp.* (Table 2).
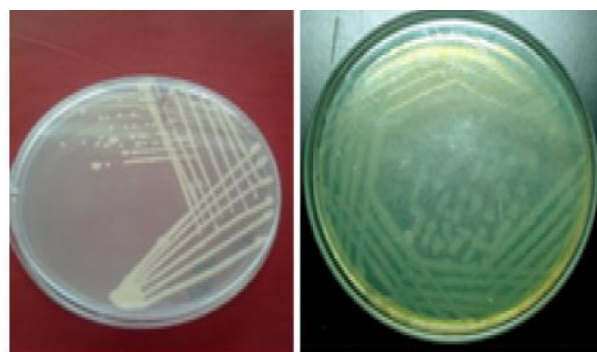
Fig.1 Colony morphology of *Acetobacter sp.* and *Pseudomonas sp.*

K.P. Vanitha[1] and B.E. Rangaswamy[2]

Table 2 Identification and Biochemical test and Carbohydrates fermentation Results

Characteristics Test	Acetobacter spp		Pseudomonas spp
	VA01	VA02	VA14
Gram Reaction	Gram Negative Rods	Gram Negative Rods	Gram Negative Rods
Motility	Motile	Non motile	Motile
Cellulose Production	+	+	+
Catalase	+	+	+
Oxidase	-	-	+
Citrate Utilization	+	-	-
Indole Test	-	-	-
Methyl Red	-	-	-
Voges Proskauers	-	-	-
Urease	-	-	-
H2S Production	+	-	-
Glucose	-	+	+
Adonitol	-	-	+
Arabinose	+	+	+
Lactose	-	-	+
Sorditol	+	+	+
Mannitol	+	+	+
Rhamnose	+	+	+
Sucrose	+	+	+
Dextrose	+	+	+
Xylose	+	+	+
Maltose	+	+	+
Fructose	+	+	+
Galactose	+	+	+
Rafinose	+	+	+
Trehalose	+	+	+
Melibiose	+	+	+
L-Arabinose	+	+	+
Mannose	+	+	+
Insulin	+	+	+
Sodium Gluconate	+	+	-
Glycerol	+	+	+
Inositol	+	+	-
Sorbital	+	+	
Erythritol	+	+	-
α-Methyl-D-glucoside	+	+	-

3.3 Detection of Cellulose

In previous studies also, fluorescent brightener (Calcofluor white) which is present in the screening medium binds to -D glucans in a definable, reversible manner and cellulose producing bacterial colony fluoresces when observed under UV light has been reported (Ross et al., 1991; Hungund and Gupta, 2010). In present study the fluoresces colony was repeated streaked into Hestrin- scharamm agar and purity was confirmed and accepted as cellulose producer (Figure:2). The pellicle formed broth were treated with alkali 0.5N NaOH at 80^0c for 30 minutes and pellicle were washed three times with distilled water and dried at room temperature.(Chawla et al., 2009). In this present study similar method is followed and cellulose is harvested. Further yield has to find out with respect to organism.
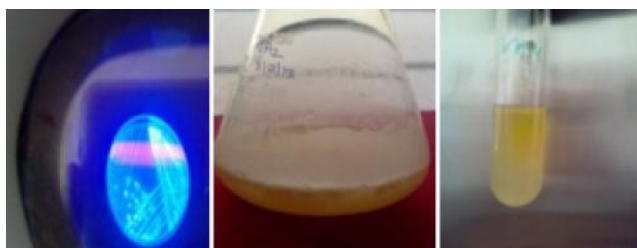

Fig.2 Fluorescence colony under UV and pellicle formed at air liquid interface

4. CONCLUSION

In this study glucose rich sources were collected to isolate cellulose producer among 25 isolates five isolate showed cellulose production in that two organism were identified are *Acetobacter sp.* and *Pseudomonas sp.* other threeare unidentified. Further studies as to carry out to find out yield of cellulose with respect to organism. Optimization of media and isolation as to proceed further to obtain high yield cellulose production and fermentation process as to carry out to meet the commercial production.

REFERENCES

[1] R.M.Brown, "Bacterial Cellulose, In: Cellulose:Structural and Functional Aspects", Ed Kennedy, Phillips, & Williams. Ellis Horwood Ltd., Journal. 1989, pp.145-151.

[2] R. M. Brown, Journal of Polymer Science: Part A: Polymer Chemistry, Vol.42, 2004, pp.487-495.

[3] R. E. Buchanan & N. E. Gibbons, "Bergey's Manual of Determinative Bacteriology (8th ed.). Baltimore: Williams and Wilkins, 1974.

[4] P. R. Chawla, I. B. Bajaj, S. A. Survase and S.S. Rekha, "Food Technology and Biotechnology", Vol.47, 2009, pp.107-124.

[5] Firdaus JahanDr.Saxena, "Production of Microbial cellulose by a Bactrium Isolated from Fruit", Journal Applied Biochem Biotechnology, doi: 10.1007/s12010-012-9595-x., 2012, Vol.167, pp.1157-1171.

[6] J.D. Fontana, V.C. Franco, S.J. deSouza, I.N. Lyra, and A. M de Souza. "Nature of Plant Stimulators in the Production of Acetobacter Xylinum ("Tea Fungus") Biofilm Used in Skin Therapy", Applied Biochem. & Biotechnology, No.24-25, 1991, pp. 341-351.

[7] S. Hestrin and M.Schramm, "Synthesis of Cellulose by Acetobacter Xylium", J.Biochem., Vol.58, 1954, pp.345-352.

[8] S. Hestrin and M.Schramm, Biochemical Journal, Vol.58, 1954, pp.345-352.

[9] B. S.Hungund and S.G.Gupta, "Production of Bacterial Cellulose from Enterobacter AmnigenusGH-1 Isolated from Rotten Apple", World Journal of Microbiol Biotechnol, Vol.26, 2010, pp.1823-1828.

[10] B. S.Hungund and S.G.Gupta, "Improved Production of Bacterial Cellulose from Gluconacetobacter Persimmonis GH-2", Journal of Microbial Biochem Technology, doi:10.4172/1948-5948.1000037, Vol.2, 2010, pp.127-133.

[11] M.M. Lapuz, E.G. Gallardo and M. A. Palo, "The nata Organism-cultural Requirements, Characteristics, and Identity", The Philippine Journal of Science, Vol.96, 1969, pp. 91-109.

[12] Panesar,P.S., Y.V. Chavan, M.B. Bera, O. Chand and H. Kumar. 2009. Evaluation of Acetobacter Strain for the Production of Microbial Cellulose. Asian Journal of Chemistry Vol. 21, No. 10 (2009).

[13] P. Ross, R. Mayer and M. Benziman, "Microbiological Reviews", Vol.55, 1991, pp.35-58.

[14] H. Toyosaki, T. Naritomi, A. Seto, M. Matsuoka, T. Tsuchida and F. Yoshinaga, "Bioscience Biotechnology & Biochemistry", Vol.59, 1995, pp.1498-1502.

Outer Membrane Proteins and Lipopolysaccharides of *Yersinia Enterocolitica* Isolated from Milk and Raw Milk Products

Shanmuga Priya, S.T. Senthil Murugan and Tha. Thayumanavan

School of Biotechnology, Dr. G.R. Damodaran College of Science, Coimbatore - 641 014, Tamil Nadu

E-mail: spriyabiotech@ymail.com

Abstract

Of 50 raw milk (30) and milk product (20) samples collected, 29 (19 raw milk and 10 milk products) of them were found positive for Y. enterocolitica. All the isolates have produced both outer membrane proteins and lipopolysaccharides. Biotyping profiles revealed that only four strains (three from raw milk and one from milk products) falling under the category biotype 1B. All the four biotype 1B strains proteins between the range of 120 – 150 kDa, which is proved as toxin. In addition to this, all the four biotype 1B strains were also found to be the producers of haemolysin. All the four biotype 1B strains have produced good levels of lipopolysaccharides (LPS). Of three strains from raw milk products, only one isolate has produced both rough and smooth LPS, while, remaining three have produced smooth LPS. This is the most significant finding of the study.

Keywords: Haemolysin, LPS, Milk, Milk products, OMP, Y.enterocolitica

1. INTRODUCTION

Yersinia enterocolitica is a Gram-negative psychrotrophic enterobacterium causing gastrointestinal disorders [1]. It has been isolated from water, dairy products, foods, animals and humans in every country where isolation has been attempted [2, 3] but frequently isolated from sewage water, raw milk and milk products [4, 5]. The bacterium was surrounded by two membranes, the inner membrane (IM) and the outer membrane (OM). The Inner membrane is a bilayer composed of phospholipids and the Outer membrane is asymmetric, having phospholipids in its inner lea et and, in most Gram-negative bacteria, lipopolysaccharides (LPS) in its outer lea et [6]. Embedded in the OM are also a number of outer membrane proteins (OMPs) that function in solute and protein translocation, pathogenesis, structural linkers, and signal transduction [6, 7]. Both OMPs and LPS may function as speci c phage receptors [7, 8]. Some of these outer membrane proteins (OMP) are encoded by plasmid and play significant role in the pathogenicity of these bacteria [9]. The outer membrane protein of the *Y. enterocolitica* is probably involved in the host - bacterial interactions; Because OMP is dependent on the presence of plasmid for expression [10]. The LPS-containing asymmetric bilayer of the bacterial outer membrane serves as an efficient barrier against rapid penetration by these lipophilic antibiotics and chemotherapeutic agents [11]. Protein level typing mostly determines the pathogenic species diversity.

2. EXPERIMENTAL MATERIALS AND METHODS

2.1 Sample Collection and Isolation

A total of 50 samples, (raw milk (30) and milk product (20)) were collected from different locations, mainly in and around Coimbatore, Tamil Nadu. One ml of well-mixed milk samples and 0.1 g of milk products samples were inoculated into 10 ml of *yersinia* enrichment broth (Hi Media, India) and incubated at 30 °C for 24 hr. Then a loopful of culture was transferred and streaked on to CIN agar (Hi Media, India), followed by incubated at 28 °C for 18-24 h. After incubation, the plates were analyzed for characteristic colony.

2.2 Confirmation of *Y. enterocolitica*

All the isolates were subjected to biochemical methods of identification, according to Bergey's manual of determinative bacteriology [12]. All the isolates were also examined for Voges-Proskauer, urease, sorbitol, ornithine decarboxylation, citrate, dnase, raffinose, esculin hydrolysis, salicin fermentation and lysine iron agar (LIA). In order to confirm *Y. enterocolitica*, all the isolates were subjected to 16S rRNA PCR [13].

2.3 Extraction of Outer Membrane Protein (OMP)

The *Y. enterocolitica* strains were grown in 20 ml of Nutrient broth (Hi Media, India) overnight at 37°C.

Preparation of OMP was done according to Winder *et al.* [14]. The pellet containing the OMP was resuspended in deionised water (1 ml) and stored at - 20 C until required. The samples were subjected to 12 % polyacrylamide gels containing SDS (SDS-PAGE) and the gel was stained with Coomassie brilliant blue R-250 [15].

2.4 Extraction of Lipopolysaccaride (LPS)

Cells were grown on nutrient broth for 48 h at 37°C. LPS from cells was obtained by the hot phenol - water method [16]. 20 µl of LPS suspension was applied in each slot of 12.5 % SDS - PAGE gel. The separated LPSs were visualized by silver staining [17].

3. RESULTS AND DISCUSSION

In a study, of 30 raw milk samples collected, 36.6 % of them were positive for this organism [18]. Similarly, the incidence of *Y. enterocolitica* has been reported from raw milk samples as 20 %, 81.4 % and 10.6 % by Franzin et al. [19], Vidon and Delmas, [20] and Subha et al. [21] respectively. In our study, 64 % of the raw milk samples were recorded as positive for this bacterium. Of 76 cheese curd samples tested, 9.2 % (n=7) were positive for *Y. enterocolitica* [4]. This study report 50 % of milk products samples were contaminated with *Y. enterocolitica* (Table 1). This might be due to the improper cleaning and poor hygienic practices during the collection of samples. All the isolates were subjected to biochemical tests according to Bergey's manual of determinative bacteriology [12] and the positive isolates were undergone 16S rRNA gene amplification which shows 330 bp confirms *Y. enterocolitica* [13].

Table 1 Incidence of *Y. enterocolitica* in Various Samples

Sample	No. of Samples	% Positive
Raw milk	30	64% (n=19)
Packed Foods	20	50% (n=10)

The full expression of virulence due to 70 Kb pYV plasmid, which correlates with the massive release of a set of proteins (Yops) [22]. It became clear that pYV and Yops are essential for the pathogenicity of yersinia species including *Yersinia enterocolitica* [23].

In our study, Biotyping profiles revealed that only four strains (three from raw milk and one from milk products) falling under the category biotype 1B. All the four biotype 1B strains proteins between the range of 120 – 150 kDa, which is proved as toxin. In general, the banding pattern of total and membrane proteins did not seem very useful in distinguishing between strains because of the numerous bands displayed [24]. High molecular weight protein (HMWP) with a molecular weight of 120 – 150 kDa determines pathogenic isolates. From 29 strains tested, we observed that four isolates have produced similar kind of protein, which confirms the presence of high pathogenic strains among our isolates and eleven different banding patterns (Fig. 1). In another study the presence of both HMWP1 and HMWP2 are present in pathogenic strains of *Y. enterocolitica* [25].

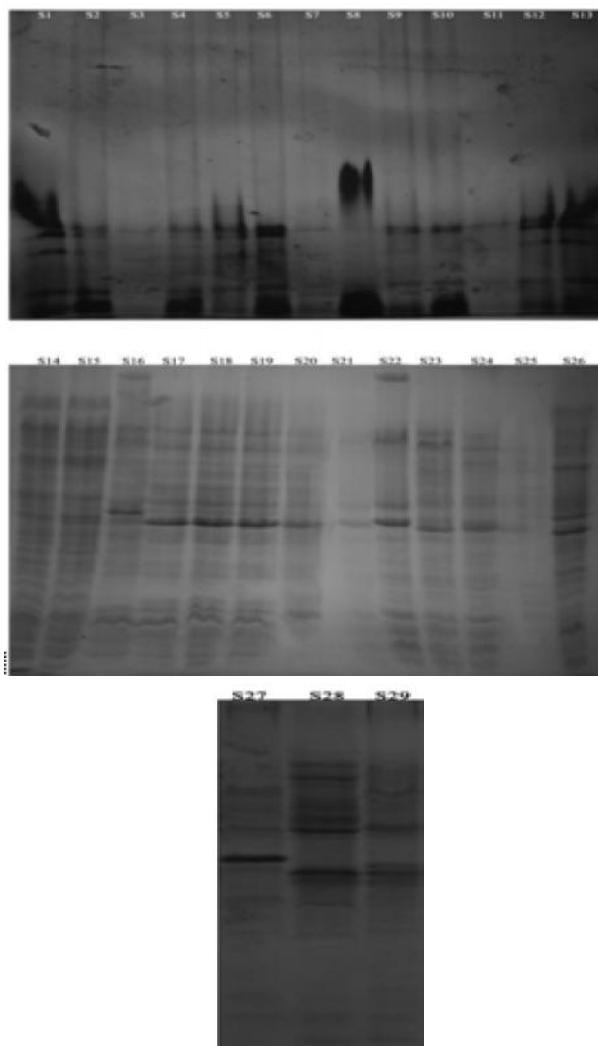Fig.1 Outer membrane protein of isolated *Y. enterocolitica.* Indicates HMWP present only in biotype 1B strains

LPS is the major immunogenic component of the Gram-negative enterobacterium *Y. enterocolitica*. LPS has branched repeating pentasaccharide units, therefore, we observed the distinct repeating bands. *Y. enterocolitica* cultures incubated at 25 and 37°C differ in several characteristics. Pathogenic strains can be

identified under the temperature of 37°C, so we undergone the protein isolation in the same temperature. *Y. enterocolitica* bio-serotype 1B/O: 8 show pathogenicity when incubated at 37 °C in the absence of Ca^{2+} [26]. Several investigators worked on the characterization of LPSs produced by *Y. enterocolitica* [27-31]. In our study, all the four biotype 1B strains have produced good levels of lipopolysaccharides (LPS). Of three strains from raw milk products, only one isolate has produced both rough and smooth LPS, while, remaining three have produced smooth LPS (Fig. 2). The isolates could be rough mutants that arose from an originally smooth isolate during *in vivo* passage [32]. This is the most significant finding of the study.
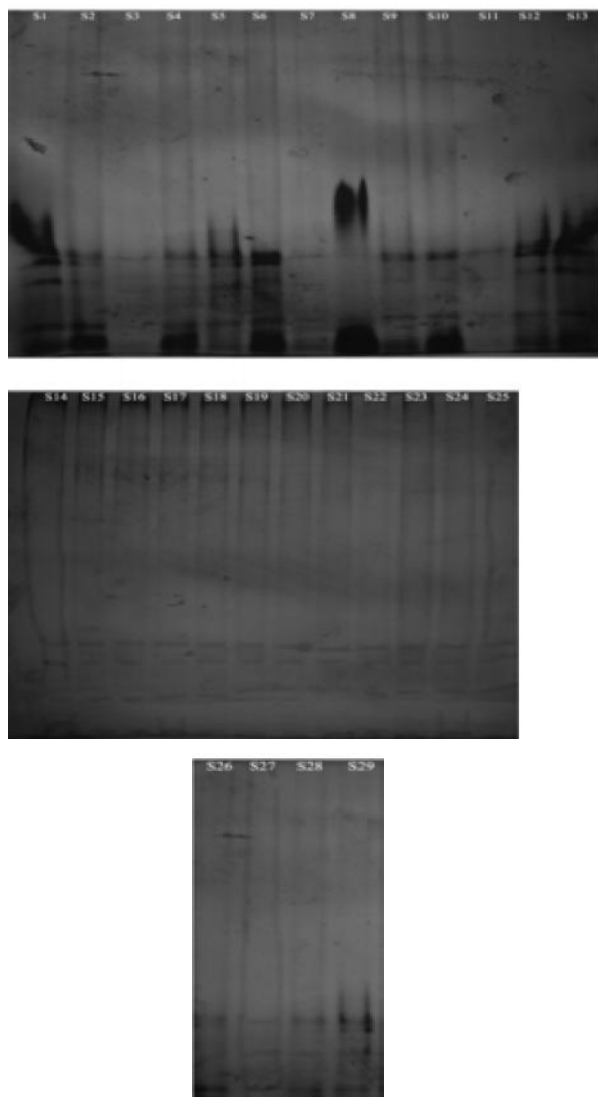

Fig.2 Lipopolysaccaride of isolated *Y.enterocolitica*

REFERENCES

[1] TL. Cover and RC. Aber, "Yersinia enterocolitica", N Engl Journal of Med, 1989, Vol.321, pp.16-24

[2] EJ. Bottone, "Current Trends of Yersinia Enterocolitica Isolates in the New York City Area", Journal of Clin Microbiology, Vol.17, 1983, pp.63-67.

[3] M. Shayegani, De Forge, DM. McGlynn and T.Root, "Characteristics of Yersinia Enterocolitica and Related Species Isolated from Human, Animal, and Environmental Sources", Journal of Clin Microbiology, Vol.14, 1983, pp.304-312.

[4] DA.Schiemann, "Association of Yersinia Enterocolitica with the Manufacture of Cheese and Occurrence in Pasteurized Milk", Applied Environmental Microbiology, Vol.36, 1978, pp.274-277.

[5] DA. Schiemann and S. Toma, "Isolation of Yersinia Enterocolitica from Raw Milk", Applied Environmental Microbiology, Vol.35, 1978, pp.54-58

[6] PJ. Bond and MS. Sansom, "The Simulation Approach to Bacterial Outer Membrane Proteins", Mol Membr Biology, Vol.21, 2004, pp.151–161.

[7] R. Koebnik, KP.Locher and P. Van Gelder, "Structure and Function of Bacterial Outer Membrane Proteins: Barrels in a Nutshell", Mol Microbiology, Vol.37, 2000, pp.239–253.

[8] A. Wright, M. McConnell and S. Kanegasaki, "Lipopolysaccharide as a Bacteriophage Receptor", In L. L. Randall and L. Philipson (ed.), Virus receptors. Chapmann and Hall, London, United Kingdom, 1980.

[9] G.Cornelis, Y.Laroche, G.Balligand, MP. Sory and G. Wauters, "Yersinia Enterocolitica, A Primary Model for Bacterial for Bacterial Invasiveness", Rev infect Dis, Vol.9, 1987, pp.64-87.

[10] DL. Zink, JC. Feeley, C.Wells, C.Vandezant, JC. Vickey, WD.Roof and GA. Dononvan, "Plasmid-mediated Tissue Invasiveness in Yersinia Enterocolitica", Nature, 1980, pp.283- 224.

[11] MP. Bos, B.Tefsen, J. Geurtsen and J. Tommassen, "Identification of an Outer Membrane Protein Required for the Transport of Lipopolysaccharide to the Bacterial cell Surface", Proc Natl Acad Sci USA, 101, Vol.25, No.94, 2004, pp.17-22.

[12] RS. Breed, EGD. Murray and AP. Hitchens, "The Outline Classification Used In The Bergey Manual Of Determinative Bacteriology", Bacteriol Rev., Vol.8, 1944, pp. 255-260.

[13] H. Neubauer, A.Hensel, S.Aleksic and H. Meyer, "Identi cation of Yersinia Enterocolitica within the Genus Yersinia", System Appl Microbiology, Vol.23, 2000, pp.58-62

[14] CL. Winder, IS. Al-Adham, SM. bdel Malek, TE. Buultjens, AJ.Horrocks and J. Collier, "Outer Membrane Protein Shifts in Biocide-resistant Pseudomonas Aeruginosa PAO1", Journal of Applied Microbiology, Vol.89, 2000, pp.289-295.

[15] UK. Laemmli, "Cleavage of Structural Proteins during the Assembly of the Head of Bacteriophage T4", Nature (London), Vol.227, 1970, pp.680-685.

[16] S. Rezania, N. Amirmozaffari, B.Tabarraei, M.Jeddi-Tehrani, O.Zarei, R. Alizadeh, F. Masjedian and AH. Zarnani, "Extraction, Purification and Characterization of Lipopolysaccharide from Escherichia Coli and Salmonella Typhi", Avicenna Journal of Med Biotechnology, Vol.3, 2011, pp.3-9.

[17] CM.Tsai and CE. Frasch, "Staining of Lipopolysaccharide in SDS Polyacrylamide Gels Using Silver Staining Method", Anal Biochemistry, Vol.119, 1982, pp.115-119.

[18] A. Hamama, A. Marrakchi and F.Othmani, "Occurrence of Yersinia Enterocolitica in Milk and Dairy Products in Morocco", Int J Food Microbiology, Vol.16, No.1, 1992, pp.69-77.

[19] L. Franzin, P. Fantino and V.Valerio, "Isolation of Yersinia Enterocolitica and Yersinia like Organisms from Raw Milk in Italy", Curr Microbiology, Vol.10, 1984, pp. 357-360

[20] DJM.Vidon and CL.Delmas, "Incidence of Yersinia Enterocolitica in Raw Milk in Eastern France", Appl Environ Microbiology, Vol.4, 1981, pp.355-359.

[21] B. Subha, D.Ramakrishnan and V. Suganthi, "Antimicrobial Resistance Pattern of Selected Yersinia Enterocolitica Isolates from Raw Cow Milk and Pork Samples of Namakkal District, Tamilnadu, South India", Global J Environ Res, Vol.3, No.3, 2009, pp.169-177.

[22] P. Gemski, JR. Lazere and T. Casey, "Plasmid Associated with Pathogenicity and Calcium Dependency", Infect Immun, Vol.27, 1980, pp.682-685.

[23] JB. Bliska, K. Guan, JE.Dixon and S.Falkow, "Tyrosine Phosphate Hydrolysis of Host Proteins by An Essential Yersinia Virulence Determinant", Proc Natl Acad Sci USA, Vol.88, 1991, pp.1189-1191.

[24] JKP. Kwaga and JO. Iversen, "Laboratory Investigation of Virulence among Strains of Yersinia Enterocolitica and Related Species Isolated from Pigs and Pork Products", Can J Microbiology, Vol.38, 1992, pp.92-97.

[25] S.Schubert, A. Rakin, H. Karch, E. Carniel and J. Heesemann, "Prevalence of the "High-pathogenicity Island" of Yersinia Species among Escherichia coli Strains that are Pathogenic to Humans", Infect Immunology, Vol.66, 1998, pp.480-5.

[26] T. Michiels, P.Wattiau and R. Brasseur, "Secretion of Yop proteins by Yersiniae", Infect Immunology, Vol.58, 1990, pp.2840-9

[27] CH. Pai and V. Mors, "Production of Enterotoxin by Yersinia Enterocolitica", Infect Immunology, Vol.19, 1978, pp.908-911.

[28] JM. Boyce, EJ. Evans Jr, DG. Evans and HL. DuPont, "Production of Heat-stable, Methanol-soluble Enterotoxin by Yersinia Enterocolitica", Infect Immunology, Vol.25, 1979, pp.532-537.

[29] DWFrancis, PL. Spaulding and J. Vitit, "Enterotoxin Production and Thermal Resistance of Yersinia Enterocolitica in Milk", Applied Environmental Microbiology, Vol. 40, 1980, pp.174-176.

[30] J. Hoffman, B. Lindberg and RR. Brubaker, "Structural Studies of the O-specific Side-chains of the Lipopolysaccharide from Yersinia Enterocolitica Ye 128", Carbohydr Res., Vol.78, 1980, pp.212-214.

[31] L. Zhang, J. Radziejewska-Lebrecht, D. Krajewska-pietrasik, P. Toivanen and M. Skurnik, "Molecular and Chemical Characterization of the Lipopolysaccharide O-antigen and its role in the Virulence of Yersinia Enterocolitica Serotype O: 8. Molecular Microbiology, Vol.23, 1997, pp.63-76.

[32] Y. Kawaoka, G. Wauters, K. Otsuki and M. Tsubokura, "Identification of Yersinia Enterocolitica O15 lipopolysaccharide as a Rough Antigen", Journal of Clin Microbiology, Vol.24, No.2, 1986, pp.272-4.

High Speed, Low Power and Area Efficient Processor Design Using Square Root Carry Select Adder

G. Dhanasekaran, N. Parthasarathy and B. Achuthan

Department of Information Technology, Manakula Vinayagar Institute of Technology, Puducherry-605 107
Email:dhanagsekaran@gmail.com, sarathy2393@gmail.com,achuthan002@gmail.com

Abstract

Carry Select Adder (CSLA) is one of the fastest adders used in many data-processing processors to perform fast arithmetic functions. From the structure of the CSLA, it is clear that there is scope for reducing the area and power consumption in the CSLA. This work uses a simple and efficient gate-level modification to significantly reduce the area and power of the CSLA. Based on this modification 8-, 16-, 32-, and 64-b square-root CSLA (SQRT CSLA) architecture have been developed and compared with the regular SQRT CSLA architecture. The proposed design has reduced area and power as compared with the regular SQRT CSLA with only a slight increase in the delay. This work evaluates the performance of the proposed designs in terms of delay, area, power, and their products by hand with logical effort and through custom design . The results analysis shows that the proposed CSLA structure is better than the regular SQRT CSLA.

Keywords: Area, Delay, Data processing, Gate level modification, Processors, Power, Speed

1. INTRODUCTION

The saying goes that if you can count, you can control. Addition is a fundamental operation for any digital system, digital signal processing or control system. A fast and accurate operation of a digital system is greatly influenced by the performance of the resident adders. Adders are also very important component in digital systems because of their extensive use in other basic digital operations such as subtraction, multiplication and division. Hence, improving performance of the digital adder would greatly advance the execution of binary operations inside a circuit compromised of such blocks. The performance of a digital circuit block is gauged by analyzing its power dissipation, layout area and its operating speed.Generally in VLSI techniques we need to satisfy any two of the following criteria such as area, speed and power. The normal adders which we use are satisfying only one trade off but in this SQRT CSLA there is trade off in both area and power. Here we are using 6-Bit BEC(binary to excess-1 converter) to implement the adder element.

2. LITERATURE SURVEY

In this work we will review the implementation technique of several types of adders and study their characteristics and performance. These are

i. Ripple carry adder, or carry propagate adder,
ii. Carry look-ahead adder
iii. Carry skip adder,
iv. Manchester chain adder,
v. Carry select adders
vi. Square root Carry select adders

For the same length of binary number, each of the above adders has different performance in terms of Delay, Area, and Power.

Parallel adders are digital circuits that compute the addition of variable binary strings of equivalent or different size in parallel.
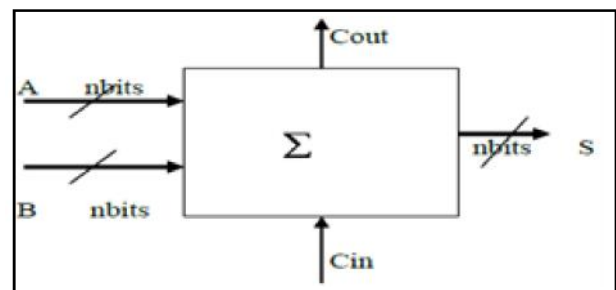
Fig. 1 Block Diagram Of Parallel adders

In ripple carry adders, the carry propagation time is the major speed limiting factorMost other arithmetic operations, e.g. multiplication and division are implemented using several add/subtract steps. Thus, improving the speed of addition will improve the speed of all other arithmetic operations. Accordingly, reducing the carry propagation delay of adders is of great importance. Different logic design approaches have been

employed to overcome the carry propagation problem. One widely used approach employs the principle of carry look-ahead solves this problem by calculating the carry signals in advance, based on the input signals. This type of adder circuit is called as carry look-ahead adder (CLA adder).
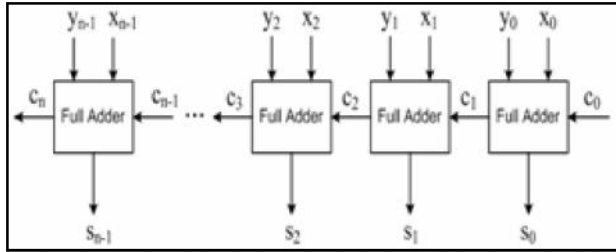

Fig. 2. Block Diagram Of Carry Look ahead adders

A carry-skip adder consists of a simple ripple carry-adder with a special speed up carry chain called a **skip chain**. This chain defines the distribution of ripple carry blocks, which compose the skip adder.

2.1 Carry Skip Mechanics

The addition of two binary digits at stage i, where i 0, of the ripple carry adder depends on the carry in, C_i, which in reality is the, in order to calculate the sum and the carry out, C_{i+1}, of stage i, it is imperative that the carry in, C_i, be known in advance. It is interesting to note that in some cases C_{i+1} can be calculated without knowledge of C_i.
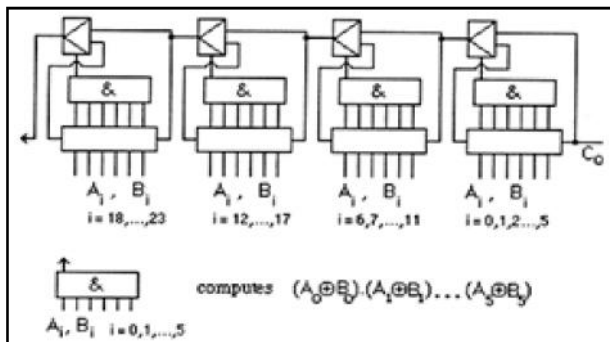

Fig.3 Block diagram of carry skip adders

A ripple carry adder allows you to add two k-bit numbers. We use the half adders and full adders and add them a column at a time.Let's put the adder together one step at a time. Arithmetic operations like addition, subtraction, multiplication, division are basic operations to be implemented in digital computers using basic gates like AND, OR, NOR, NAND etc. Among all the arithmetic operations if we can implement addition then it is easy to perform multiplication (by repeated addition), subtraction (by negating one operand) or division

(repeated subtraction).Half Adders can be used to add two one bit binary numbers. It is also possible to create a logical circuit using multiple full adders to add N-bit binary numbers.Each full adder inputs a **Cin,** which is the **Cout** of the previous adder. This kind of adder is a **Ripple Carry Adder**, since each carry bit "ripples" to the next full adder.
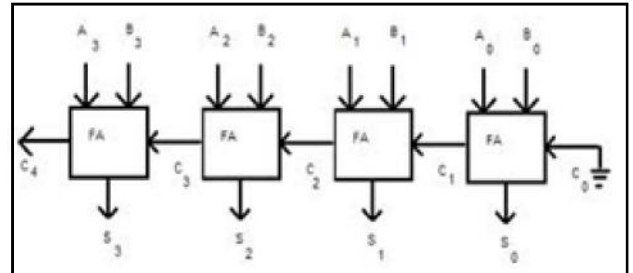

Fig.4 Block diagram of ripple carry adders

The concept of the carry-select adder is to compute alternative results in parallel and subsequently selecting the correct result with single or multiple stage hierarchical techniques [8]. In order to enhance its speed performance, the carry-select adder increases its area requirements. In carry-select adders both sum and carry bits are calculated for the two alternatives: input carry "0" and "1". Once the carry-in is delivered, the correct computation is chosen (using a MUX) to produce the desired output. Therefore instead of waiting for the carry-in to calculate the sum, the sum is correctly output as soon as the carry-in gets there. The time taken to compute the sum is then avoided which results in a good improvement in speed.
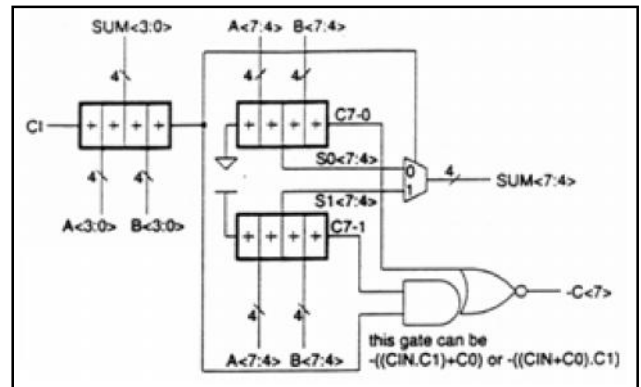
Fig.5 Block diagram of carry select adders

The Manchester Carry-Chain Adder is a chain of pass-transistors that are used to implement the carry chain. During precharge, all intermediate nodes (e.g. $Cout_0$) are charged to Vdd. During the evaluation phase, Cout_k is discharged if there is an incoming carry Cin_0 and the previous propagate signals ($P_0...P_{k-1}$) are high. Only 4 diffusion capacitances are present at each node, but the

distributed RC-nature of the chain results in a delay that is quadratic with the number of bits. Transistor sizing was performed to improve performance. The details are elaborated on in the design strategy section.

3. PROPOSED ALGORITHM

The basic idea of this work is to use Binary to Excess-1 Converter (BEC) instead of RCA with cin=1 in the regular CSLA to achieve lower area and power consumption [2]–[4]. The main advantage of this BEC logic comes from the lesser number of logic gates than the n-bit Full Adder (FA) structure. As stated above the main idea of this work is to use BEC instead of the RCA with Cin=1in order to reduce the area and power consumption of the regular CSLA. To replace the n-bit RCA, an n+1bit BEC is required. A structure and the function table of a 4-b BEC. Fig. 6 illustrates how the basic function of the CSLA is obtained by using the 4-bit BEC together with the mux. One input of the 8:4 mux gets as it input (B3, B2, B1, and B0) and another input of the mux is the BEC output. This produces the two possible partial results in parallel and the mux is used to select either the BEC output or the direct inputs according to the control signal Cin. The importance of the BEC logic stems from the large silicon area reduction when the CSLA with large number of bits are designed. The Boolean expressions of the 4-bit BEC is listed as (note the functional symbols ~NOT, & AND, ^XOR). The Modified CSLA architecture has been developed using Binary to Excess -1 converter (BEC). This paper proposes an efficient method which replaces a BEC using common Boolean logic. The result analysis shows that the proposed architecture achieves the three folded advantages in terms of area, delay and power.
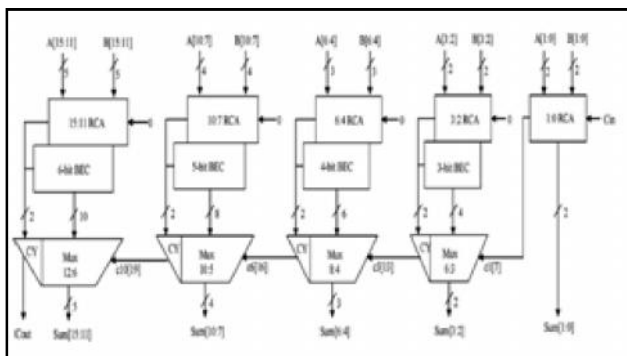
Fig.6 Block diagram of proposed sqrt carry select adders

4. 6-BIT BEC

A BEC(binary to excess-1 converter) is a converter which provides the excess 1 value of a corresponding code which is provided at the input.

Table 1 BEC Input-output

B[3:0]	X[3:0]
0000	0001
0001	0010
1	1
1	1
1	1
1	1
1110	1111
1111	0000
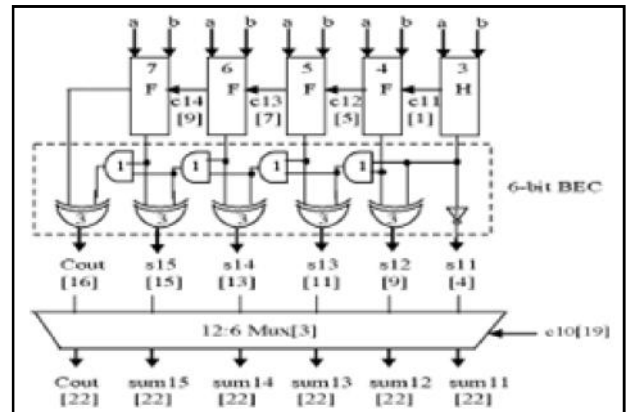
Fig.7 Block diagram of 5 bit BEC

5. SIMULATION RESULTS
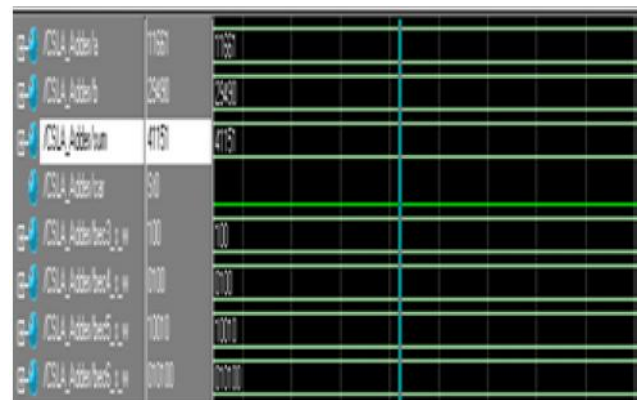
Fig.8 Simulation results for proposed adder

6. RTL SCHEMATIC LAYOUT & FLOOR PLAN IN FPGA

Fig. 9 RTL schematic layout
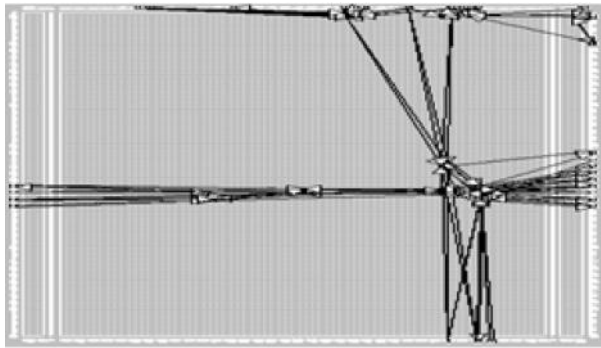
Fig. 10. Floor plan in FPGA

7. COMPARISON OF AREA, SPEED AND POWER

Table 2 Comparision of Area, Speed and Power

Sl.No	Parameters	RCA	CLA	CSA	CSL	PA
1	2 Input Xor Gate	32	32	-	-	-
2	3 Input Xor Gate	-	-	16	48	41
AFTER SYNTHESIS						
3	Number of Slices	19	18	22	18	25
4	4 Input LUT	33	32	39	32	44
5	Bonded IOB	50	50	50	50	49
6	Combinational Delay Path (ns)	27.81	27.07	29.38	17.03	14.97
AFTER MAPPING						
7	4 Input LUT	33	32	39	32	44
8	Number of Slices	24	24	25	21	25
9	Gate Count	198	192	234	192	267
AFTER PLACE AND ROUTE						
10	External IOB	50	50	50	50	49
11	Number of Slices	24	24	25	21	25
POWER CONSUMPTION						
12	Power Consumption (mW)	141	141	141	141	63
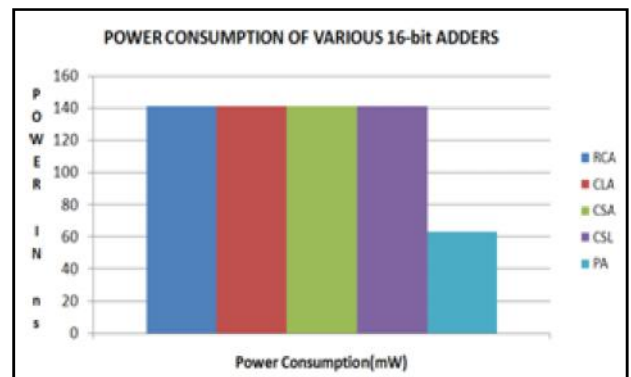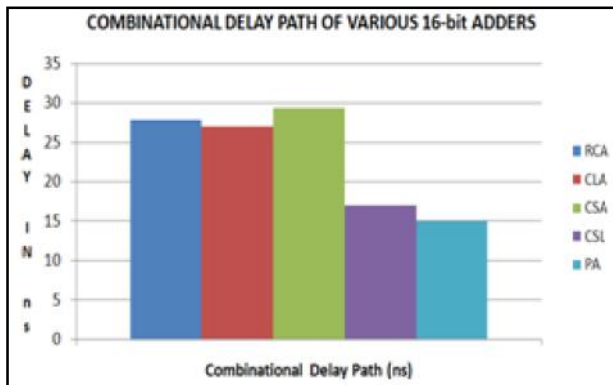
8. CONCLUSION

The Proposed adder is very faster when compared to other conventional adders. The proposed adder consumes low power when compared to other conventional adders. Hence a high speed low power adders is proposed. In this proposed adder a set of 20 bits will be evaluated in just 8 clock pulses.

REFERENCES

[1] Beaumont-Smith, N. Burgess, S.Lefrere, C.C.Lim, "Reduced latency IEEE floating-point standard adder architectures", Computer Arithmetic, 1999. Proceedings. 14th IEEE Symposium on ,14-16 April 1999.

[2] M.D. Ercegovac and T. Lang,"Digital Arithmetic", San Francisco: Morgan Daufmann, 2004.

[3] J.D. Bruguera and T. Lang, "Using the Reverse-carry Approach for Double Datapath Floating-point Addition", In Proceedings of the 15th IEEE Symposium on Computer Arithmetic, pp.203-10.

Optimization of Structural Parameters of Polyester Filament Plain Knitted Fabric for its Comfort Properties for Different Climates

P. Rahothami[1] and R.Varadaraju[2]

[1]Apparel Technology and Management, [2]Department of Fashion Technology,
Kumaraguru College of Technology, Coimbatore - Tamil Nadu
E-mail: rahoselvi@gmail.com

Abstract

The thermal and moisture comfort of a fabric depends on air permeability and vapor transport, sweat absorption and drying ability. Polyester knitted fabric is mostly used in sportswear. 15 samples of 100% polyester filament yarn is knitted in single jersey structure with variation in filament denier ,fabric loop length and yarn denier and tested for its water vapor permeability, air permeability, water absorbency and drying time . In this study analysis of variance is done for the moisture comfort properties. With the decrease in filament denier there is an increase in moisture absorbency rate, WVP, drying rate but there is a decrease in air permeability. With the decrease in loop length there is increase in WVP, absorbency rate and drying rate but there is a decrease in air permeability. With increase in yarn denier there is an increase in WVP, absorbency rate and drying rate but there is a decrease in air permeability. The regression equations were predicated for water vapor permeability, air permeability absorbency rate and drying rate. Optimization are made with these parameter using Box and Behnken design for three climates viz hot and Humid , Hot and Dry and Cold weather.

Keywords: Air permeability, Filament denier, Fabric loop length, Water vapor permeability, Water

absorbency, Yarn denier.

1. INTRODUCTION

Textiles worn in direct contact with the skin, especially with active wears, support the functions of the body. It should be comfortable to the wearer defined by fit, elasticity in movement, tailored shape and feel, better moisture absorbency and moisture regain, dimensionally stable. Comfort plays main role in various applications, particularly sportswear. It is expected from a garment to help to protect thermal balance of the body, and to maintain the body temperature and humidity. The heat and fluid transmitting properties of textiles, which are fundamental factors that affect clothing comfort. The thermal and moisture comfort of a fabric depends on several factor i.e. heat and vapor transport, sweat absorption and drying ability. Moisture comfort is measured with various aspects of water vapor resistance, wick ability – horizontal/vertical. Polyester is a man-made fiber which is hydrophobic in nature and it is widely used in sports apparel due to its high strength, elongation, abrasion and moisture Vapor permeability when compared to cotton. The main objective of this study is to study the moisture comfort properties of 100% polyester filament knitted fabric by making changes in the fabric structural factors filament denier, fabric loop length and yarn denier and optimization are made with this parameter using Box and Benkens design with 15 samples.

2. MATERIALS AND METHODS

Table 1 shows that the 15 samples of 100% polyester filament yarn is knitted in single jersey structure with the following variation in Filament denier ,Fabric loop length and Yarn denier in a Mesdan Lab knitting machine with 240 needles and 3.5 inch diameter.

2.1 TESTING OF FABRIC PROPERTIES
2.1.1 Water Vapour Permeability

Water Vapour Permeability was carried out by cup method. A Test specimen is sealed over the open mouth of a test dish which contains water. Following a period of time to establish equilibrium of the water vapour pressure gradient across the sample, successive readings of the assembled specimen is calculated. ASTM standard E96, BS 7209.

Table 1 Samples of Filament Denier, Fabric Loop Length and Yarn Denier

Sample No.	Yarn Denier	Loop Length	Filament Denier
1	155	2.7	4.5
2	155	3.1	4.5
3	155	3.5	4.5
4	155	2.7	3.2
5	155	3.1	3.2
6	155	3.5	3.2
7	155	2.7	1.4
8	155	3.1	1.4
9	155	3.5	1.4
10	155	3.8	1.4
11	155	2.7	2.1
12	155	2.7	0.5
13	80	2.3	1.4
14	100	2.5	1.4
15	235	3.8	1.4

2.1.2 Air Permeability

This method is based on the measuring of the rate of flow of air through a given area of fabric by a given pressure drop across the fabric. ASTM D737-96.

2.1.3 Water Absorbency

The rate of water absorbency in grams/minute is measured by allowing the water drop by drop from 10 mm height on a 10cm*10cm fabric sample

2.1.4 Drying Rate

The time required in minutes to completely dry the absorbed moisture/minute at skin Temperature of 33 deg C and 65% RH is recorded as drying time.

3. RESULT & DISCUSSION
3.1 Effect of Various Factors
3.1.1 Filament denier

Decrease in filament denier results in more surface area of the filament for the same Yarn denier. It also reduces the yarn diameter and bending rigidity. More surface area is the reason for increasing the WVP, absorbency and drying rate.

3.1.2 Yarn Denier

Decrease in yarn denier reduces the fabric thickness, loose structure, lesser GSM, lesser surface area lesser into yarn friction. All the above conditions are the reason for lower WVP, lower absorbency and higher air permeability with lesser yarn denier

3.1.3 Loop Length

Decrease loop length result in more tighter fabric, higher stitch density, higher GSM, higher thickness, lesser air space within the Fabric, higher inter yarn friction. Extreme tightness reduces absorbency due to higher inter yarn friction. Moderate tightness absorbs the water easily and holds it. Low loop length even though have access for water absorbency it doesn't hold the water.

3.2 Surface Plot

The surface plots on the effects various factors on the moisture comfort properties are given below:
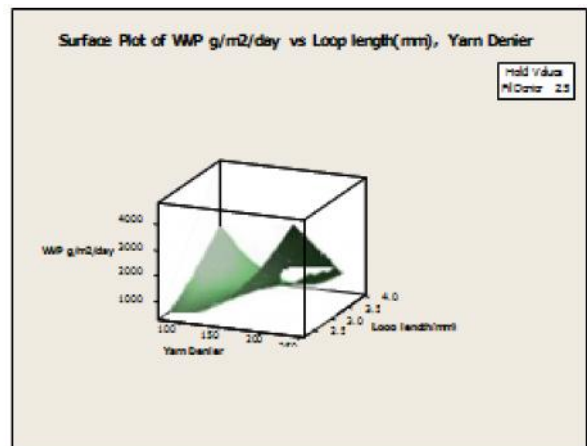

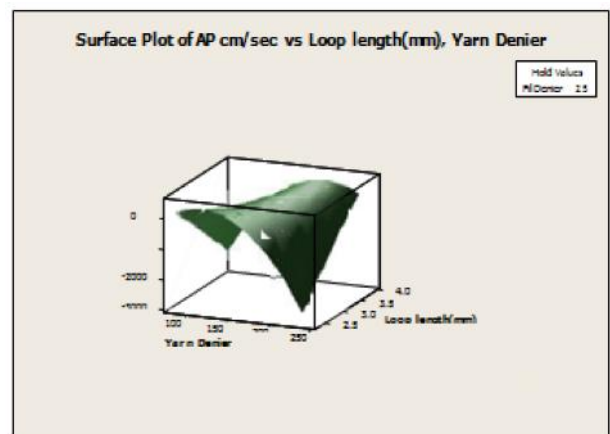Fig.1 Surface plot for water vapor permeability Vs Looplength, Yarn denier

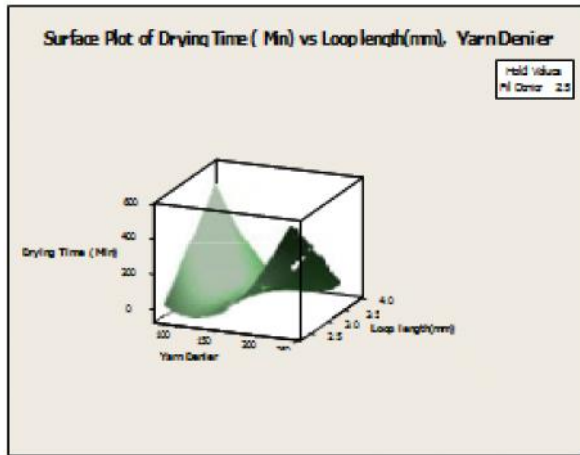Fig. 2 Surface plot for air permeability Vs Looplength, Yarn denier

Fig.3 Surface plot for drying time Vs Looplength, Yarn denier

Fig.4 Surface plot of water vapour permeability Vs Loop length, Fil denier
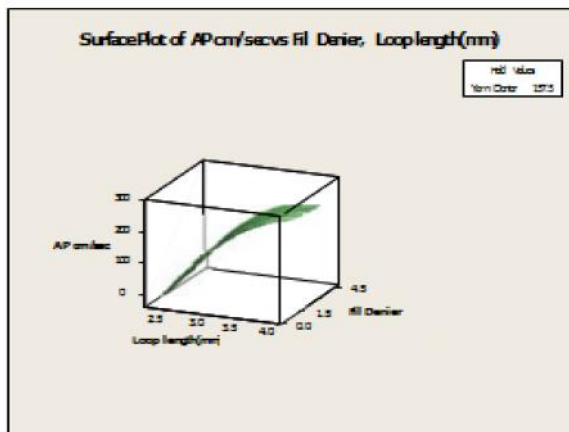
Fig.5 Surface plot of air permeability Vs Loop length, Filament denier

Fig. 6 Surface plot for drying time Vs Looplength, Filament denier

3.3 ANALYSIS OF VARIANCE OF DIFFERENT PROPERTIES

3.3.1 Water Vapour Permeability

WVP increases with increase in yarn denier (41%) decrease in loop length (39%) decrease in filament denier (20%). The increase in WVP is due to higher surface area of filaments with shorter loop length, higher yarn denier and lower filament denier.

3.3.2 Air Permeability

Air permeability with increase in loop length (81%) and increase in filament denier (19%). The air permeability increases due to the increase in () due to longer loop length and increase in filament denier.

3.3.3 Water Vapor Absorbency

The water vapor absorbency increases with increase in yarn denier (12%), decrease in filament denier (77%) increase in loop length (11%). This is due to the availability of more surface area and loose structure.

3.3.4 Drying Time

The drying time increases with increase in yarn denier (24%) and decrease in filament denier (41%) and increase in loop length (72%). This is due to availability of more surface area and loose structure.

P. Rahothami[1] and R. Varadaraju[2]

3.4 REGRESSION COEFFICIENTS FOR WVP, AIR PERMEABILITY, ABSORBENCY, DRYING TIME

Table 3 Regression Coefficients

Regression Coefficients	WVP	Air Permeability	Absorbency	Drying Time
Constant	-3480.74	4484.67	-156.00	-989.19
Yarn Denier(X_1)	18.72	-4.34	0.02	0.47
Loop length(mm)(X_2)	2140.00	-2725.01	102.86	658.05
Fil Denier(X_3)	-145.73	36.31	-0.10	-5.94
Yarn Denier*Yarn Denier	0.19	-0.20	0.01	0.04
Loop length(mm)*Loop length(mm)	126.96	-89.85	-0.05	-0.69
Fil Denier*Fil Denier	-9.14	2.58	-0.01	0.50
Yarn Denier*Loop length(mm)	-22.29	22.03	-0.66	-4.32
Loop length(mm)*Fil Denier	60.06	-16.01	0.00	0.92

3.5 Regression Equation

$Y = aX_1 + bX_2 + cX_3 + dX_1{}^2 + eX_2 + fX_3 + gX_1X_2 + hX_2X_3 +$ Constant.

3.6 Structural Factors for Optimum Moisture Comfort

The fabric must allow for high water vapor transmission and air permeability in order to reduce the thermal strain. To be effective under this condition, fabric must retain minimum amount of moisture this will facilitate moisture transfer by diffusion and forced convection. Higher water absorption rate makes the skin dry but slow rate of drying gives buffering effect.

3.6.1 Hot and dry climate (>35degC & <50% RH) Parameters

Global Solution

Yarn Denier	235.000
Loop length(	3.796
Fil Denier	4.500

Parameters	Goal	Lower	Target	Upper	Weight	Import
WVP g.m2/day	Target	600.0	1000.0	2000.0	1	1
AP cm/sec	Target	10.0	150.	250.	1	1
Absorbancy g	Target	0.5	1.2	1.5	1	1
Drying Time	Target	5.0	50.0	60.0	1	1

Predicted Responses

WVP g/m2/day = 1367.47	desirability = 0.63253
AP cm/sec = 154.21	desirability = 0.95791
Absorbancy g = 1.20	desirability = 1.00000
Drying Time = 47.84	desirability = 0.95206

Composite Desirability = 0.87150

Parameters

Parameters	Goal	Lower	Target	Upper	Weight	Import
WVP g.m2/day	Target	600.0	1000.0	2000.0	1	1
AP cm/sec	Target	10.0	150.	250.	1	1
Absorbancy g	Target	0.5	1.2	1.5	1	1
Drying Time	Target	5.0	10.0	60.0	1	1

Global Solution

Yarn Denier	155.489
Loop length(	3.032
Fil Denier	1.643

Composite Desirability = 0.78501

3.6.3 Cold climate

Insulation of clothing is the main factor in cold weather. The effective fabric must have good WVP to

Parameters

Parameters	Goal	Lower	Target	Upper	Weight	Import
WVP g.m2/day	Target	600.0	1200.0	2000.0	1	1
AP cm/sec	Target	10.0	15	250.0	1	1
Absorbancy g	Target	0.5	1	1.5	1	1
Drying Time	Target	5.0	10	60.0	1	1

Global Solution

Yarn Denier	159.519
Loop length(	3.077
Fil Denier	3.198

Composite Desirability = 0.61455

3.6.2 Hot and humid climate (>35Deg C & >75% RH)

To be effective under this condition the fabric must have higher water vapor transmission, air permeability, moisture absorbency and quicker drying time.

Predicted Responses

WVP g/m2/day =1081.21	desirability=0.91879
AP cm/sec = 16.10	desirability= 0.87903
Absorbancy g = 1.20	desirability= 1.00000
Drying Time = 36.49	desirability= 0.47019

transmit insensible perspiration, lower air permeability to reduce heat loss from the body.

Predicted Responses

WVP g/m2/day =1080.20	desirability= 0.80034
AP cm/sec = 163.75	desirability= 0.36701
Absorbancy g = 1.00	desirability= 1.00000
Drying Time = 35.72	desirability= 0.48559

P. Rahothami[1] and R.Varadaraju[2]

4. CONCLUSION

With the decrease in filament denier there is an increase in moisture absorbency rate, WVP, drying rate but there is a decrease in air permeability. With the decrease in loop length there is increase in WVP, absorbency rate and drying rate but there is a decrease in air permeability. With increase in yarn denier there is an increase in WVP, absorbency rate and drying rate but there is a decrease in air permeability. The regression equations were predicated for water vapor permeability, air permeability absorbency rate and drying rate. The structural factors for moisture comfort is optimized for single jersey knitted fabrics from polyester filament are given below.

Climate	Yarn Denier	Filament	Loop Length	Desirability
Hot and Dry	235	4.5	3.8	87%
Hot and Humid	155	1.6	3.0	78%
Cold Weather	159	3.0	3.2	61%

REFERENCES

[1] George Havenith, Ivana Salopek Cubric and Zenum Skenderi, "Impact of Impact of Raw Material, Yarn and Fabric Parameter, and Finishing on Water Vapour Resistance", Textile Research Journal, february 2013.

[2] Ayse Okur and Sibel Kaplan. "Thermal Comfort Performance of Sports Garments with Subjective and Objective Measurement
", Indian Journal of Fibre & Textile Research, Vol. 37, March 2012, pp. 46-56.

[3] Yoon and Buckly, "The Parameters Affecting Air Permeability in Knits", Textile Research Journal, Vol 54, 1984, pp.289-298.

[4] Bongdan wi cek, Bozena wilbik-halgas, Krzyszt and Remigiusz danych, "Air and Water Vapour Permeability in Double-Layered Knitted Fabrics with Different Raw Materials" , Fibres & Textiles in Eastern Europe July/ September 2006, Vol. 14, No.3, pp.57.

[5] Nilgun Ozdil, "A Study on the Moisture Transport Properties of the Cotton Knitted Fabrics In Single Jersey Structure", Tekstil Ve Konfeksiyon 3/2009.

[6] W.H Rees., "The Relationship of Air Permeability of Knitted Fabrics", TEX.MON1969, pp.59-61.

[7] Ni Wang, Anxia Zha, and Jinxiu Wang, "Study on the Wicking Property of Polyester Filament Yarns", Fibers and Polymers Vol.9, No.1, 2008, pp.97-100.

[8] Apurba Das, Brojeswari Das, Mario D. Araujo, Raul Fanguiero, Vijay Kothari, "Moisture Flow through Blended Fabrics – Effect of Hydrophilicity", Journal of Engineered Fibers and Fabrics, Vol.4, No.4, 2009, Fiber and Textile Research in India.

Optimisation of Process Parameters for Bio- Retting of Nettle Fibre Using Box-Behnken Statistical Design

A. Preethi[1] and R. Shanthi[2]

[1]PG Scholar, Apparel Technology and Management, [2]Associate Professor,
Department of Fashion Technology, Kumaraguru College of Technology, Coimbatore - 641 409, Tamil Nadu
E-mail: iipreti63@gmail.com,shanradkri@gmail.com

Abstract

With increase in living standards of the population and the concept of consumption, the development of fibers and fabrics focusing on green and environmental protection for apparel will be based on natural fabrics. Since the 21st century, the "green" consumption of the world has risen rapidly, and green fiber and eco-textiles has become the developing trend of the textile industry. The new trend for nettle fibre has been driven by concern over the environmental damage caused by the production of natural and synthetic fibres. Retting is the main challenge faced during the processing of nettle plants for the production of long fibres.The traditional methods for separating the long fibres are by dew and water retting. Both methods require 14 to 28 days to degrade pectin materials, hemicellulose and lignin. Even though the fibres produced from water retting can be of high quality, the long duration and polluted water have made this method less attractive. The alternative method is bio-retting where enzyme is used for removing the fibre from the stem of the plant. The enzymatic retting process has apparent advantages over the other retting processes by having significantly shorter time and good quality of the fibre. For bio- retting process of the nettle fibre the process parameters have to be optimized in order to improve the efficiency of the fibre to be removed from its bark.

Keywords: Bio-retting, Enzyme, Box - Behnken analysis, Nettle

1. INTRODUCTION

Nettle occurs as a perennial plant in Europe and in the temperate zones of Asia and America. It is a dioecious plant growing 30-150cm tall. The plant has simple, opposite, sharply toothed leaves (5-10cm long) with persistent stipules and stinging trichomes. The hairs covering the stems and leaves are filled with fluid and break off when touched, leaving a sharp point like a small hypodermic needle that allows the fluid to enter the skin and cause blistering. The unpleasant compounds are thought to be a histamine and acetyl-choline. The nettle plant contains high quality fibre, with properties similar to flax and hemp, consisting up to 17% by weight of the plant. The fibre has remarkable high tensile strength, fineness, low specific weight and average length of 4m, this allows production of fine fabrics and technical applications. Fibre from the nettle plants has a cellulose content of 86.5%. High cellulose content of the crop may also be utilised in industrial applications.

2. OBJECTIVE

To optimize the process parameter for bio-retting of nettle fibre using Box- Behnken statistical design.

3. MATERIALS

The nettle stems were sourced from North India. The outer region of the stem of the nettle plant is the source of the nettle fibre.The fibre from these raw materials have to be extracted using either mechanical or enzymatic process. Enzymatic retting was chosen as the process for extraction of fibre and pectinase enzyme was used for the bio-retting process. To optimize the process for bulk treatment of the fibre the variables taken are enzyme concentration, pH and temperature.

3.1 Material Particulars

Table 1 Material Particulars(Raw Fibre)

PROPERTIES		PARTICULARS
FIBER	Fiber diameter	$3\mu m$
	Fiber length	30mm
	Flexural Rigidity	$1.39mg.Cm^2$
	Strength	4.29gf/tex
	Elongation	2.2mm

A. Preethi[1] and R. Shanthi[2]

4. PROCESS PARAMETERS
4.1 Design of Experiment

Box-Behnken design is amethod for developing a mathematical model used to find combinations of factors that yieldoptimalbusinessperformance. Box-Behnken design is a type of response surface method, which providesdetailedinformation about the solution space, allowing researchers to better understand the forces affecting the output of the model. The advantages of Box-Behnken Design include the fact that they are all spherical designs which require factors to be run at only three levels. Box- behnken analysis is an effective statistical method based on a multivariate non-linear model, and has been widely used for optimizing complex process variables (Liu 2012).The software MINITAB 17 was used for the statistical analysis of the optimization process This method was adopted to formulate the experimental design, with three variables in three levels to give fifteen different combinations of processing treatments as given in Table 2 and Table 3.

Table 2 Process Parameters

LEVEL	Enzyme Concentration (On weight of material) X_1	pH X_2	Temperature (°C) X_3
-1	0.5 %	4.5	50
0	1%	5	55
+1	1.5%	5.5	60

Table 3 Details of Experiment According to Box Behnken Design of Experiment

RUN	Coded Levels of Process Parameters			Experimental Process Paramete		
	X_1	X_2	X_3	X_1	X	X_3
1	+1	0	-1	1.5	5	50
2	0	0	0	1	5	55
3	0	0	0	1	5	55
4	-1	-1	0	0.5	4.	55
5	-1	0	+1	0.5	5	60
6	0	+1	+1	1	5.	60
7	0	+1	-1	1	5.5	50
8	-1	0	-1	0.5	5	50
9	0	0	0	1	5	55
10	+1	+1	0	1.5	5.	55
11	0	-1	-1	1	4.	50
12	+1	0	+1	1.5	5	60
13	-1	+1	0	0.5	5.	55
14	0	-1	+1	1	4.	60
15	+1	-1	0	1.5	4.	55

Pectinase enzyme is used for the bio-retting process of the fibre.Pectinasesare a heterogeneous group of related enzymes that hydrolyze the pectic substances, present mostly in plants. Pectinase has a quite specific three-dimensional structure and is adsorbed onto the pectin substrate in lock and key function. At the interface between the pectinase/pectin associated complex, hydrolysis of the pectin is very strongly accelerated. The hydrolysis produces products that diffuse away from the primary wall matrix, loosing the matrix structure and releasing the enzyme to become very rapidly attached to another area of the pectin substrate.They are of prime importance for plants as they help in cell wall extension and softening of some plant tissues during maturation and storage. They also aid in maintaining ecological balance by causing decomposition and recycling of waste plant materials.Gyro washing machine was used for the processing of the fibre.The ingredients were added with

the water inside the machine and was worked for 15 minutes. After the intial run the fibrewas added along with the other ingredients. The machine was run for 45 minutes with different parameters mentioned above. After the process, the fibrewas washed with hot water at 70°C in order to deactivate the enzyme. This process is followed by cold rinse of the fibre at room temperature.

4.2 Statistical Analysis

The optimization based on theanalysis of the relationship of each response with the three independent variables is given in the equation 1.

$$Y= B+(B_1*X_1)+(B_2*X_2)+(B_3*X_3)+(B_{12}*X_1*X_2)+(B*X1*X3)+(B_{23}*X_2*X_3)+(B_{11}*X1*X1)+B_{22}*X2*X2)+(B_{33}*X3*X3) \quad \text{_____} \quad Eq.1$$

y= predicted response, B= model constant.
B1=slope or linear effect of the input factor *X1*, *B2*= quadratic effect of input factor *X2,*
B3= quadratic effect of input factor *X3,*

B12= linear interaction effect between the input factor *Xi* and *Xj*.

Accordingly *Xj*and *Xij*represent the coded independent variables, respectively.

5. RESULTS AND DISSCUSSION

The strength and flexural rigidity values were taken as the response for the different combinations (y). Enzyme concentration was taken as X1, pH as X2and temperature was X3.The constants B1,B2,B3, B12 etc were taken from the multiple regression equation as mentioned above.

4.3 Strength

Strength is the maximum stress that a fibre can withstand while being stretched or pulled before failing or breaking. The strength of the fibre is measured using INSTRON.\

4.4 Flexural Rigidity

The flexural rigidity of coarse monofilaments may be measured by deformation of loops under an applied load.the flexural rigidity is given by the formula

Flexural rigidity(mg.cm²)= KWL² (cos Ø/tanØ) Where,
K = applied load in grams
L = circumferential length of the ring in cms
Ø = 493d/L
d = deflection of lower end of the ring under action of applied load
W is chosen such that Ø lies between 40° and 50°. W is in gms.

Table 4 Observed Values of Strength and Flexural Rigidity of the Fibre

Runs	X1	X2	X3	Strength	Flexural Rigidity
1	1.5	5	50	2.934	1.109
2	1	5	55	2.390	1.081
3	1	5	55	2.323	1.085
4	0.5	4.5	55	2.325	1.051
5	0.5	5	60	2.892	1.162
6	1	5.5	60	2.625	1.262
7	1	5.5.	50	2.243	1.220
8	0.5	5	50	2.532	1.281
9	1	5	55	2.395	1.082
10	1.5	5.5	55	2.736	1.062
11	1	4.5	50	2.592	1.236
12	**1.5**	**5**	**60**	**3.005**	**1.156**
13	0.5	5.5	55	2.432	1.186
14	1	4.5	60	2.432	1.186
15	1.5	4.5	55	2.784	1.086

A. Preethi[1] and R. Shanthi[2]

5.1 Response Surface Regression: Strength Versus Enzyme Concentration, pH, Temperature

$$Y=B+(B_1*X_1)+(B_2*X_2)+(B_3*X_3)+(B_{12}*X_1*X_2)+$$

$$(B_{13}*X_1*X_3)+(B_{23}*X_2*X_3)+(B_{11}*X_1*X_1)+$$

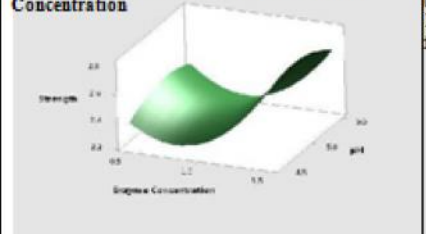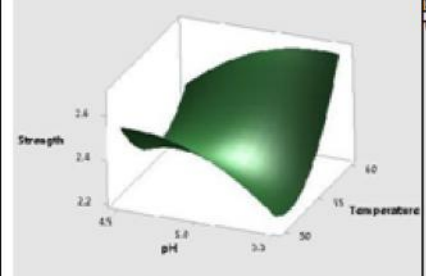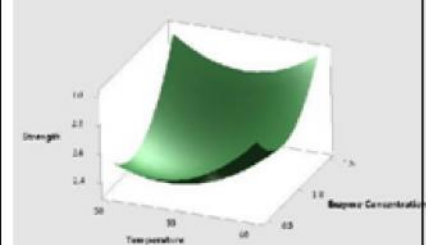$$(B_{22}*X_2*X_2)+(B_{33}*X_3*X_3)$$

$$Strength=2.363+(0.1598X_1)+(-0.0121X_2)+(0.0816X_3)+$$
$$(-0.0387X_1X_2)+(-0.0723X_1X_3)$$
$$+(0.1355X_2X_3)+(0.2838X_1X_1)+$$
$$(-0.0839X_2X_2)+(0.1876X_3X_3)$$

The coefficient values were substituted for all the constants in the multiple regression equation as per the results obtained in the minitab analysis. The r^2 value was found to be 97.34% and the F-value was 20.31 showing that the the results of the optimization process was significant at 1% level .the analysis of variance results are given in table 5. The surface plots showing the effect of pH, enzyme concentration and temperature on strength are given in table 6.

Table 5 Analysis of Variance

Source	DF	Adj SS	Adj MS	F-Value	P-Value
Model	9	0.810087	0.090010	20.31	0.002
Linear	3	0.258638	0.086213	19.45	0.003
Square	3	0.451122	0.150374	33.93	0.001
2-Way	3	0.100328	0.033443	7.55	0.026
Error	5	0.022159	0.004432		

Table 6 Surface Plot of Strength vs Enzyme Concentration, pH, Temperature

Sl.No.	Surface Plot	Analysis
1	Surface Plot of Strength vs pH, Enzyme Concentration	The surface plot highlights that the strength is the highest value at 1.5% enzyme concentration; the strength was found to be highest in value at pH 5.
2	Surface Plot of Strength vs Temperature, pH	At pH 5 the strength is found to be high when compared to the values at 4.5 and 5.5 pH. At 60°C the strength is high when compared to the other two values.
3	Surface Plot of Strength vs Enzyme Concentration, Temperature	The strength values were highest at 1.5% enzyme concentration and temperature at 60°C showing that the above parameters gave good results.

5.2 Response Surface Regression: Flexural Rigidity Versus Enzyme Concentration, pH, Temperature

$Y=B+(B_1*X_1)+(B_2*X_2)+(B_3*X_3)+(B_{12}*X_1*X_2)+(B_{13}*X_1*X_3)+(B_{23}*X_2*X_3)+(B_11*X1*X1)+(B_{22}*X2*X2)+(B_{33}*X3*X3)$
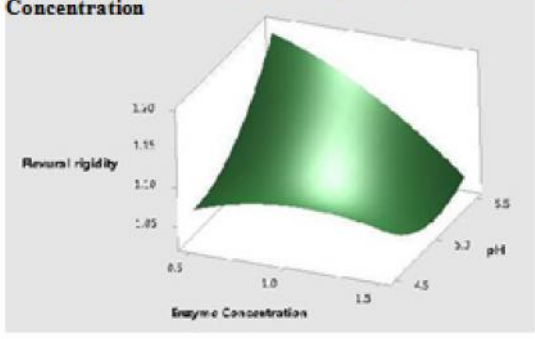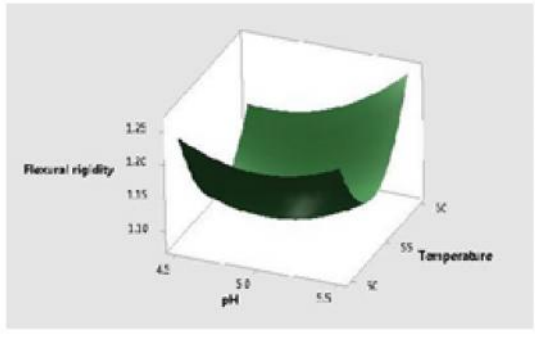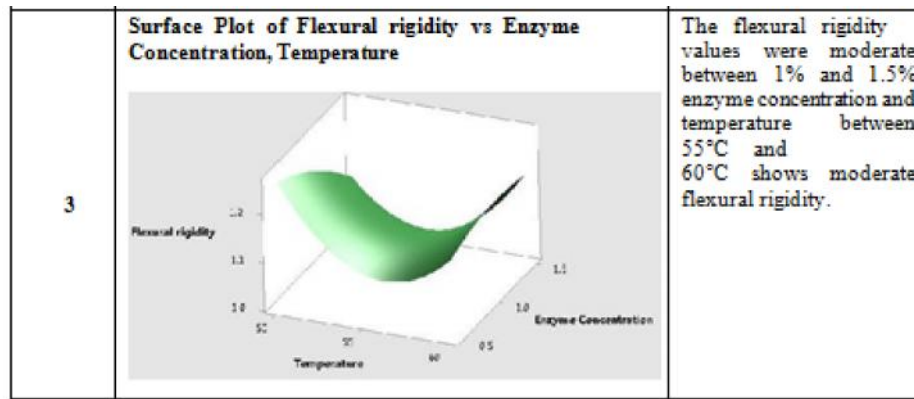
Flexural Rigidity$=1.0827+(-0.0337X_1)+(0.02138X_2)+(-0.01000X_3)+(-0.3975X_1X_2)$
$+(0.04150X_1X_3)+(0.02300X_2X_3)+(-0.01771X1X1)+(0.03129X2X2)+(0.11204X3X3)$

The coefficient values were substituted for all the constants in the multiple regression equation as per the results obtained in the minitab analysis. The r^2 value was found to be 97.75% and the F-value was 24.17 showing that the results of the optimization process was significant at 1% level . The analysis of variance results are given in table 7 . The surface plots showing the effect of pH, enzyme concentration and temperature on strength are given in table 8.

Table 7 Analysis of Variance

Source	DF	Adj SS	Adj MS	F-Value	P-Value
Model	9	0.079867	0.008874	24.17	0.001
Linear	3	0.013366	0.004455	12.13	0.010
Square	3	0.051176	0.017059	46.46	0.000
2-Way Interaction	3	0.015325	0.005108	13.91	0.007
Error	5	0.001836	0.000367	-	-
Lack-of-Fit	3	0.001827	0.000609	140.56	0.007
Pure Error	2	0.000009	0.000004	-	-
Total	14	0.081703	-	-	-

Table 8 Surface Flexural Rigidity vs Enzyme concentration, pH, Temperature

Sl. No.	Surface Plot	Analysis
1	**Surface Plot of Flexural rigidity vs pH, Enzyme Concentration**	The surface plot highlights that the flexural rigidity is the lowest value at 1.5% enzyme concentration; the flexural rigidity was found to be lowest at 5pH.
2	**Surface Plot of Flexural rigidity vs Temperature, pH**	At pH 5 the flexural Rigidity is found to be lowest when compared to the values. At 55°C the flexural rigidity is low when compared to the other two values.

A. Preethi[1] and R. Shanthi[2]

| 3 | Surface Plot of Flexural rigidity vs Enzyme Concentration, Temperature

 | The flexural rigidity values were moderate between 1% and 1.5% enzyme concentration and temperature between 55°C and 60°C shows moderate flexural rigidity. |

5. CONCLUSION

The retting process of the nettle fibre is made easy with the help of the enzymatic treatment. The optimized processing parameters for bio-retting of the nettle fibre is enzyme concentration- 1.5, pH-5 and temperature- 60°C. Box - Behnken model has been used to prove that the optimized process parameters were statistically significant at 1% level. The enzymatic process ps to remove fibre from the pith of the plant easily during the retting process. The bio-retting process help to save the processing time and it is also free from chemicals.

REFERENCES

[1] Ranjith Kumar Bakku , RamanaTerli , Subba Rao Somalanka and Mary AnupamaPalukurty, "Optimization of Borassusflabellifer Amylase Extraction Procedure Using Box-Behnken Design and Development of Simple Affinity Chromatographic Technique for Purification of Amylases", British Biotechnology Journal, Vol.2, No.3, 2012, pp.146-156.

[2] G. Liu, H. Guo and Y.Sun, "Optimization of the Extraction of Anthocyanins from the Fruit Skin of Rhodomyrtustomentosa (Ait.) Hassk and Identification of Anthocyanins in the Extract Using High-Performance Liquid Chromatography-Electrospray Ionization-Mass Spectrometry (HPLC-ESI-MS)", International Journal of Molecular Sciences, 2012, pp. 6292-6302.

Automatic 2D to 3D Image and Video Conversion

M. Sreemaa[1], E. Vishnukandhi[2] and J.Karthikeyan[3]

Department of Computer Science Engineering, Surya Groups of Institutions-School of Engg. & Tech. Villupuram -

Abstract

Among 2D-to-3D image conversion methods, those involving human operators have been most successful but also time-consuming and costly. Automatic methods, that typically make use of a deterministic 3D scene model, have not yet achieved the same level of quality as they often rely on assumptions that are easily violated in practice. In this paper, we adopt the radically different approach of "learning" the 3D scene structure. We develop a simplified and computationally-efficient version of our recent 2D-to-3D image conversion algorithm. Given a repository of 3D images, either as stereopairs or image+depth pairs, we find k pairs whose photometric content most closely matches that of a 2D query to be converted. Then, we fuse the k corresponding depth fields and align the fused depth with the 2D query. Unlike in our original work, we validate the simplified algorithm quantitatively on a Kinect-captured image+ depth dataset against the Make3D algorithm. While far from perfect, the presented results demonstrate that online repositories of 3D content can be used for effective 2Dto-3D image conversion.

1. INTRODUCTION

The availability of 3D-capable hardware today, such asTVs, Blu-Ray players, gaming consoles, and smartphones,is not yet matched by 3D content production. Althoughconstantly growing in numbers, 3D movies are still anexception rather than a rule, and 3D broadcasting (mostlysports) is still minuscule compared to 2D broadcasting. Thegap between 3D hardware and 3D content availability islikely to close in the future, but today there exists an urgentneed to convert the existing 2D content to 3D.A typical 2D-to-3D conversion process consists of twosteps: depth estimation for a given 2D image and depthbasedrendering of a new image in order to form astereopair. While the rendering step is well understoodand algorithms exist that produce good quality images,the challenge is in estimating depth from a single image(video). Therefore, throughout this paper the focus is ondepth recovery and not on depth-based rendering, althoughwe will briefly discuss our approach to this problem later.There are two basic approaches to 2D-to-3D conversion:one that requires a human operator's intervention and onethat does not. In the former case, the so-called semiautomaticmethods have been proposed where a skilledoperator assigns depth to various parts of an image orvideo. Based on this sparse depth assignment, a computeralgorithm estimates dense depth over the entire image orvideo sequence. The involvement of a human operator mayvary from just a few scribbles to assign depth to variouslocations in an image to a precise delineation of objectsand subsequent depth assignment to the delineated regions.In the case of

automatic methods, no operator interventionis needed and a computer algorithm automaticallyestimates the depth for a single image (or video). Tothis effect, methods have been developed that estimateshape from shading, structure from motion or depth fromdefocus. Although such methods have been shown to workin some restricted scenarios they do not work well forarbitrary scenes. In an attempt to equip 3D TVs, Blu-Rayplayers and gaming consoles with real-time automatic 2Dto-3D conversion, consumer electronicsmanufacturers havedeveloped simpler techniques that rely on various heuristicassumptions but such methods fail on more challengingscenes. Recently, machine-learning-inspired methods havebeen proposed to automatically estimate the depth mapof a single monocular image by applying image parsing.Although restricted to architectural scenes, these methodsopened a new direction for 2D-to-3D conversion. We willreview both semi-automatic and automatic methods inSection II in detail.The methods we propose in this paper, carry the "bigdata" philosophy of machine learning. In consequence, theyapply to arbitrary scenes and require no manual annotation.Our data-driven approach to 2D-to-3D conversion has beeninspired by the recent trend to use large image databases forvarious computer vision tasks, such as object recognition and image saliency detection . In particular, wepropose a new class of methods that are based on theradically different approach of learning the 2D-to-3D conversion from examples. We develop two types of methods.The first one is based on learning a point mapping fromlocal image/video attributes, such as color, spatial position,and motion at each pixel, to scene-depth

M. Sreemaa[1], E. Vishnukandhi[2] and J.Karthikeyan[3]

at that pixel usinga regression type idea. The second one is based on globallyestimating the entire depth map of a query image directlyfrom a repository of 3D images (image+depth pairs orstereopairs) using a nearest-neighbor regression type idea.Early versions of our learning-based approach to 2D-to-3Dimage conversion, either suffered from high computationalcomplexity or were tested on only a single dataset. Here, we introduce the local method and evaluate thequalitative performance and the computational efficiencyof both the local and global methods against those of theMake3D algorithm and a recent method proposed byKarschet al. We demonstrate the improved quality ofthe depth maps produced by our global method relativeto state-of-the-art methods together with up to 4 ordersof magnitude reduction in computational effort. We alsodiscuss weaknesses of both proposed methods.The paper is organized as follows. In Section II, wereview the state of the art in 2D-to-3D image conversion.In Section III, we describe the conversion based on localpoint transformation and in Section IV we provide detailsof the global approach to the conversion. In Section V, weshow numerous experimental results.

2. STATE OF THE ART

Semi-automatic methods Generating depth maps in a segmentation-based framework is an intuitiveprocess. Rather than just considering each label as a separateobject, we now consider each label as a separate depth, and can ultimatelybe seen as a case of multi-label segmentation. The usermerely has to mark each object and specify their relative depths.This is sufficient, as noted in , the exact depth values do not haveto be known. Our proposed method is a two stage process using thesmoothing properties of Random Walks , and the hard segmentationreturned by Graph Cuts . Like , Random Walks is the solution to a linear system and has problems preserving strong edges,but Graph Cuts does this quite well. However, the hard segmentationwith Graph Cuts does not respect smooth gradients or fine detail. Bycombining the two, we can retain strong object boundaries while alsoallowing for smooth gradients.

2.1 Final Depth Map Generation with Depth Prior

To incorporate the two together, ideally, the merging should use theedge-preserving properties of the depth prior to provide strong objectboundaries while still preserving the fine detail inside of the objects.Furthermore, Random Walks should provide a

smoothing action inareas where the hard edges of Graph Cuts are not appropriate, suchas an area of gradually increasing distance like the groundto the user-provided normalized depth values. We can do this sincewe assume that a finite number of user labels, and initial labelling isstored inside an 8-bit image. After the depth prior is obtained, weuse T[k] to convert the depth prior to match the normalized initialuser-provided depth values.To finally incorporate the aforementioned information into theRandom Walks algorithm, we append this information into the edgeweights. In the original SSRW framework, the edge weights werecalculated using Eq. 2 in the same color space, and with the sameparameters, with the exception of = 1.

2.2 Automatic Method

The problem of depth estimation from a single 2D image,which is the main step in 2D-to-3D conversion, can beformulated in various ways, for example as a shape-fromshadingproblem. However, this problem is severelyunder-constrained; quality depth estimates can be foundonly for special cases. Other methods, often called multiviewstereo, attempt to recover depth by estimating scenegeometry from multiple images not taken simultaneously.For example, a moving camera permits structure-frommotionestimation while a fixed camera with varyingfocal length permits depth-from-defocus estimation .Both are examples of the use of multiple images of thesame scene captured at different times or under differentexposure conditions Several electronics manufacturers have developed realtime2D-to-3D converters that rely on stronger assumptionsand simpler processing than the methods discussed above,e.g., faster-moving or larger objects are assumed to becloser to the viewer, higher frequency of texture is assumedto belong to objects located further away, etc. Althoughsuch methods may work well in specific scenarios . In our first attempt,we developed a method that fuses SIFT-aligned depth mapsselected from a large 3D database, however this approachproved to be computationally demanding . Subsequently,we skipped the costly SIFT-based depth alignment and useda different metric (based on histogram of gradients) forselecting most similar depth fields from a database.
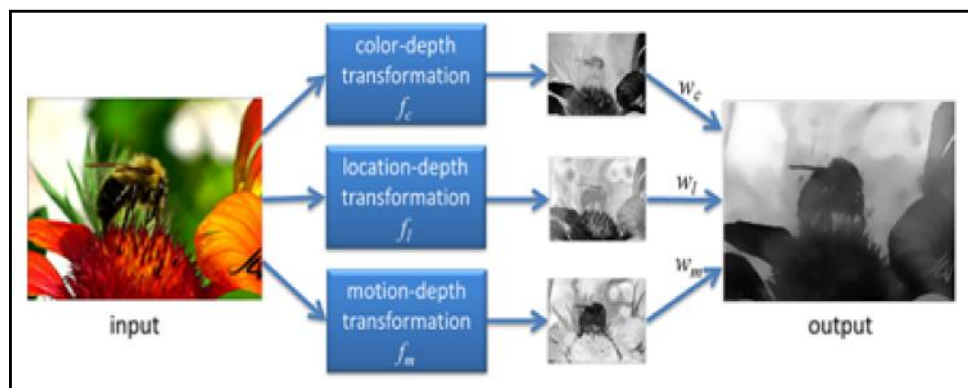
3. 2D-TO-3D CONVERSION BY LEARNING A LOCALPOINT TRANSFORMATION

The first class of conversion methods we are presentingis based on learning a point transformation that

relates locallow-level image or video attributes at a pixel to scene-depthat that pixel. Once the point transformation is learned, it isapplied to a monocular image, i.e., depth is assigned to apixel based on its attributes. This is in contrast to methodsdescribed in Section IV where the entire depth map of aquery is estimated directly from a repository of 3D images(image+depth pairs or stereopairs) using a nearest-neighborregression type idea.A pivotal element in this approach is a point transformationused to compute depth from image attributes. Thistransformation can be estimated either by training on aground-truth dataset, the approach we take in this paper, ordefined heuristically. Let I = {(~I1, d1), (~I2, d2), ..., (~IK, dK)}denote a training dataset composed of K pairs (~Ik, dk),where ~Ikis a color image (usually in YUV format) anddkis the corresponding depth field. We assume that allimages and depth fields have the same spatial dimensions.Such a dataset can be constructed in various waysWe now discuss how the individual color-depth, locationdepth,and motion-depth

transformations as well as theweights are learned.Fig. 1 shows a sample video frame with depth mapsestimated from color, location and motion cues separately,as well as the final combined depth map. In order to obtaina color-depth transformation fc, we first transform the YUVspace, commonly used in compressed images and videos,to the $HS\,V$ color space. We found out that the saturationcomponent (S) provides little depth discrimination capacityand therefore we limit the transformation attributes to hue(H) and value (V). Let [$Hk[\mathbf{x}]$, $S\,k[\mathbf{x}]$, $Vk[\mathbf{x}]$]Tbe the $HS\,V$components of a pixel at spatial location $\mathbf{x}$ quantized to$L$ levels. The depth mapping $fc[h, v]$, h, $v = 1$, ..., L iscomputed as the average of depths at all pixels in I withhue h and value v:$fc[h, \ v] \ = \ \mathrm{P}Kk{=}1 \ \mathrm{P}\mathbf{x}1(Hk[\mathbf{x}] \ = \ h, \ Vk[\mathbf{x}] \ = \ v)dk[\mathbf{x}]\mathrm{P}Kk{=}1 \ \mathrm{P}\mathbf{x}1(Hk[\mathbf{x}] \ = \ h, \ Vk[\mathbf{x}] \ = \ v)$ (1)
The location-depth transformation $fl$is simply the averagedepth computed from all depth maps in Iat the same location:

$fl[\mathbf{x}] \ =1KK \ \mathrm{X}k{=}1dk[\mathbf{x}]$. (2)

4. 2D-TO-3D CONVERSION BASED ON GLOBALNEAREST-NEIGHBOR DEPTH LEARNING

While 2D-to-3D conversion based on learning a localpoint transformation has the undisputed advantage of computationalefficiency – the point transformation can belearned off-line and applied basically in real time – thesame transformation is applied to images with potentiallydifferent global 3D scene structure. This is because this typeof conversion, although learning-based, is based on purelylocal image/video attributes, such as color, spatial position,and motion at each pixel. To address this limitation, inthis section we develop a second method that estimates theglobal depth map of a query image or video frame directlyfrom a repository of 3D images (image+depth pairs orstereopairs) using a nearest-neighbor regression type idea.

1) **search for representative depth fields**: find k 3Dimages in the repository Ithat have most similar depthto the query image, for example by performing a $k$nearest-neighbor (kNN) search using a metric basedon photometric properties,

2) **depth fusion**: combine the k representative depth fields, for example, by means of median filteringacross depth fields

3. **cross-bilateral depth filtering**: smoothing of themedian-fused depth field to remove spurious variations,while preserving depth discontinuities,

4. **stereo rendering**: generation of the right image ofthe stereopair using the 2D query (left) image andsmoothed median depth field followed by suitable processingof occlusions and newly-exposed area.

M. Sreemaa[1], E. Vishnukandhi[2] and J.Karthikeyan[3]

2.1. kNN Search

There exist two types of images in a large 3D imagerepository: those that are relevant for determining depth ina 2D query image, and those that are irrelevant. Imagesthat are not photometrically similar to the 2D query need tobe rejected because they are not useful for estimating depth(as per our assumption). Note that although we might misssome depth-relevant images, we are effectively limiting thenumber of irrelevant images that could potentially be moreharmful to the 2D-to-3D conversion process. The selectionof a smaller subset of images provides the added practicalbenefit of computational tractability when the size of thedictionary is very large.Our 2D query image Q is the left image from a stereopairwhose right image QR is unknown. We assume that adatabase of 3D images or videos I, such as the NYU depthdatabase or YouTube 3D, is available, and thatfor eachRGB image Ii in the database the corresponding depth field

2.2. Depth Fusion

In general, none of the NN image+depth pairs(Ii, di), i " K match a query Q accurately (Figure 2). However,the location of some objects (e.g., furniture) and partsof the background (e.g., walls) is quite consistent with thosein the query. If a similar object (e.g., table) appears at a similarlocation in several kNN images, it is likely that such anobject also appears in the query and the depth field beingsought should reflect this. We compute this depth field byapplying the median operator across the kNN depths at eachspatial location $\mathbf{x}$ as follows:
d[$\mathbf{x}$] = median{di[$\mathbf{x}$], "i " K}.(1) Fig. 4 shows search results for two outdoor query imagesperformed on the Make3D dataset #1. Although none of the four kNNs perfectly matches the corresponding 2D query,the general underlying depth is somewhat related to that expected in the query. In Fig. 5 we show search results for two indoor query images (office and dining room)performed on the NYU Kinect dataset. While some of the retained images share local 3D structures with the query image, e.g., a large table in the dining room, other images do not.

2.3 Cross-bilateral Depth Filtering

While the median-based fusion helps make depth moreconsistent globally, the fused depth is overly smooth and locally inconsistent with the query image due to:
1. misalignment of edges between the fused depth field and query image

2. lack of fused depth edges where sharp object boundaries occur
3. lack of fused depth smoothness where smooth depthchanges are expected.

2.4 Stereo Rendering

In order to generate an estimate of the right imagebQRfrom the monocular query Q, we need to computea disparity δ from the estimated depth bd. Assuming thatthe fictitious image pair (Q, bQR) was captured by parallelcameras with baseline B and focal length f , the disparity issimply δ[x, y] = Bf /bd[$\mathbf{x}$], where $\mathbf{x}$ = [x, y]T . We forwardprojectthe 2D query Q to produce the right image:bQR[x + δ[x, y], y] = Q[x, y] (5)while rounding the location coordinates (x + δ[x, y], y) tothe nearest sampling grid point. We handle occlusions bydepth ordering: if (xi + δ[xi, yi], yi) = (xj+ δ[xj, yi], yi) forsome i, j, we assign to the location (xi + δ[xi, yi], yi) inbQRan RGB value from that location (xi, yi) in Q whosedisparity δ[xi, yi] is the largest. In newly-exposed areas, i.e.,forxjsuch that no xi satisfies (xj, yi) = (xi + δ[xi, yi], yi).

5. EXPERIMENTAL RESULTS

We have tested our approach on two datasets: theMake3D dataset #1 composed of 534 outdoor images with depth fields captured by a laser rangefinder and the NYU Kinectdataset composed of1449 pairs of RGB images and corresponding depth fields.Note that the Make3D images are of 240×320 resolutionbut the corresponding depth fields are only of 55×305spatial resolution and relatively coarse quantization. In order to evaluate the performance of the proposedalgorithms quantitatively, we first applied leave-one-outcross-validation (LOOCV) as followswhere$N$ is the number of pixels in b$d$and dQ, μb$d$and μdQarethe empirical means of b$d$and dQ, respectively, while σb$d$and σ$dQ$are the corresponding empirical standard deviations.The normalized cross-covariance C takes values between -1 and +1 (for values close to +1 the depths are very similarand for values close to -1 they are complementary).An important parameter in the global algorithm is thenumber of nearest neighbors$k$ to be used. The original Make3Dalgorithm was trained on images from the Make3D dataset#1 and associated laser-scanned depth maps of mostlyarchitectural structures. Admittedly, it was not optimizedfor indoor scenes that the Kinect depth dataset is composedof, however there is no option provided to re-train Make3Don other

datasets. The method of Karsch *et al.* is essentiallybased on our earlier work using SIFT flow . It consistsof finding nearest neighbors using high-level features (theyuse $k =$ 7), followed by SIFT-flow to warp the k depthfields to the current image, and optimization to combinethe warped depths while imposing a smoothness constraintand a global depth prior. They do not, however, use mediandepth fusion and CBF.Table I shows experimental results obtained from 534.have no training phasebut learn the depth from k best examples found for eachquery image. As we have already mentioned, the Make3D algorithm. However, the skew of the building and lamp post in the first row and the edge jaggedness on the building wall in the second row for images produced by the Make3D algorithm are visually disturbing1..

6. CONCLUSION

We have proposed a simplified data-driven 2D-to-3D conversion method and have objectively validated its performanceagainst state-of-the-art Make3D algorithm. Theproposed algorithm compares favorably in terms of both estimateddepth quality and computational complexity. Admittedly,the validation was limited to a database of indoorscenes on which Make3D was not trained. The generatedanaglyph images produce a comfortable 3D perception butare not completely void of distortions. With the continuouslyincreasing amount of 3D data on-line and with therapidly growing computing power in the cloud, the proposedalgorithm seems a promising alternative to operator assisted 2D-to-3D conversion.

REFERENCES

[1] L. Agnot, W.-J.Huang and K.-C. Liu, "A 2D to 3D Video and Image Conversion Technique Based On a Bilateral Filter", In Proc. SPIE Three-Dimensional Image Processing and Applications, Vol.7526, Feb. 2010.

[2] T. Brox, A. Bruhn, N. Papenberg and J. Weickert, "High High Accuracy Optical Flow Estimation Based On a Theory for Warping", Proc.European Conf. Computer Vision, 2004, pp.25-36.

[3] N. Dalal and B. Triggs, "Histograms of Oriented Gradients for Human Detection", In Proc. IEEE Conf. Computer Vision Pattern Recognition, 2005, pp.886-893.

[4] F. Durand and J. Dorsey, "Fast Bilateral Filtering for The Display of High-Dynamic-Range Images", ACM Transaction Graph., Vol.21, July 2002, pp.257-266.

[5] M. Grundmann, V. Kwatra and I. Essa, "Auto-Directed Video Stabilization with Robust L1 Optimal Camera Paths", IEEE Transaction. pp.225-232.

PAPR Reduction and Performance Analysis of Alamouti MIMO-OFDM Systems Using P-SLM Scheme

A. Vanathi[1], S. Venkatachalam[2] and Dr. T. Manigandan[3]

[1&2]Department of Electronics and Communication Engineering, Kongu Engineering College,
Erode - 638 052, Tamil Nadu

[3]Principal, P. A College of Engineering and Technology, Pollachi - 642 002, Tamil Nadu

E-mail: vanu.nathi@gmail.com, sv@kongu.ac.in, manigandan_t@yahoo.com.

Abstract

Multiple input and multiple output orthogonal frequency division multiplexing (MIMO-OFDM) is a high-flying technology for fourth generation mobile radio communication. OFDM is a special case of multi-carrier-modulation (MCM) technique that divides the high data rate input bit streams into large number of lower rate sub streams and each sub stream is transmitted over orthogonal subcarriers. The main benefit of MIMO-OFDM system is its resourceful deployment of bandwidth, multipath delay spread tolerance and alleviation of inter symbol interference (ISI) in frequency selective fading channels. However, the main drawback of MIMO-OFDM system is high peak to average power ratio (PAPR). One of the well-known peak to average power ratio (PAPR) reduction schemes for MIMO-OFDM systems is selected mapping (SLM) scheme. In this paper, phase offset selected mapping (P-SLM) scheme is proposed which is used to reduce the PAPR in Alamouti coded MIMO-OFDM systems. The P-SLM scheme does not need to reserve bits for the transmission of side information, resulting in increase of the data rate. Theoretical analysis and simulation results show that the P-SLM scheme could offer good PAPR reduction performances compared to the conventional SLM scheme.

Keywords: Multiple input multiple output orthogonal frequency division multiplexing (MIMO-OFDM), Peak-to-average power ratio (PAPR), Phase offset - selected mapping (P-SLM), Blind selected mapping (B-SLM).

1. INTRODUCTION

Multiple-input multi-output orthogonal frequency division multiplexing (MIMO-OFDM) systems have achieved significant interests due to its potential in achieving high data rate and providing reliable performance of diversity and spatial multiplexing. However, the shortcoming of OFDM-based transmission systems is the high peak-to-average power ratio (PAPR) of the transmitted signals [9]. This in turn leads to in-band distortion across subcarriers and undesired spectral regrowth if the linear range of the high power amplifier (HPA) is not sufficient at the OFDM transmitter.

To reduce the PAPR of the OFDM many techniques have been developed such as clipping and filtering [4], partial transmit sequence (PTS) [10], selective mapping (SLM) [2], companding [8] and adaptive all pass filters [3]. Many techniques have been proposed to reduce PAPR in MIMO-OFDM [7] also. SLM technique is considered as the best among the available techniques, since it reduces the PAPR value without causing any

distortion to the signal. In conventional SLM technique, the OFDM signal is phase rotated using the phase rotation sequence and the sequence is transmitted as side information (SI) along with the transmitted signal. Due to these extra bits, data rate is decreased. Further, the SI interferes in the frequency selective fading channels, leading to huge degradation of the system in terms of bit error rate (BER). The available blind SLM (B-SLM) scheme for Alamouti MIMO-OFDM systems performs PAPR reduction without the use of SI [5]. The phase rotation sequence in B-SLM uses only 1,-1 which is not suitable for many cases.

In this paper, a phase offset SLM scheme, called as the P-SLM scheme, is proposed to reduce the PAPR in Alamouti MIMO-OFDM systems without SI. In P-SLM scheme, the signals at different transmitting antennas are differentiated from one another using phase offsets. These phase offsets correspond to the phase rotation sequence and hence transmission of SI is not required here. At the receiver, minimum Euclidean distance (MED) decoder is proposed, which decodes the signal

with phase offset that has minimum Euclidean distance. Since SI can be estimated from the phase offsets, no extra bits are reserved.

The rest of the paper is organized as follows: In Section 2, a brief description of Alamouti MIMO-OFDM systems is given. Section 3 reviews about C-SLM scheme. The P-SLM scheme is proposed in detail in Section 4. In Section 5, simulation results of P-SLM scheme compared with other schemes are shown. The conclusion is summarized in Section 6.

2. ALAMOUTI MIMO – OFDM SYSTEMS
2.1 Alamouti MIMO-OFDM Systems Selecting a Template

In this paper, Alamouti MIMO-OFDM systems with two transmit antennas [1] based on Alamouti space frequency block coding (SFBC) is considered. Hence the input data block, X={X(k), k=0,1,…,N-1} is encoded into two vectors X_1 and X_2, given by equation (2.1),

X_1 = [X(0), -X*(1), …, X(N-2), - X*(N-1)],
X_2 = [X(1), X*(0), …, X(N-1), X*(N-2)]   - (2.1)

where X(k) is modulated by a given signal constellation , N is the number of sub-carriers, and (.)* denotes the complex conjugate operation.

After inverse fast Fourier transform (IFFT) operation, the time domain signal, x_i = [x_i(0), x_i(1),…, x_i(JN-1)] is given by equation (2.2),

$$x_i(n) = \frac{1}{\sqrt{N}} \sum_{k=0}^{N-1} X_i(k) e^{\frac{j2\pi kn}{JN}}$$ - (2.2)

where, i = 1, 2 and n = 0, 1, … JN-1. The oversampling factor J is an integer.

2.2 PAPR in Alamouti MIMO-OFDM Systems

Generally, the PAPR of MIMO-OFDM signals at each antenna is defined by the equation (2.3),

$$PAPR_i = \frac{\max_{0 \le n \le JN-1} |x_i(n)|^2}{E[|x_i(n)|^2]}$$ - (2.3)

where, E[.] represents the expectation.

The PAPR of Alamouti MIMO-OFDM signals is defined as given in the equation (2.4),

$$PAPR = \max_{i=1,2}\{PAPR_i\}$$ - (2.4)

3. C-SLM SCHEME

In C-SLM scheme, the U phase rotation sequence is given by equation (3.1),

$$P^u(k) = e^{j\Psi^u(k)}$$ - (3.1)

where,   =[0,2š), k=0,1,…N-1, and u=0,1,…N-1. The phase rotated signal is obtained by multiplying the original signal with that of the phase rotation sequence as in equation (3.2)

$X^u(k) = P^u(k)*X(k)$ - (3.2)

The phase rotated signal is then encoded into two vectors namely   , using   Alamouti SFBC [6] which is given in equation (3.3) and (3.4) respectively,

= [P^u(0)X(0), - P^{u*}(1) X*(1), …, P^u(N-2) X(N-2), -P^{u*}(N-1) X*(N-1)]   - (3.3)

= [P^u(1)X(1), P^{u*}(0) X*(0), …, P^u(N-1) X(N-1), P^{u*}(N-2) X*(N-2)]   - (3.4)

Then the encoded phase rotated signals are converted into time domain signals by IFFT operation, and the signal with minimum PAPR is chosen as the optimal set for transmission.

The U phase rotation sequences are transmitted as the SI to the receiver with $\log_2 U$ bits.

4. P-SLM SCHEME

In P-SLM scheme, for U different phase rotation sequence, corresponding U phase offsets are generated as given by the equation (4.1),

$$Po(u) = e^{j2\pi u /U}$$ - (4.1)

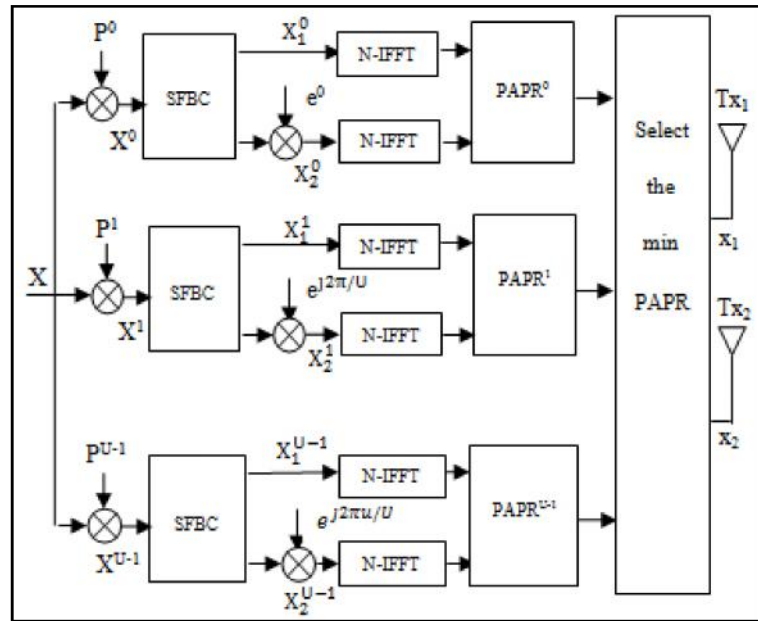A.Vanathi[1], S.Venkatachalam[2] and Dr. T. Manigandan[3]

Fig.1 Block diagram of P-SLM Scheme

The block diagram of the P-SLM scheme at the transmitter end is as shown in the Figure 1.

As shown in Figure 1, the OFDM signal is first phase rotated by the unique phase rotation sequence and then encoded into two vectors using SFBC, and then phase offsets corresponding to the phase rotation sequence are added to the second encoded signals. The signal is converted into time domain via IFFT operation. Finally, the signals with minimum PAPR (x_1 and x_2) are transmitted to the receiver via two antennas Tx_1 and Tx_2 respectively, via the fading channel with additive white Gaussian noise (AWGN).

At the receiver, the received signal is multiplied by the phase offset values, and the signal with minimum Euclidean distance (MED) is recovered, since the phase offset value can be detected using MED decoder, the unique phase rotation sequence corresponding to it can be obtained, hence no need of transmission of SI is needed in P-SLM scheme.

5. SIMULATION RESULTS

In this section, simulations are conducted to evaluate the performance of the proposed P-SLM scheme in terms of PAPR reduction and BER and its performance is compared with that of B-SLM scheme. The OFDM signals with data block of size 10^4 and N=1024 are generated. The phase offset is chosen in [-1,1].

The simulations are done using MATLAB for P-SLM, and B-SLM schemes.
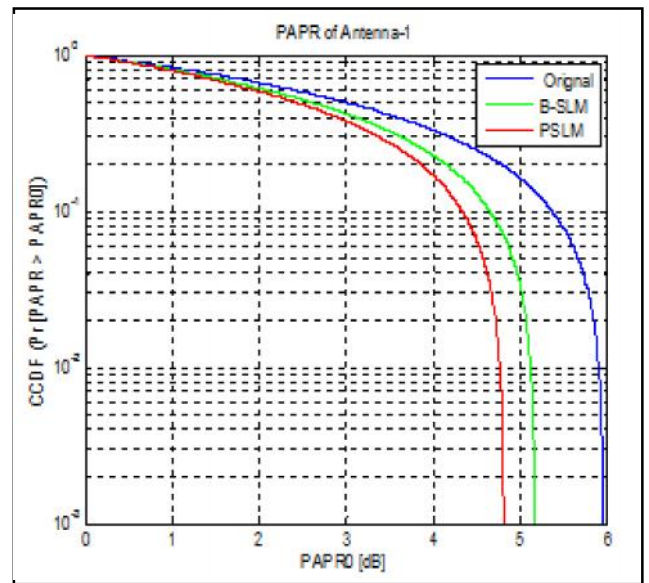
Fig.2 Comparison of PAPR Reduction Performances for Original signal, B-SLM SCHEME, P-SLM SCHEME at Antenna-1

The complementary cumulative distribution functions (CCDF) of the PAPR of the original signal, and other signals generated using B-SLM scheme, P-SLM scheme at antenna 1 and 2 respectively are shown in Figures 2 and 3.
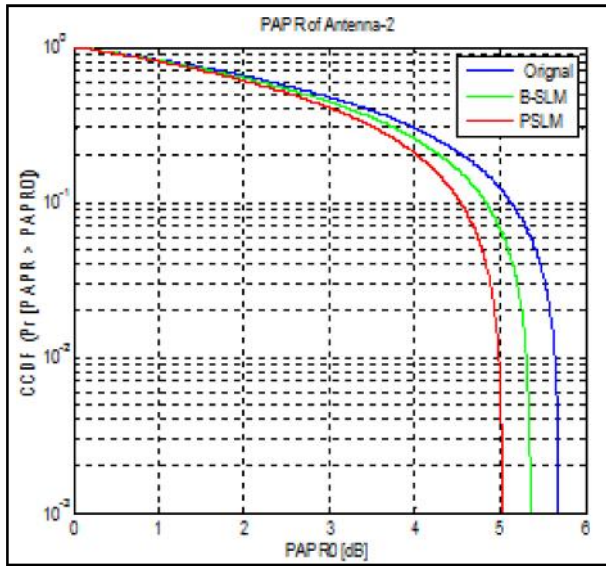
Fig.3 Comparison of PAPR Reduction Performances for Original signal, B-SLM SCHEME, P-SLM SCHEME at Antenna-2

From Figures 2 and 3, it is obvious that the PAPR reduction Performance of P-SLM scheme is better than that of B-SLM scheme and the original signal.

PAPR values for different OFDM signals at antenna 1 and antenna 2 are calculated and are shown in Table 1 and 2 respectively, which show that the performance of P-SLM scheme is better than the B-SLM scheme.

The BER performance of P-SLM and B-SLM schemes obtained after recovering the signal at the receiver is shown in the Figure 4.

Table 1 PAPR Values For Different OFDM Signals At Antenna-1

Original OFDM Signal	5.9723	6.1383	6.2231	6.1964	6.7751
B–SLM	5.2113	5.5245	5.2965	4.9518	5.3633
P–SLM	4.8146	5.0202	5.1782	4.4777	4.9064

Table 2 PAPR Values For Different OFDM Signals At Antenna-2

Original OFDM Signal	5.7158	6.1792	5.9466	6.2393	6.8830
B–SLM	5.3812	5.4525	5.3584	4.9860	5.1494
P–SLM	5.0982	4.6889	5.3361	4.9269	4.4784
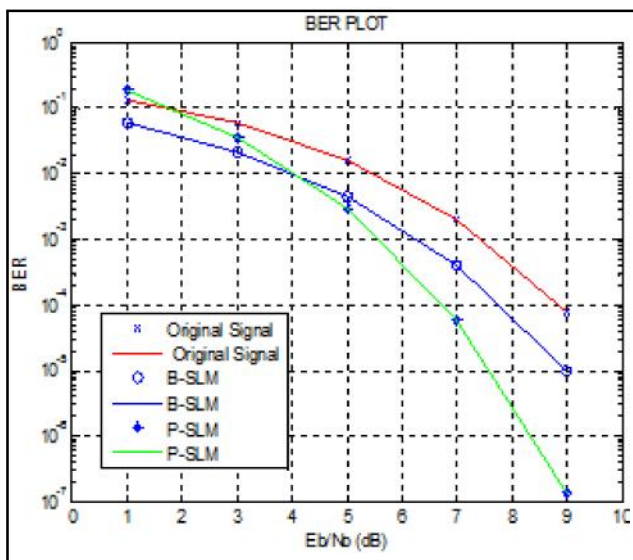
Fig.4 BER Performance of Original signal, B-SLM scheme, P-SLM scheme

From Figure 4, it is observed that the performance of P-SLM scheme is better than that of the B-SLM scheme.

6. CONCLUSION

In this paper, P-SLM scheme is proposed to reduce the PAPR in Alamouti MIMO-OFDM systems without side information, by using the phase offset values corresponding to the phase rotation sequences used. Since no SI needs to be transmitted in this scheme it provides increase in the data rate compared to C-SLM scheme. From the simulation results it is clear that the PAPR reduction performance of P-SLM scheme is better than that of B-SLM scheme.

A.Vanathi[1], S.Venkatachalam[2] and Dr. T. Manigandan[3]

REFERENCES

[1] S. M. Alamouti, "A Simple Transmit Diversity Technique for Wireless Communications", IEEE J. Sel. Areas Commun., Vol. 16, Oct. 1998, pp.1451-1458.

[2] R.W.Bäuml, R. F. H. Fischer and J.B. Huber, "Reducing the Peak-To Average Power Ratio of Multicarrier Modulation by Selective Mapping", Electron. Lett., Vol.32, No.22, Oct.1996, pp.2056-2057.

[3] E.Hong and D. Har, "'Peak-to-average Power Ratio Reduction for MISO OFDM Systems with Adaptive All-Pass Filters", IEEE Trans. Wireless Commun., Vol.10, No.10, Oct. 2011, pp.3163-3167.

[4] X. Li and L.J. Jr. Cimini, "Effects of Clipping and Filtering on The Performance of OFDM", IEEE Commun. Lett., Vol.2, No.5, May 1998, pp.131-133.

[5] M. F. Naeiny and F. Marvasti, "Selected Mapping Algorithm for Papr Reduction of Space-Frequency Coded OFDM Systems without Side Information", IEEE Trans. Veh. Technol., Vol.60, No.3, Mar. 2011, pp.1211-1216.

[6] V. Tarokh, H. Jafarkhani and A.R. Calderbank, "Space-Time Block Codes From Orthogonal Designs", IEEE Trans. Inf. Theory, Vol.45, No.5, Jul. 1999, pp.1456-1467.

[7] S. H. Wang and C. P. Li, "A Low-Complexity PAPR Reduction Scheme for SFBC MIMO-OFDM Systems", IEEE Signal Process. Lett., Vol.16, No.11, Nov. 2009, pp.941-944.

[8] Y. Wang, L.-H, Wang, J.-H. Ge and B. Ai, "Nonlinear Companding Transform Technique for Reducing PAPR of OFDM Signals", IEEE Transactions on Consumer Electronics, Vol.58, No.3, Aug. 2012.

[9] Yasir Rahmatallah and Seshadri Mohan, "Peak-To-Average Power Ratio Reduction in OFDM Systems: A Survey And Taxonomy", IEEE Communications Surveys & Tutorials, Accepted for Publication.

[10] Y. Zhou and T. Jiang, "A Novel Multi-Points Square Mapping Combined with PTS for PAPR Reduction of OFDM Signals Without Side Information", IEEE Trans. Broadcast., Vol.55, No.4, Dec. 2009, pp.831-835.

Information for Authors

1. All papers should be addressed to The Editor-in-Chief, Indian Journal of Engineering, Science, and Technology (IJEST), Bannari Amman Institute of Technology, Sathyamangalam - 638 401, Erode District, Tamil Nadu, India.
2. Two copies of manuscript along with soft copy are to be sent.
3. A CD-ROM containing the text, figures and tables should separately be sent along with the hard copies.
4. Submission of a manuscript implies that : (i) The work described has not been published before; (ii) It is not under consideration for publication elsewhere.
5. Manuscript will be reviewed by experts in the corresponding research area, and their recommendations will be communicated to the authors.

Guidelines for submission

Manuscript Formats

The manuscript should be about 8 pages in length, typed in double space with Times New Roman font, size 12, Double column on A4 size paper with one inch margin on all sides and should include 75-200 words abstract, 5-10 relevant key words, and a short (50-100 words) biography statement. The pages should be consecutively numbered, starting with the title page and through the text, references, tables, figure and legends. The title should be brief, specific and amenable to indexing. The article should include an abstract, introduction, body of paper containing headings, sub-headings, illustrations and conclusions.

References

A numbered list of references must be provided at the end of the paper. The list should be arranged in the order of citation in text, not in alphabetical order. List only one reference per reference number. Each reference number should be enclosed by square brackets.

In text, citations of references may be given simply as "[1]". Similarly, it is not necessary to mention the authors of a reference unless the mention is relevant to the text.

Example

[1] M.Demic, "Optimization of Characteristics of the Elasto-Damping Elements of Cars from the Aspect of Comfort and Handling", International Journal of Vehicle Design, Vol.13, No.1, 1992, pp. 29-46.
[2] S.A.Austin, "The Vibration Damping Effect of an Electro-Rheological Fluid", ASME Journal of Vibration and Acoustics, Vol.115, No.1, 1993, pp. 136-140.

SUBSCRIPTION

The annual subscription for IJEST is Rs.600/- which includes postal charges. To subscribe for IJEST a Demand Draft may be sent in favour of IJEST, payable at Sathyamangalam and addressed to IJEST. Subscription order form can be downloaded from the following link http:// www.bitsathy. ac.in./ ijest.html.

For subscription / further details please contact:

Indian Journal of Engineering, Science, and Technology

Volume 8, Number 1&2, January - December 2014

CONTENTS